Effect of Chemistry on the Transformation of Austenite to Martensite for Intercritically Austempered Ductile Iron

Sayanti Banerjee

Thesis submitted to the faculty of the Virginia Polytechnic Institute and State University in partial fulfillment of the requirements for the degree of

Master of Science
In
Materials Science and Engineering

Alan P. Druschitz
Norman Dowling
William Reynolds
Jerry Hunter

7th December 2012
Blacksburg, Virginia

Keywords: martensitic transformation, critical stress, neutron diffraction, ductile iron, intercritical heat treatment, lattice strain, diffraction elastic constants, scanning electron microscopy, transmission electron microscopy, residual stress, intergranular stress, intragranular stress

Effect of Chemistry on the Transformation of Austenite to Martensite for Intercritically Austempered Ductile Iron

Sayanti Banerjee

ABSTRACT

Intercritically austempered ductile iron (IADI) with a matrix microstructure of ferrite plus metastable austenite has an excellent combination of strength and toughness. The high strength and good ductility of this material is due to the transformation of metastable austenite to martensite during deformation. In the present study, the transformation of austenite to martensite for intercritically austempered ductile irons of varying alloy chemistry (varying amounts of nickel and/or manganese) were examined using in-situ neutron diffraction under strain-controlled loading at VULCAN at the Spallation Neutron Source at Oak Ridge National Laboratory (ORNL). Both diffraction and tensile data were collected and synced using the VDRIVE software (a proprietary ORNL software package). The single peak fit method was employed in the analysis of the diffraction data.

In this thesis, the stress and strain for the start of the transformation of metastable austenite to martensite were determined. The development of residual stresses during deformation and the elastic diffraction constants for both the ferrite and austenite phases were also determined. The material was characterized using optical microscopy, backscattered imaging in the scanning electron microscopy, energy dispersive spectroscopy and transmission electron microscopy.

DEDICATION

I would like to dedicate my work to my grandfather, Mr. Asoke Kumar Banerjee and to my sister, Semanti Banerjee, both of whom give me the inspiration of moving past all difficulties.

ACKNOWLEDGEMENTS

At the concluding steps of my Master of Science degree I would like to acknowledge many people from various institutions who have made this journey possible for me. Firstly, I would like to thank my adviser, Dr. Alan P. Druschitz, who has guided me through these two years of hard work. His valuable inputs and endless support not only made this degree possible but also introduced me to a field of metals and experimentation. I will like to express my sincere gratitude to him for his insights and thank him for sharing his knowledge with me.

I would also like to thank my committee members, Dr. Norman Dowling, Dr. William Reynolds and Dr. Jerry Hunter, not only for their academic advice and insights, but also the care and help they showed towards my academic and personal betterment throughout my stay in Virginia Tech. In a situation where I lost all hope, Dr. Dowling gave me the confidence to move forward and without him this degree was not possible. Dr. Reynolds was there to help with my endless queries and he was ever so supportive in all my academic pursuits. Dr. Hunter, or Jerry as he wants his students to call him, is one of the friendliest professors I ever took a class with and his support and words of wisdom will help me throughout my career. I am really lucky to get a chance to come in touch with them and I will cherish my experience working with them forever.

I would also like to show my gratitude towards Dr. Mitsu Murayama, Dr. Niven Monsegue, Stephen McCartney, Jay Tuggle and all those who have helped me getting trained in NCFL, ICTAS and made me have a wonderful time doing so. I will also like to thank Dr. Ke An, Dr. Alexandru D. Stoica, Dr. Dong Ma, Spallation Neutron Source, Oak Ridge National Laboratory. for their co-operation and guidance. I will also like to express my gratitude to Dr. Carlos Suchicital, Kim Grandstaff, Diane Folz, and all of MSE who was my family during my stay here at Virginia Tech.

In the end, I will like to thank my family back in India, my parents and grandparents, my loving fiancé, Tamoghna Roy and all my friends at Virginia Tech without whose support, encouragement and love nothing would have been possible.

TABLE OF CONTENTS

LIST OF TABLES

LIST OF FIGURES

Chapter 1 Introduction

1.1 Overview

The materials used in modern motor vehicles are chosen on the basis of specific mechanical and physical properties. Normally, a change of materials is only considered if a cost reduction or performance improvement can be realized. Current reasons for a material change are increased strength and toughness, improved fatigue properties or reduced manufacturing cost. Weight reduction results in improved performance and increased fuel efficiency.

Ductile irons that exhibit transformation induced plasticity (TRIP) have tremendous potential for automotive applications. Presently, steel and aluminum are the primary materials of choice. TRIP ductile iron has high yield strength (380-550 MPa), high ultimate tensile strength (500-900 MPa), good ductility (14-20%), good fracture toughness (45-55 MPa-$m^{1/2}$), good resistance to environmental cracking, excellent castability and good machinability, and is therefore a viable alternative to presently used materials [1-14]. Figure 1-1 shows, the weight and cost per unit yield strength for TRIP ductile iron (intercritically austempered ductile iron or IADI) are better in comparison to aluminum alloys and even some steels. (Forged steel normalized to 1)[15].

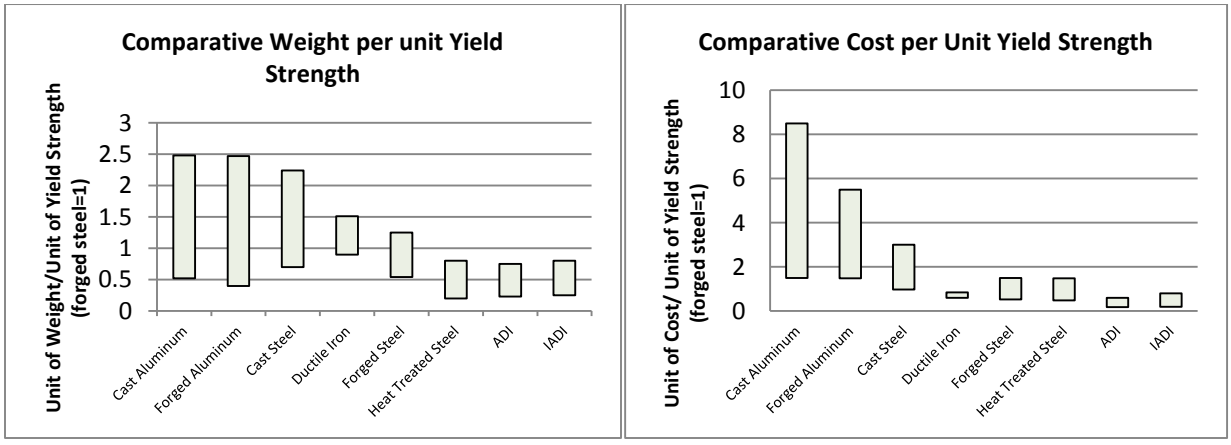

Figure 1-1: Comparative Weight and Cost per unit Yield Strengths (based on data by Keough. J.R. and Hayrynen. K.L [15])

1.2 Ductile Iron

Ductile iron is a type of cast iron. The carbon in the microstructure of cast irons may be present as iron carbide or elemental carbon (graphite). One of the various ways to classify cast iron is by the shape of the carbon in the microstructure. Ductile iron is also known as nodular cast iron [16], as the graphite in the microstructure is in form of nodules or spheres. Usually a magnesium based treatment alloy is added to the molten metal to produce the spheroidal graphite. Changing the shape from flakes (grey iron) to nodules (ductile iron) in the microstructure produces the improved toughness and improved fatigue properties by minimizing the stress concentration factor due to the graphite flakes.

The matrix in ductile iron can be ferritic, pearlitic, martensitic, austenitic or a combination of these phases. Addition of certain austenite stabilizers, like nickel or manganese can promote the formation of metastable austenite. The matrix has a great deal of influence over the mechanical properties. A dual-phase matrix composed of ferrite and austenite can enhance the mechanical properties of ductile iron. It is clear from figure 1-2 that dual-phase intercritically austempered ductile iron shows noticeable improvement in ductility compared to pearlitic ductile iron and strength compared to ferritic ductile iron [10]. Compared to ferritic ductile iron, IADI has twice the yield strength with similar ductility. Intercritically austempered ductile iron has slightly higher yield strength than pearlitic ductile iron and almost double the elongation to fracture.

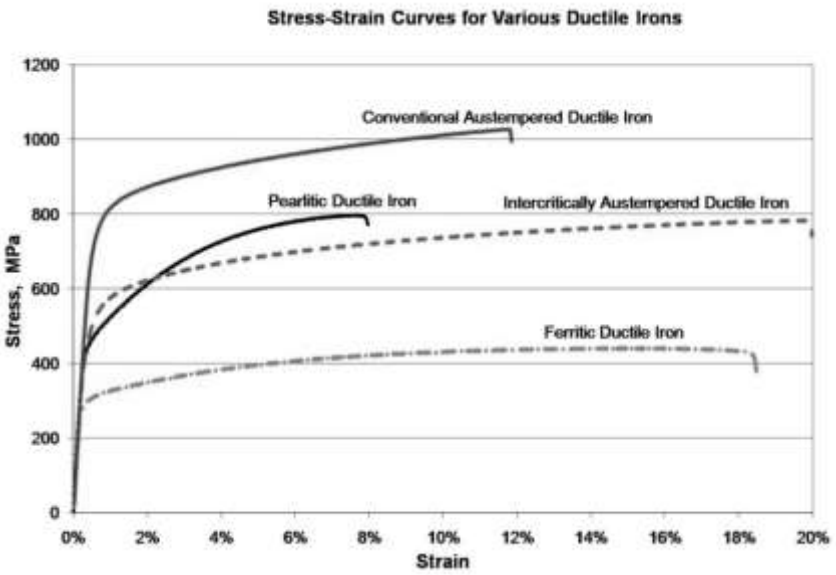

Figure 1-2: Effect of matrix microstructure on properties of ductile iron

Ductile iron is an alloy of iron, carbon and various other alloying elements. Carbon, silicon and sulfur are needed to be held at a particular level for desired distribution and shape of graphite nodules. Sulphur must be reduced to less than 0.02%. Magnesium and rare earth alloys are introduced in the melt for the desired shape, size and distribution of graphite nodules[16]. It is necessary to minimize lead, antimony, titanium, bismuth, zirconium etc. [17]. Unalloyed magnesium or rare earth metal and magnesium-based ferrosilicon nodulizers can also be used in certain special cases depending on requirements[17]. Rare earth elements are also used to neutralize the harmful effect of lead.

The phase matrix of ductile iron primarily depends on the carbon content of the matrix, which can be given by equation 1.

$$C_{Matrix} = C_{total} - C_{graphite}$$

$$= C_{total} - (Vol\,\%\,of\ graphite\ nodules \times \rho_C) \quad (1)$$

Where C_{total} is the total % of carbon in the alloy, C_{Matrix} is the % of carbon in the matrix, $C_{graphite}$ is the % of carbon present as graphite nodules, ρ_C is the density of graphite under ambient temperature and atmospheric pressure.

If the matrix has more than 0.008% C in it, the iron-iron carbide equilibrium phase diagram suggests there will be some amount of pearlite present. However, the presence of equilibrium phases can be varied by non-equilibrium heat treatments, like annealing and quenching, or the addition of alloying elements [1-4, 6-9, 17, 18]. Silicon (~2%) greatly modifies the equilibrium phase diagram by changing the carbon equivalent and makes intercritical heat treatment possible [17]. Alloying elements like nickel, manganese etc. improves the hardenability [17] and causes the carbon in the pearlite to go into solid solution in the austenite forming martensite upon cooling. Thus, ductile iron containing nickel or manganese may have a dual phase matrix microstructure containing ferrite and metastable austenite. The presence of metastable austenite in the microstructure is crucial for TRIP ductile iron alloys like IADI, because the transformation of metastable austenite to martensite which absorbs energy and thus has superior mechanical properties compared to ferritic or pearlitic ductile iron [3, 10-14]

1.3 Heat Treatment

Alongside alloying, various heat treatments are employed to most of the iron based alloys to modify the microstructure and consequently mechanical properties to make them suitable for certain applications. The heat treatments may be thermal or thermo-mechanical depending on the application. Most common thermal processes include annealing, normalizing, stress-relieving, quenching and tempering. Annealing, normalizing and stress relieving are mostly done for highly deformed materials to regain ductility. Tempering involves heating the material to an elevated temperature and holding it there for a set amount of time. The temperature the material is heated to and the time for which the material is held at the temperature are the two major factors in predicting their final properties. The tempering temperature may be below the A_1 temperature of that alloy if the major intention is stress-relieving. The presence of around 2% Si in the microstructure allows ductile iron to have a ferrite-austenite two phase region above A_1 even for >2% C.

Intercritical austempering requires heating into a two-phase ferrite austenite region followed by quenching to prevent pearlite formation. But the material is quenched to a high enough temperature to prevent the formation of martensite. After holding the material at the desired temperature to stabilize the austenite due

to segregation of alloying elements, the material is allowed to cool to ambient temperature. The end result is a matrix composed of ferrite and metastable austenite. A detailed heat-treatment scheduled is schematically shown in figure 1-3.

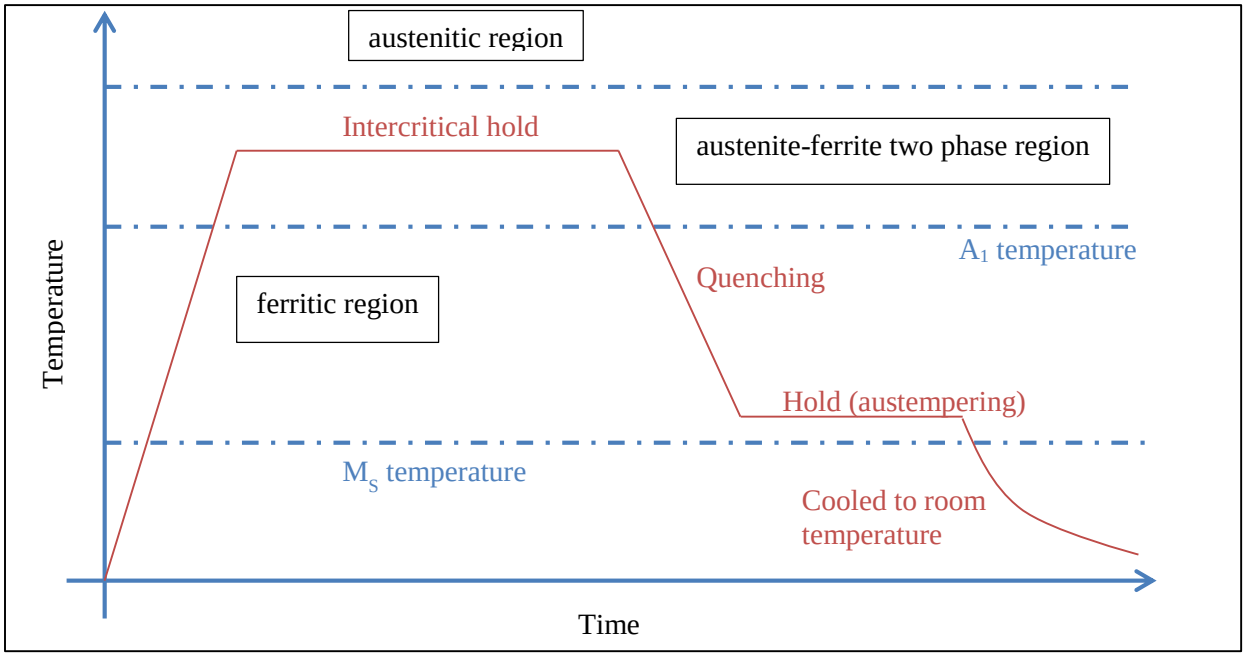

Figure 1-3: Schematic heat treatment schedule of IADI, time and temperature not to scale

The metastable austenite that is retained in the microstructure, as in case of IADI, is partially stabilized by addition of alloying elements like manganese and nickel which [17] retards the formation of pearlite. It also reduces the M_s temperature to some degree producing a larger temperature range for austempering. More will be discussed on heat treatments and alloying of IADI later on in this paper.

1.4 Intercritical heat treatment

For a given alloy chemistry, the volume fraction of austenite in the equilibrium microstructure is a function of the austenitizing temperature. The volume fraction of austenite in the microstructure can be deduced utilizing the lever rule. In a Fe-C-2%Si equilibrium phase diagram as given by figure 1-4, it is evident that as the austenitizing temperature increases, the volume fraction of austenite in the microstructure also increases[19, 20].

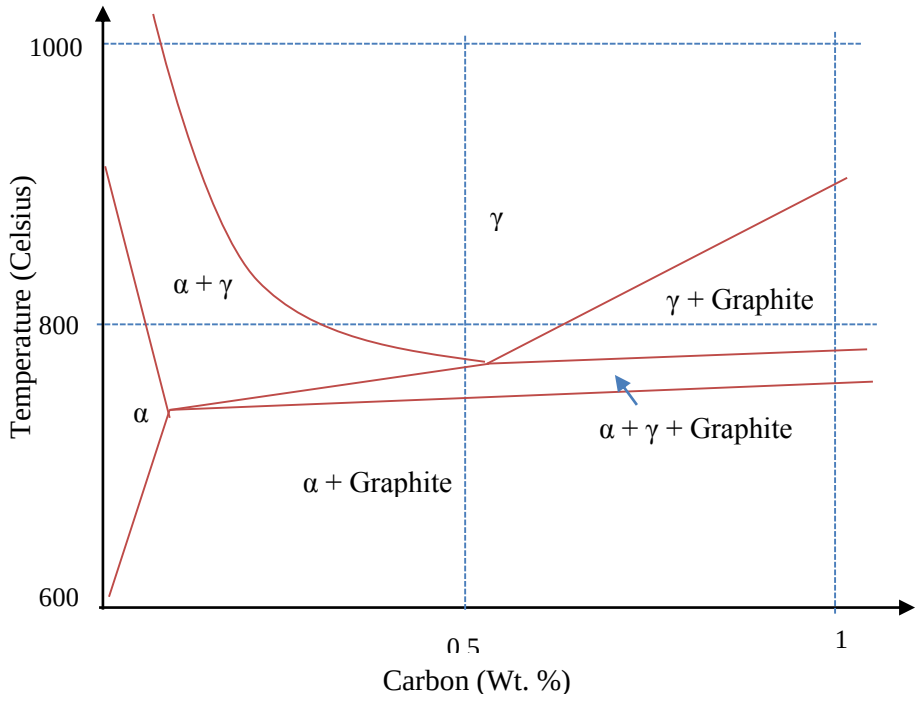

Figure 1-4: Fe-C-2% Si equilibrium phase diagram adapted from web resources, Herring, D.H. Industrial Heating.com, December 2004, pg.24 [21]

The austenite formation in the intercritical temperature range has three steps. The nucleation of austenite at ferrite-pearlite boundaries, dissolution of pearlite and growth of austenite are the initial steps. The second step is partitioning of carbon in the austenite. The third step is marked by the diffusion of substitutional elements like manganese and silicon in the ferrite-austenite grains. So, under the intercritical austenitizing conditions, equilibrium conditions can be achieved in terms of the austenite volume fraction and carbon content, but compositional equilibrium conditions for subsitutional alloying elements is not possible due to limited time for diffusion[22, 23]. Thus, the austenite is in a state of para-equilibrium rather than complete equilibrium, the equilibrium being limited by comparatively short holding time at intercritical temperatures [24].

1.4.1 Intercritical heat treatment in ductile iron

Intercritical heat treatments in ductile iron have three phases. First, the material is partially austenitized, then it is quenched and lastly it is austempered. Quenching from austenite to room temperature will produce martensite, which is hard and brittle. So, quenching to a temperature above martensite start temperature is performed. The material is then held at this temperature for a prescribed period of time to stabilize the austenite before cooling to room temperature. Austempering gives rise to dual-phase austenite-ferrite microstructure in ductile irons, the volume of austenite being dependent on the chemistry of the alloy and intercritical austenitizing temperature.

During austenitizing, the heterogeneous nucleation of austenite starts from intercellular boundaries [25]. The carbon content of austenite is primarily a function of austenitizing temperature. For unalloyed ferritic ductile iron, the necessary carbon for the formation of austenite at higher temperatures comes from the graphite nodules. Thus increasing the austenitizing temperature causes more carbon from graphite to go into solution in austenite, increasing the carbon content [2, 26]. For IADI, a ferritic matrix cannot be used because the austenitizing temperature is too low for significant dissolution and diffusion of carbon from graphite nodules. Using ductile iron with ferrite-pearlite matrix, Druschitz et al. suggested that carbon for the austenite comes from the carbon in pearlite. Thus under these conditions, the diffusion from carbon from the graphite nodules is limited [27].

The partitioning of alloying elements like manganese, nickel, copper in the austenite is limited due to low diffusivity of these elements at the intercritical temperature range [22, 23]. Very few studies have been conducted on the segregation of these elements in dual phase ductile iron. But referring to the studies conducted on dual-phase steels, it is safe to assume that, austenite formed by dissolution of pearlite has higher concentration of manganese due to dissolution of ferro-manganese carbide complexes, and those formed near the graphite shows elevated concentration of copper or nickel which do not form carbides in ferrous alloys.

1.4.1.1 Intercritical heat treatment in dual-phase ductile iron

A chronological study of experimental intercritical heat treatment effectively demonstrates the evolution of IADI. In 1981, Wade et al. made the first known attempt to achieve a dual phase ferritic-ausferritic matrix in ductile iron. The starting material had a ferritic microstructure. It was austenitized in the single phase austenite region, the holding time being short and hence the material was only partially austenitized. The volume fraction of austenite was thus a function of holding time, the nucleation being limited to the areas surrounding the graphite nodules, and the carbon being supplied solely by the nodules. The resultant microstructure had duplex matrices of various proportions consisting mainly of ferrite-pearlite. [28]

In 1988, Kobayashi et al. used ductile iron alloyed with silicon, nickel, manganese and copper, and austenitized it in the intercritical range. The treatment was followed by oil-quenching and austempering yielding a mixed microstructure composed of ferrite, bainitic ferrite, and austenite. The resultant product showed an improved toughness achieved by strengthening the intergranular area and the areas surrounding the graphite nodules which were the primary sites for micro-crack initiation. An "abnormal elongation due to the TRIP effect in the austenite phase" was also achieved due to the use of appropriate alloying elements. [29]

Aranzabal et al. also employed intercritical austenitizing of fully ferritic ductile iron followed by austempering in the upper bainitic temperature range. The resultant microstructure was ferrite-ausferrite. The heat treatment was done at constant intercritical austenitizing temperature, while variation of volume fraction of ausferrite in the structure was achieved by using different the silicon content which changes the ferrite-austenite transformation temperature. On comparison with existing grades of ductile iron it was observed that the ferrite-ausferritic matrix showed yield strength comparable to pearlitic ductile iron and ductility comparable to ferritic grades [7, 8]. High tensile strength (850MPa) and elongation to 20% was achieved by this treatment.

Kilicli and Erdogan also did intercritical austenitizing followed by austempering on a fully ferritic ductile iron. The temperature in this case was varied and the chemistry was kept constant. Increase in intercritical austenitizing temperature showed an increase in austenite and decrease in the amount of ferrite as can be predicted by the lever rule. Also, increasing the austenitizing temperature increased the concentration of carbon in austenite. The final product had better ductility that conventional ADI and yield strength similar to pearlitic grade ductile iron [2, 26]. Basso et al. used different intercritical austenitizing temperature and austempering temperatures on unalloyed ferritic ductile iron and concluded that the mechanical properties were predominantly determined by the intercritical austenitizing temperature and that the final microstructure was dependent on the austempering temperature [9].

Druschitz et al. used an intercritical austenitizing temperature ranging from 720^{o} C to 770^{o} C followed by austempering at 315^{o}C to 400^{o}C for ductile irons of various alloy chemistries. The ductile irons were alloyed with silicon, manganese, nickel, copper and molybdenum and had a ferrite-pearlite microstructure before heat treatment. The authors concluded that hardness and strength in the alloys were linearly proportional and increasing the austenitizing temperature increased the strength. Austempering temperature was found to have little effect on the tensile properties, but it improved the machinability, fatigue life and resistance to environmental cracking when compared to conventional ADI [3, 10-14, 30-32].

To sum up the effect of different heat treatments, figure 1-5 demonstrates a comparative study of the mechanical properties of various grades of ductile iron based on the heat treatment regime.

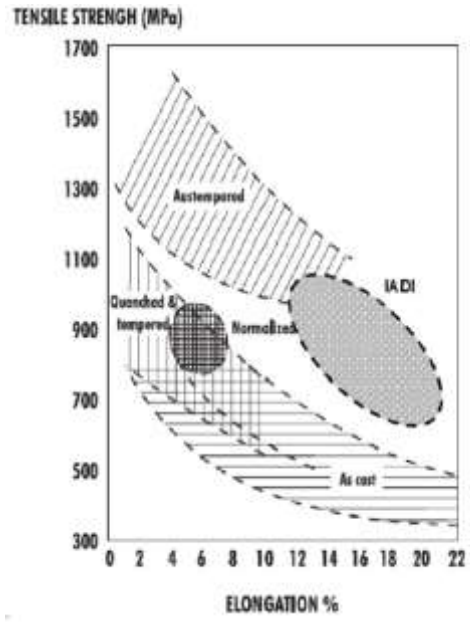

Figure 1-5: A comparative study of effect of heat treatments on the mechanical properties of ductile iron.

1.5 Alloy Chemistry

The chemistry of ductile iron is the most important factor contributing to the shape and distribution of graphite nodules and also the response of the matrix to various heat treatments. It is probably true to comment that almost all the elements in the periodic table have some effect on the microstructures and properties of ductile iron but the elements with significant importance are discussed in this section.

The Sorelmetal Book of Ductile Iron [17] classifies the elements by their influence on microstructure as follows:

- Primary elements: carbon, silicon, manganese, sulphur, phosphorus
- Spherodizing elements: magnesium, cerium, lanthanum
- Matrix controlling elements: copper, tin
- Alloying elements: nickel, molybdenum
- Carbide promoting elements: chromium, vanadium, boron, tellurium

- Subversive or graphite shape deteriorating elements: bismuth, aluminium, lead, arsenic, antimony, zirconium, nitrogen etc.

1.5.1 Carbon and Silicon

The carbon content in any form of cast iron is above 2 wt.%. For ductile iron, the carbon levels usually fall between 3.4-3.9 wt. %. Apart from carbon, the only other chief alloying element is silicon. Silicon promotes graphitization and hence helps suppress carbide formation, thus significantly increasing strength, as-cast ductility and hardness. But silicon has a negative effect on impact toughness since it raises the ductile-brittle transition temperature. This effect is most pronounced in ferritic ductile iron, as the impact toughness of pearlitic or ferritic-pearlitic grades are already considerably lower. The optimal level or recommended target level of these two elements are determined by the Hendersen Diagram [17], which gives a window so as to prevent shrinkage, graphite floatation during casting, poor impact toughness and white iron formation. Also, silicon is typically maintained in range of 2-2.75% to maintain acceptable carbon equivalent, where CE= %C+ 1/3 (%Si).

1.5.2 Manganese

Manganese is added in to ductile iron primarily to increase hardenability in the as-cast condition. Manganese promotes iron-carbide formation and some manganese forms substituional carbides, usually $(Fe\text{-}Mn)_3C$. Manganese is a very good austenite stabilizer since it pushes the pearlite start curves in TTT diagrams to longer times so that slower cooling from austenite can still lead to formation of martensite. But it must be noted that, a lot of manganese is needed to promote austenite formation at room temperature. Manganese also segregates at the last areas to solidify.

1.5.3 Sulphur and Phosphorus

Sulphur has a very strong affinity for magnesium, which is the primary nodulizer for ductile iron and readily leads to the formation of stable magnesium sulphide. So, to prevent excessive consumption of nodulizer

alloys, the sulphur concentration of the melt is kept well below 0.020% for MgFeSi treatment but can be higher for pure Mg treatment.

Phosphorus may have a detrimental effect on mechanical properties. Phosphorus is a pearlite promoting element in cast iron and can lead to Fe-P eutectic products. Increased concentration of phosphorus beyond 0.03% can cause severe embrittlement of the matrix due to segregation of phosphorus-rich phase in high energy areas like grain boundaries and graphite boundaries [17].

1.5.4 The Spherodizing or Nodulizing elements

Magnesium is the principle spherodizing element leading to formation of spheroidal graphite. In addition, magnesium is also a very potent deoxidizer of the melt.

Magnesium has a low melting point (1091^{o}C) and the temperature of molten iron may reach more than 1500^{o}C. Also, pure Mg has a lower density than iron. So, addition of elemental magnesium is tricky due to increased loss of nodulizer and also due to the fact it will float on the surface rather than sinking at the bottom [16]. So, ferrosilicon alloys enriched in magnesium are added to the melt to overcome this difficulty. Cerium, lanthanum and other rare earth elements can also be used. In the Fischer converter, magnesium in elemental form is used often.

Use of excessive manganese, above about 0.06% , may lead to the formation of carbides, porosity and dross. The risk increases with lower solidification rate, and thicker sections are more prone to carbide formation, low nodule count and other defects.

1.5.5 Alloying elements and matrix controlling elements

Copper is a pearlite enhancer which shows no tendency to form carbides. Thus, in pearlitic ductile irons it enhances the mechanical properties more efficiently than manganese. It leads to formation of finer pearlite improving the as-cast hardness and strength. The only drawback is currently the cost of copper.

Tin also serves the exact same purpose as copper. The only difference is, tin in excess of 0.1% may segregate along the grain boundaries and cause embrittlement.

Nickel is a very good austenite stabilizer, and is added in large proportions to achieve a fully austenitic matrix in as cast products. In smaller proportions (up to 4%), it is added to improve hardenability. If given a proper heat treatment, like intercritical austenitizing followed by austempering, nickel containing alloys may have a ferrite-austenite matrix as discussed in previous sections.

Molybdenum has similar effects on hardenability as nickel, but it is a ferrite stabilizer. In addition to nickel, molybdenum slows the formation of pearlite in the as cast or isothermally heat-treated matrix [17].

1.5.6 Carbide forming elements and Subversive elements

As stated in previous sections, carbide formation in the matrix is detrimental to the mechanical properties of the ductile iron. So, carbide forming elements like chromium, vanadium, boron, tellurium etc. are kept to a minimum.

When contaminated with subversive elements like bismuth, aluminium, lead, arsenic, antimony, zirconium, nitrogen, sulphur etc. the nodule count and morphology of the graphite is impaired. Flaky graphite, intercellular carbides and chunky carbides may form which deteriorate the mechanical properties of the ductile iron. The effect of lead can be counteracted by the addition of rare earth elements [17], others have a more permanent effect on the properties.

1.6 Austenite stabilizers

The unique combination of strength and ductility is the result of a microstructure of well-formed evenly distributed graphite nodules in a matrix of ferrite and austenite. The austenite can be in form of retained austenite or ausferrite.

Both manganese and nickel are austenite (γ)-stabilizers. They broaden the austenite domain of a typical iron-carbon phase diagram. The typical effect of both the elements on phases fields in the iron-cementite phase diagram for a given carbon content can be given by figure 1-6 .

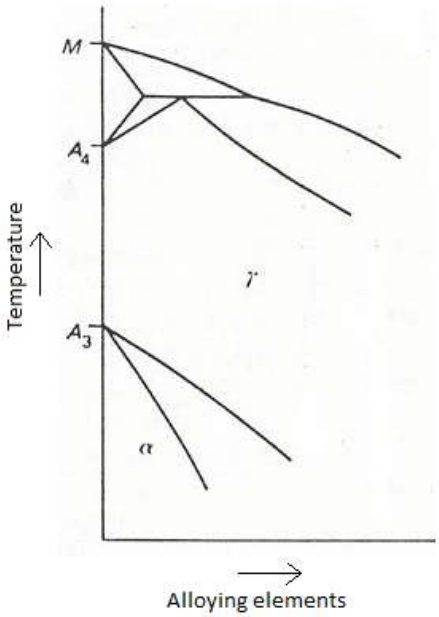

Figure 1-6: Effect of γ-stabilizers on the broadening of γ-region in Iron-Cementite system, Bain, E.C., ASM, [34]

Manganese, nickel and other austenite stabilizers not only improve the ductility and strength of iron, they also improve the hardenability, the ability of ferrous alloys to form martensite. Hardenability is typically measured as a depth below the surface of a quenched section which shows a hardness of 50 in Rockwell C scale, corresponding to a particular percentage of martensite in the microstructure [35]. Martensite containing large amounts of carbon is very brittle and thus requires tempering before use. Like carbon, alloying elements also play a very important role in determining the hardenability of ductile iron. Ferrite stabilizers like molybdenum, titanium etc. participates in competing process of carbide precipitation in the matrix, thereby depleting the austenite of both carbon and the alloying elements, thus decreasing the hardenability. Moreover, carbide precipitation forms active sites for pearlite nucleation during quenching, thus decreasing the hardenability even more. Austenite stabilizers, on the other hand, expand the austenite

field and allow for more carbon to go into solution in the austenite, thus improving the hardenability. During tempering, austenite stabilizers remain in solid solution in martensite and have a greater solid solution strengthening effect. They do not significantly retard the softening process. Ferrite stabilizers that form a fine dispersion of metallic carbides have higher hardness than martensite. They slowing down the softening process. Also, due to depletion of the carbon in the martensite, diffusion of carbon into new cementite particles is slow, which also decreases the response towards tempering [36].

Any element which stabilizes austenite in the microstructure can aid in the transformation of that austenite to martensite during deformation by altering the free energy of transformation, such that the process is not only induced by thermal energy, as in case of heat treatments but also by mechanical and chemical energies, that is through straining after alloying with favorable elements. More is discussed about this later in the chapter in section 1.7 [5, 37-40].

1.6.1 Transformation mechanism and surface free energy

Austenite stabilizers affect the transformation the austenite to martensite during deformation, the actual mechanism is dependent on the Surface Free Energy (SFE) of the alloy system.

α-ferrite deforms predominantly by slipping due the presence of numerous slip systems. If the SFE is high, the width of the extended dislocations will be relatively small further facilitating cross-slip mechanisms [37].

Austenite has many deformation mechanisms, it deforms by slipping and twinning, the predominant one is determined by SFE of the phase. The SFE, depending on the temperature and chemical composition [38], determines the width of the extended dislocation.

Most of the deformation in FCC crystals occurs on the {111} planes. One of the closed packed directions is <110> but owing to intervening atoms, this dislocation with burger's vector <110> breaks into two Shockley Partials in the <112> system. The deformed area between those two partials represents an extended dislocation [37].

If the width of the extended dislocation is small, it continues to glide in the close packed plane as a single unit. This area is also called a stacking fault. Lower the SFE, the width of the extended dislocation is larger and the stacking fault will be wider, hence it will be difficult for the fault to glide and it will chose twinning versus slipping as the preferred mode of deformation.

In figure 1-7, the dislocation with direction [110] has formed two Shockley Partials each at 60^0 to the parent dislocation in direction $[12\bar{1}]$ and [211] and the faulted region is shaded.

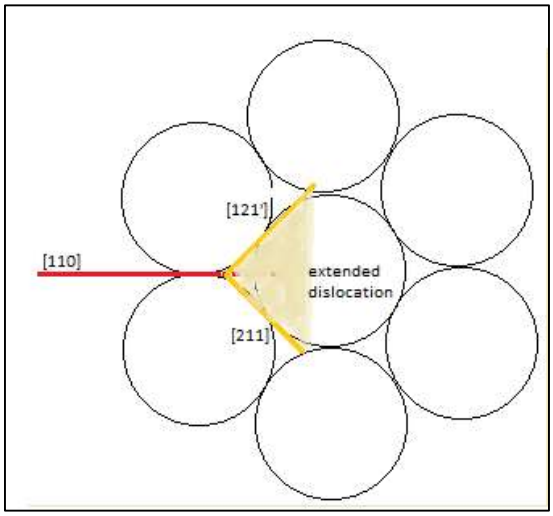

Figure 1-7: Extended dislocation formation due to Shockley Partials

The stacking fault in an ABCABC closed packed system is best represented as ABC***BAB***C with an extra B plane. The closed packed planes in the zone of the fault, as marked by the shaded zone in the figure 1-7 take the form of the hexagonal closed packed system (BABA). ε-martensite has the HCP structure in Fe-C system. So the stacking fault mimics the crystal orientation of ε-martensite in the areas of an extended dislocation. The transformation of ε-martensite to martensite occurs by twinning at the intersection of the extended dislocation.

Thus, as the dimensions of an extended dislocation increases, the chance of transformation during plastic deformation increases. The width of the extended dislocation is determined by the interaction of two opposite forces, the repulsive force between the <112> nearly parallel Shockley Partials and the surface

tension (SFE) holding them together. Similarly, the lower the SFE, greater is the width of the extended dislocations.

Studies conducted by Schramm and Reed showed that manganese, silicon, chromium and nitrogen decreases SFE and nickel and carbon increases SFE in the iron-carbon system [39]. So the use of manganese as alloying element in ductile iron directly increases the likelihood of transformation of austenite to martensite and nickel decreases it. In other words, the stability of the austenite during transformation is lower due to the presence of manganese in the ductile iron system. But, the transformation of austenite to martensite should not begin until the later stages of deformation if high ductility is desired as martensite formation at the early stages will render the material brittle due to the inherent brittleness of martensite. Thus, addition of nickel to the ductile iron should be more effective in improving ductility compared to the addition of manganese.

1.7 TRIP mechanism in IADI

TRIP or transformation induced plasticity is caused by transformation of austenite to martensite. This leads to increase in strain hardening and ductility. During this transformation of metastable austenite to martensite, there can be considerable changes in the internal volume of the transformed area, which may lead to microscopic strain fields that affect the mechanical properties of the material on a macroscopic scale.

A number of factors govern the stability of austenite in the microstructure. Carbon content of the austenite, crystallographic orientation of the grains to the strained axis, the volume of austenite in microstructure, favorable nucleation points, and alloying elements are some of the factors affecting the stability of austenite [40]. Usually increasing carbon content of the austenite increases the stability of austenite. Reisner et al. concluded that low carbon (<0.5- 0.6% carbon by weight) austenite usually transforms to martensite more readily, and the resultant martensite does little to improve the mechanical properties of the material [5].

Haidemenopoulos et al. came up with the quantity M_s^{σ}, which is the strain at which austenite will transform into epsilon martensite. This strain of transformation was found to be thermodynamically dependent on the

yield strength (σ_y), the ratio of octahedral stress on the crystal to the effective stress ($\frac{\sigma_h}{\sigma_e}$), the effective volume of the austenite ($N_v V_p$) where N_v is the number of all probable nucleation sites for martensite and V_p is the average volume of particles and (Ni) denotes the wt.% of alloying element, in this case nickel, used for stabilizing the austenite. For nickel, the relationship is given by equation 2 [40].

$$M_s{}^{\sigma} = \sigma_y \left\{0.121 + 0.0542 \left(\frac{\sigma_h}{\sigma_e}\right)\right\} + \frac{1465.3}{-4.6 - \ln(N_v V_p)} + \ [1418.92 - 33.92(Ni) - 0.5(Ni)^{2/3}] \quad (2)$$

From the above equation, it can be seen that, increasing the yield strength of the ductile iron alloy raises the strain required for transformation, while increasing the effective volume of austenite and weight percent of the alloying element, which in this case is nickel, decreases it. Thus, with a constant weight fraction of austenite stabilizers and for a given austenite volume fraction with similar probability of nucleation, the yield strength of the material plays a very important role in determining the strain at which transformation from austenite to martensite will take place. Also, according to the equation, greater austenite volume fraction will be thermodynamically more stable. But studies have shown that, larger austenite volume fraction may not necessarily lead to a more stable austenite as the average carbon content of the austenite will decrease. So an optimal carbon content is essential for the transformation to martensite [41]. The equation also displays that proper orientation of the austenite grains to the straining axis given by the quantity $\frac{\sigma_h}{\sigma_e}$ and the presence of proper nucleation sites for martensitic transformation, given by quantity N_v, also influences the transformation of austenite to martensite during straining.

Timokhina et al. predicted that the morphology of the austenite also plays a role in determining its stability during transformation. It was concluded that coarse blocks of austenite surrounded by polygonal ferrite would transform to martensite more readily during early stages of deformation while lamellar austenite present between lathes of bainitic ferric may be stable up to failure [4].

Characterization of the transformed martensite may be challenging in cases. Chemically, the martensite is similar to the untransformed austenite. So a microstructure containing martensite and austenite cannot be

distinguished from each other by chemical analysis tools like EDS, Auger electron spectroscopy and so on. Crystallographically, martensite has a body central tetragonal structure, which is very close to the ferrite that is present in the matrix of dual phase ductile iron, but very different from austenite which has a face-centered cubic structure. So, the best way to analyze the transformation is by diffraction methods. The most popular diffraction methods are x-ray diffraction and neutron diffraction. X-rays cannot penetrate more than the surface layers (5-10 microns) whereas neutrons by the virtue of their mass can penetrate deep into a material generating a better data for analysis of the transformation of austenite [42]. In-situ neutron diffraction studies can monitor the decrease in the austenite peak intensities along the course of deformation, thus determining the exact stress and strain at which the transformation of austenite to martensite occurs. In-situ neutron studies combined with a rigid tensile setup can also provide information about the diffraction elastic constants for various planes [43]. Neutron diffraction can also determine the lattice strain for the different phases providing an insight about residual stresses during deformation for a particular phase and prediction of intergranular and intragranular partitioning of stress for various crystallographic orientations for different phases.

Neutron diffraction is a popular method for studying transformational properties of TRIP steels. Zrnik et al. did extensive studies on TRIP steels of different chemistries and determined a direct relationship between the rate of transformation and thermomechnical processing of the alloy. It was also predicted that the rate of transformation in TRIP steels is not directly dependent on the initial volume of retained austenite in the microstructure [44-46]. Oliver et al. observed that transformation from austenite to martensite is preferred for some specific special orientations with respect to the loading axis. They also concluded the load carried by the austenite was transferred to the martensite during transformation which leads to strain hardening on a macroscopic scale [47].

There has been very little work done regarding the TRIP mechanism in ductile iron. Aristizabal et al. concluded that the transformation is directly related to the intercritical heat treatment as well as the alloy chemistry. Manganese was predicted to decrease the stability of austenite in the matrix [10]. Druschitz et

al. showed that the diffraction elastic constants for austenite (FCC) did not closely match the single crystal data. However the diffraction elastic constants for ferrite phase (BCC) were similar to the predicted data [48].

Although there are a few studies regarding the stability of austenite in ductile iron, it is safe to assume that alloy chemistry plays a pivotal role in determining the transformational behavior of austenite under stress.

Chapter 2 Specific Aims

The aims of the thesis are:

1. Determination of the stress and strain at the start of the transformation of austenite to martensite for four different alloy chemistries of intercritically austempered ductile iron.
2. Demonstration of lattice strain anisotropy for ferrite and austenite phases for the examined alloys.
3. Analysis of the residual stresses in ferrite and austenite along various lattice planes during the course of deformation.
4. Demonstration of partitioning of stress and strain between the austenite and ferrite phases.
5. Determination of diffraction elastic constants and lattice Poisson's ratio for different planes in the austenite and ferrite phases.

Chapter 3 Materials and Methods

3.1 Alloy Chemistry

In order to determine the effect of chemistry on the transformational properties of austenite in intercritically austempered ductile iron, four alloys of different alloy chemistry were chosen. The composition of the alloys is given in Table 3-1.

Table 3-1: Composition of the investigated alloys in weight percentage

Compositions in wt. %								
	C	Si	Mn	Ni	Cu	Mg	S	Fe
Low Ni	3.64	2.17	0.33	0.68	0.72	0.045	0.013	Bal
High Ni	3.92	2.34	0.33	2.47	0.75	0.040	0.016	Bal
High Mn	3.73	2.25	1.59	0.01	0.04	0.046	0.014	Bal
Ni-Mn	3.74	2.24	0.91	0.51	0.05	0.048	0.014	Bal

3.2 Production of ductile iron castings

The alloys were produced at the casting laboratory of the University of Alabama at Birmingham (UAB). The details of the actual melting was mentioned by Aristizabal in the materials and method chapter of his dissertation [32]. Approximately 70 pound heats of each ductile iron alloy were produced using low carbon steel punchings, granular silicon carbide, granular carbon riser, ferro-manganese, copper turnings and nickel shot. The chemistry was determined by optical emission spectroscopy (OES) of chilled samples. Carbon and sulfur were determined by combustion analyses using a Leco C/S analyzer. The treated iron was poured in Y-blocks made from chemical bonded sand using 1.5% binder and were shaken out after approximately 1 hour of cooling.

3.3 Heat Treatments

The castings were intercritically austenitized at Rex Heat Treat Facility in Anniston, Alabama in a controlled atmosphere and then austempered in a neutral salt bath. Mr. Mel Ostrander was responsible for all the heat treatments for all the samples. Details are given in Table 3-2.

Table 3-2: Heat Treatment regime for the samples

	Intercritical Austenitizing		Austempering	
	Temperature (°C)	Time (hours)	Temperature (°C)	Time (hours)
Low Ni	770	4	357	2.25
High Ni	740	4	357	2.25
High Mn	760	4	357	2.25
Ni-Mn	770	4	357	2.25

After the heat treatment the Y-blocks were machined into round tensile samples for in-situ neutron diffraction studies at VULCAN, Spallation Neutron Source at Oak Ridge National Lab [49]. The exact dimensions are given in the Figure 3-1.

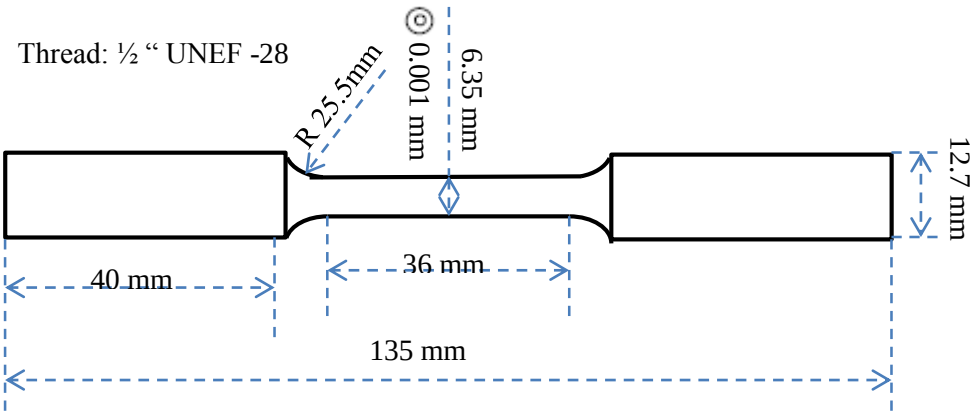

Figure 3-1: Dimensions of tensile sample for in-situ neutron diffraction tests at VULCAN in Spallation Neutron Source at Oak Ridge National Lab.

3.4 Spallation Neutron Source -VULCAN

The Spallation Neutron Source (SNS) at Oak Ridge National Laboratory provides the most intense pulsed neutron beams in the world for scientific research and industrial development. Negatively charged hydrogen ions (H^-) are produced by an ion source. Each ion consists of a proton orbited by two electrons. The ions are injected into a linear accelerator, which accelerates them from 2.5 to 1000 MeV. The ions are then passed through a stripper foil, which strips off two electrons from each ion, converting it to a proton. The protons pass into a ring where they accumulate in bunches. Each bunch of protons is released from the ring as a pulse. The high-energy proton pulses strike a heavy-metal target, which is a container of liquid mercury. This leads to spallation of 20-30 neutrons per proton that hits the target. Corresponding pulses of neutrons freed by the spallation process are slowed down in a moderator and guided through beam lines to areas containing highly specialized instruments for conducting experiments. Once there, neutrons of different energies are used in a wide variety of experiments in different beam lines. [50]

Beam Line 7-VULCAN:

VULCAN is designed to tackle a variety of problems in materials science and engineering, including deformation, phase transformation, residual stress, texture, and microstructure studies. The set-up provides rapid volumetric mapping with a specific sampling volume and a measurement time of minutes for full diffraction patterns for common engineering materials. The two +/-90 position-sensitive detectors, measures the longitudinal and transverse strain components simultaneously. VULCAN opens new research opportunities for the study of structure evolution at multiple length scales. The beam size can be varied between 2 ~17 mm horizontal and 0.2 ~17 mm vertical incident slit. Available sample environments and equipment include a unique load frame capable of multi-axial loading and fatigue tests with various furnaces and other controlled environment [51, 52].

3.4.1 Experimental Set-up

The threaded round tensile samples, machined as shown in figure 3-1 were used for in-situ tensile loading experiments, that is, measuring the diffraction data while under tensile loading. The tensile set-up consisted of a uniaxial MTS load-frame mounted on the beamline. Figures 3-2, 3-3 and 3-4 give a detailed description of the cave and the overall set-up. The round tensile samples were threaded into the grips and a 1 inch gauge length extensometer was mounted on the sample as shown in figure 3-4. The extensometer was cladded in cadmium to prevent damage caused by high speed neutron flux. A 50N preload was applied to prevent the sample from moving during set-up. The incident slit was 17 mm horizontal by 12 mm vertical with a sample to detector distance of about 2 m. The beam chopper speed was 30 Hz with a detection bandwidth of 2.88 Å. Two collimators with 5 mm receiving slits were used to the longitudinal and transverse diffraction patterns.

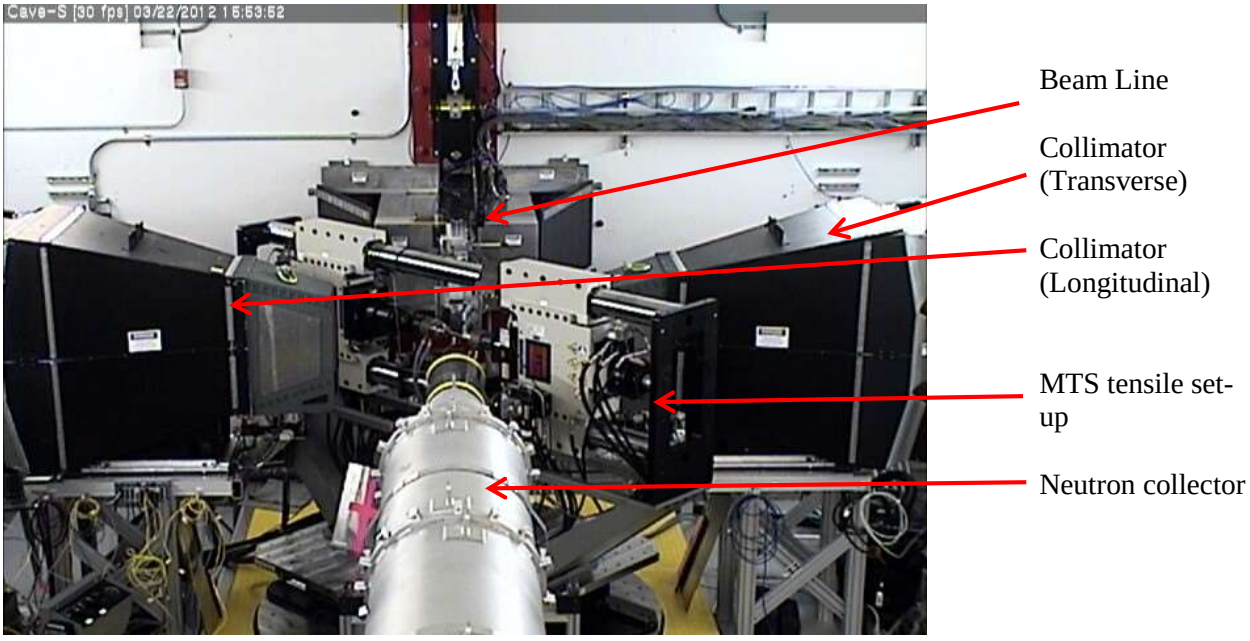

Figure 3-2: Overall experimental set-up in VULCAN sample cave

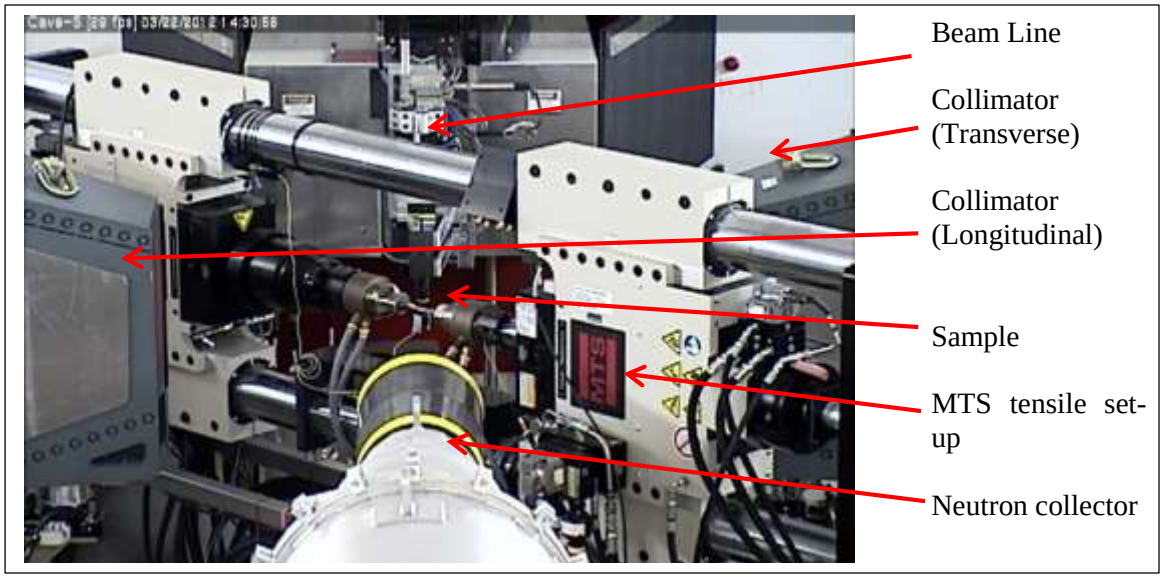

Figure 3-3: Close-up of different components of the experimental set-up

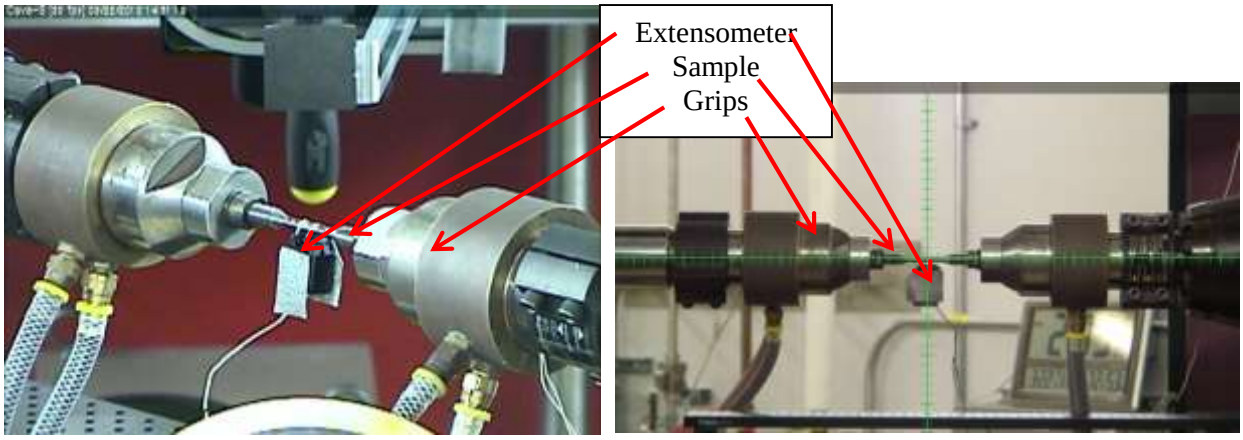

Figure 3-4: Sample set-up and alignment

After clearing and securing the cave for safety, the neutron beam aperture was opened and the sample was scanned for alignment. Horizontal alignment was done by eye estimation, making sure the center of the gauge length of the extensometer was aligned with the beam aperture as given by the cross-hairs. For vertical alignment, a scan was run long the vertical axis and the intensity was plotted against vertical location. The intensity points were plotted, and the location along the vertical axis corresponding to the mean intensity was aligned with the beam line aperture. The perfectly aligned sample is shown in Figure 3-5.

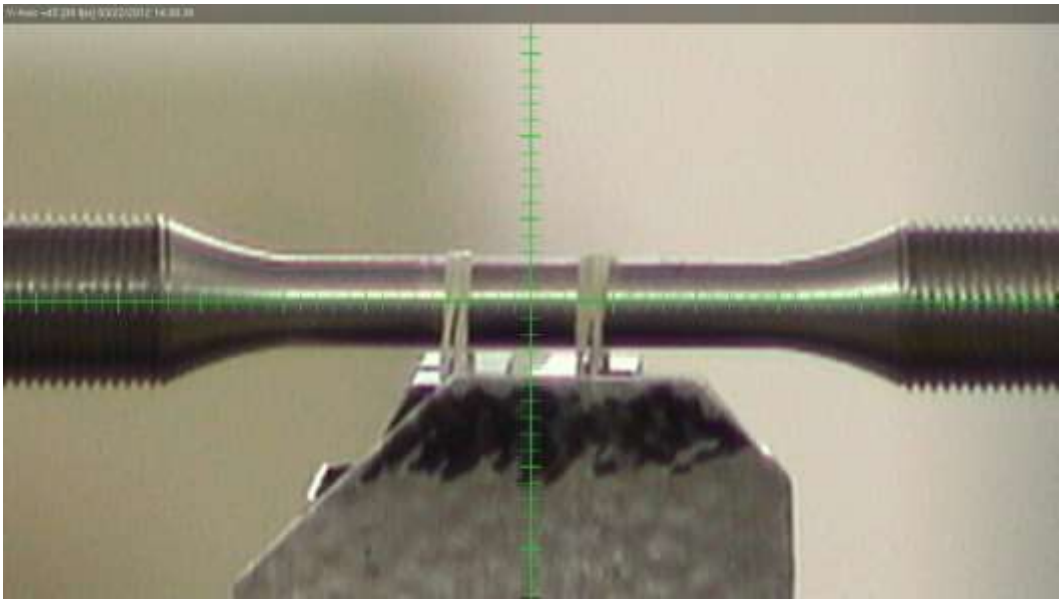

Figure 3-5: Alignment of the sample with the beam aperture by eye estimation and alignment scan

After alignment, pre-programmed strain-controlled tensile tests were run for each of the samples. The high nickel, low nickel and the nickel-manganese samples were strained to 15% in tension and the high manganese samples were strained to 5% in tension. A detailed loading sequence for each of the samples is given in Table 3-3 (a) and (b). The loading-unloading cycle were chosen to demonstrate the change in loading-unloading modulus after transformation, if any, at various levels of straining.

After the experiment, the samples were carefully examined for any residual radio-activity with a Geiger counter. All the samples read <50,000 counts per minute, so were safe for handling. The samples were then removed from the cave, stored in labeled bags in the ORNL facility for further inspection and were finally cleared and returned after 3 months for analysis.

Table 3-3 (a): Tensile test cycles for the samples loaded to 15% elongation

Sample Chemistry	Loading/ Unloading	Target Stress(MPa)/ Strain(%)/ Force(N)	Control	Rate	Time (mins)	Total time
Low Ni	Hold	100 N (force)	load		4	14 hours
	Load to	7500 N (force)	load	150 N/min		
	Load to	2.5% (strain)	strain		90	
	Unload to	100 N (force)	load		60	
	Load to	5% (strain)	strain		90	
	Unload to	100 N (force)	load		60	
	Load to	10% (strain)	strain		90	
	Unload to	100 N (force)	load		60	
	Load to	15% (strain)	strain		90	
	Unload to	100 N (force)	load		60	
High Ni	Hold	100 N (force)	load		4	14 hours
	Load to	7500 N (force)	load	150 N/min		
	Load to	2.5% (strain)	strain		90	
	Unload to	100 N (force)	load		60	
	Load to	5% (strain)	strain		90	
	Unload to	100 N (force)	load		60	
	Load to	10% (strain)	strain		90	
	Unload to	100 N (force)	load		60	
	Load to	15% (strain)	strain		90	
	Unload to	100 N (force)	load		60	
Ni-Mn (sample 1)	Hold	100 N (force)	load		4	14 hours
	Load to	7500 N (force)	load	150 N/min		
	Load to	2.5% (strain)	strain		90	
	Unload to	100 N (force)	load		60	
	Load to	5% (strain)	strain		90	
	Unload to	100 N (force)	load		60	
	Load to	10% (strain)	strain		90	
	Unload to	100 N (force)	load		60	
	Load to	15% (strain)	strain		90	
	Unload to	100 N (force)	load		60	
Ni-Mn (sample 2)	Hold	100 N (force)	load		4	14 hours
	Load to	7500 N (force)	load	150 N/min		
	Load to	2.5% (strain)	strain		90	
	Unload to	100 N (force)	load		60	

	Load to	5% (strain)	strain		90	
	Unload to	100 N (force)	load		60	
	Load to	10% (strain)	strain		90	
	Unload to	100 N (force)	load		60	
	Load to	15% (strain)	strain		90	
	Unload to	100 N (force)	load		60	

Table 3-3 (b) Tensile test cycles for the samples loaded to 5% elongation

Sample Chemistry	Loading/ Unloading	Target Stress(MPa)/ Strain(%)/ Force(N)	Control	Rate	Time (mins)	Total time
High Mn (sample 1)	Hold	100 N (force)	load		4	8 hours
	Load to	10000 N (force)	load		120	
	Unload to	100 N (force)	load		60	
	Load to	2.5% (strain)	strain		90	
	Unload to	100 N (force)	load		60	
	Load to	5% (strain)	strain		90	
	Unload to	100 N (force)	load		60	
High Mn (sample 2)	Hold	100 N (force)	load	150 N/min	4	7.5 hours
	Load to	7500 N (force)	load			
	Load to	2.5% (strain)	strain		180	
	Unload to	100 N (force)	load		60	
	Load to	5% (strain)	strain		90	
	Unload to	100 N (force)	load		60	
High Mn (sample 3)	Hold	100 N (force)	load		4	7.5 hours
	Load to	70 MPa (stress)	load		30	
	Unload to	100 N (force)	load		30	
	Load to	140 MPa (stress)	load		40	
	Unload to	100 N (force)	load		40	
	Load to	1% (strain)	strain		90	
	Unload to	100 N (force)	load		60	
	Load to	2.5% (strain)	strain		90	
	Unload to	100 N (force)	load		60	

3.5 Analysis of results

After the data was gathered, it was processed using the VDRIVE (VULCAN Data Reduction and Interactive Visualization) software in the SNS analysis portal. This software package performs the neutron time of flight data reduction and visualization for engineering diffractometer in the VULCAN facility. This also includes subprograms for different data reduction processes, sequential data analysis functions, visualization as well as synchronization of neutron and experimental data and generates outputs for GSAS analysis in a more professional setting. [53]

Each experimental run was chopped into 120 seconds sections using the VDRIVECHOP function, and the new data were binned in the server. All further analysis was done on the binned data. The steps of the analysis includes

- Calculation of true stress and strain
- Generation of the d-spacing data
- Analysis of the diffraction data
- Calculation of volume fraction of austenite
- Determination of true stress and true strain at transformation,
- Calculation of elastic diffraction constants
- Calculation of residual strains in the phases

3.5.1 Calculation of true tress and true strain

The tensile data generated by the data acquisition system was engineering tensile data. In order to do further analysis, the true stress and true strain was calculated. The true strain (ε) was calculated from the engineering strain (e) using Equation 3.

$$\varepsilon = \ln(1 + e) \tag{3}$$

After calculating the true strain, it was used to calculate the true stress. In order to calculate the true stress, the true cross sectional area and the load on the sample was used.

The acquisition system recorded the load (P) along the course of deformation. The cross sectional area (A) was calculated using the initial cross sectional area (A_i) and the true strain (ε) using equation 4. The true strain (σ) can then be calculated using equation 5. After the calculation of the true stress and true strain, the elastic moduli (E) was calculated using equation 6, at the initial elastic loading and compared with the unload-load loops at higher strains.

$$A = \frac{A_i}{\exp(\varepsilon)} \tag{4}$$

$$\sigma = \frac{P}{A} \tag{5}$$

$$E = \frac{\sigma}{\varepsilon} \tag{6}$$

Equations 3, 4 and 5 are valid under the assumption that the sample is under plain stress and there is no necking. Equations 4 and 5 are not valid for the unload-load cycles during plastic deformation. Also, the calculation of the elastic modulus for the unloading-loading loops differ from the calculation of elastic modulus during initial elastic loading. The calculation of true stress and elastic modulus is explained using figure 3-6 with the aid of the unload-load loop for run # 13583 (High Mn) at 2.5% engineering strain. The strain axis is cropped between 1.9% and 2.6% of engineering stress for ease of explanation.

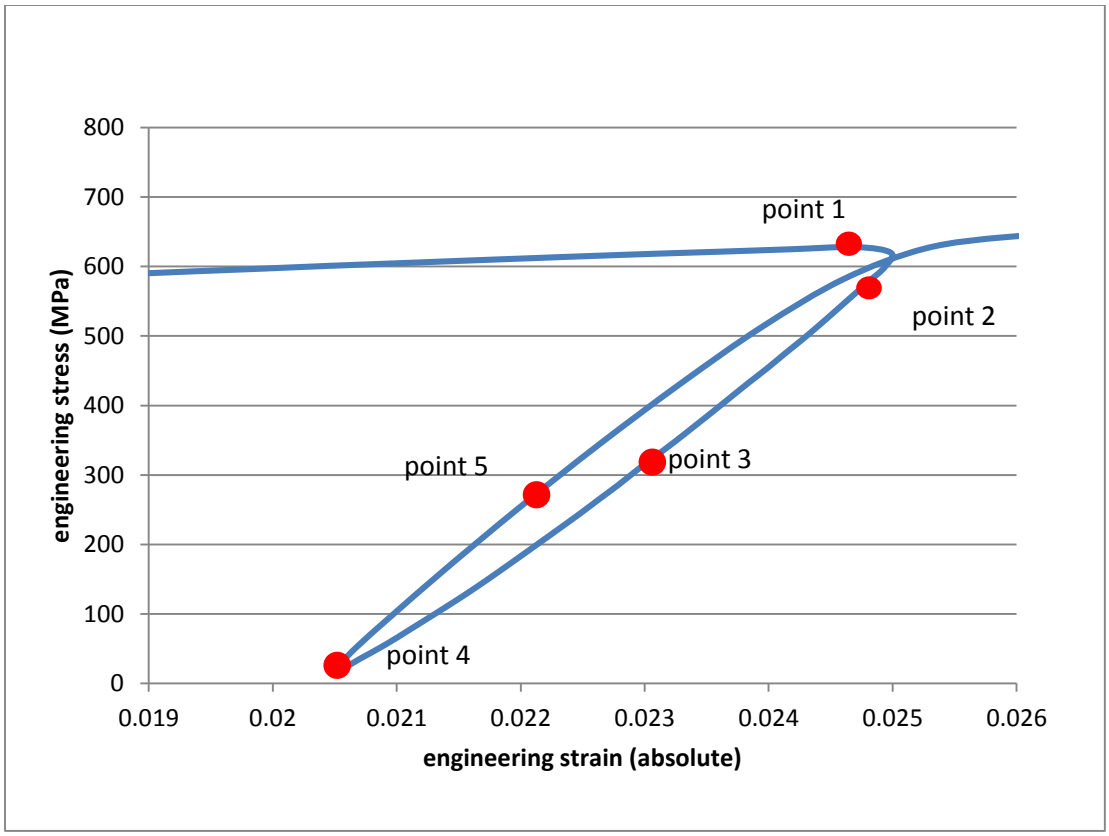

Figure 3-6: Engineering tensile data showing the points of interest between 1.9% and 2.6% engineering strain

In figure 3-6, point 1 represents the point on the tensile axis before the unload-load cycle starts. Point 2 represents the first point on the unloading cycle. Below point 3, the unloading curve loses its linearity. Therefore, the section of the unloading curve from point 2 to point 3 denotes the linear region of the unloading cycle. Point 4 on the graph denotes the termination of the unloading cycle and initiation of the loading cycle of the loop. So, the section of the unloading graph between points 3 and 4 is non-linear. Similarly for the loading cycle, the region of curve between points 4 and 5 denotes the linear region.

For calculating the true stress for the loop, the instantaneous load and true cross sectional area of point 1 was used for all the points of the loop. The true stress was then calculated using equation 5. This was done under the assumption that the unloading-loading loop was purely elastic and no change in cross sectional area occurred from the initiation of the unloading cycle, till the end of the loading cycle.

For calculating the elastic moduli for the loop, only the linear portions were considered. So the data points between points 2 and 3 and points 4 and 5 were plotted and a linear trendline was drawn, the slope of which gave the value of the unloading and loading elastic moduli respectively.

To determine the precision of the true stress and true strain calculation, the final cross-sectional area of the samples after the test was compared to the final cross-sectional area of the samples calculated using equation 4.

3.5.2 Generation of d-spacing data

After chopping and binning the data for all the test runs, the d-spacing data was generated for tabulation. With the data visualization program VDRIVEVIEW, intensity versus d-spacing histograms were generated for preloading condition. Peaks corresponding to each d-spacing were carefully tabulated manually by comparing it with CRYSTMET database [54] with known d-spacing for iron (FCC,BCC) and carbon (HCP). Hence the d-spacing data corresponding to each plane system for body centered cubic iron (ferrite), face centered cubic iron (austenite) and hexagonal close packed carbon (graphite) was sorted and made into a database for each of the tested alloy chemistries. The tabulated d-spacing data were used for further analysis.

After generating the database, the d-spacing data for the entire experimental run for each of the samples was plotted into a three dimensional plot and a two dimensional contour plot, using the VDRIVEVIEW command. This was done to examine any major shifts in peak position or peak merging.

3.5.3 Analysis of the diffraction data

After constructing a database of the d-spacing data for all the phases for all the different alloy chemistries, the database was used to analyze the diffraction data. The analysis was done using the general structure analysis system or GSAS for a single peak fit. This program was run on the entire database of each of the samples. The initial peak position was considered as the reference run and the whole system was calibrated using the vanadium file. The proton charge was also normalized to unity for a more uniform fit for each of

the peaks. After the analysis, the generated data includes, the fitting parameters, the proton time of flight, diffracted and backscattered intensities, full width at half maximum, strain with respect to the reference run, and the errors for each of the data within the chopped segment for both the longitudinal and transverse directions. The generated results were pristine only for non-overlapping peaks

3.5.4 Calculation of volume fraction of austenite

The volume fraction of austenite was calculated using the integrated intensities of each of the phases. The integrated intensities were given by the area under the intensity histograms and were calculated using the peak intensity and full width at half maximum (FWHM).

The calculation is explained with the help of figure 3-7, where each intensity histogram is treated as an equilateral triangle, with height as the peak intensity (I). The base width (b) is exaggerated.

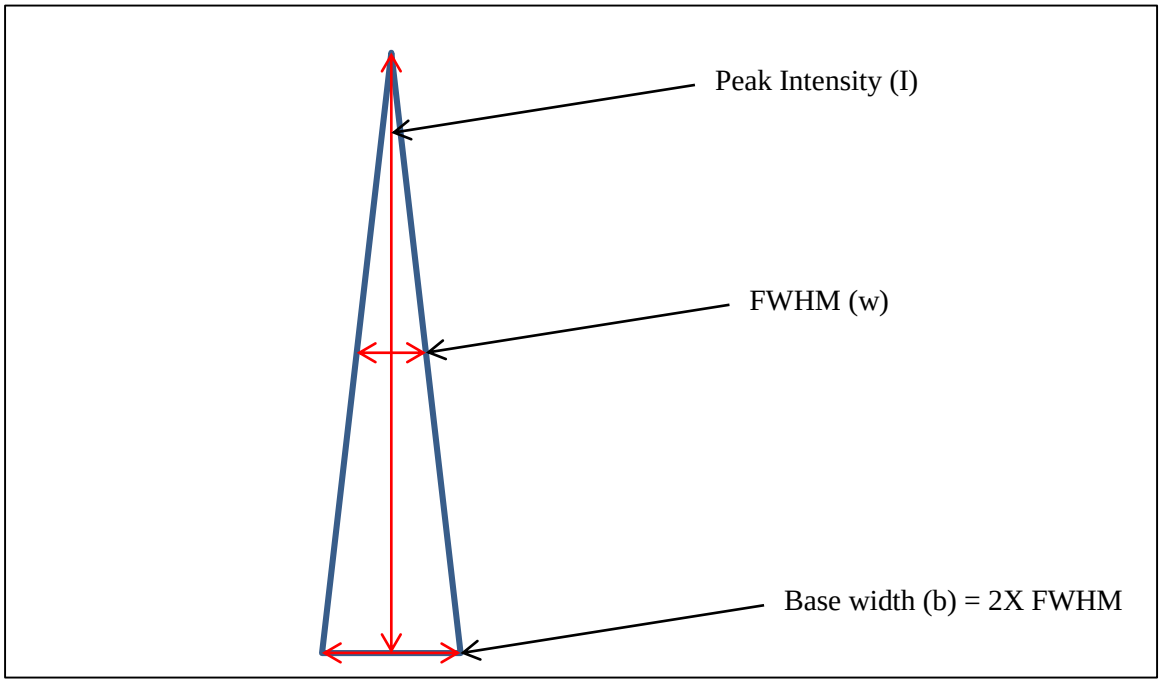

Figure 3-7: Figure representing a single peak histogram with exaggerated base width

For an equilateral triangle, the base width (b) is double the FWHM (w) by geometry. The area of the equilateral triangle is given by half of base times height. So, the area under the intensity histogram, i.e., the estimated intensity is given by equation 7.

Estimated Intensity= Area under the intensity histogram

$$= \frac{1}{2} \times b \times I = \frac{1}{2} \times 2 \times w \times I = w \times I = FWHM \times Peak\ Intensity \quad (7)$$

The estimated intensities for each set of planes for each of the phases were calculated using this equation. Once the estimated intensities are calculated for all the planes for each of the phases, the volume fraction of austenite was calculated using equation 8.

$$\text{Fraction of austenite} = \frac{intensity\ of\ FCC(hkl)}{intensity\ of\ BCC(mno) + intensity\ of\ FCC(hkl)} \quad (8)$$

The FCC or austenite planes are represented by (hkl) and the BCC or ferrite planes are represented by (mno). For this analysis, a set of FCC and BCC planes were selected after consulting with the ASTM standard practice for determination of retained austenite in randomly oriented polycrystalline iron alloys [55]. The set of FCC and BCC planes chosen for the analysis are given in Table 3-4.

Table 3-4: Set of BCC and FCC planes chosen for analysis of volume fraction of retained austenite

	BCC Planes	**FCC Planes**
1.	110	111
2.	200	200
3.	211	220
4.	220	220
5.	220	222

The choice of the planes was primarily based on similarity of orientation so that the stress and strain component of the unidirectional tension is comparable if not similar along the planer directions.

After determination of volume fraction of austenite using each of the plane sets, the fraction was then rationalized using the initial fraction of austenite at zero stress for those plane sets. This was done using equation 9, to enable the comparison of volume fractions of austenite using all the planes for a specific alloy, thus helping to determine the stress and strain at which the transformation of austenite to martensite takes place.

Rationalized fraction of austenite= $\frac{fraction\ of\ retained\ austenite\ at\ strain/stress=s}{fration\ of\ retained\ austenite\ at\ strain/stress=0}$ (9)

The rationalized fraction of retained austenite was then plotted to analyze the stress and strain of transformation.

3.5.5 Determination of true stress and true strain at transformation

The rationalized fraction of austenite was plotted against the true stress and true strain. The trend of decreasing rationalized volume fraction of austenite from unity was observed. The stress at which there was a marked decrease from the initial volume of austenite was noted as the stress at which transformation of austenite to martensite began. Similar studies were also done using the true strain.

3.5.6 Calculation of elastic diffraction constants

The longitudinal and transverse lattice strains for the FCC and BCC planes were calculated using the GSAS single peak analysis in the VDRIVE software. During the course of macroscopic unidirectional tensile test, the change in the lattice spacing for the planes from the initial lattice spacing was given as the lattice strain, as shown in equation 10.

$$Lattice\ strain = \frac{(d\ spacing\ for\ plane\ (hkl) at\ \sigma=s) - (d\ spacing\ for\ plane\ (hkl) at\ \sigma=0)}{(d\ spacing\ for\ plane\ (hkl) at\ stress=0)} \quad (10)$$

To determine the elastic diffraction constants, the lattice strain for each of the FCC and BCC planes in both transverse and longitudinal direction were plotted against true macroscopic stress. There were very prominent linear parts in the plots, given by the elastic strains in the lattice and there were non-linearities indicating the strain at which the slip or movement of dislocations starts. The elastic diffraction constants were determined by taking the slope of the linear part of the lattice strain plots.

The generated data contains lattice strain data from both the longitudinal and transverse directions to the loading axis. Hence the Poisson's ratio was easily calculated by plotting the transverse lattice strain versus the longitudinal strain and taking the linear slope of the plot.

3.5.7 Demonstration of residual strains in the phases

The longitudinal and transverse lattice strains for the FCC and BCC planes were plotted against the true macroscopic strain along the loading axis. The nature of residual stresses in the planes was noted along the loading unloading cycles, that is, it was noted if any plane was going into compression when the macroscopic strain was still zero. It was also noted whether the FCC or the BCC planes bear more strain under the same macroscopic strain.

3.6 Characterization

Sample preparation and instrument specification for light microscopy and scanning electron microscopy (SEM):

The samples tested at VULCAN were cut with a low speed diamond saw into approximately 0.5 inch long sections. Sections were taken transverse to the loading axis (from strained and unstrained locations) and parallel to the loading axis (strained zone). The unstrained sections were not mounted. For ease of polishing the strained sections, both transverse and parallel were mounted in black mounting wax, or Mounting Wax 100 supplied from Electron Microscopy Sciences rimmed with a one inch diameter copper tube.

The samples were prepared using standard metallographic procedures. First, samples were ground using successive finer grits of silicon carbide paper (120, 240, 320, 400, 600 grit). Then, they were polished using 9 micron, 1 micron, 0.3 micron and 0.05 micron alumina suspension. The samples were alternately etched and polished in between the final 3 steps of polishing, that is polishing with 1, 0.3 and 0.05 micron of alumina, using 3% nital etchant. After final polishing, the samples were lightly etched with 3% nital.

After etching, the samples were examined under light microscope Olympus BH-2 UMA at a magnification of 500X in order to determine the primary microstructures and regions of interests in the samples.

The samples were then examined using FEI Quanta 600 FEG environmental scanning electron microscopy. A high vacuum mode of 6×10^{-4} Pascals was used for this purpose. The operating accelerating voltage was 20KeV and a standard spot size was 5 on analysis. Samples were analyzed at various magnifications from 500X to 1500X for general inspection and 5000X for special features using a backscattered electron

detector. The contrast in the backscattered detector for the austenite and the ferrite phases were primarily due to the crystal structure and also due to the topography generated due to the difference in etch rates of the phases, ferrite being etched faster than austenite.

Energy dispersive spectroscopy (EDS) was performed on the samples. Area mapping was done at 1000X and multipoint scans on the samples were run at 1500X. However, due to a large beam interaction volume, the data from the tests were not precise.

Once the electron beam bombards on the sample, the energy of the beam spreads deep into the sample into a pear-shaped volume called beam interaction volume as shown in figure 3-8 [56].

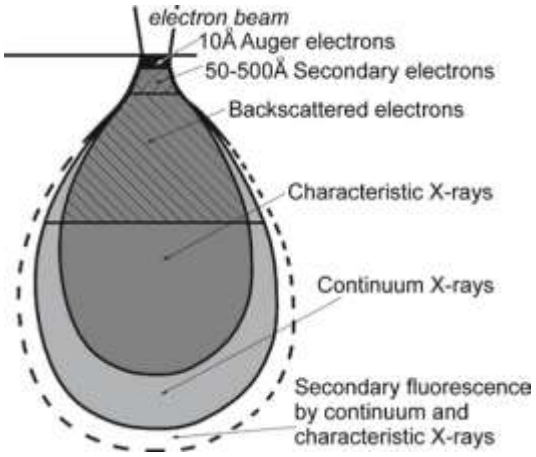

Figure 3-8: Electron Beam interaction volume and signal generation

The secondary electrons are generated from the top 5-50 nm of the samples, the backscattered electrons are generated from 0.5-5 microns and the x-rays can be generated from further depth. However, the beam interaction volume is inversely proportional on the accelerating voltage and the atomic number of the matrix which correlates to the matrix stopping power. So, it is very difficult to get a precise measurement of chemistry of the phases present as small grains solely by performing EDS analysis.

Sample preparation and instrument specification for transmission electron microscopy (TEM):

TEM analysis was performed on the strained high manganese and high nickel samples previously tested by Druschitz et al. at the high flux isotope reactor (HFIR) in Oak Ridge National Lab[48]. Sections of approximately 1mm length were taken from the tested samples. The samples were ground to 100 micron width using 600 grit silicon carbide papers. Samples with 3 mm diameter were punched from the polished

foil for further processing. They were then ground to less than 50 micron using a dimple grinder. Then, the samples were made electron transparent using ion-milling. For ion-milling, a regular sample holder was used and it was inserted in the vacuum chamber of the ion mill at a pressure of 2×10^{-5} Torr. Argon ions were used to mill the sample under 5KV voltage and 5mA ion beam current. The samples were held at 10 degrees to vertical and rotated 360 degrees for approximately 8 hours until they become electron transparent. The samples were then carefully removed from the sample holder of the ion mill and placed in the sample holder of the TEM.

The Philips EM420 was used under 120KV operating voltage. The system has a tungsten thermionic electron gun. Micrographs were taken at various magnifications for analysis.

Chapter 4 Results and Discussion

In-situ neutron diffraction tests were performed on samples with different alloy chemistries using uni-directional loading-unloading tensile tests. The data was collected and analyzed as discussed in the previous chapter. The results of the analysis are tabulated in this chapter.

4.1 True Stress and True Strain

Engineering strain is calculated assuming the cross sectional area remains constant during straining, but for accurate analysis, this assumption is not valid. As a correction, true strain is calculated using the instantaneous cross sectional area. The true stress is calculated in this case assuming the volume remains constant for a material before necking. True stress-true strain analysis gives a more realistic and accurate view of the tensile behavior of the material.

The details of calculation are explained in section 3.5.1 of previous chapter. The comparison between the true tensile curve and the engineering tensile curve for the Ni-Mn alloy is displayed in figures 4.1. The rest of the curves are provided in Appendix A as figures A-1 to A-6.

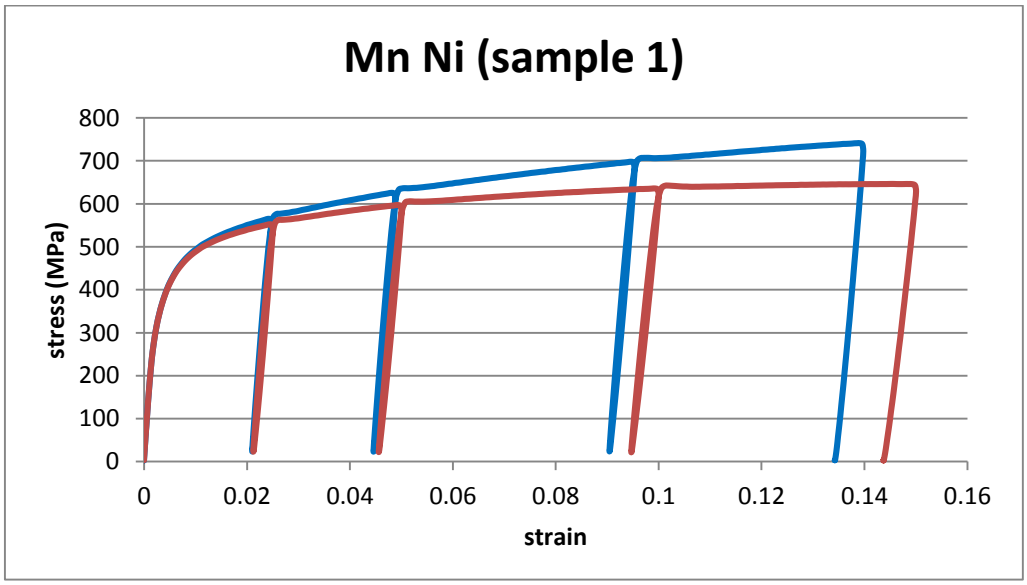

Figure 4-1: True stress-true strain curve (blue) and engineering stress-engineering strain curve (red) for Mn Ni alloy sample 1

From the above figure, it is evident that the calculated true strain is lower than the engineering strain whereas the true stress is higher. The tensile curves of the low nickel alloy in Appendix A figure A-1 show some kinks in the tensile graph due to flawed MTS programming. After the initial unloading at 2.5% engineering strain, it was supposed to be loaded to 5% strain in 1.5 hour, but due to a programming error it started to be loaded to 5 mm elongation in 1.5 hour. The error was quickly noted and the system was paused and the programming error was promptly corrected.

The high manganese sample 2, as shown in figure A-4 was programmed to follow the stress-strain cycle as given in table 3-3 of previous chapter. But the sample failed at 3.466% strain stopping the experiment.

The accuracy of the true stress calculation is directly dependent on the accuracy of the true strain calculation. This quantity can be judged by the difference between the calculated final diameters which can be calculated by given by equation 11. Table 4-1 gives the differences in calculated and measured values of the final diameter.

$$Final\ Diameter\ (d_f) = \sqrt{{d_i}^2 \Big/ \exp(\varepsilon)} \tag{11}$$

where the d_i is the initial diameter and ε is the maximum true strain.

Table 4-1: Calculation of % difference between measured and calculated diameters

Sample	Initial Diameter (in mm)	True Strain (absolute)	Calculated Final Diameter (in mm)	Measured Final Diameter (in mm)	Difference (in mm)	Difference (% relative to initial diameter)
Low Ni	6.345	0.133	5.93	6.09	0.16	2.42
High Ni	6.343	0.133	5.93	6.07	0.14	2.16
High Mn (sample 1)	6.382	0.043	6.24	6.29	0.05	0.71
High Mn (sample 2)	6.350	0.034	6.24	6.28	0.04	0.71
High Mn (sample 3)	6.347	0.021	6.28	6.31	0.03	0.46
Mn Ni (sample 1)	6.370	0.134	5.96	6.04	0.08	1.30
Mn Ni (sample 2)	6.335	0.134	5.92	6.01	0.09	1.37

Table 4-1 shows there is no more than 2.5% difference in calculation of final diameter using true strain. The original strain was much lower than the calculated true strain. The volume expansion for each samples are explained in table 4-2.

Initial Volume= $V_i = {l_i \times \pi {d_i}^2}/{4}$ (12)

Final Volume= $V_f = {l_f \times \pi {d_f}^2}/{4}$ (13)

Volume expansion= $V_f - V_i$

Or, $V_f - V_i = {l_f \times \pi {d_f}^2}/{4} - {l_i \times \pi {d_i}^2}/{4}$

Or, $V_f - V_i = \frac{\pi}{4}\left(l_f {d_f}^2 - l_i {d_i}^2\right)$ (14)

% Volume expansion = ${l_f {d_f}^2 - l_i {d_i}^2}/{l_i {d_i}^2}$

Or, % Volume expansion = $\left({}^{l_f d_f{}^2}\Big/_{l_i d_i{}^2} - 1 \right) \times 100$

Or, % Volume expansion = $\{\exp(\varepsilon)\left({}^{d_f{}^2}\Big/_{d_i{}^2}\right) - 1\} \times 100$ $(since\ {}^{l_f}\Big/_{l_i} = e^{\varepsilon})$ (15)

Equations 12, 13, 14 and 15 explains the volume change taking into consideration of true strain, ε. V, l and d represents the volume, length and diameter of the sample with subscripts i denoting the initial value and f denoting the final value.

Table 4-2 shows the change in volume for all the alloys tested.

Table 4-2: Volume expansion during straining

Sample	Initial Diameter (in mm)	True Strain (absolute)	Calculated Final Diameter (in mm)	Measured Final Diameter (in mm)	Difference (in mm)	Difference (% relative to initial diameter)	Apparent Volume Expansion (%)
Low Ni	6.345	0.133	5.93	6.09	0.16	2.42	5.23
High Ni	6.343	0.133	5.93	6.07	0.14	2.16	4.60
High Mn (sample 1)	6.382	0.043	6.24	6.29	0.05	0.71	1.40
High Mn (sample 2)	6.350	0.034	6.24	6.28	0.04	0.71	1.35
High Mn (sample 3)	6.347	0.021	6.28	6.31	0.03	0.46	0.93
Mn Ni (sample 1)	6.370	0.134	5.96	6.04	0.08	1.30	2.80
Mn Ni (sample 2)	6.335	0.134	5.92	6.01	0.09	1.37	2.90

The Interrupted tensile tests were performed on low Ni IADI, MADI and low carbon steel to measure the diameter at various strain levels. The change in diameter for Table 4-3 shows the change in diameter and volume in case of the Low Ni IADI sample at various strain levels. Similar data for the low carbon steel and MADI is provided in table A-1 and A-2.

Table 4-3: Difference in diameter and volume at various strains for High Ni IADI

Engineering Strain	True Strain	Diameter Calculated (in mm)	Diameter Measured (in mm)	Difference (in mm)	Difference (% of initial diameter)	Volume change%
0.0000	0.0000	6.30	6.30	0.000	0.00	0
0.0002	0.0002	6.30	6.30	0.000	0.01	0.020
0.0010	0.0009	6.30	6.30	0.000	0.05	0.100
0.0050	0.0049	6.28	6.29	0.010	0.09	0.181
0.0100	0.0099	6.27	6.28	0.010	0.179	0.361
0.0250	0.0247	6.22	6.23	0.010	0.116	0.236
0.0500	0.0488	6.15	6.18	0.030	0.506	1.039
0.0451	0.0440	6.16	6.18	0.020	0.275	0.564
0.0750	0.0723	6.08	6.11	0.030	0.536	1.114
0.1000	0.0953	6.01	6.04	0.030	0.528	1.111
0.0942	0.0900	6.02	6.04	0.020	0.276	0.578
0.1251	0.1178	5.94	5.98	0.040	0.642	1.366
0.1501	0.1398	5.87	5.91	0.040	0.561	1.207

Thus, the volume change of about 2% for all the 3 materials can be explained by the deviation from the assumption of constant volume for calculation of true strain or sample measurement error.

The change in volume can be a result of increase in volume during phase change and increase in the volume of voids in the austenite phase due to prolonged exposure to high speed neutrons. Chopra and Rao explains that material chemistry has a significant effect on the void swelling in FCC phases in iron [57]. However, this phenomenon can only occur in case of high speed high flux neutron beams which was not used for this experiment. The change in diameter can be explained in part by possible error in measurement as the difference in the diameters is of the order of the sensitivity of the calipers which is 0.02 mm. The apparent change in diameter and volume if any due to transformation is very low and in the range of experimental error. The martensitic transformation can result in some expansion of volume due to shear strain fields as developed around the carbon atoms due to accommodation of excess carbon in the crystal lattice as explained by Ahler [58].

4.2 Loading and Unloading Elastic Moduli

Transformation from one phase to another usually leads to a change in elastic modulus of the material. But the change in the elastic modulus depends on the amount of phases present in the matrix as well as how much actually transforms. In order to inspect the effect of transformation on the modulus of our material, the slope of the linear region of the loading-unloading cycles for each tensile test was measured.

Figure 4-7 displays the calculated elastic moduli, given in MPa for Ni-Mn (sample 1). The rest of the figures are provided in Appendix B as figures B-1 to B-6.

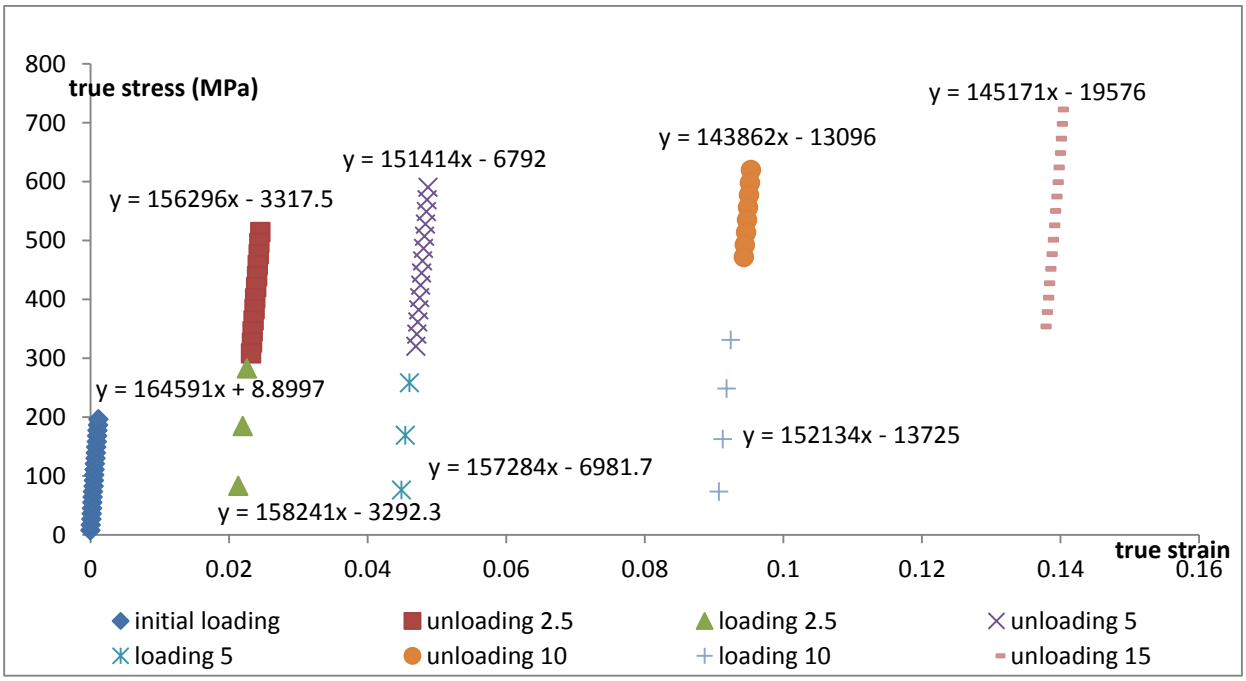

Figure 4-2: Modulus data for Ni Mn alloy (sample 1) showing linear region of loading/unloading cycles

It must be noted that all the modulus calculations are done using the true stress and true strain. The calculations were done using the method explained in the previous chapter with the help of figure 3-6. The loading and unloading moduli for each of the runs are tabulated in Tables 4-4 to 4-10 for each of the runs with the variance of the loading and unloading moduli at a particular strain.

The variance is calculated to give an insight of how much the elastic modulus changes along the course of transformation and whether there is enough transformation happening to change the modulus substantially. In most cases of cyclic loading, there is about 5% change in modulus even if there is no transformation.

Table 4-4: Elastic Moduli data for low nickel alloy

Low Nickel					
Strain	Loading Modulus (GPa)	Unloading Modulus(GPa)	Diff. between loading and unloading E (ΔE) in GPa	ΔE as % of loading E	ΔE as % of unloading E
0% (initial)	167				
2.50%	N/A	152	N/A	N/A	N/A
5%	159	151	8	5.03	5.30
10%	159	145	14	8.81	9.66
15%		142			

Table 4-5: Elastic Moduli data for high nickel alloy

High Nickel					
Strain	Loading Modulus (GPa)	Unloading Modulus(GPa)	Diff. between loading and unloading E (ΔE) in GPa	ΔE as % of loading E	ΔE as % of unloading E
0% (initial)	163				
2.50%	158	161	3	1.90	1.86
5%	159	154	5	3.14	3.25
10%	158	151	7	4.43	4.64
15%		149			

Table 4-6: Elastic Moduli data for high manganese (sample 1)

High Manganese (sample 1)					
Strain/Load	Loading Modulus (GPa)	Unloading Modulus(GPa)	Diff. between loading and unloading E (ΔE) in GPa	ΔE as % of loading E	ΔE as % of unloading E
0% (initial)	161				
10,000N (load)	171	171	0	0.00	0.00
2.50%	156	153	3	1.92	1.96
5%		145			

Table 4-7: Elastic Moduli data for high manganese (sample 2)

High Manganese (sample 2)					
Strain	Loading Modulus (GPa)	Unloading Modulus(GPa)	Diff. between loading and unloading E (ΔE) in GPa	ΔE as % of loading E	ΔE as % of unloading E
0% (initial)	176				
2.50%	169	155	14	8.28	9.03

Table 4-8: Elastic Moduli data for high manganese (sample 3)

High Manganese (sample 3)					
Strain/Load	Loading Modulus (GPa)	Unloading Modulus(GPa)	Diff. between loading and unloading E (ΔE) in GPa	ΔE as % of loading E	ΔE as % of unloading E
0% (initial)	172				
10,000KN (load)	176	171	5	2.84	2.92
1%	168	161	7	4.17	4.35
2.5%		155			

Table 4-9: Elastic Moduli data for nickel manganese (sample 1)

Nickel Manganese (sample 1)					
Strain	Loading Modulus (GPa)	Unloading Modulus(GPa)	Diff. between loading and unloading E (ΔE) in GPa	ΔE as % of loading E	ΔE as % of unloading E
0% (initial)	165				
2.50%	158	156	2	1.27	1.28
5%	157	151	6	3.82	3.97
10%	152	144	8	5.26	5.56
15%		145			

Table 4-10: Elastic Moduli data for nickel manganese (sample 2)

Nickel Manganese (sample 2)					
Strain	Loading Modulus (GPa)	Unloading Modulus(GPa)	Diff. between loading and unloading E (ΔE) in GPa	ΔE as % of loading E	ΔE as % of unloading E
0% (initial)	175				
2.50%	165	158	7	4.24	4.43
5%	159	155	4	2.52	2.58
10%	157	152	5	3.18	3.29
15%		149			

Figure 4-3 and 4-4 shows an elastic modulus vs strain plot for all the samples to sum up the observation from tables 4-4 to 10, for loading and unloading moduli respectively.

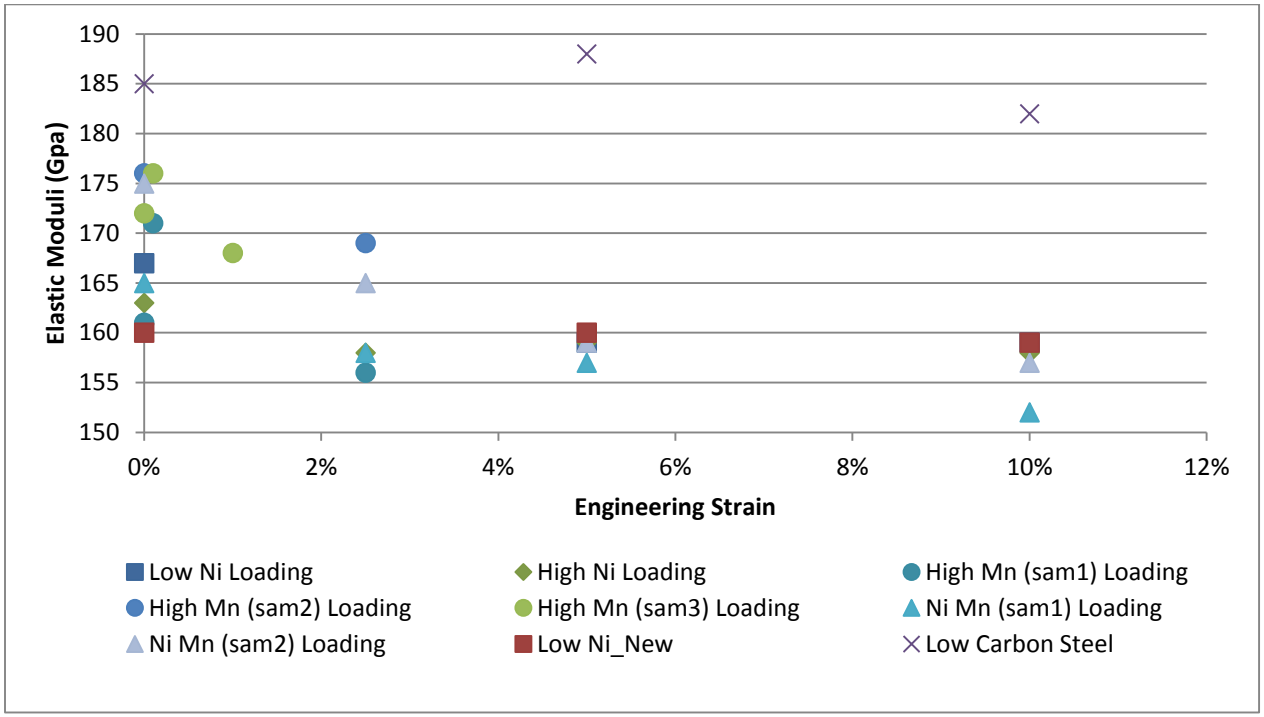

Figure 4-3: Elastic moduli vs. Engineering strain for all alloys for loading cycles showing the trend in Elastic moduli

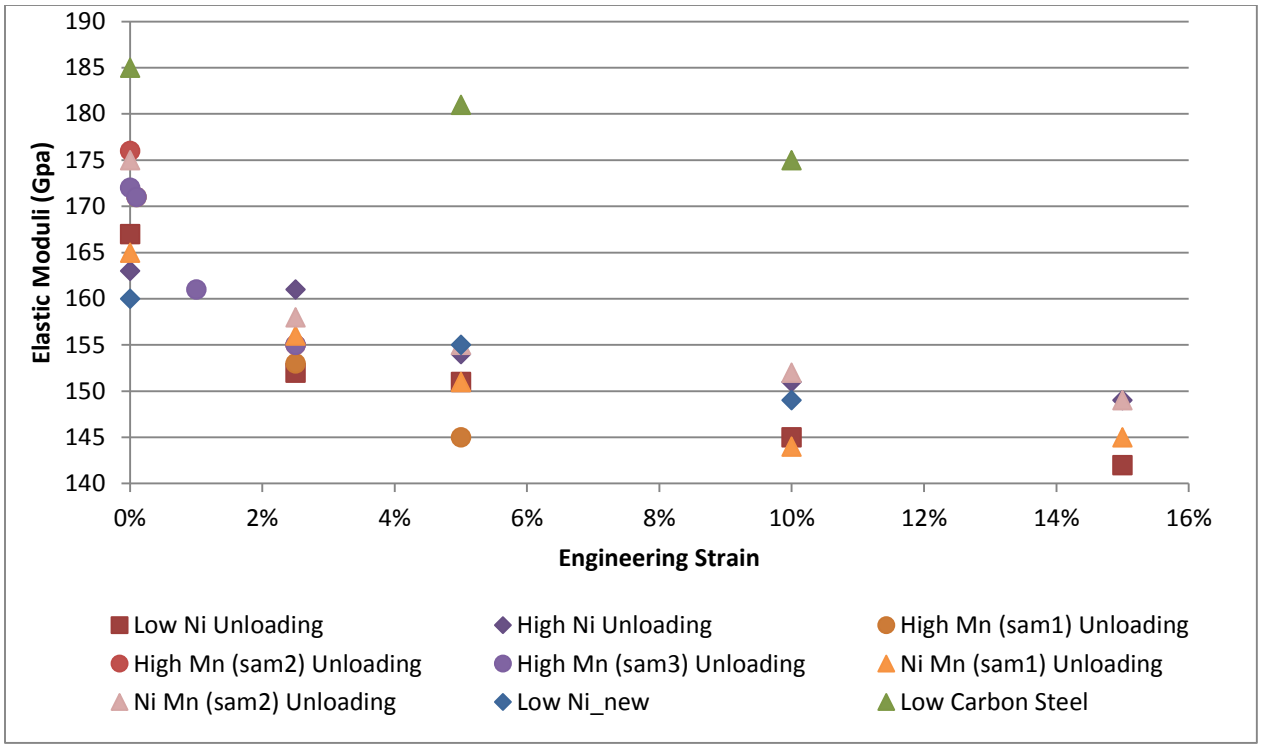

Figure 4-4: Elastic moduli vs. Engineering strain for all alloys for unloading cycles showing the trend in Elastic moduli

The difference between loading and unloading elastic modulus (ΔE) at a particular strain/load level is also calculated. ΔE is then expressed as a percentage of loading and unloading elastic moduli for that strain/load level. It was observed that for most of the cases the percentage variance is less than 5%. The loading modulus is usually higher than the unloading modulus at the same strain, with a few exceptions.

Overall, there is a decreasing trend in the loading and unloading elastic moduli with increasing deformation. Also, the moduli observed for different samples of same alloys is essentially same.

The high manganese samples have the highest overall modulus, followed by nickel-manganese samples, high nickel sample and lastly low nickel sample.

The loading and unloading moduli data for the tensile test on low Ni IADI and low carbon steel without any exposure to neutrons are plotted in figure 4-3 and 4-4, and are marked in the legends as Low Ni_new and Low carbon steel. The loading and unloading moduli for these samples also showed a decreasing trend. The low carbon steel does not undergo any transformation but still displays a decrease in modulus with

increasing strain. So this observation is a general property of materials and cannot be solely attributed to the transformation from austenite to martensite in IADI. Also, this is observed in the low nickel IADI tested without exposure to neutrons. So, it can be concluded that the decrease in moduli for the tested alloys should not be attributed to neutron exposure.

4.3 D-spacing data and whole spectral analysis

The spectral analysis was done using the VDRIVEVIEW function in the VDRIVE software package as discussed in the previous chapter. The diffraction data along with the tensile data was chopped into segments of 2 minutes. Using the VDRIVEVIEW function, we can view the intensity histogram for any one of such segments, otherwise known as "runs" in a 2 dimensional plot or view the intensity histograms for a series of consecutive runs in a 3 dimensional plot, for visual inspection of intensity as a function of time. The histogram for the initial run, that is for the first 2 minutes of diffraction and tensile data was used as a reference to create the data banks of peaks at various d-spacings, which was then used for single peak fitting using GSAS.

Figures 4-5, a and b show the intensity histograms in the transverse for the initial run and the final run for Ni-Mn sample 1 respectively. The intensity histogram for all the other tested samples is provided in Appendix C, section C-i. The peak locations were zoomed on to determine the exact d-spacing for each peak which was then tabulated in banks containing peak data. The d-spacing data for FCC, BCC and Graphite (HCP carbon) is tabulated in Appendix C in section C-ii. The histograms can be generated for both the longitudinal and transverse directions, but d-spacing and intensities were almost the same for both the banks.

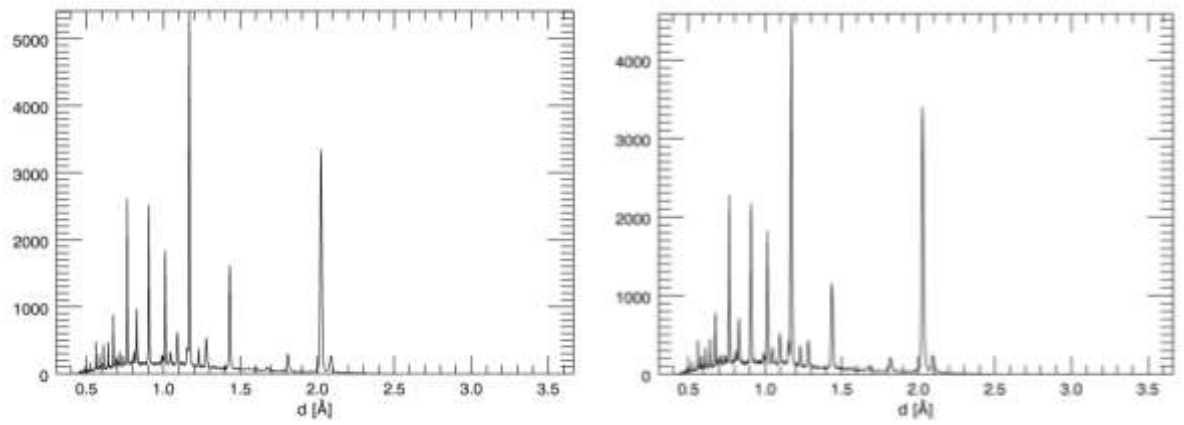

(a) (b)

Figure 4-5: Intensity histograms for (a) run 1 and (b) run 400 for nickel manganese alloy (sample 1)

The above figure and the figures in the appendix suggests that although there is almost no change in the peak positions there is a considerable change in the intensities. Even if the change in d-spacing cannot be seen in these figures, single peak fitting analysis showed that the d-spacings do change in the course of straining of the samples due to lattice strains.

But the change in the peak intensities is quite high and is clearly visible by the progressive reduction of intensity in the austenite peaks and an increase in intensity of the ferrite peaks. This is because of the transformation of face-centered cubic austenite to body-centered tetragonal martensite. The tetragonality of the martensite is dependent primarily on the carbon content of the parent austenite phase, which in this case is very small since martensite is close to the structure of body-centered cubic ferrite, a rise in the intensity of the ferrite peaks occurs during straining.

The initial intensity histograms, for run 1 or 2 are used to generate databanks for FCC (austenite), BCC (ferrite) and carbon peaks by comparison with standard crystallographic data, which are used for single peak fitting as discussed in the next section.

Another use for the VDRIVEVIEW command is to inspect the evolution of intensity histograms over a range of chopped runs or time segments. This data can display the evolution of intensities along the course

of unidirectional straining of the sample. The generated figures are a three dimensional surface and a corresponding contour plot for the surface. The surface plot for the Ni-Mn sample is given in Figure 4-6. The other surface plots are in Appendix C in section C-iii.

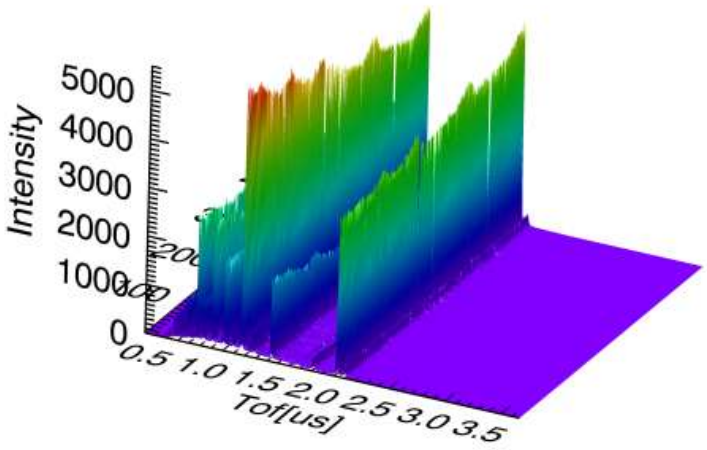

Figure 4-6: Surface plot for nickel manganese alloy (sample 1)

The surface plots are color-coded with red being the highest intensity and blue being the lowest. These surfaces can give an idea about the increase or decrease in intensity during deformation.

The surface plots of the intensity histograms are a tool to observe the increase or decrease in intensity of each of the peaks. The decrease in peak intensity leads to a decrease in the integrated intensity assuming there is no peak broadening, which can be related to the volume fraction of the phase in the matrix that the histogram represents. For example, hypothetically if the peak intensity corresponding to FCC hkl plane decreased along the course of deformation while all the other peaks maintained constant intensity, it could be concluded that the volume fraction of the austenite phase in the matrix was decreasing. This marks the transformation of the austenite phase.

The d-spacing for the planes also changes along the course of deformation, the change corresponding to the lattice strain in different planes. But the change is so small it is not evident in the figures.

The increase in the intensity of BCC 110 peak (close to 2 angstoms) and the decrease in the intensity of FCC 311 peak (close to 1.25 angstoms) is particularly noteworthy for all the alloys. However, sudden jumps in intensity for the whole spectra, as observed in figure C-10 for high manganese alloy sample 3 is due to the sudden increase in power of the neutron beam.

The VDRIVEVIEW command is also capable of zooming in on a range of d-spacings to inspect the merging of peaks if any. On closer inspection, it was found that the 111 FCC (austenite) peak merges with the 110 BCC (ferrite) peak along the course of deformation for all the high manganese samples. Figures 4-7 to 4-9 (a) provide a close-up view of the d-spacing data from 1.7-2.2 angstrom for the high manganese alloy samples 1,2 and 3. Figures 4-7 to 4-9 (b) show the contour maps in the same samples displaying the progressive merging of the peaks.

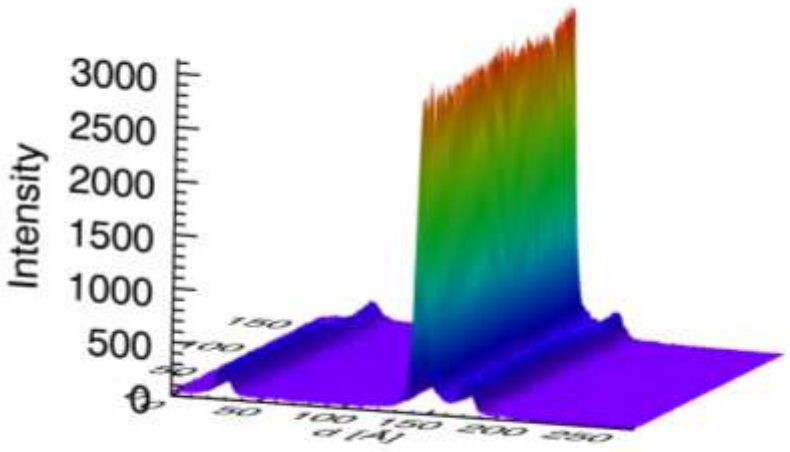

Figure 4-7 (a): Intensity histograms from start run=1 to end run=165 for High Mn alloy (sample 1)

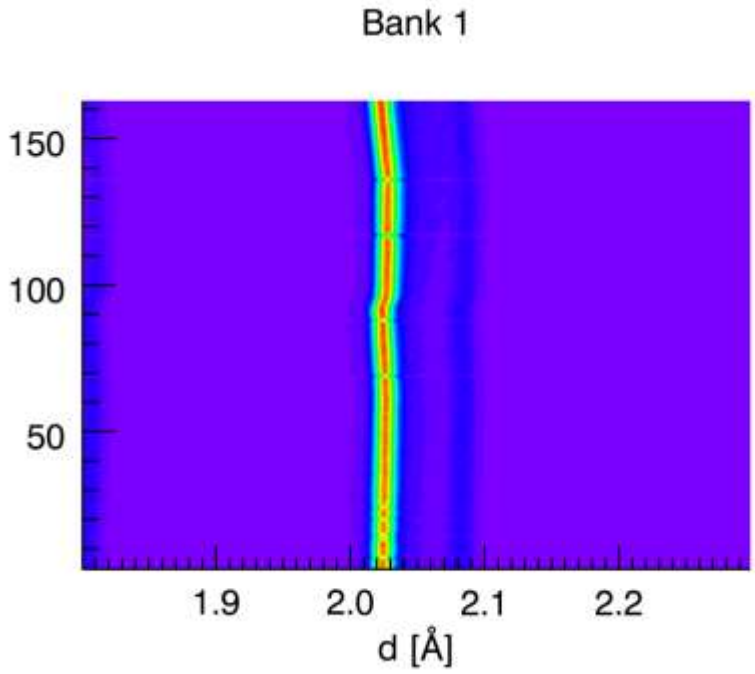

Figure 4-7(b): Contour plot for the surface in figure 4-7(a) displaying the merging of FCC 111 and BCC 110 peaks

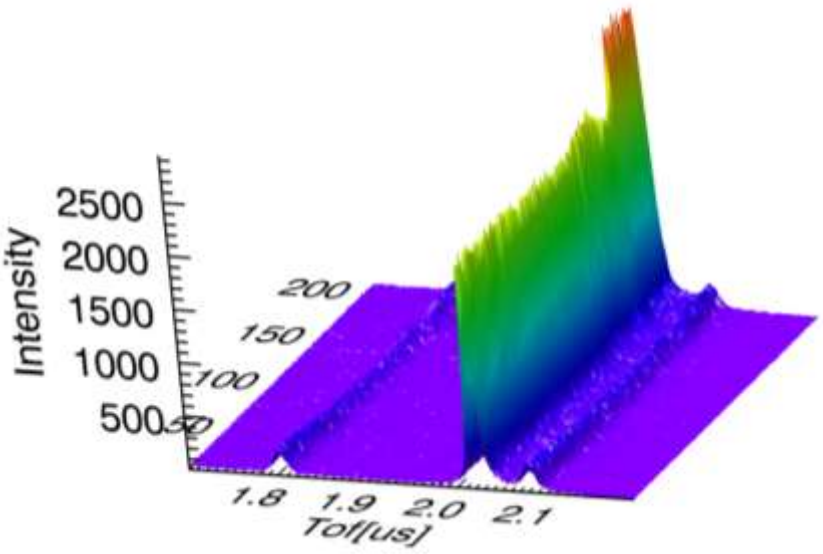

Figure 4-8 (a): Intensity histograms from start run=1 to end run=200 for High Mn alloy (sample 2)

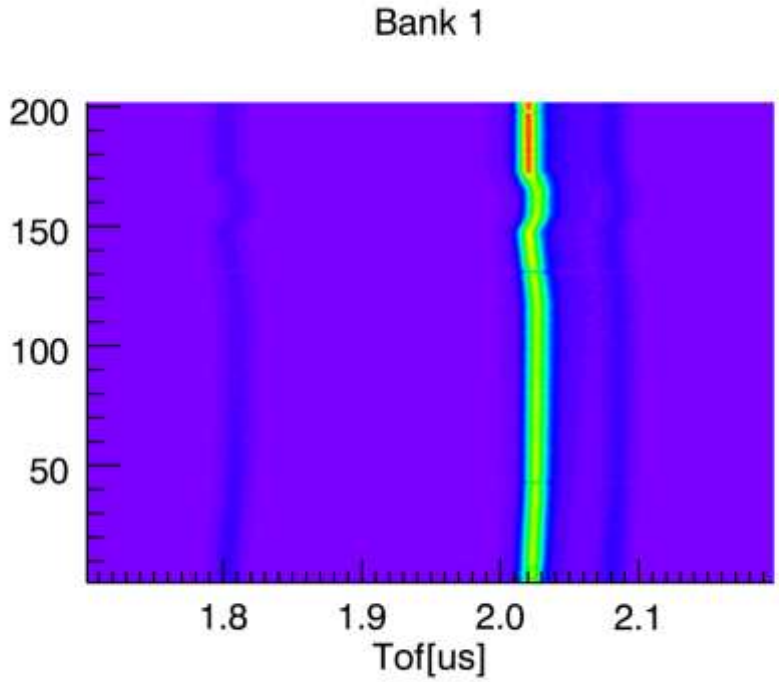

Figure 4-8(b): Contour plot for the surface in figure 4-8(a) displaying the merging of FCC 111 and BCC 110 peaks

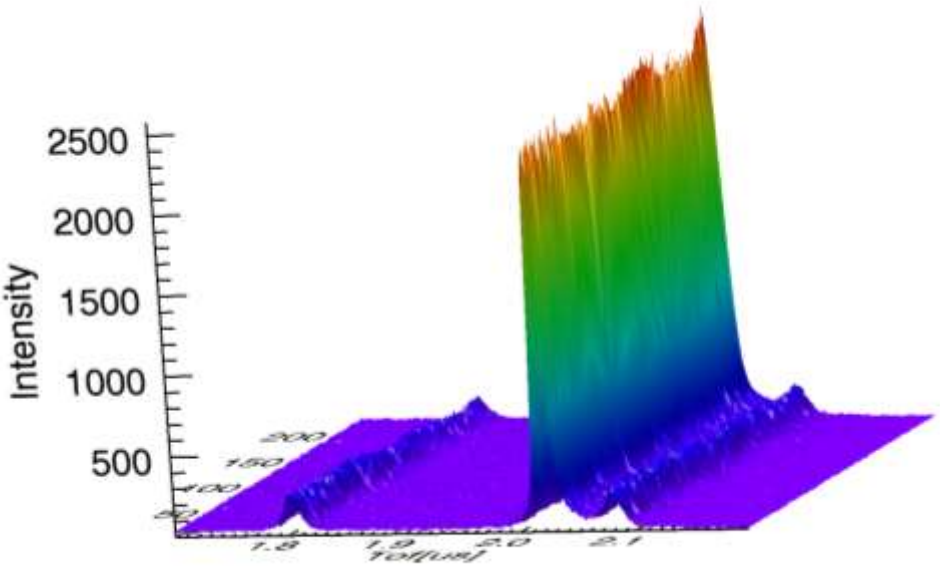

Figure 4-9 (a): Intensity histograms from start run=1 to end run=220 for High Mn alloy (sample 3)

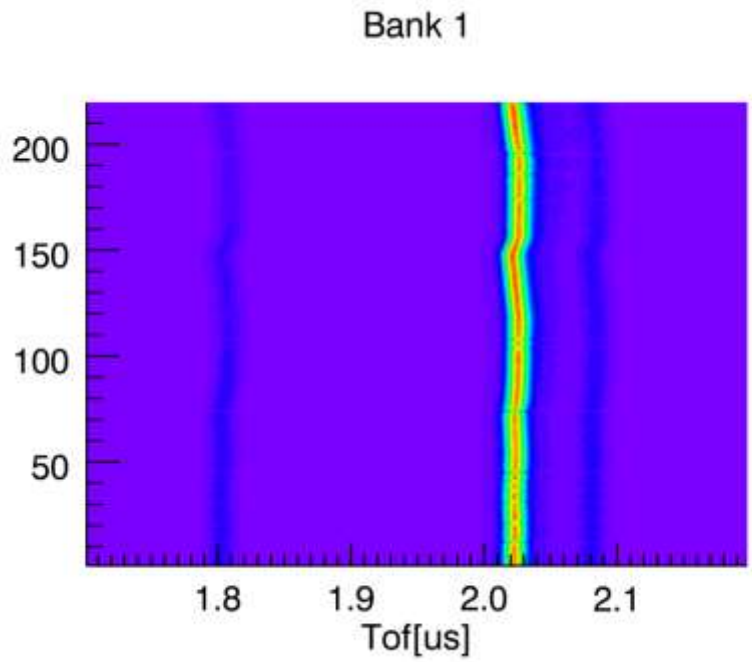

Figure 4-9(b): Contour plot for the surface in figure 4-9(a) displaying the merging of FCC 111 and BCC 110 peaks

In figures 4-7 to 4-9, the zero intensity is represented by the color violet, which is equivalent to background radiation. The base of the peaks, the broadest part, which is just above the violet background are color-coded blue. If examined carefully, it can be observed along the course of deformation, represented in this case by time or run number of the y axis of the contour plots, the base of the intensity histogram for FCC 111 plane merges with that for the BCC 110 plane, marked by the disappearance of the violet strip separating the base of the two histograms.

Table 4-11 gives an estimated time, stress and strain during the observed merging of the intensity histograms. The stress and strain data is from the generated true stress-true strain curve. However, this stress does not represent the stress at which the actual transformation occurs. This stress represents the stress at which the transformed martensite starts to show BCT structure, which is similar to BCC ferrite.

Table 4-11: Run number, time, stress and strain during observed merging of FCC 111 intensity histogram with BCC 110 intensity histogram.

Sample Number	Approximate run number	Time elapsed from start of the tensile test (mins)	True stress (MPa)	True strain (%)
High Mn (sample 1)	120	240	566	1.50
High Mn (sample 2)	165	330	687	3.12
High Mn (sample 3)	190	380	621	2.28

The austenite phase transforms to martensite during straining. Martensite exhibits a body centered tetragonal crystal (BCT) structure, which is very close to the body centered cubic (BCC) structure of ferrite. The tetragonality of the BCT martensite is strongly dependent on the carbon content of the parent austenite. If the carbon content of the austenite is very low, the tetragonality will not be pronounced [59]. So, the diffraction peaks generated by the martensite are very close to the ferrite peaks. The merging of the FCC and BCC intensity histograms can be explained by the transformation of FCC austenite to BCT martensite, which as explained possesses a crystal structure very close to BCC ferrite.

The peak merging however is observed at a much higher stress than the stress at which the transformation occurs marked by the decrease in the integrated intensities of austenite which will be discussed further in next section.

4.4 Stress and Strain at Transformation

4.4.1 True stress at transformation

The primary goal of the research was to determine the stress and strain for the start of the austenite to martensite transformation. Transformation of metastable austenite to martensite occured during tensile straining for all the tested alloys. The amount of austenite at different stresses was calculated using the integrated intensity for different peaks based on the method discussed in section 3.5.4.

The rationalized amount of austenite as calculated using equations 8 and 9 is plotted against true stress in figures 4-10 and 4-11 for Ni-Mn alloy (sample 1). For clarity of the stress at transformation, the unloading-loading cycles have been removed. The data for the other alloys can be found in Appendix D, figures D-1 to D-6.

The intensity and FWHM data for this graph was generated by single peak fit (SPF) method. The command VDRIVESPF is used to generate the single peak fit data in VDRIVE. Table 4-12 gives the approximate true stress at which the transformation of metastable austenite to martensite begins. This stress is marked by the decrease in fraction of austenite, which is expressed as a percentage of initial austenite fraction. The calculations were done based on the peaks specified by the ASTM standard of X-ray diffraction [44].

Figure 4-10 demonstrates the decrease in the rationalized volume fraction of austenite for all the peaks in Ni-Mn alloy (sample 1).

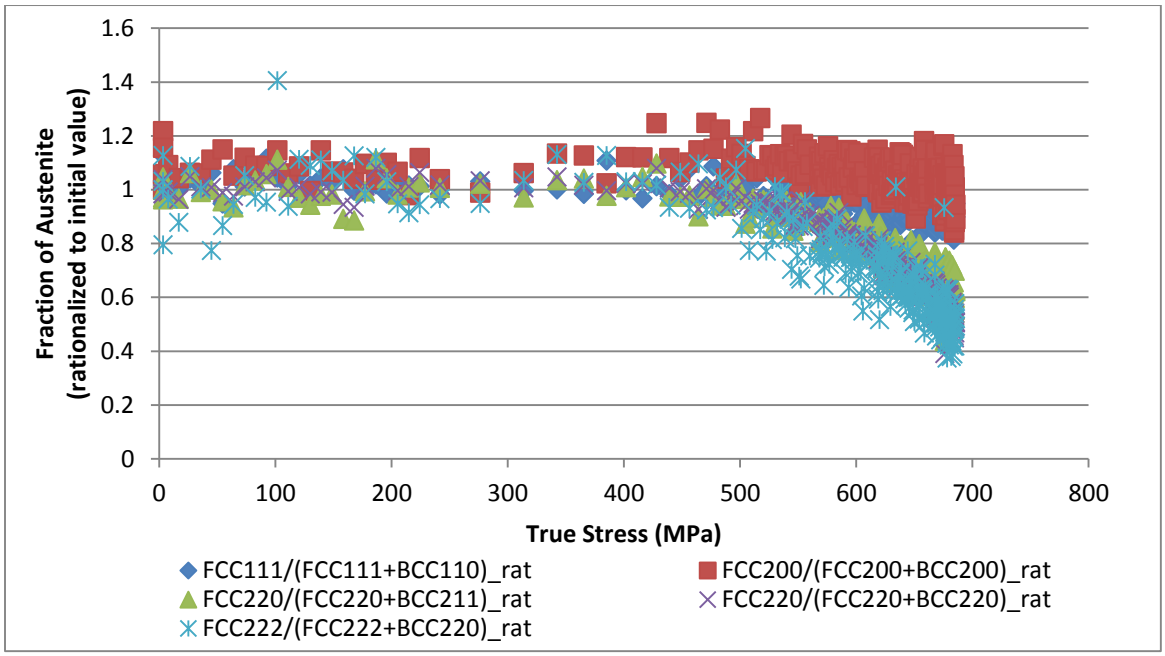

Figure 4-10: Rationalized fraction of austenite vs true stress for Ni-Mn alloy (all peaks)

For visual clarity only the FCC 220 and BCC 220 and 211 are chosen and display in figures 4-11, 4-13 and D-1 to 12. These two peaks also provide the best data for determination of the true stress and strain at transformation. In figure 4-11 these two peaks are shown for Ni-Mn alloy (sample 1) and the figures for the rest of the samples are provided in Appendix D in section D.i.

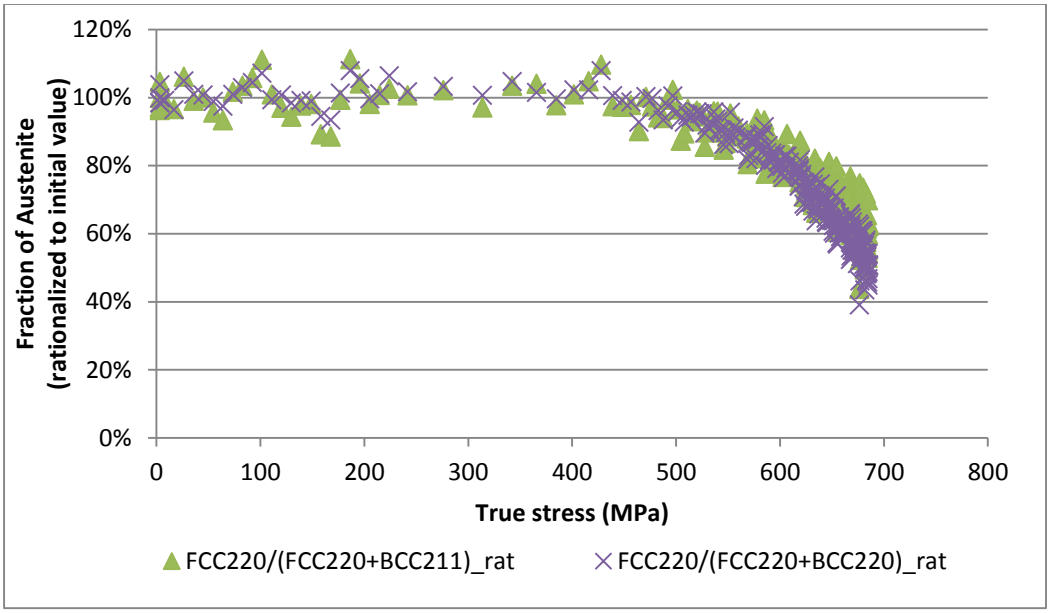

Figure 4-11: Rationalized volume fraction of austenite vs true stress for Ni-Mn alloy (sample 1)

From figure 4-11 and figures D-1 to 6, which show the rationalized version of austenite with respect to true stress, it can be observed that all the considered peaks showed decreases in the amount of austenite with increasing strain. The true stress at which the transformation starts is represented by the decrease in the rationalized amount of austenite. The calculation of volume fraction of austenite is semi-quantitative. Thus it is rationalized using the initial volume fraction of austenite equals to unity. So, the data here does not reflect how much austenite was there in the matrix before and after straining, but it does give an estimate of how much austenite, relative to the initial amount has transformed to martensite during tensile loading.

Table 4-12 has the stress at transformation for each of the different alloys listed along with the published data for comparison. However, data published by Druschitz et. al. used engineering stress, so for the sake of comparison we include the engineering stress corresponding to the true stress at which the transformation

begins in Table 4-12. The comparison between the published stress and the observed stress is given in Table 4-12A.

Table 4-12: Stress at transformation of metastable austenite for all the runs

Sample	True Offset Yield Stress (MPa)	True Stress at Transformation (MPa)	Engineering Stress at Transformation (MPa)	< or > than Yield Stress
Low Ni	489	535	524	>YS
High Ni	427	570	562	>>YS
High Mn (sample 1)	401	345	340	< YS
High Mn(sample 2)	400	365	358	< YS
High Mn (sample 3)	399	345	339	< YS
Ni-Mn (sample 1)	415	464	457	>YS
Ni-Mn (sample 2)	414	471	466	>YS

Table 4-12A: Published data by Druschitz et. al [48]

Sample	Engineering Offset Yield Stress (MPa)	Engineering Stress at Transformation (published [42]) (MPa)	Engineering Stress at Transformation (observed avg) (MPa)
Low Ni	498	N/A	524
High Ni	415	N/A	562
High Mn	403	300	345
Ni Mn	432	400	461

The true stress at transformation is greater than the offset yield stress for all of the materials except the high Mn alloys. For all the nickel containing alloys, the transformation occurs right after the material starts to yield as shown by (>YS) in the final column where YS is the true yield stress of the material. But for high manganese alloys the transformation occurs before the material starts to yield.

The stress at which austenite started transforming to martensite was different for the different alloys. For a comparative idea of this stress, Figure 4-12 is used to plot the rationalized fraction of retained austenite for the four alloys tested. It should be noted that only sample 1 for high Mn and Ni-Mn alloy is plotted here.

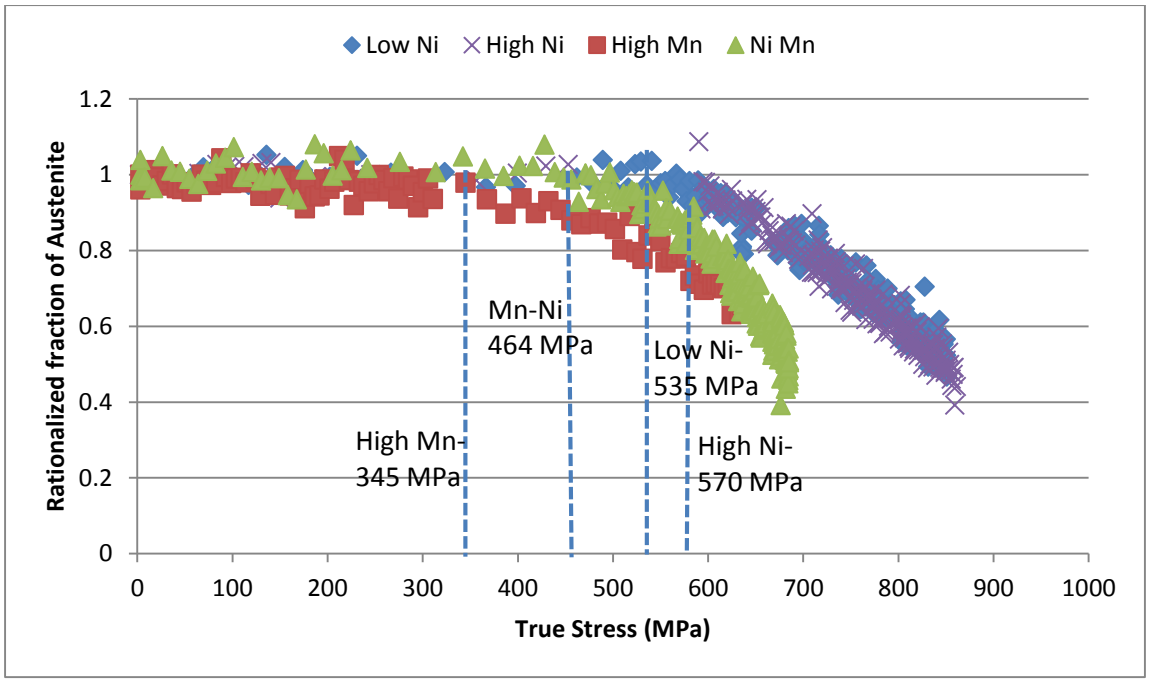

Figure 4-12: Comparison of true stress at which transformation begins for each alloy, using FCC 220 and BCC 220

4.4.2 True strain at transformation

The rationalized amount of austenite as calculated using equations 8 and 9 is plotted against true strain in figure 4-13 for Ni-Mn alloy. The plots for other samples are in Appendix D section D.ii.

For clarity of the strain at transformation, the unloading-loading cycles have been removed. The fraction of austenite is expressed as a percentage of the initial value as calculated from integrated intensity data using equation 8 and 9. Also, as in previous section, only FCC 220 and BCC 220 and 211 peaks are used, the others being omitted for better clarity.

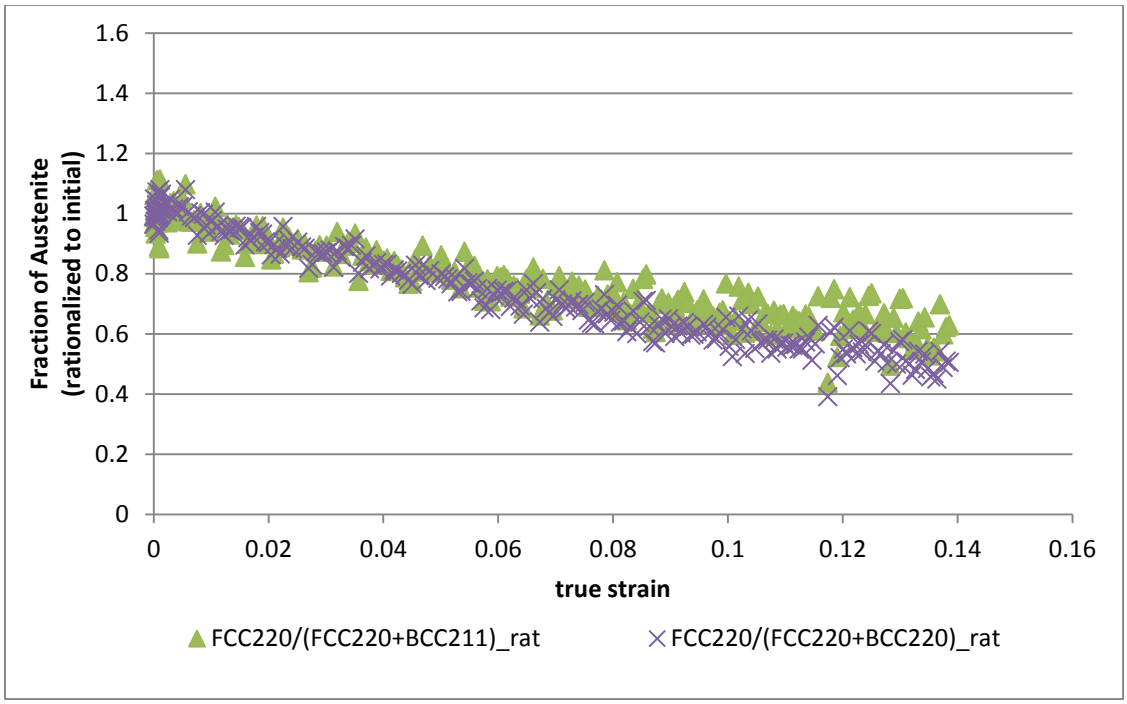

Figure 4-13: True strain vs. fraction of austenite (rationalized to initial) for Ni-Mn alloy (sample 1)

Although there is a fixed stress at which the transformation begins for all the individual materials, the transformation continues linearly as the strain increases as evident from the plots. But there is a small initial strain for which there is no change in the value of rationalized fraction of austenite.

Table 4-13 has the true strain at transformation listed for each of the different alloys for comparison as observed from the plots.

Table 4-13: Strain at transformation of metastable austenite for all the runs

Sample	True Strain at Transformation(absolute)
Low Ni	0.010
High Ni	N/A
High Mn (sample 1)	0.002
High Mn(sample 2)	0.001
High Mn (sample 3)	0.001
Ni-Mn (sample 1)	0.010
Ni-Mn(sample 2)	0.007

The true strain at which the transformation occurs for High Ni alloy is not available as the neutron beam was interrupted by a power surge. Also, as the order of the strain is very low, it is not conclusive. But from the above chart it is clear that the transformation approximately starts at similar values of true strain for all the alloys except the high Mn ones. For further investigation, Figure 4-14 is used to plot the rationalized fraction of retained austenite for the four alloys inspected as a function of true strain. It must be noted that only sample 1 for high Mn and Ni-Mn alloy is plotted here. The strain axis is plotted in figure 4-15 till 2.5% for clarity.

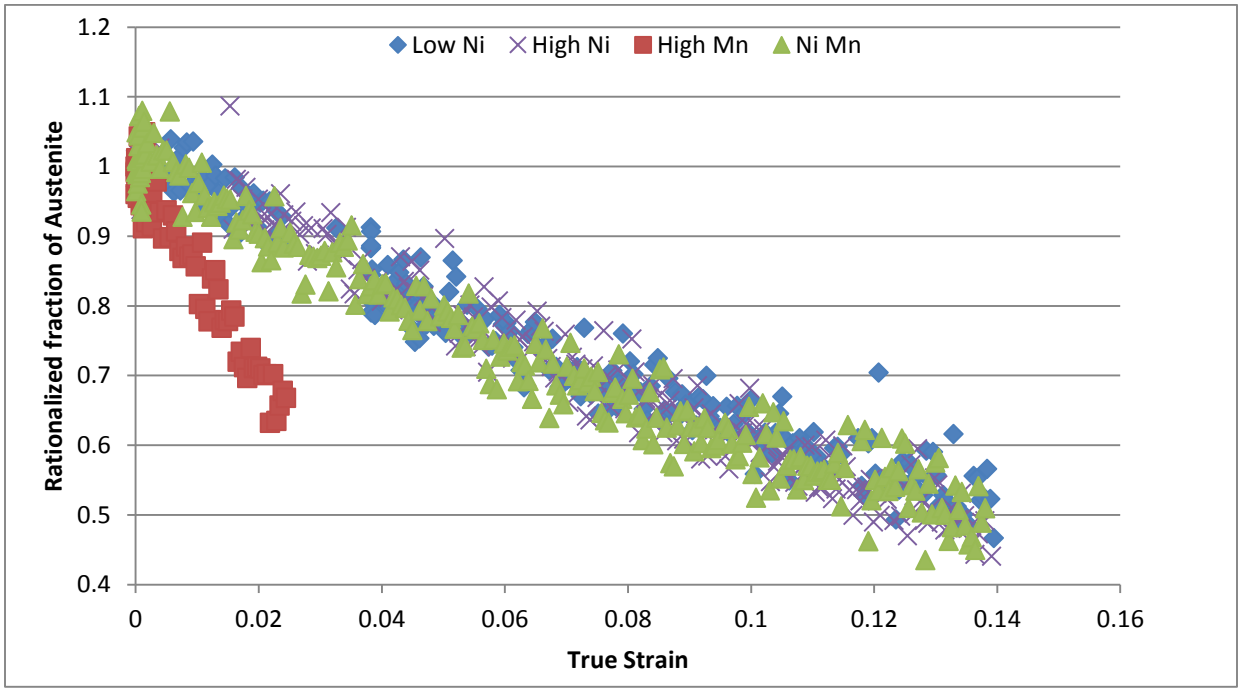

Figure 4-14: Comparison between strains at which transformation begins for each alloy, using FCC 220 and BCC 220

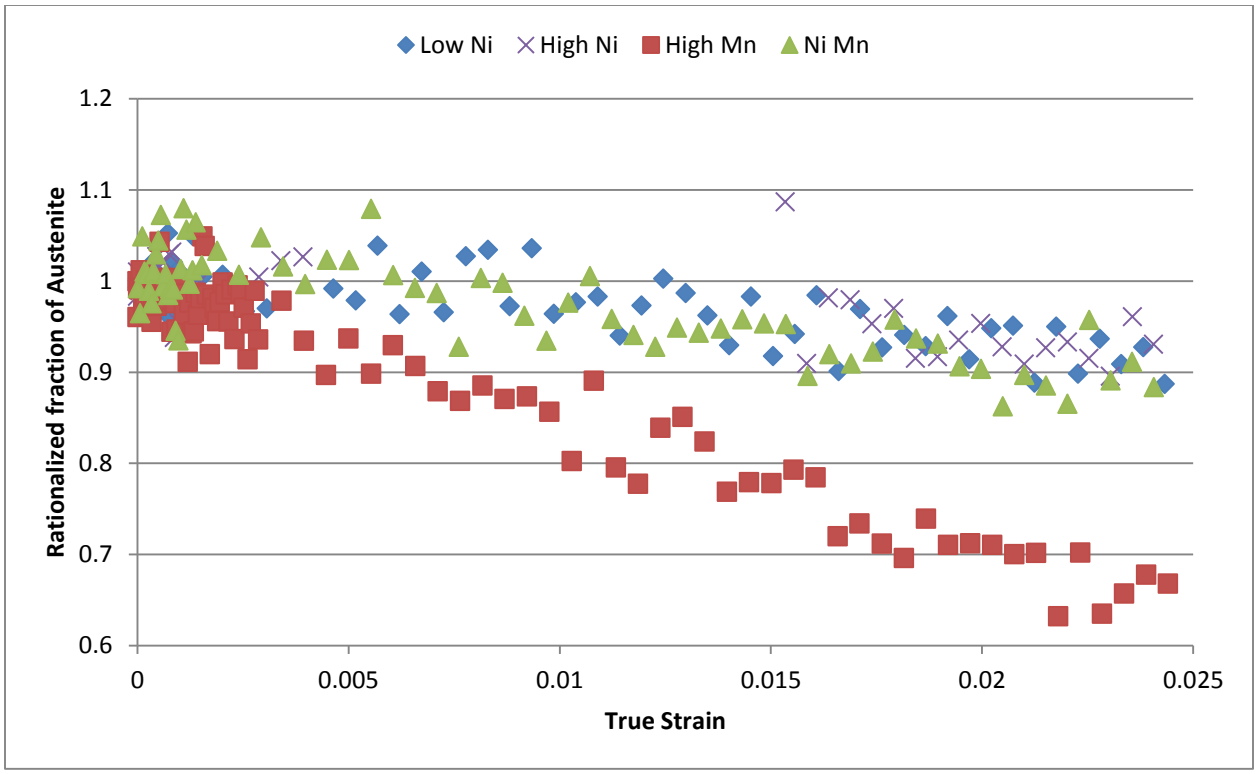

Figure 4-15: Comparison between strains at which transformation begins for each alloy, using FCC 220 and BCC 220 (upto 2.5% strain)

In Figures 4-14 and 4-15, it can clearly be noticed that the transformation approximately starts at the same true strain for all the alloys except high Mn alloy samples. But the rate at which it proceeds is very different. The rate of transformation in high Mn alloy is much faster in comparison to the other three types of alloys. It is also evident that the rate of transformation with respect to true strain is approximately linear.

4.5 Diffraction Elastic Constants

The elastic diffraction constants were calculated using the lattice strain data as generated by VDRIVE single peak fit command (VDRIVESPF). The lattice strain is calculated by the system using equation 10. The lattice strains for different planes of austenite (FCC) and ferrite (BCC) in the longitudinal and transverse directions were plotted against the true stress. The overall plots are shown in figures 4-16 and 4-17 for Ni-Mn (sample 1). The figures show the lattice strain vs. true macroscopic stress for FCC and BCC planes respectively. The plots for other samples are provided in Appendix E section E.i.

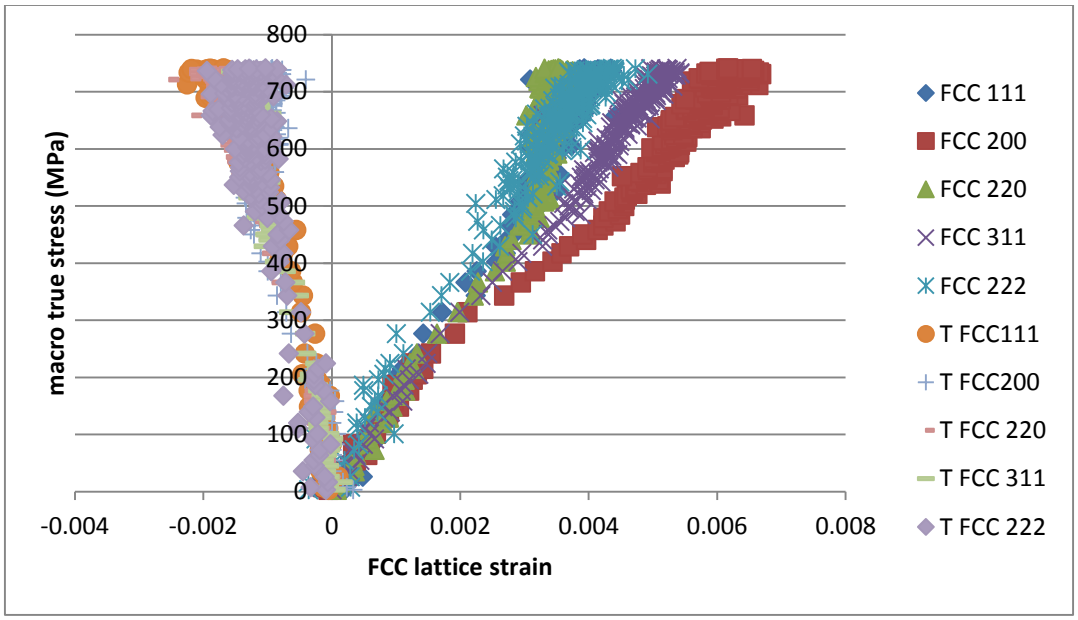

Figure 4-16: True stress vs. lattice strain for FCC planes in Ni-Mn alloy (sample 1)

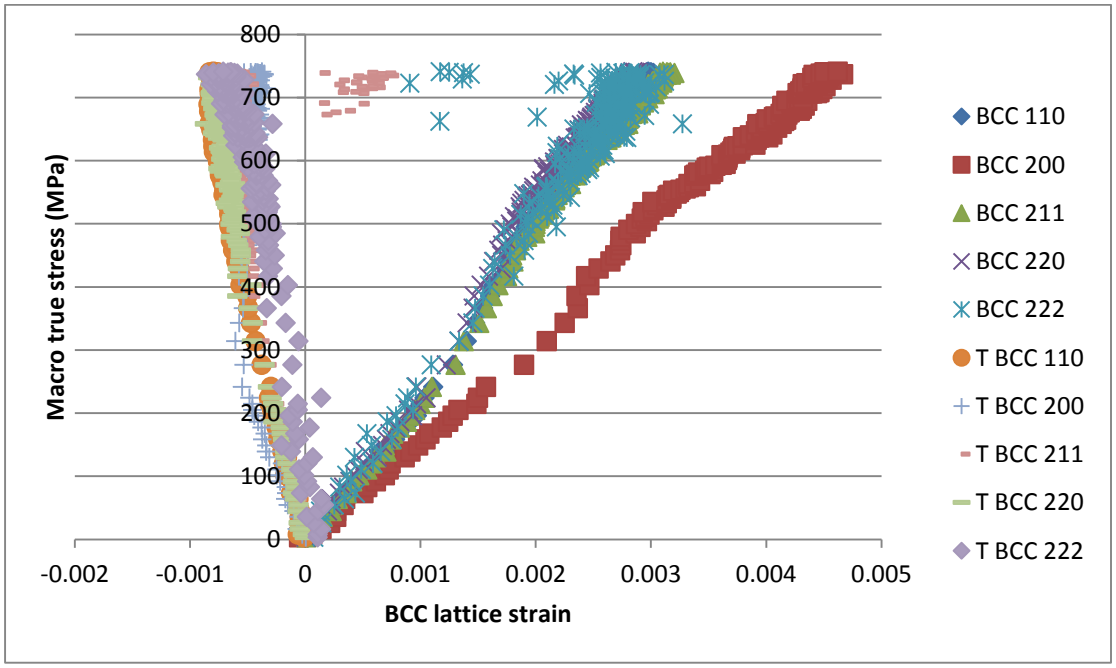

Figure 4-17: True stress vs. lattice strain for BCC planes in Ni-Mn alloy (sample 1)

It is observed from figure 4-16 and 4-17, that for the uniaxial straining, the lattice strain plots for both FCC and BCC planes has a prominent linear and non-linear part. The linear part corresponds to the elastic straining of the crystal lattice where the strain in the crystal lattice is proportional to the applied stress.

However beyond a critical stress, this linearity is lost. This critical stress is related to deformation occurring by slip and movement of dislocations and not by straining of the atom bonds.

Diffraction Elastic Constant: Some planes like BCC (110) and (222) are stiffer than other planes like BCC (200) for the investigated materials. This can be quantified taking into account the slope of the lattice strain vs. true stress plots up to the end of linearity. This slope is known as the Diffraction Elastic Constant (DEC) for the planes. For a polycrystalline multiphase material, the macroscopic strain is represented by a parallel (A) or series (B) or a combination (C) of lattice strains of a set of planes with similar orientation, otherwise known as 'grains' with different orientation as displayed in figure 4-18.

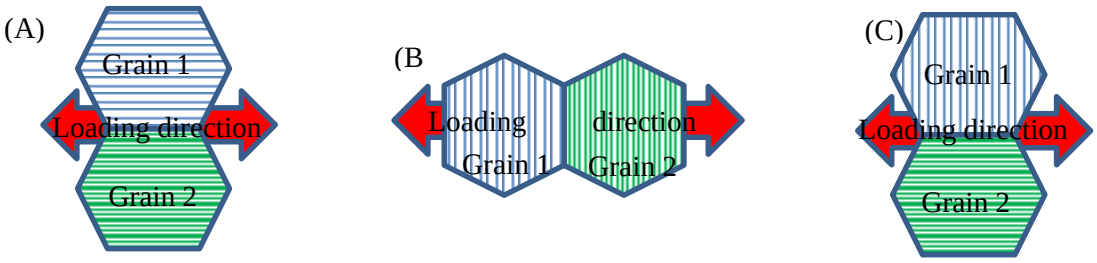

Figure 4-18: Grains showing (A) parallel, (B) series orientation to loading axis, and (C) a combination of orientations

Intergranular and Intragranular Stress: The plots have distinct linear and non-linear regions. The linear region represents the relationship between true stress and lattice strain for a particular planer direction. In a polycrystalline material, planes are oriented similarly in a single grain. The adjacent grain may have different planer orientation. Elastic deformation in such a material occurs by physical straining of the crystallographic planes with no slip. Such deformation is contained within the grain, and thus the linear region represent intragranular strain. At the onset of plastic deformation, the deformation in the material occurs primarily by movement of dislocations along the planes across the grain boundaries. During this stage, the lattice strain plots starts to deviate from the linear behavior. This is known as intergranular stress and is represented by the deviation of the lattice strain from the projected linear slope.

"Soft" and "Hard" orientations: The nonlinear deviation of stress can either be positive or negative. The positive deviation suggests the intergranular non-linear strain for that orientation is more than what is predicted by extrapolating the strain using the diffraction elastic constant for that orientation and the negative deviation suggest the the intergranular non-linear strain for that orientation is less than what is predicted by extrapolating the strain using the diffraction elastic constant for that orientation. The positive deviation is observed for FCC 200 plane and the negative deviation is observed in FCC 111 plane in Ni-Mn alloy as shown in figure 4-19. The predicted strains for each planes using DEC is given by the dashed red and blue lines for FCC 200 and 111 respectively. The former type is known as "hard orientation" and the latter is known as "soft orientation". Plastic deformation occurs along the planes with softer orientation.

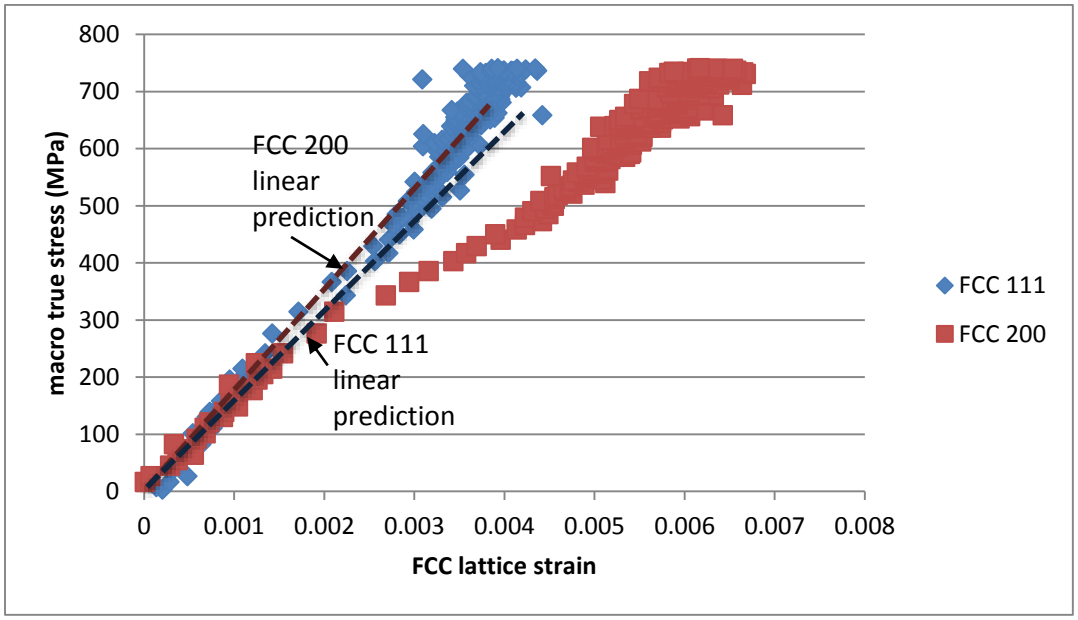

Figure 4-19: Hard and Soft orientation of FCC planes in Ni-Mn alloy (sample 1)

It is evident from the graphs that there are clear linear and non-linear parts to the lattice strain plots for all the planes. The diffraction elastic constants (DEC) of the planes are calculated taking the slope of the linear part of the plot for each of FCC and BCC plane systems as shown in figure 4-20 for BCC planes in Ni-Mn alloy (sample 1). The critical stress till for the linear region to be considered is 250 MPa, which is assumed

with a very conservative estimation. The Poisson's ratio can be calculated for each of the plane using the longitudinal and transverse lattice strains for the planes as shown in figure 4-21 for BCC planes in Ni-Mn alloy (sample 1).

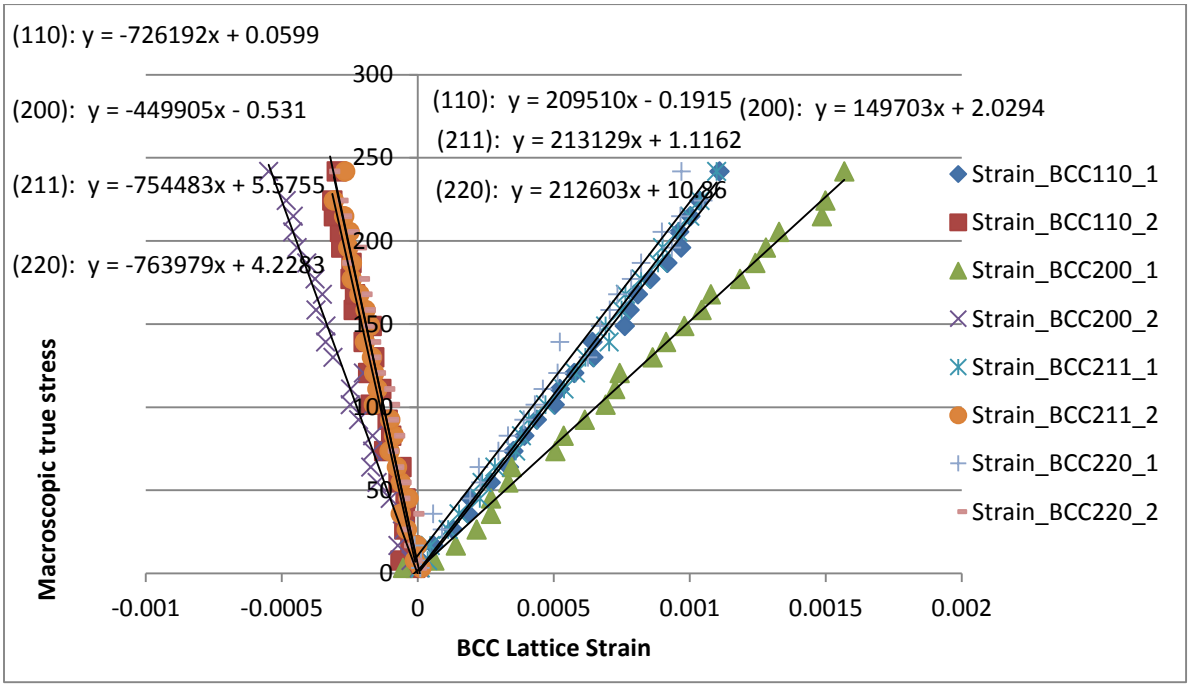

Figure 4-20: Plot showing linear fitting of BCC planes in Ni-Mn alloy (sample 1) to calculate the Diffraction Elastic Constant

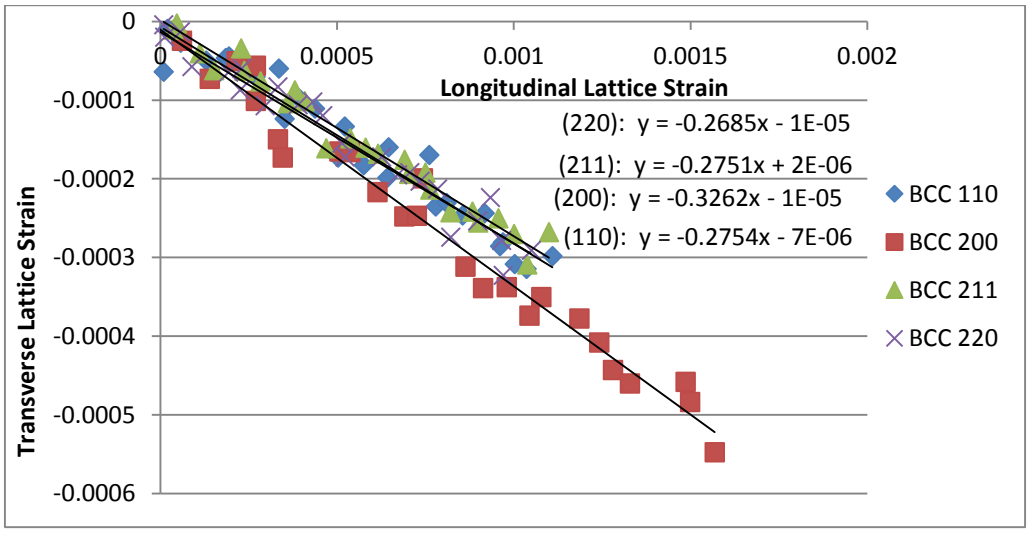

Figure 4-21: Plot showing linear fitting of BCC planes in Ni-Mn alloy (sample 1) to calculate the lattice Poisson's ratio

Table 4-14 shows the DEC for FCC 111 and 220 and BCC 110 and 220 for all the tested. Table E-1 in Appendix E section E.ii shows the diffraction elastic constants (DEC) and the Poisson's ratio for all the observed planes for each of the materials.

Table 4-14: Diffraction Elastic Constants for selected planes

			DEC in GPa (Longitudinal)	**DEC in GPa (Transverse)**	**Poisson's Ratio**
FCC	111	Low Ni	182	552	0.242
		High Ni	197	481	N/A*
		High Mn (sample 1)	146	450	0.299
		Mn Ni (sample 1)	176	304	0.397
	220	Low Ni	173	529	0.292
		High Ni	187	451	0.270
		High Mn (sample 1)	176	416	0.322
		Mn Ni (sample 1)	169	447	0.277
BCC	110	Low Ni	204	670	0.300
		High Ni	206	694	0.276
		High Mn (sample 1)	238	750	0.308
		Mn Ni (sample 1)	209	726	0.275
	220	Low Ni	141	416	0.334
		High Ni	154	447	0.312
		High Mn (sample 1)	159	592	0.247
		Mn Ni (sample 1)	150	450	0.326

*Note: The data with poor linear fit was omitted from the chart.

The scope of error in the calculation of the DEC and Poisson's ratio is high which can be displayed by lack of repeatability of the DEC data. The possible sources of errors are listed below:

- Small values of lattice strain: The values of lattice strains are in ppm levels, hence very small. Even a small error in measurement can cause a large error in DEC calculations. The source of the error in measurement can originate from the diffraction data or error in peak fitting.
- Error in calculation of true stress: The exact diameter during deformation was unknown, which may lead to errors in true stress calculations. This is thoroughly discussed in section 4.1.
- Error in lattice strain data: The peak fitting and calculation of lattice strain may not be precise enough to produce repeatable results. Especially for FCC111 and 222 planes in high manganese alloys, the fitting data is erroneous due to peak merging. These error can be resolved by using Reitveld analysis.

There are a few studies performed on the DEC of various planes of austenite and ferrite. The observed results were compared to the published data by Druschitz et.al [48] and with the calculated data from Chung and Buessem [60]. The published and calculated results are however available only in the longitudinal direction for FCC (111) and (311) planes and BCC (110) and (200) planes. This data is tabulated in Table 4-15 with the published data marked with a '*' and the tabulated data with a '#' symbol. Taking the scope of errors under consideration, the previously published and calculated data somewhat matches the observed data.

Table 4-15: Published and calculated data for FCC and BCC planes

Material	DEC Data (*published by Druschitz or # calculated for single crystals by Chung) in GPa			
	FCC 111	FCC 311	BCC 110	BCC 200
Low Ni*	N/A	N/A	228	117
High Ni*	182	153	205	112
High Mn*	239	189	284	175
Ni-Mn*	169	182	271	164
Single crystal data #	300	139	221	132

4.6 Residual Stresses and distribution of load

The longitudinal and transverse lattice strains for the FCC and the BCC planes were plotted against macroscopic strains to examine the distribution of load between the ferrite and austenite phases. Only FCC 200 and 220, and BCC 110 and 200 planes in both longitudinal and transverse directions are plotted for clarity. Figure 4-22 and 4-23 represents the longitudinal and transverse strains in FCC planes for Ni-Mn alloy (sample 1). Similarly, figure 4-24 and 4-25 displays these in BCC planes for Ni-Mn alloy (sample 1). The plots for the other materials are provided in Appendix F.

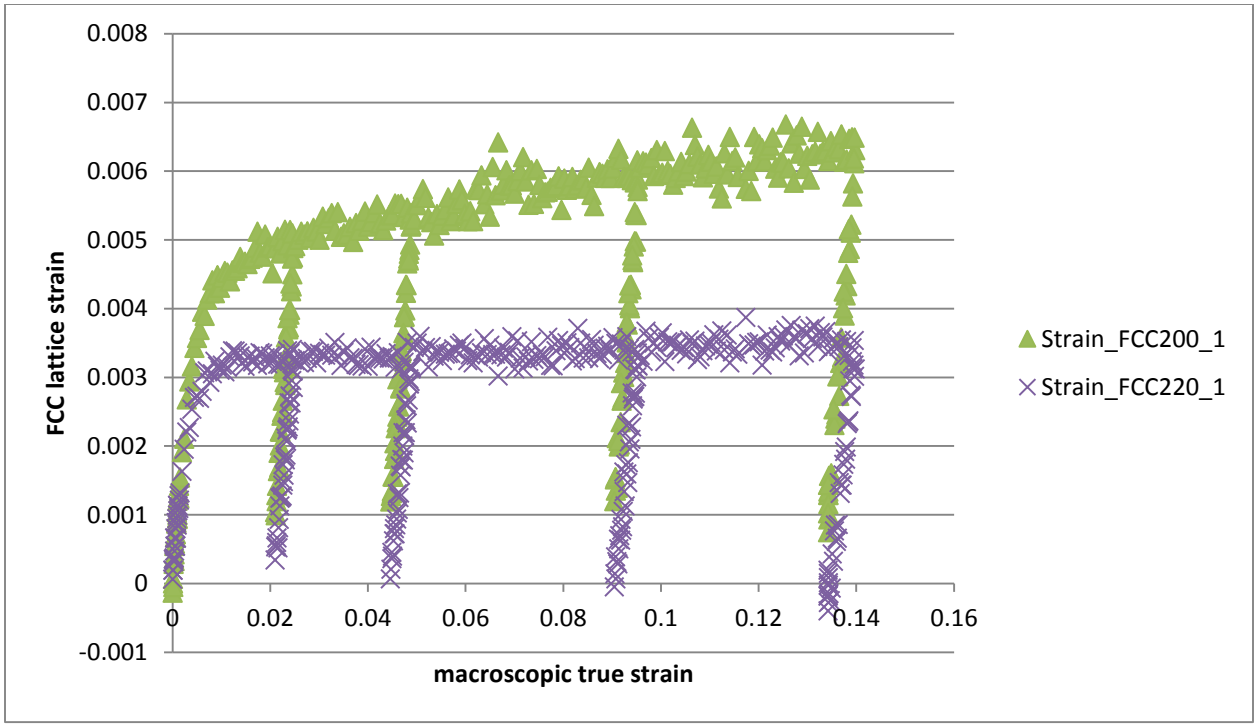

Figure 4-22: True strain vs. longitudinal lattice strains for FCC planes in Ni-Mn alloy (sample 1)

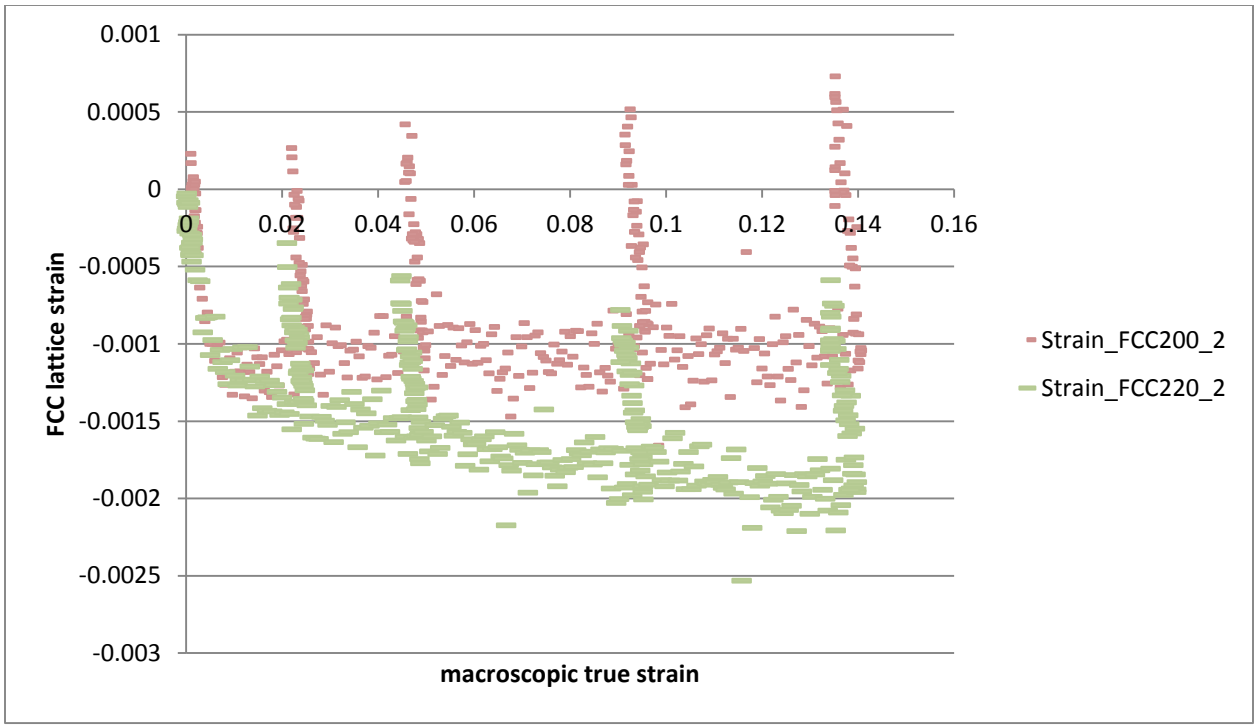

Figure 4-23: True strain vs. transverse lattice strains for FCC planes in Ni-Mn alloy (sample 1)

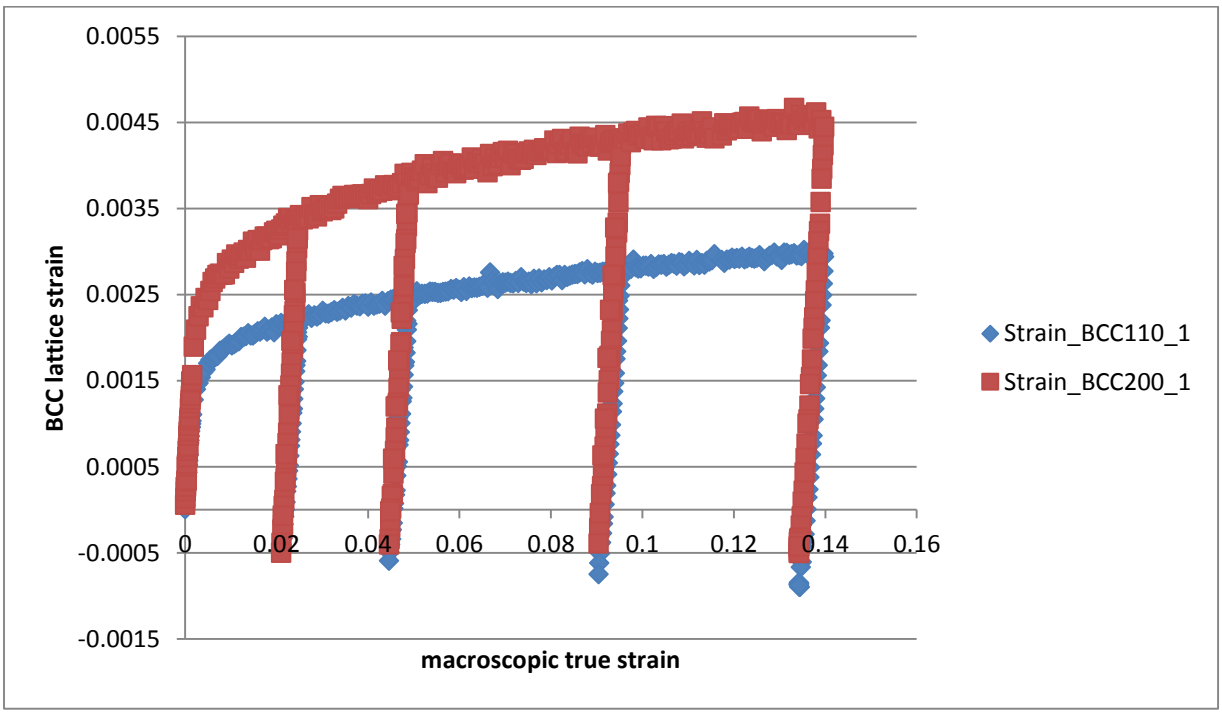

Figure 4-24: True strain vs. longitudinal lattice strains for BCC planes in Ni-Mn alloy (sample 1)

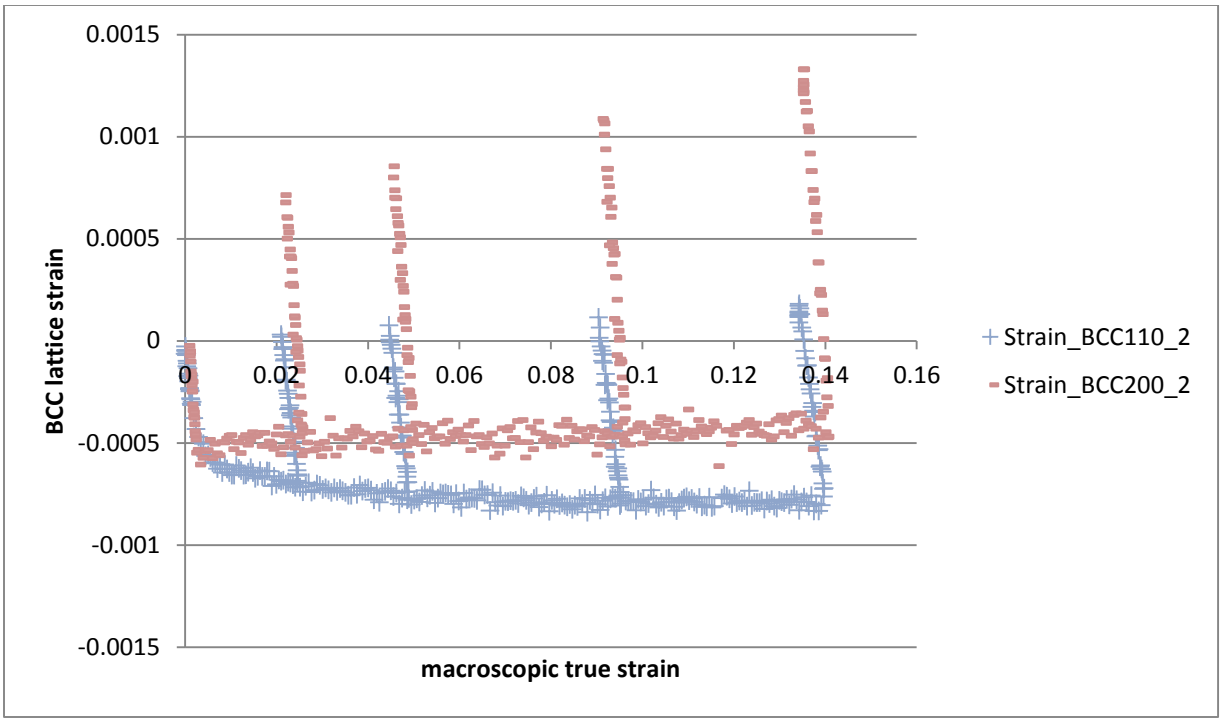

Figure 4-25: True strain vs. transverse lattice strains for BCC planes in Ni-Mn alloy (sample 1)

The longitudinal and transverse lattice strains beyond the elastic region in FCC planes is greater than the lattice strains in BCC planes (both tensile and compressive), at a fixed macroscopic true strain for all alloys. So at any given point of straining, the majority of the load beyond the elastic region is carried by the austenite.

The distribution of stresses during the loading and unloading cycles is demonstrated by the strain state of the different phases. Unloading from a higher stress, when the macroscopic true strain drop to zero, the lattice strain in FCC planes approaches zero, and in some cases goes slightly into compression. But in case of BCC planes, the longitudinal lattice strain goes well into compression, marked by the negative lattice strain axis and the transverse lattice strain goes into tension, while the macroscopic strain is still zero. This gives rise to residual strains in the crystallographic planes. This also demonstrates the partitioning of stress and strain among the two phases. It can be observed that, lower the lattice strain for both FCC and BCC, higher will be the residual strain of opposite nature. Table 4-16 the residual strain and maximum strain for FCC 200 and 220 and BCC 110 and 200 planes of all alloys is tabulated. The distribution of load also plays

an important part in determination of intergranular and intragranular stresses. The grain boundaries act as a hindrance to the movement of dislocation during plastic deformation and act as strain raisers. So, even if the macroscopic strain goes down to zero, the lattice strain in the grains either goes into compression or tension due to difference in intergranular stresses.

Table 4-16: Maximum and Residual Lattice strains for FCC and BCC planes

			Longitudinal Direction			Transverse Direction		
Alloy	**Cryst. Lattice**	**Planes**	**Max. Lattice strain**	**Residual lattice strain**	**Residual /Max. strain**	**Max. Lattice strain**	**Residual lattice strain**	**Residual /Max. strain**
Low Ni	FCC	200	0.0061	0.0002	0.0328	-0.0011	0.0004	-0.3636
		220	0.0037	-0.0004	-0.1081	-0.0025	0.0008	-0.3200
	BCC	110	0.0032	-0.0009	-0.2813	-0.0007	0.0003	-0.4286
		200	0.0048	-0.0007	-0.1458	-0.0003	0.0013	-4.3333
High Ni	FCC	200	0.0033	-0.0005	-0.1515	-0.0014	0.0008	-0.5714
		220	0.0067	-0.0002	-0.0299	-0.0018	-0.0005	0.2778
	BCC	110	0.0034	-0.0008	-0.2353	-0.0008	0.0001	-0.1250
		200	0.0058	-0.0001	-0.0172	-0.0004	0.0016	-4.0000
High Mn (sample 1)	FCC	200	0.0026	-0.0005	-0.1923	-0.0009	0.0006	-0.6667
		220	0.0039	-0.0002	-0.0513	-0.0011	-0.0001	0.0455
	BCC	110	0.0018	-0.0007	-0.3889	-0.0005	0.0001	-0.2000
		200	0.0032	-0.0009	-0.2813	-0.0003	0.0009	-3.0000
High Mn (sample 2)	FCC	200	0.0030	-0.0001	-0.0333	-0.0005	0.0007	-1.4000
		220	0.0043	-0.0002	-0.0465	-0.0010	-0.0001	0.1000
	BCC	110	0.0021	-0.0007	-0.3333	-0.0005	0.0002	-0.4000
		200	0.0034	-0.0010	-0.2941	-0.0003	-0.0009	3.0000
High Mn (sample 3)	FCC	200	0.0026	-0.0002	-0.0769	-0.0010	0.0006	-0.6000
		220	0.0040	0.0001	0.0250	-0.0012	0.0001	-0.0833
	BCC	110	0.0021	-0.0006	-0.2857	-0.0006	0.0001	-0.1667
		200	0.0032	-0.0004	-0.1250	-0.0003	0.0008	-2.6667
Ni-Mn (sample 1)	FCC	200	0.0060	0.0007	0.1167	-0.0011	0.0007	-0.6364
		220	0.0030	-0.0002	-0.0667	-0.0020	-0.0006	0.3000
	BCC	110	0.0031	-0.0006	-0.1935	-0.0007	0.0001	-0.1429
		200	0.0045	0.0004	0.0889	-0.0004	0.0013	-3.2500
Ni-Mn (sample 2)	FCC	200	0.0063	0.0010	0.1587	-0.0015	0.0002	-0.1333
		220	0.0035	0.0001	0.0286	-0.0018	-0.0006	0.3333
	BCC	110	0.0030	-0.0007	-0.2333	-0.0007	0.0001	-0.1429
		200	0.0046	-0.0005	-0.1087	-0.0004	0.0013	-3.2500

4.7 Sample Characterization

4.7.1 Light Microscope

The initial sample imaging was done using an Olympus light microscope at 500X. The microstructure of the unstrained section was examined taking a section from the gripped section of the tensile bar. The strained section from the middle of the sample was examined for comparison. A section was also taken parallel to the loading axis to look for micro-cracks. Figures 4-26 to 4-29 displays the images taken with the light microscope, fig (a) of the unstrained region, (b) of the strained zone and (c) of the section parallel to the loading axis.

In the figures, the bright white matrix is the ferrite and the blackish etched lamellar region is the austenite. The round dark black structures are the graphite nodules. The dark-etched bands, is a mixture of ferrite and austenite which cannot be resolved properly. The size of the graphite nodules ranges from 10-40 microns. The direction of loading is shown with a yellow arrow. As evident from the figures, the transformation does not change the microstructure significantly. For the high nickel and low nickel alloys, the austenite is dispersed evenly throughout the matrix, while in the manganese containing alloys the austenite forms clusters further away from the graphite nodules.

These images served as a primary tool for determination of basic microstructure before doing SEM imaging. The SEM images shed more light into the microstructure at a higher magnification.

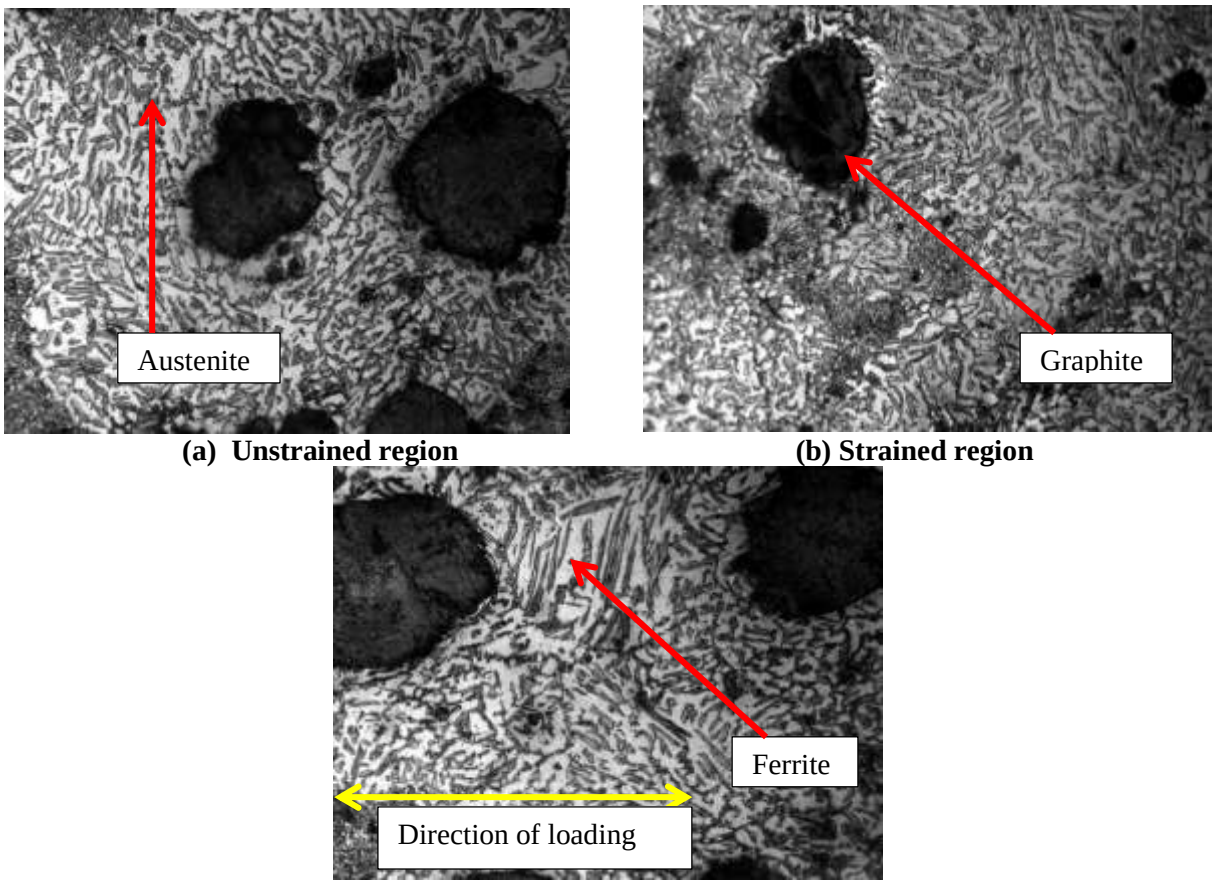

(a) Unstrained region **(b) Strained region**

(c) Strained region

Figure 4-26: Optical microscope image showing nodular graphite, islands of austenite in white ferrite in Low Ni at 500X

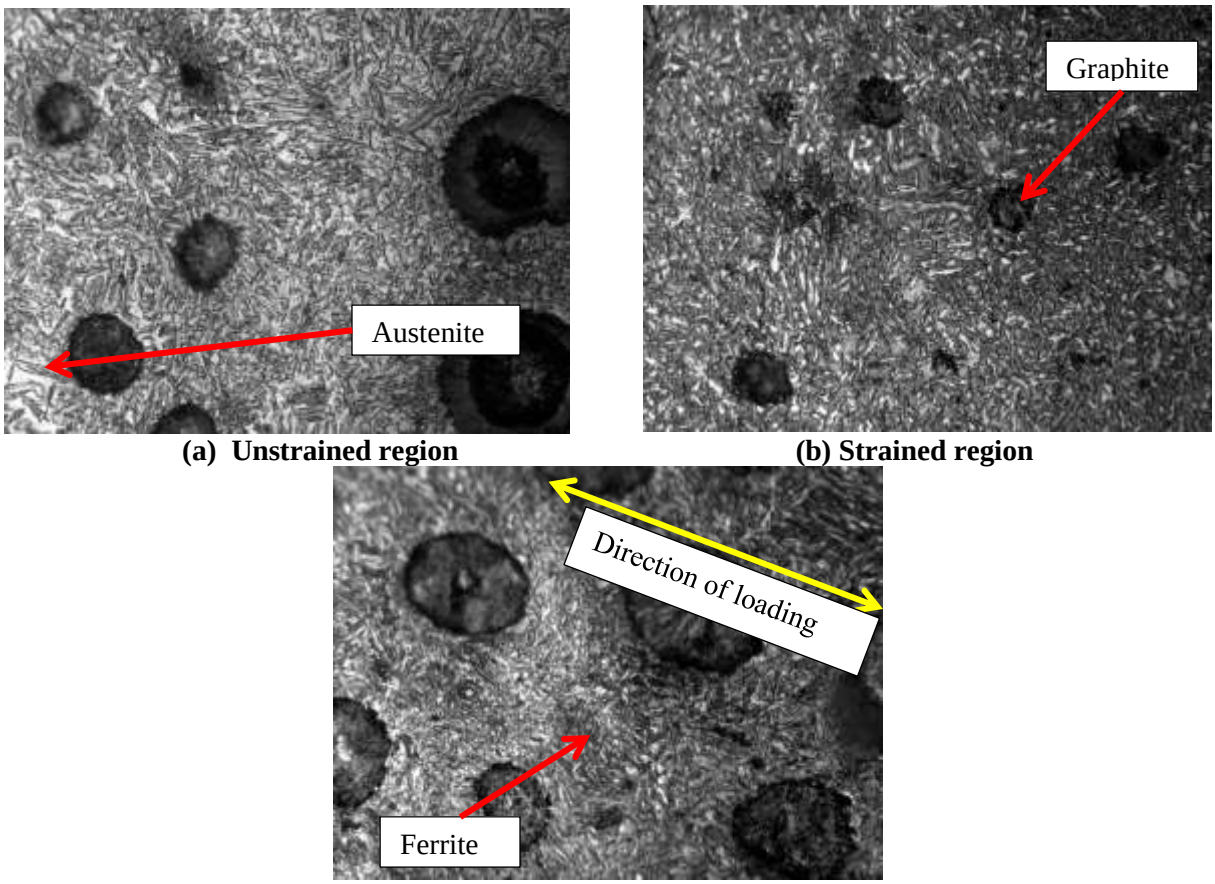

(a) Unstrained region **(b) Strained region**

(c) Strained region

Figure 4-27: Optical microscope image showing nodular graphite, grey lamellar austenite in ferrite in High Ni alloy at 500X

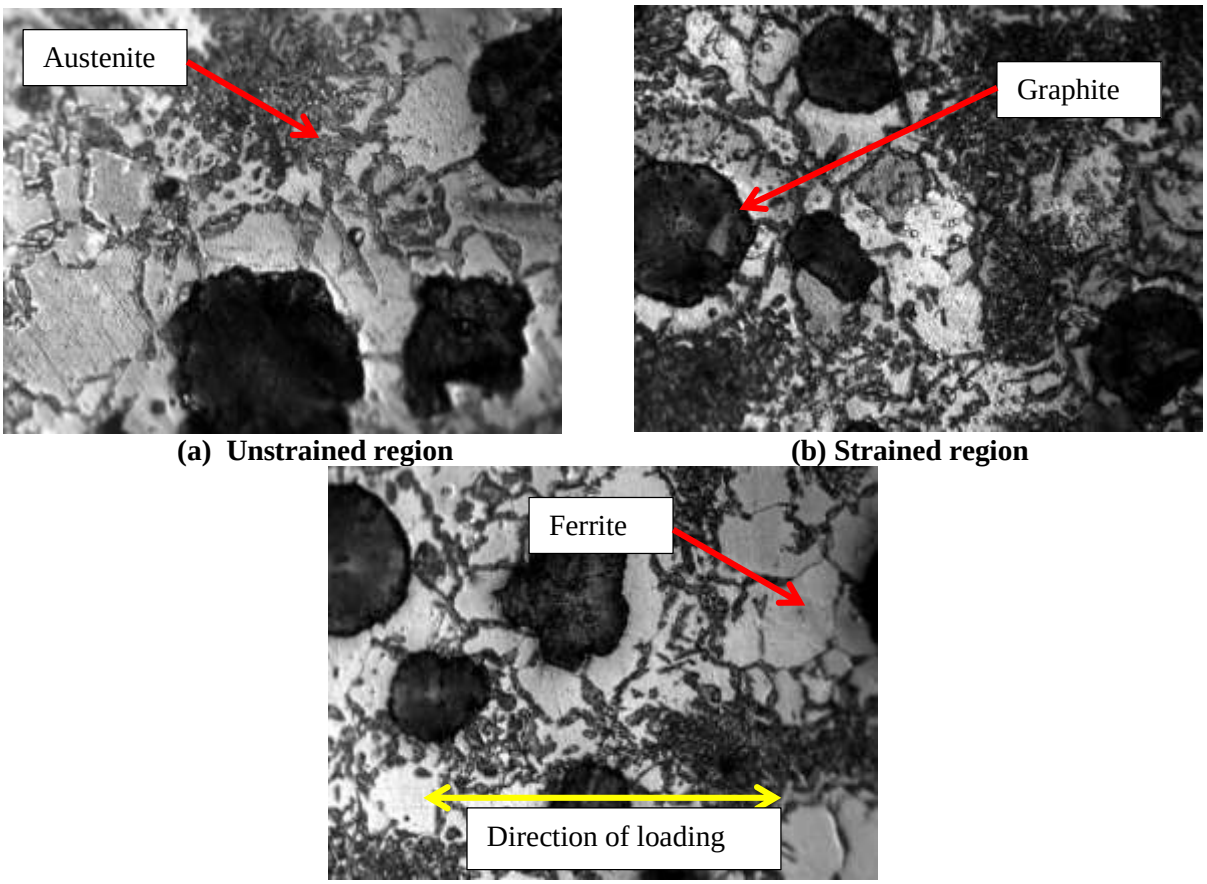

(a) Unstrained region **(b) Strained region**

(c) Strained region

Figure 4-28: Optical microscope image showing nodular graphite, islands of austenite in ferrite in High Mn alloy at 500X

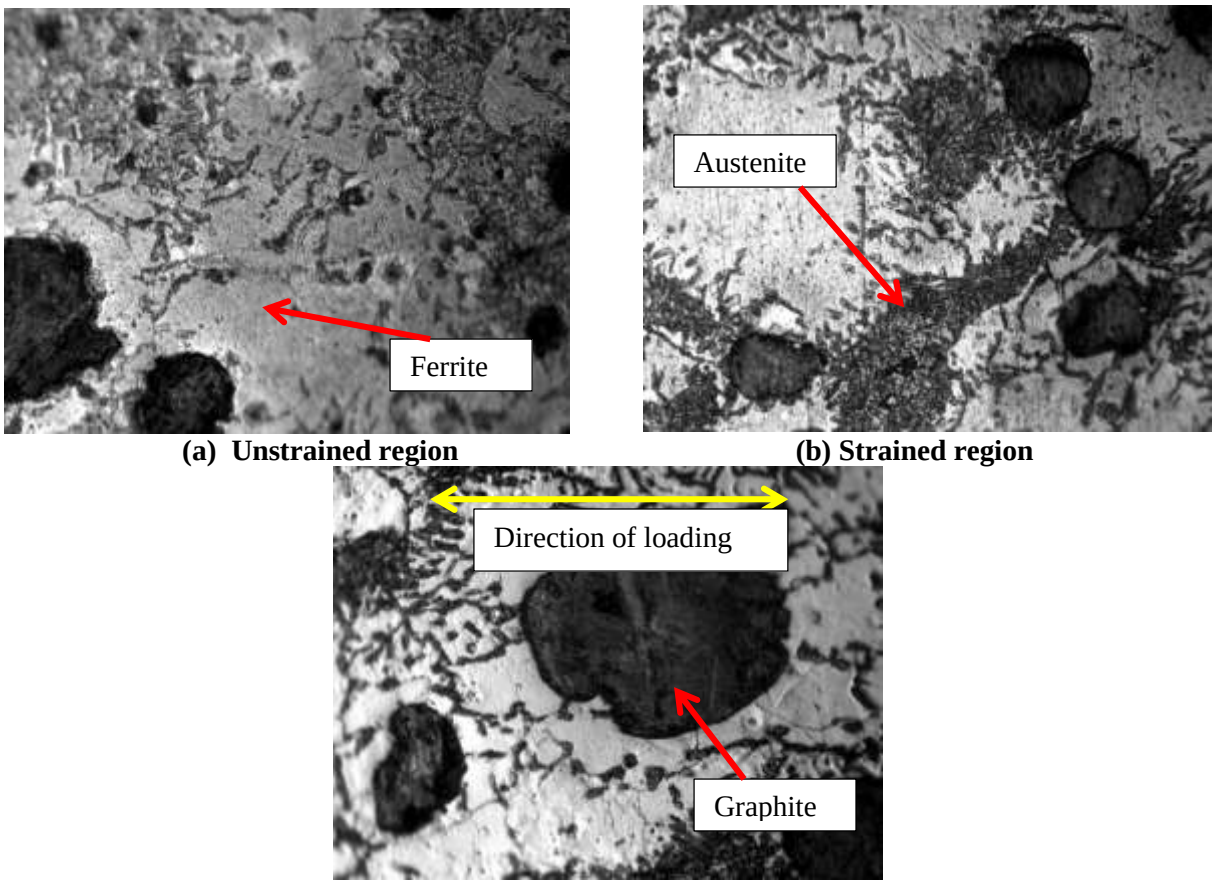

(a) Unstrained region **(b) Strained region**

(c) Strained region

Figure 4-29: Optical microscope image showing nodular graphite, islands of austenite in ferrite in Ni-Mn alloy at 500X

4.7.2 Scanning Electron Microscopy

The samples were then examined using FEI Quanta 600 FEG environmental scanning electron microscopy. Samples were examined at various magnifications from 500X to 1500X for general inspection and 5000X for special features using backscattered electron imaging. The images are presented as figures 4-30 to 4-41.

Low nickel sample

Figures 4-30 to 4-32 show the microstructure of unstrained, strained and strained (transverse) samples of low nickel alloy using backscattered electron imaging. As the elements with lower atomic number generate lesser backscattered electrons, they appear darker under BSE. So, the graphite nodules appear black. The contrast among the ferrite and austenite phase is due to the difference in the crystallographic structure of the two phases. Austenite has a FCC lattice and hence has an atomic packing efficiency higher than BCC ferrite. So, austenite appears brighter under BSE. Also, the contrasts in these samples were enhanced by etching them slightly with 3% nital.

In the pictures, it can be observed that the distribution of austenite was uniform in both the longitudinal and transverse directions. Being a cast material, this was expected. Also, austenite was distributed as feathery needle-like orientation within the ferrite. So, it cannot be resolved properly unless viewed at 5000X. The images of the microstructure taken parallel to the loading axis showed the nodules to be elongated in the direction of loading. Also, there are small microcracks present perpendicular to the direction of loading.

Un-deformed Sample

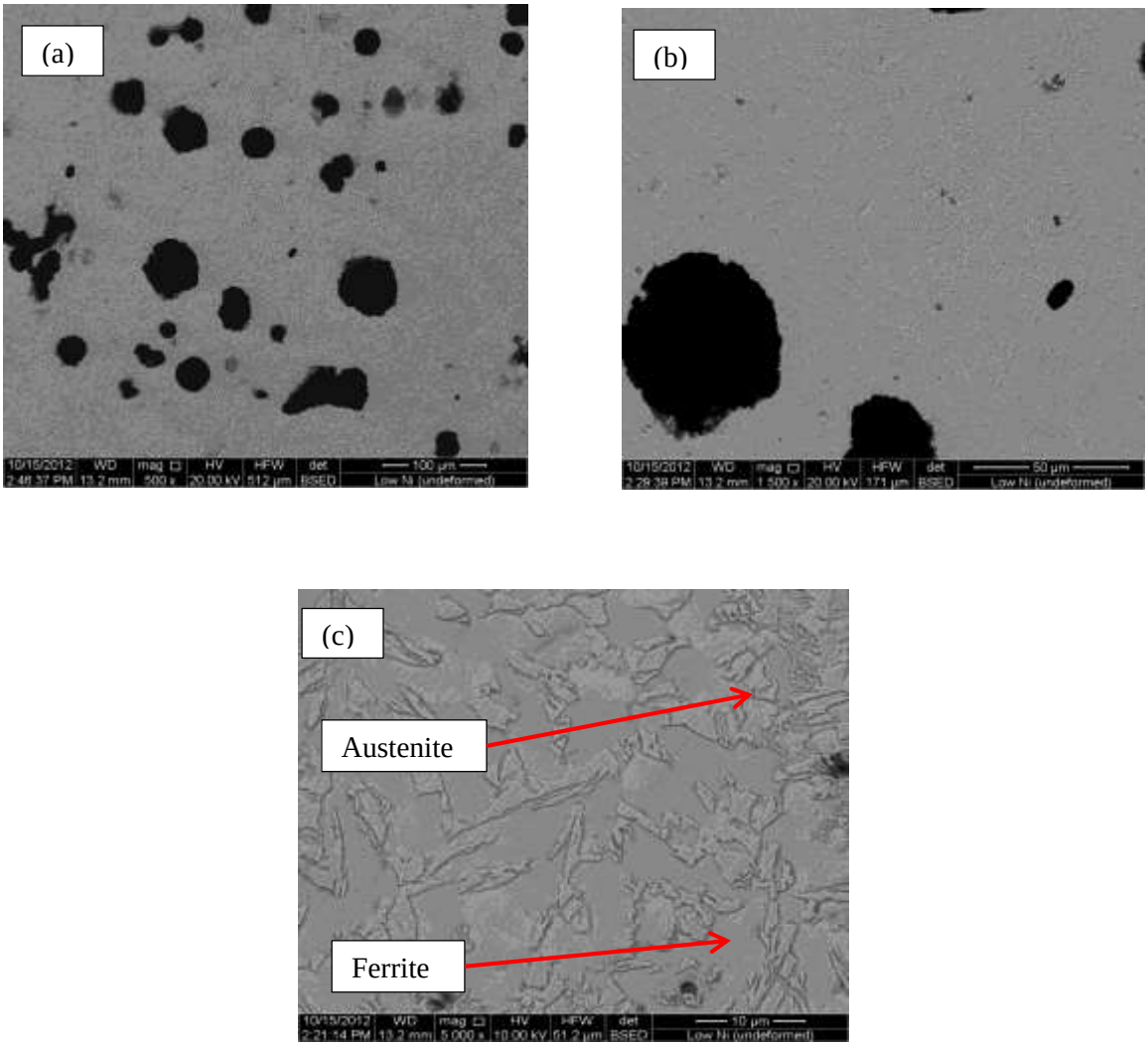

Figure 4-30: BSE images of low Ni (undeformed) sample at (a) 500X, (b) 1500X and (c) 5000X

Deformed Sample

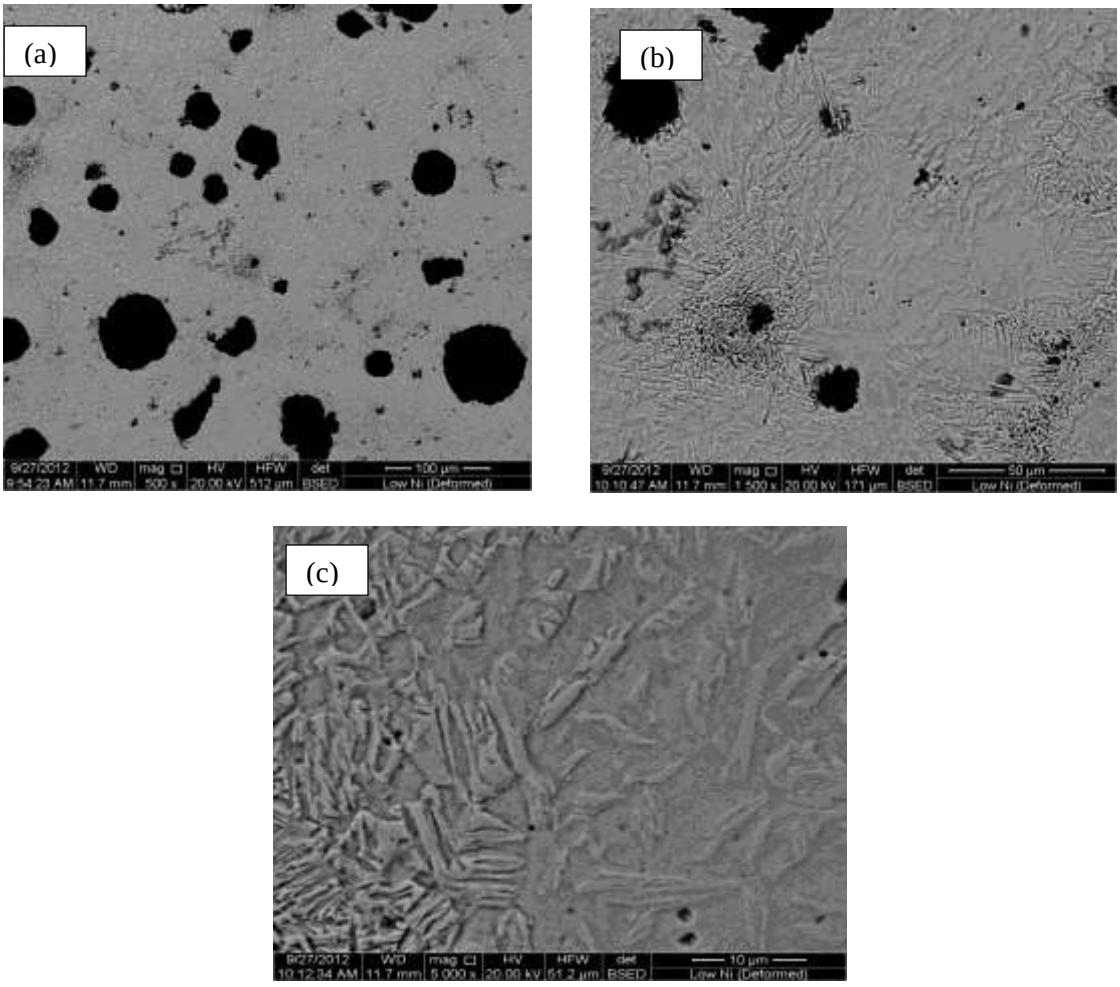

Figure 4-31: BSE images of low Ni (deformed) sample at (a) 500X, (b) 1500X and (c) 5000X

Deformed Sample (Parallel to loading axis)

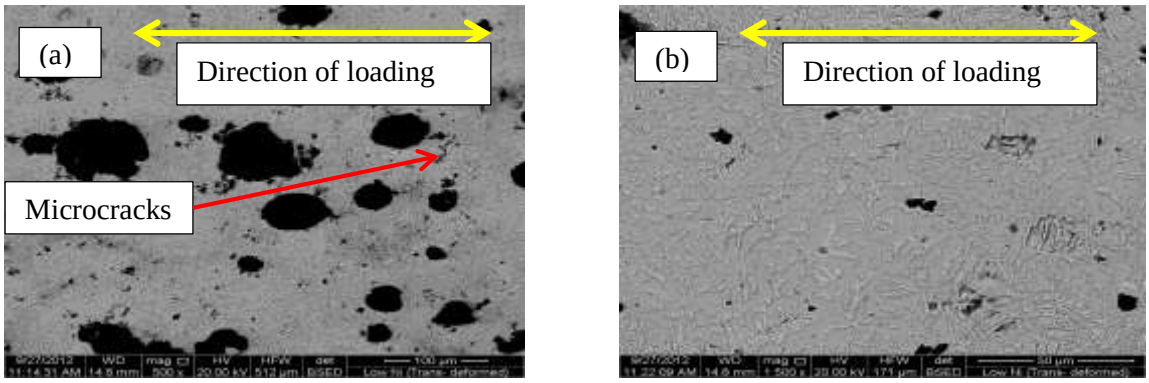

Figure 4-32:BSE images of low Ni (deformed, parallel to loading axis) sample at (a) 500X, (b) 1500X

High nickel sample

Figures 4-33 to 4-35 show the microstructures of unstrained, strained and strained (transverse) samples of high nickel alloy using backscattered electron imaging. The contrast mechanism works in a similar way as explained for low nickel sample. The nature and distribution of austenite in the high nickel sample was very similar to the low nickel sample. The austenite is properly resolved only at 5000X. The images of the microstructure taken parallel to the loading axis shows the nodules to be elongated in the direction of loading, but there were no observed microcracks.

Un-deformed Sample

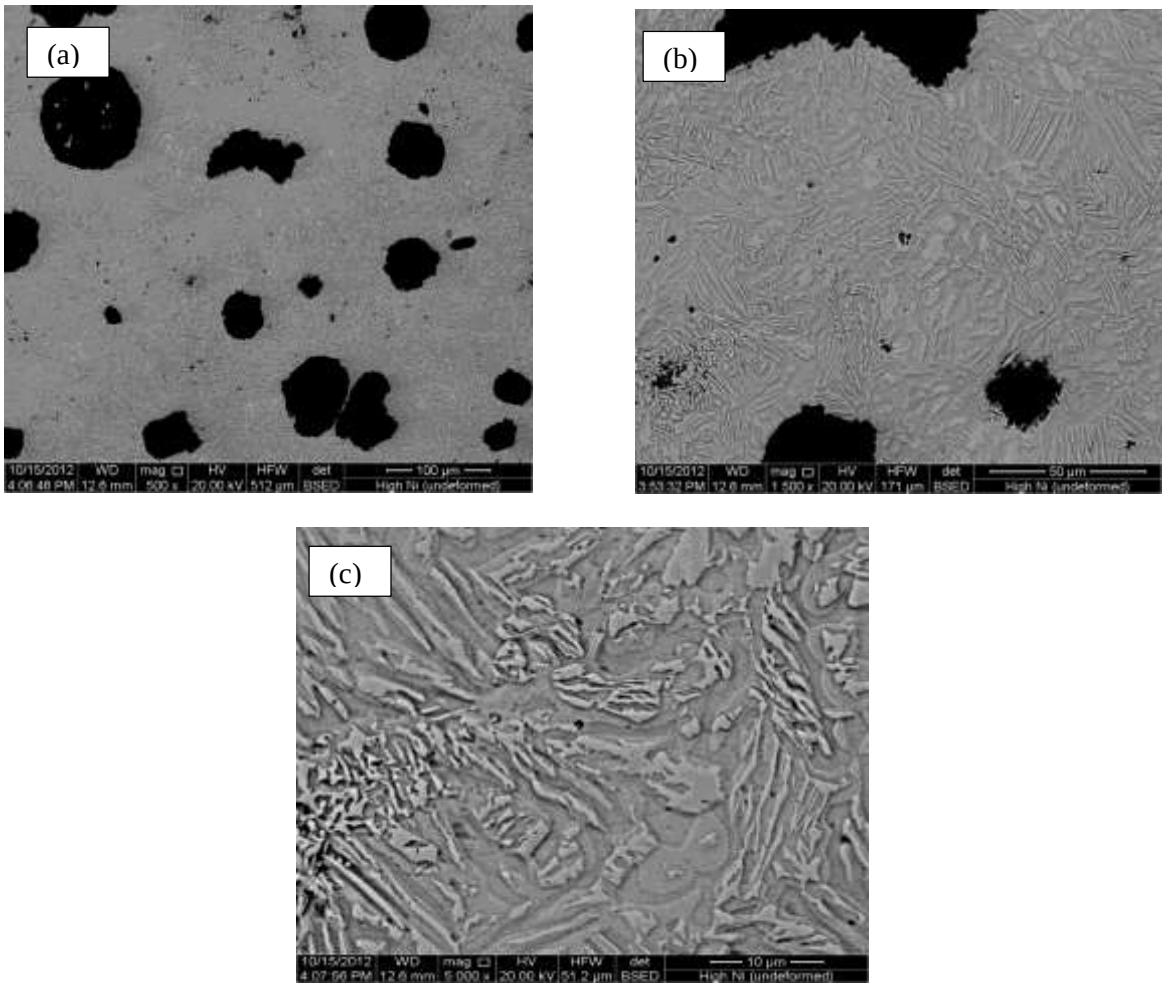

Figure 4-33: BSE images of high Ni (undeformed) sample at (a) 500X, (b) 1500X and (c) 5000X

Deformed Sample

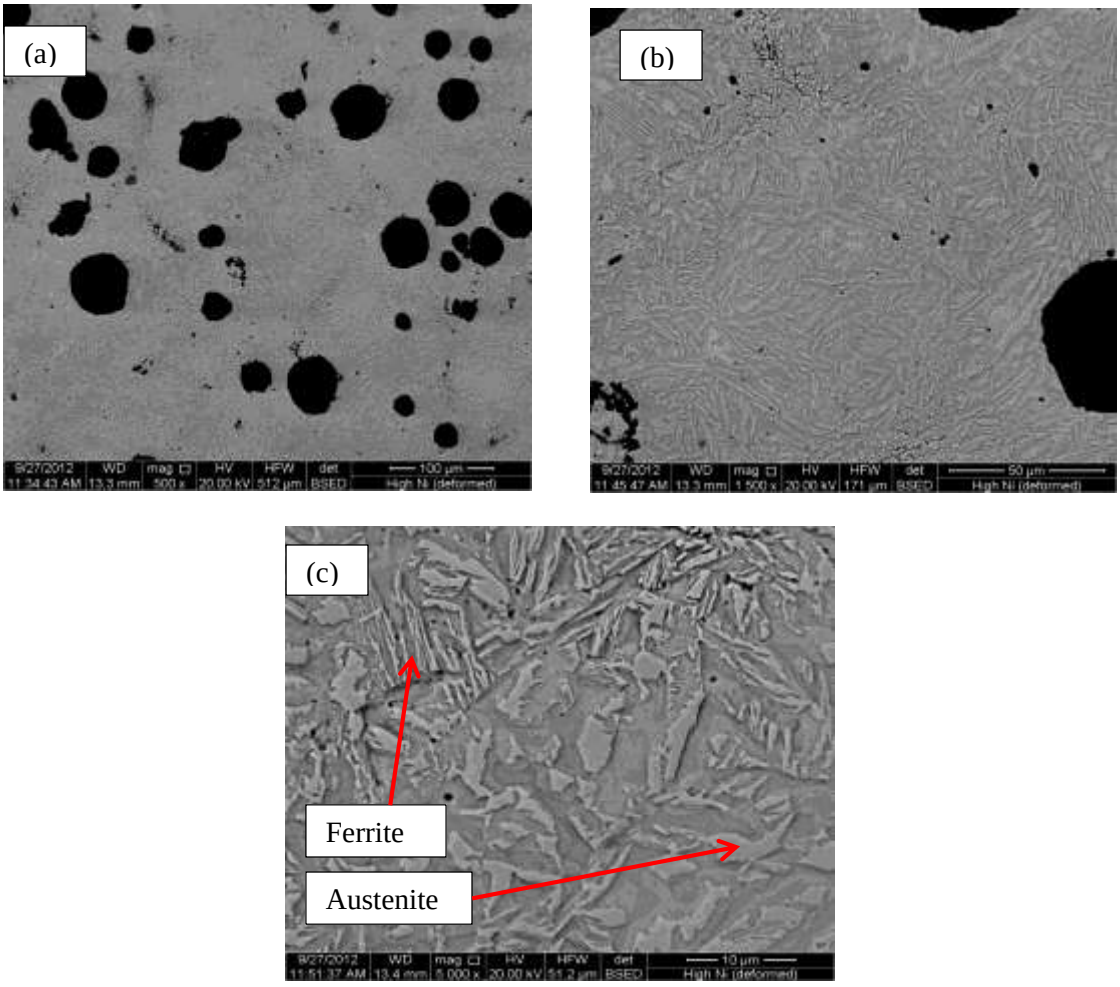

Figure 4-34: BSE images of high Ni (deformed) sample at (a) 500X, (b) 1500X and (c) 5000X

Deformed Sample (parallel to loading axis)

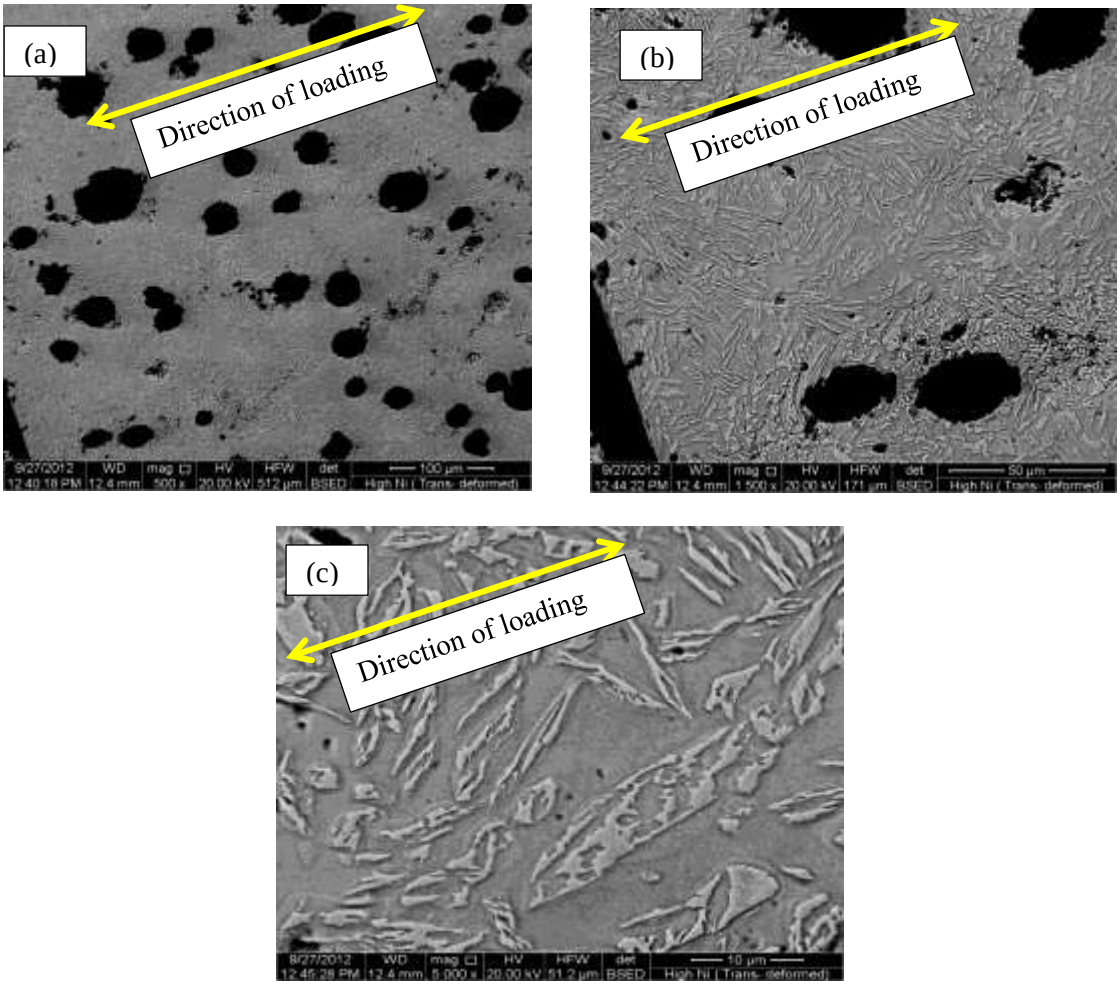

Figure 4-35: BSE images of high Ni (deformed, parallel to loading axis) sample at (a) 500X, (b) 1500X and (c) 5000X

High manganese sample

Figures 4-36 to 4-38 show the microstructure of unstrained, strained and strained (transverse) samples of high manganese alloy using backscattered electron imaging. The nature and distribution of austenite in the high manganese sample is different than the low and high nickel samples. The austenite was distributed in chunks, usually away from the graphite nodules. Being present in chunky form, the austenite is resolved even at a lower magnification. The images of the microstructure taken parallel to the loading axis show

very little change in the shape and morphology of the graphite nodules because it was only strained 5%. However, there were some microcracks observed in the direction perpendicular to the loading direction.

Un-deformed Sample

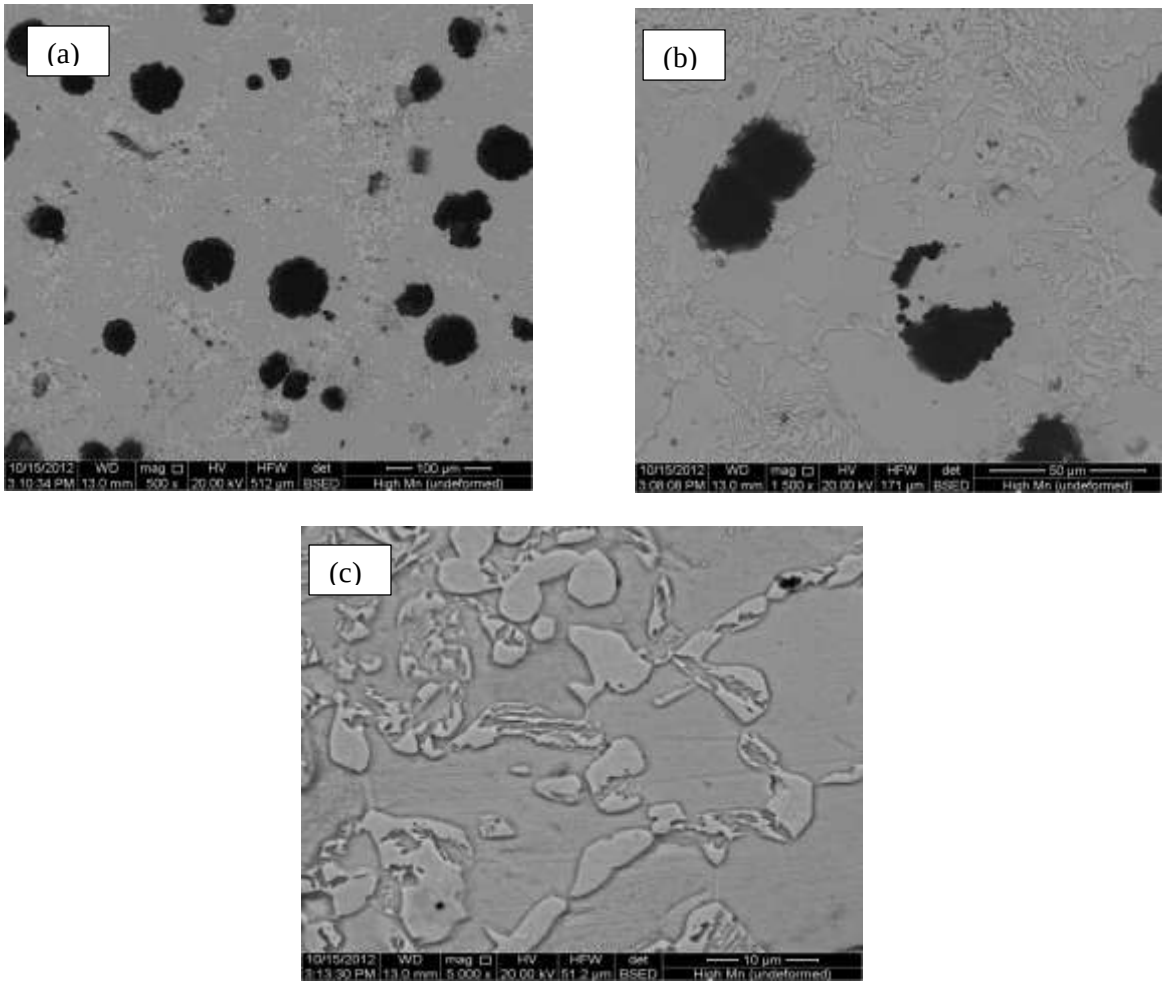

Figure 4-36: BSE images of high Mn (undeformed) sample at (a) 500X, (b) 1500X and (c) 5000X

Deformed Sample

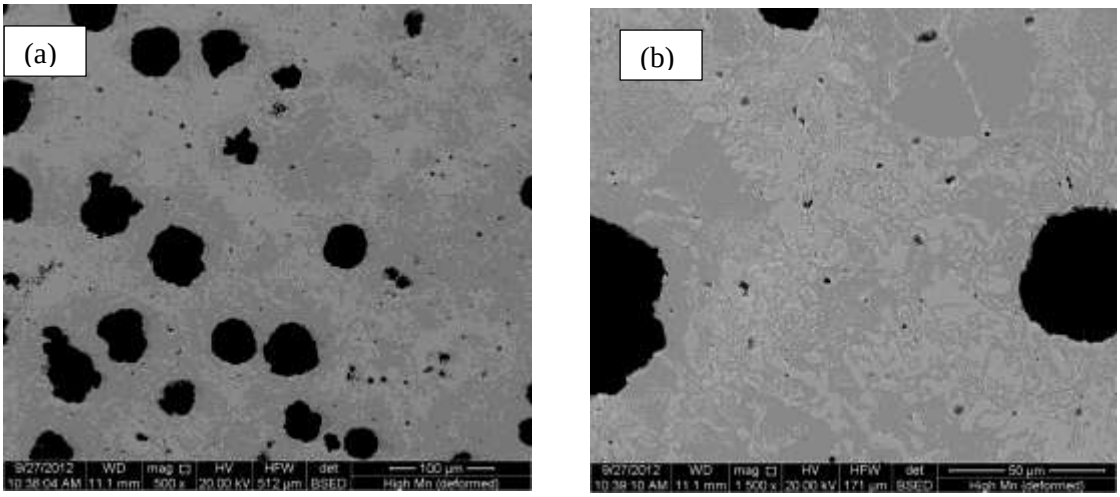

Figure 4-37: BSE images of high Mn (deformed) sample at (a) 500X and (b) 1500X

Deformed Sample (parallel to loading axis)

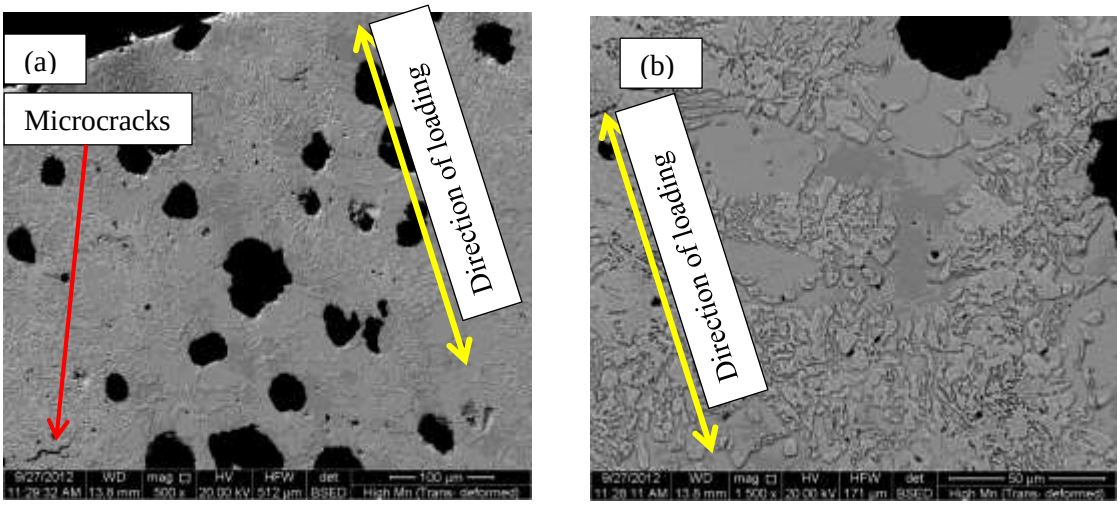

Figure 4-38: BSE images of high Mn (deformed, parallel to loading axis) sample at (a) 500X and (b) 1500X

Nickel-manganese sample

Figures 4-39 to 4-41 show the microstructure of unstrained, strained and strained (transverse) samples of nickel manganese alloy using backscattered electron imaging. The nature and distribution of austenite in the high manganese sample was a combination of the types found in the low and high nickel and high

manganese alloy samples. The austenite was distributed in chunks, usually away from the graphite nodules, but some were also present as fine needles of austenite surrounded by ferrite. Being present in chunky form, the austenite was resolved even at a lower magnification. The images of the microstructure taken parallel to the loading axis showed the graphite nodules are somewhat elongated. There were some microcracks observed in the direction perpendicular to the loading direction.

Un-deformed Sample

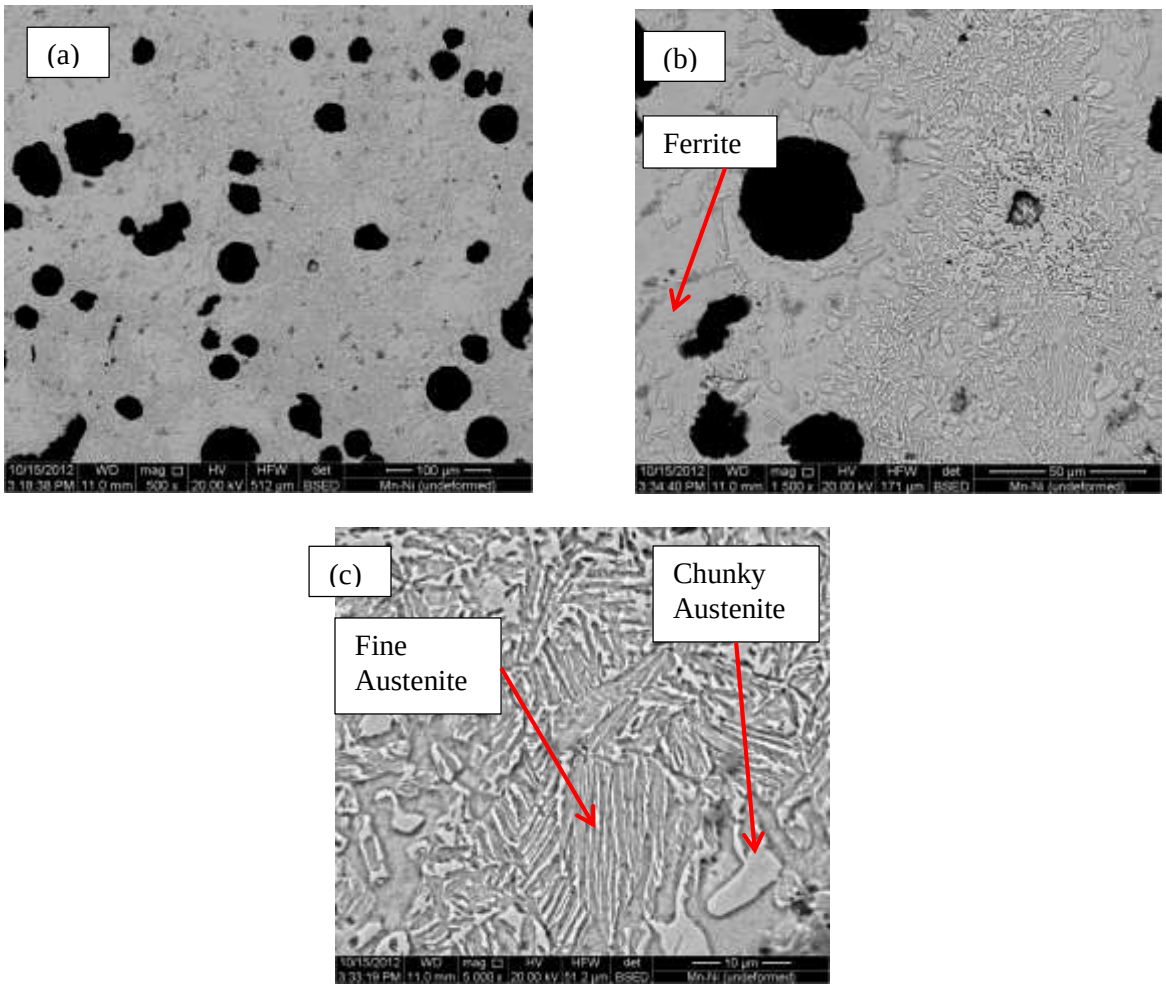

Figure 4-39: BSE images of Ni-Mn (undeformed) sample at (a) 500X, (b) 1500X and (c) 5000X

Deformed Sample

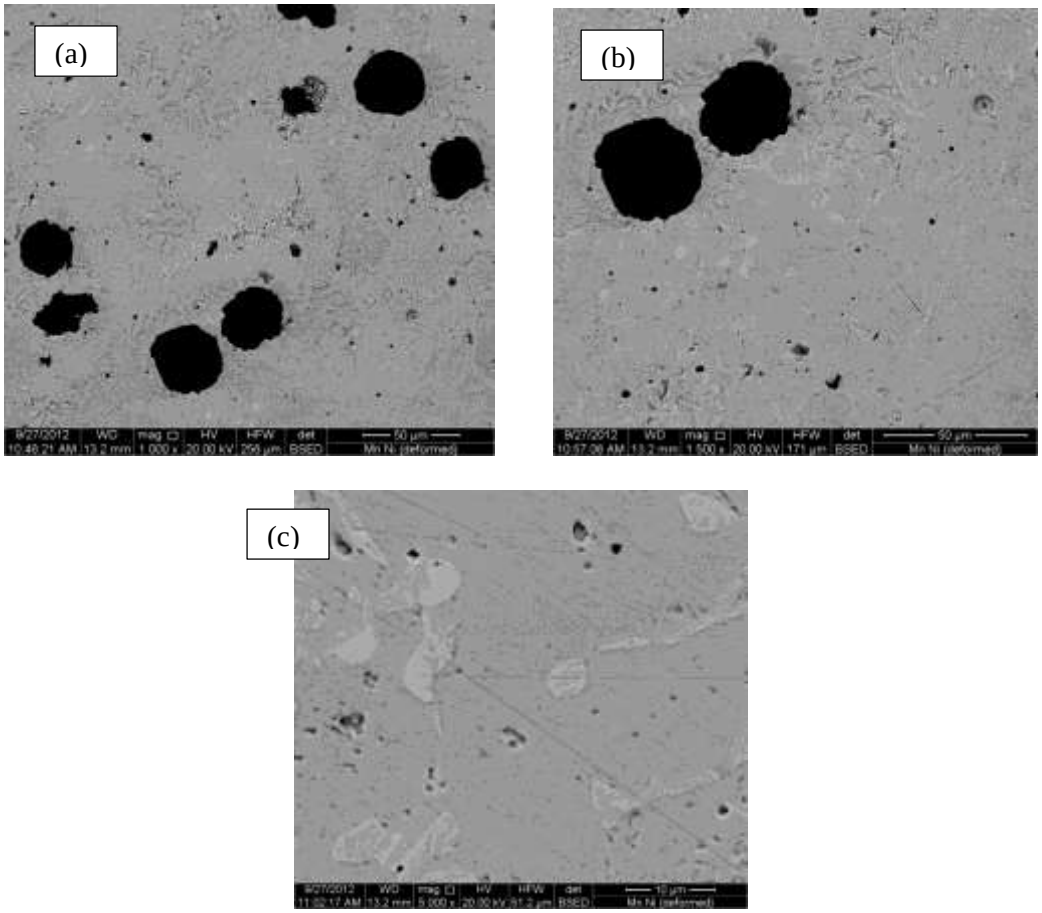

Figure 4-40: BSE images of Ni-Mn (deformed) sample at (a) 1000X, (b) 1500X and (c) 5000X

Deformed Sample (parallel to loading axis)

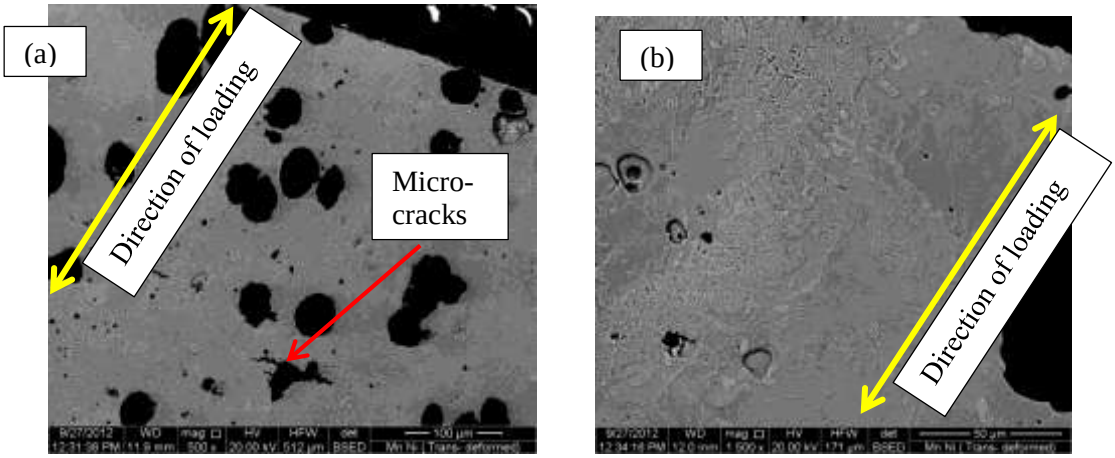

Figure 4-41: BSE images of Ni-Mn (deformed, parallel to loading axis) sample at (a) 500X and (b) 1500X

In section 1.7, equation 2 shows that the average volume of austenitic particle leads to a thermodynamically more stable austenite. Although, the high manganese alloy had a higher volume of the austenite chunks, the overall volume fraction of austenite was greater for high and low nickel alloys. This factor along with the effect of alloying element and yield strength, caused the austenite to transform to martensite at a lower stress for manganese containing alloys.

4.7.3 Energy Dispersive Spectroscopy (EDS) Analysis

EDS analysis was also done in the FEI Quanta 600 FEG environmental scanning electron microscopy. Area mapping was done at 1000X and multipoint scans on the samples were run at 1500X. However as explained in section 3.6, data from EDS is not precise due to large beam interaction volume.

4.7.3.1 EDS Maps

The EDS maps are displayed for each of the tested samples. The areas were scanned for 3 minutes with an average count-rate of 45 cps. The high and low nickel alloys were examined for segregation of Ni and Cu. As evident from figures 4-42 and 4-43, no segregation of these alloying elements was observed for the alloys at 1000X magnification. However, when the manganese containing alloys, that is, the high manganese and nickel manganese alloys were mapped as shown in figures 4-44 and 4-45, there was a rise in the amount of manganese signal coming from the austenite zone compared to the ferrite zone. Similarly, for these alloys, silicon seemed to be preferentially segregated in the ferrite region. Nickel showed no segregation even for the nickel manganese alloy. For all alloys, carbon was concentrated only in the graphite nodules as seen clearly in figures 4-42 to 4-45 (c), so there was no pearlite present in any of the alloys as expected.

As the amount of alloying elements in all the alloys was very low, and the segregation is not that prominent, mapping is used as an overview to help run the multipoint scanning. Multipoint EDS gives a better insight to the actual percentage of alloying elements. It must however be noted that the spot size on the surface is

small, but the signal for EDS scan comes from a bigger interaction volume underneath he sample surface. So the data, inspite of being precise, is not very accurate.

Low Ni:

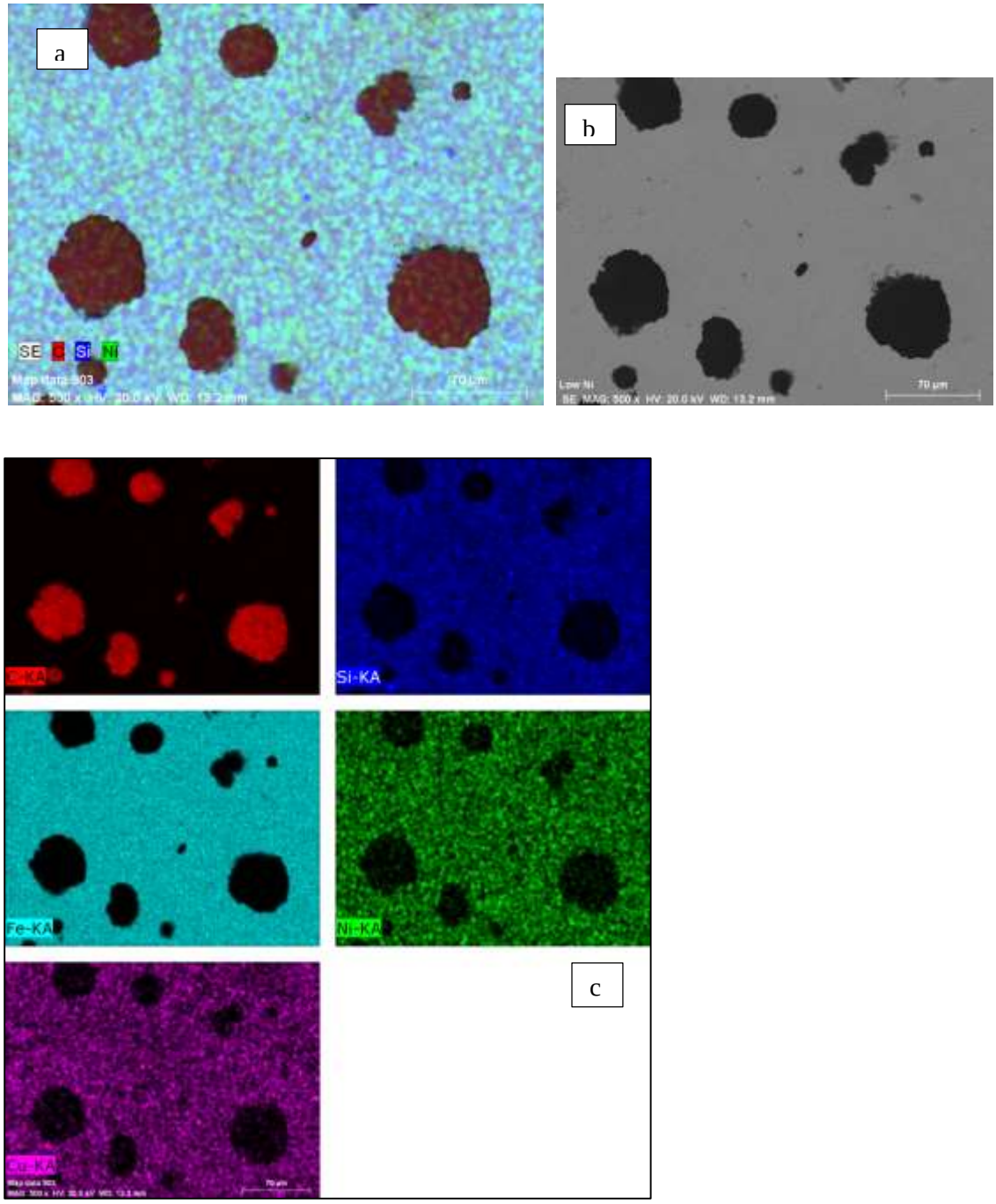

Figure 4-42: EDS map of Low Ni alloy (a) Elemental mapping on SE image showing no segregation of alloying elements, (b) Inspected area at 1000X, (c) individual elemental maps

High Ni:

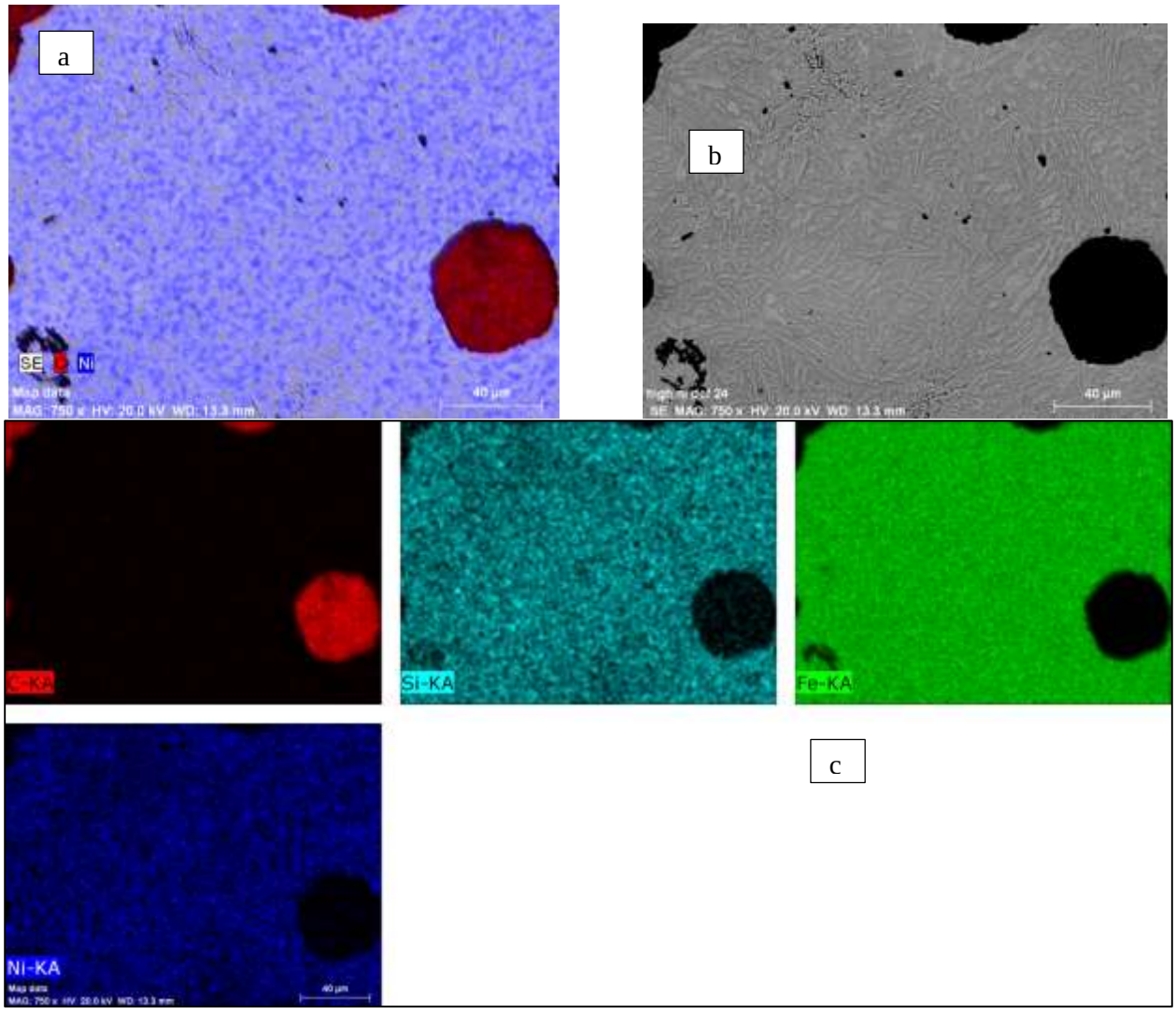

Figure 4-43: EDS map of High Ni (a) Elemental mapping on SE image showing no segregation of alloying elements, (b) Inspected area at 1000X, (c) individual elemental maps

High Mn:

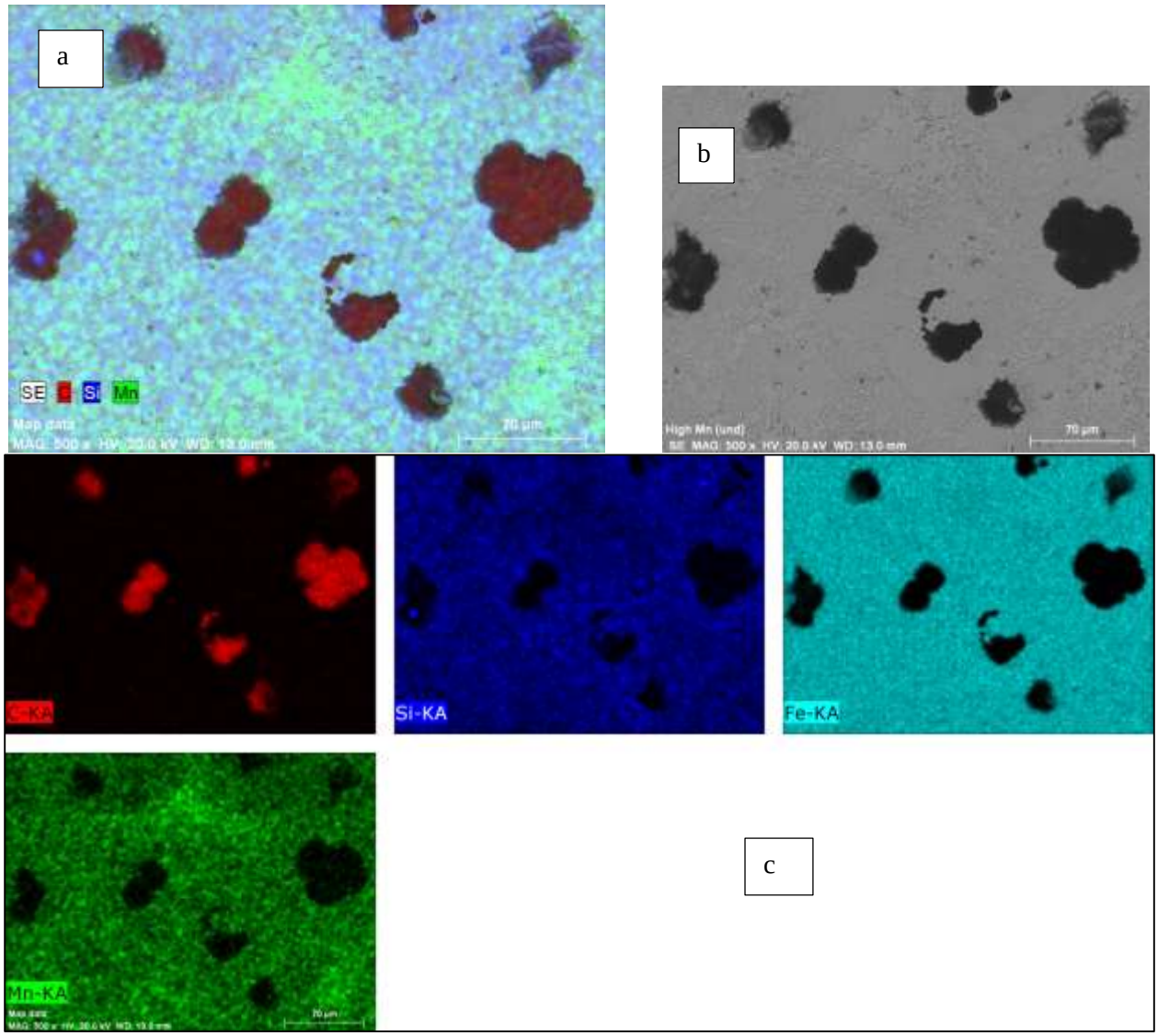

Figure 4-44: EDS map of High Mn alloy (a) Elemental mapping on SE image to show segregation of Mn in the austenite and Si in the ferrite, (b) Inspected area at 1000X, (c) individual elemental maps

Ni Mn:

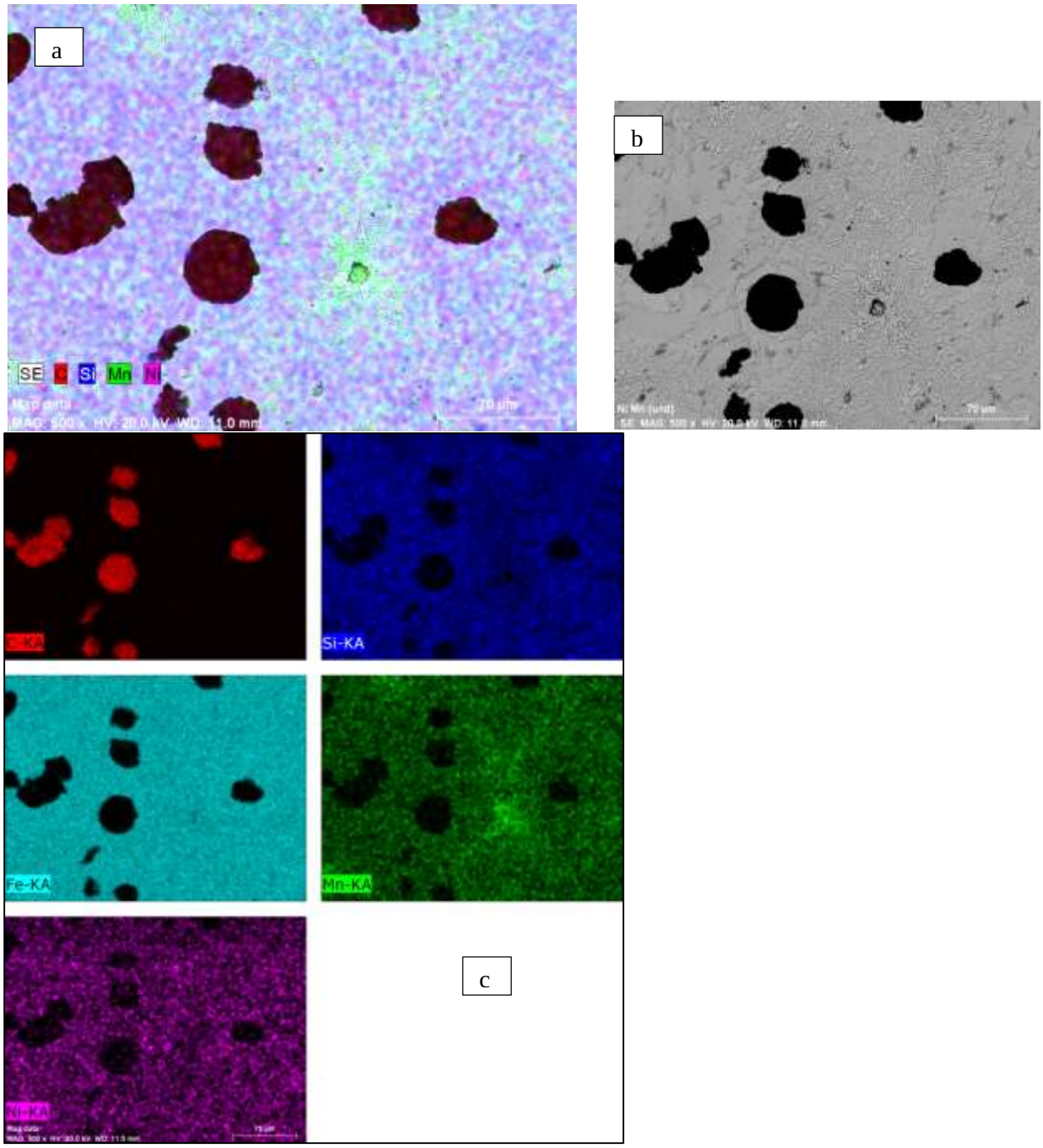

Figure 4-45: EDS map of Ni Mn (a) Elemental mapping on SE image showing no segregation of Ni, Segregation of Mn in the austenite and Si in the ferrite, (b) Inspected area at 1000X, (c) individual elemental maps

4.7.3.2 EDS Data (Multipoint)

The multipoint scans were taken at 1500X, the point scans being run for 1 minute per point. Points were chosen in the ferrite region, austenite region and graphite region. Due to the large beam interaction volume, which may range to a few cubic microns, the most of the signal for the EDS came from underneath the surface. So even if the data point was taken on the austenite grain, there could be some interfering signal generated from the ferrite lying underneath the surface.

All the manganese containing alloys, in figures 4-48 and 4-49 showed higher concentration for manganese in the austenite region. Manganese segregated in the last regions to solidify, which were in between graphite nodules. There was almost no segregation of nickel for any of the alloys as evident from figures 4-46 to 4-49.

Low Ni :

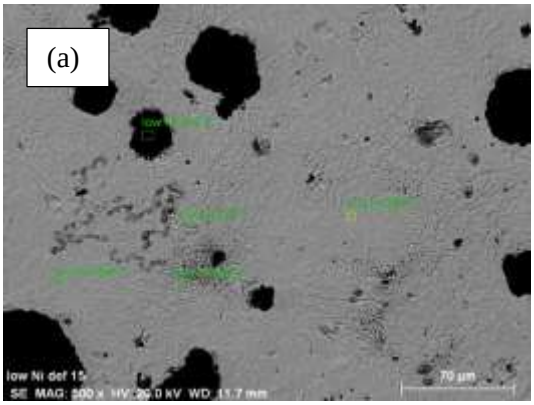

(b)

Spectrum	Mass percent (%) C	Si	Mn	Fe	Ni	Cu
Austenite_1	9.65	1.30	0.87	87.00	0.48	0.70
Austenite_2	10.77	0.80	1.29	86.23	0.27	0.64
Ferrite_1	6.46	1.79	0.68	88.99	0.74	1.34
Graphite	74.68	0.39	-	24.93	-	-
Ferrite_2	6.49	1.69	0.69	89.39	0.64	1.10

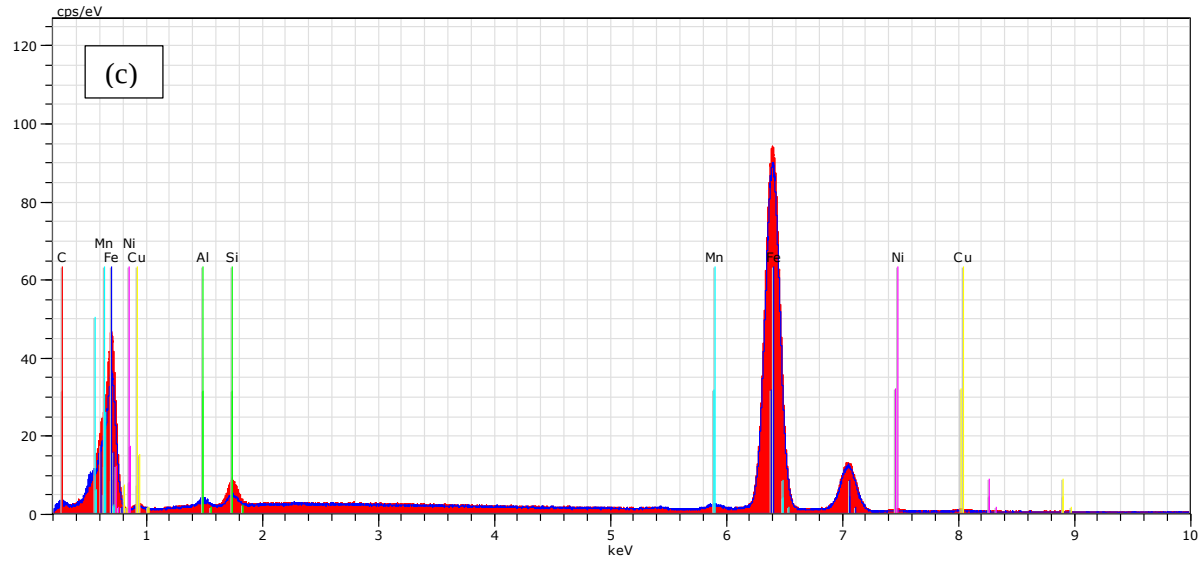

Figure 4-46: Low Ni multipoint scan: (a) Points scanned, (b) Mass % analysis, (c) Spectrum for Austenite_2 (blue) & Ferrite_2 (red)

High Ni :

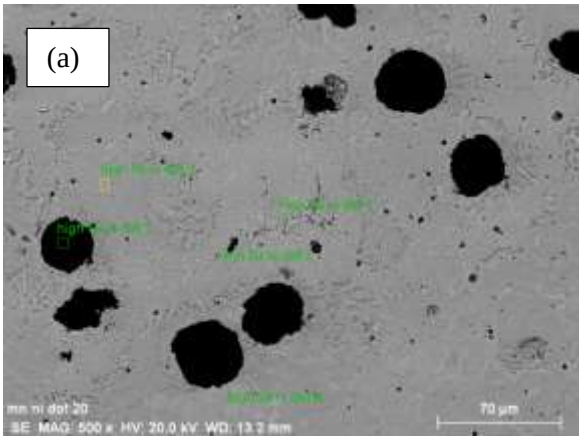

(b)

Spectrum	Mass percent (%) C	Si	Fe	Ni	Cu
Ferrite_1	7.29	2.09	86.69	2.61	1.31
Asutenite_1	8.75	1.46	87.27	1.66	0.87
Ferrite_2	7.63	1.83	86.92	2.37	1.25

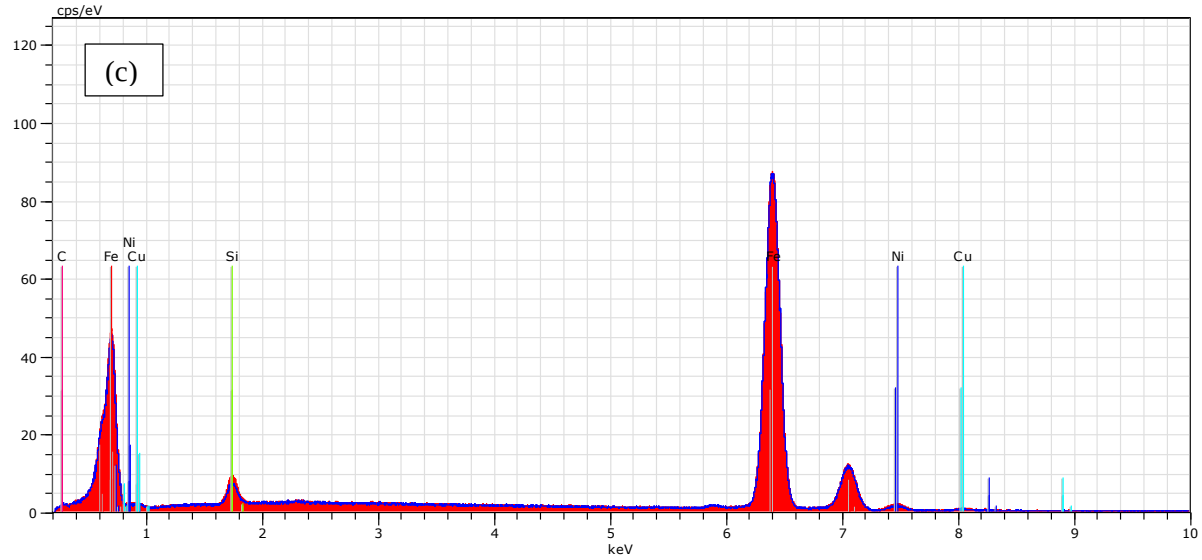

Figure 4-47: High Ni multipoint scan: (a) Points scanned, (b) Mass % analysis, (c) Spectrum for points Ferrite_1 (red) & Austenite_1 (blue)

High Mn :

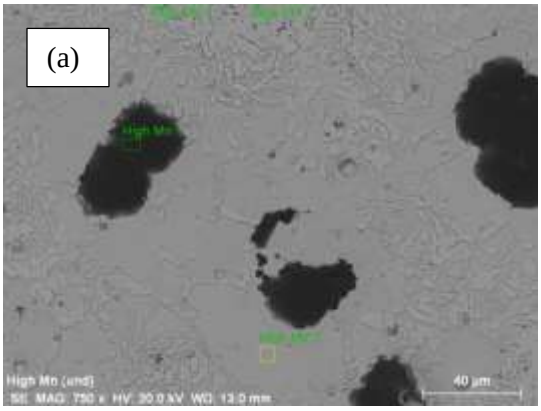

(b) Mass percent (%)

Spectrum	C	Si	Mn	Fe
Graphite	80.02	0.26	0.38	19.34
Ferrite	6.09	1.81	1.64	90.46
Asutenite_1	7.85	1.11	3.43	87.61
Asutenite_2	7.81	1.31	2.86	88.02

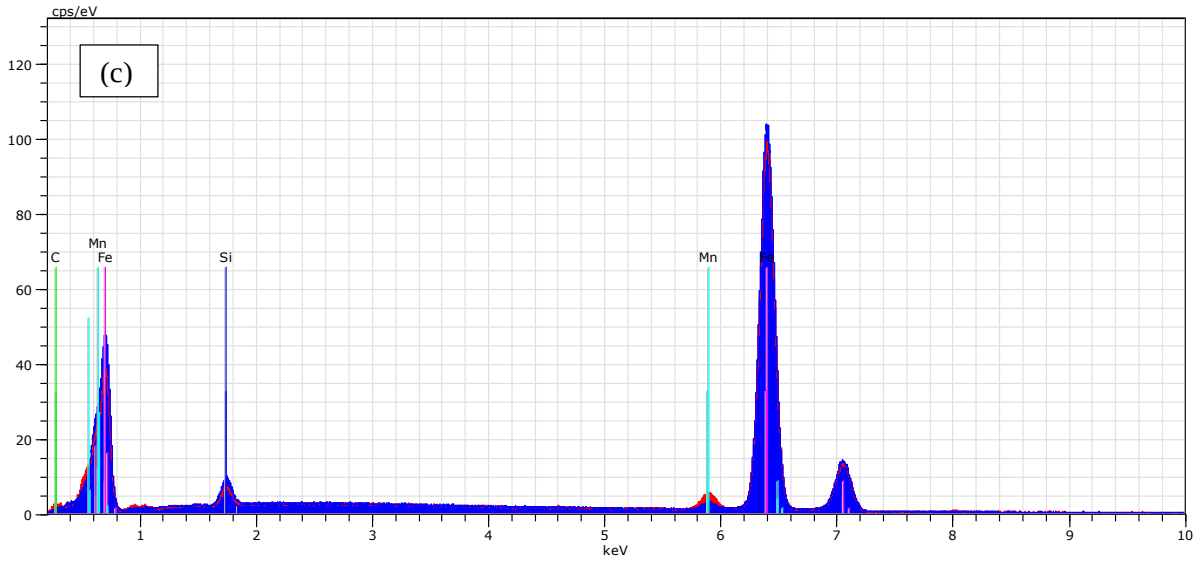

Figure 4-48: High Mn multipoint scan: (a) Points scanned, (b) Mass % analysis, (c) Spectrum for Ferrite (blue) & Austenite_1 (red)

Ni Mn :

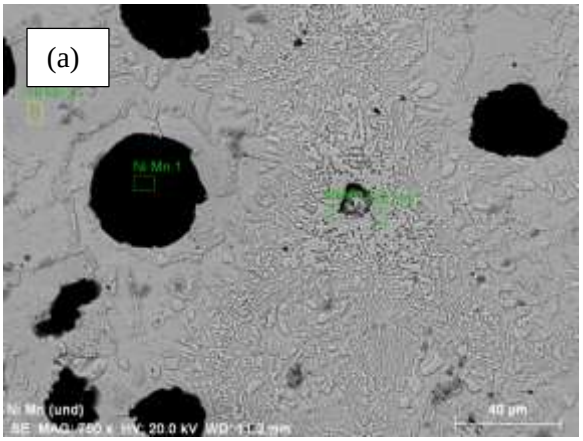

(b) Mass percent (%)

Spectrum	C	Si	Mn	Fe	Ni
Graphite	98.77	0.04	0.07	1.02	0.10
Austenite_1	10.63	0.66	4.72	83.50	0.49
Asutenite_2	8.81	0.95	3.36	86.41	0.47
Ferrite	10.47	1.86	0.92	86.09	0.66

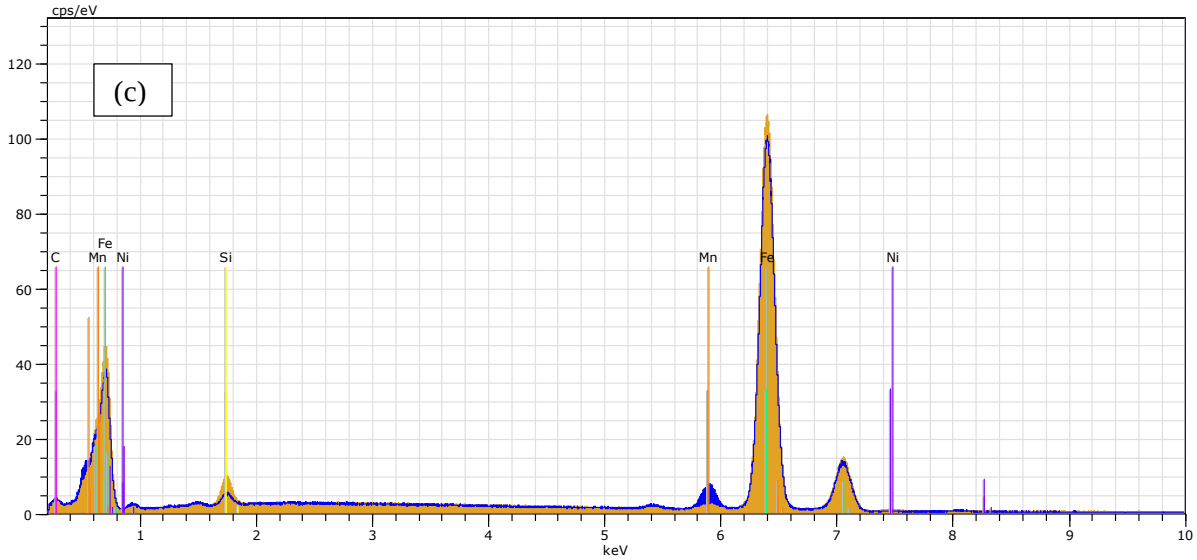

Figure 4-49: Ni-Mn (undeformed) multipoint scan: (a) Points scanned, (b) Mass % analysis, (c) Spectrum for Austenite_1 (blue) & Ferrite (yellow)

4.7.4 Transmission Electron Microscopy

Transmission electron microscopy was done on deformed high nickel and high manganese alloys previously tested at the High Flux Isotope Reactor (HFIR) in Oak Ridge National Lab. These samples were from the in-situ neutron diffraction testing done by Druschitz et. al. The details of those experiment can be found in references [48] and [42].

The Philips EM420 Transmission electron microscope was used for this study. The emission current was set at 60 and the accelerating voltage at 120KeV. The micrographs were taken at various magnifications, principally to look for twinning, dislocation fields and stacking faults.

Overall, there were quite a few deformation twins observed in case of the deformed high nickel sample. No such twins were observed in high manganese alloys. Twinning can be a preferred mode of deformation for the nickel containing samples.

The width of the stacking faults or extended dislocations represent the surface free energy of the materials as discussed in the introduction. However, calculation of surface free energy from the width of extended dislocations requires a lot of experimental and empirical calculations which can be considered as future work in this project. Although, it is possible to obtain images of stacking faults, the actual calculation and experimentation is beyond the scope of this study.

Figure 4-50 to 4-56 represent the TEM micrographs for the examined deformed alloys at various magnifications. The features are labeled accordingly.

High Nickel

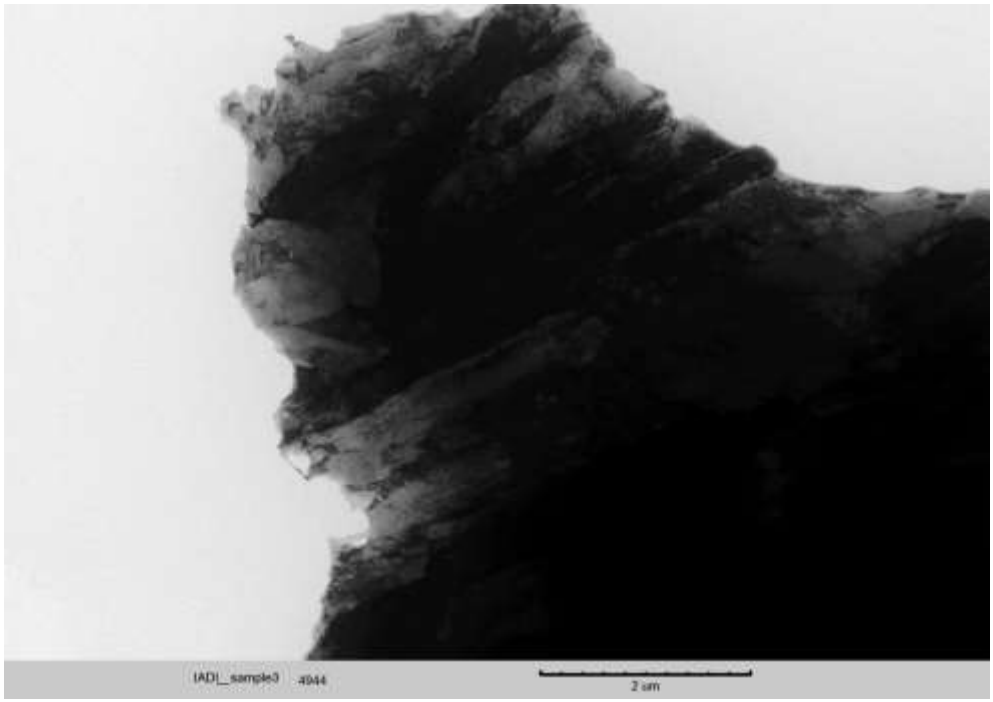

Figure 4-50: Bands of austenite (dark) in ferrite (light)

Figure 4-51: Stacking Faults in Austenite

Figure 4-52: Deformation Twins

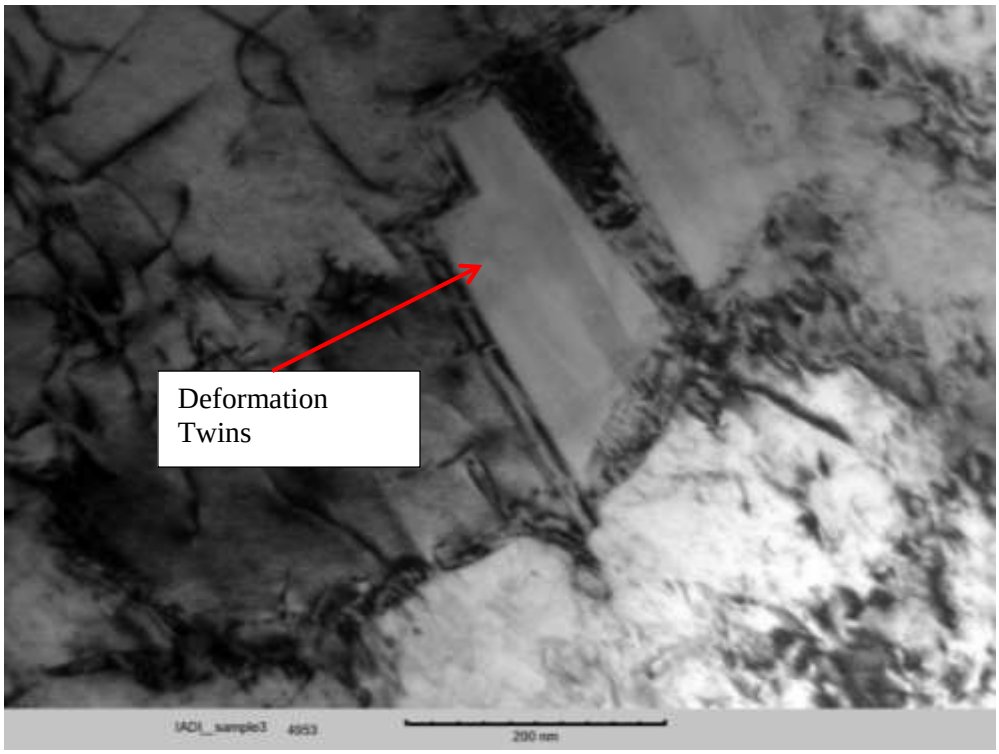

Figure 4-53: Deformation Twins (magnified)

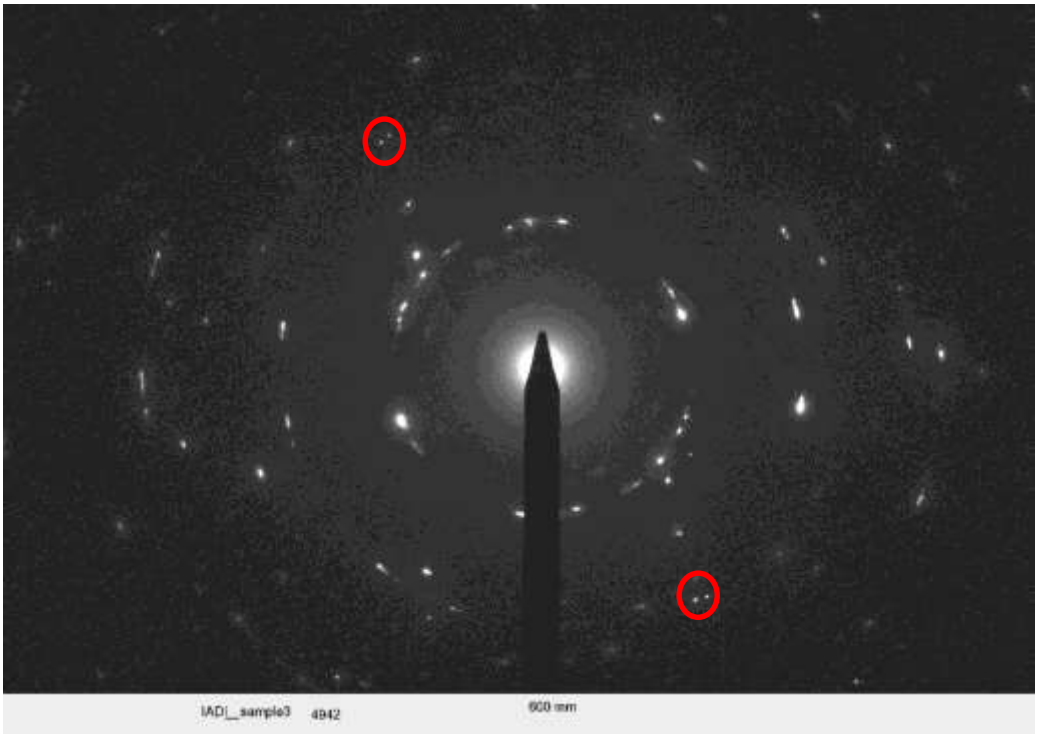

Figure 4-54: Evidence of twins in Diffraction Pattern (magnified)

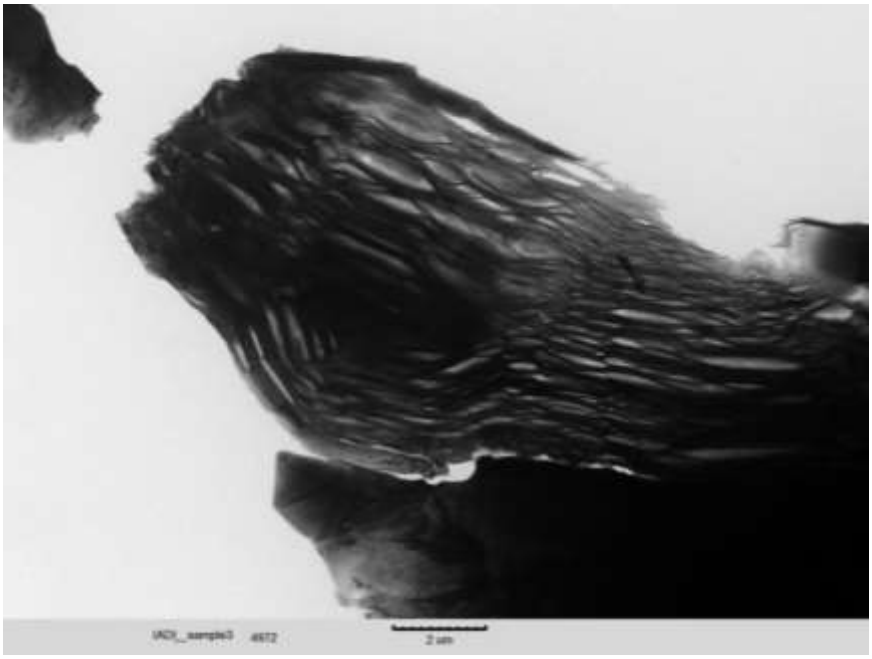

Figure 4-55: A partial graphite nodule

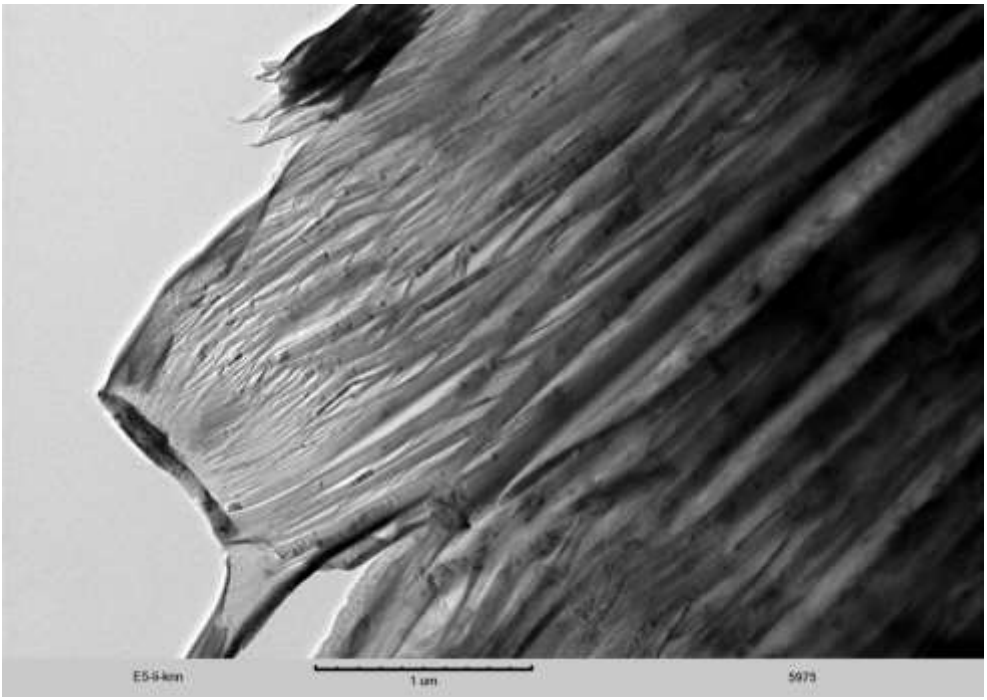

Figure 4-56: Bands of Austenite (dark) and Ferrite (light)

Chapter 5 Conclusions

The overall goal of this thesis was to determine the effect of alloy chemistry on the transformation of austenite to martensite during tensile deformation. The studies performed provide insight into how the chemistry effects the transformation as well as sheds light on the how it affects microstructure as well as lattice strains.

Intercritically austempered ductile iron alloyed with nickel shows ductility higher than that achieved by alloying it with manganese alone. Analysis of the true stress and true strain revealed that, there was some volume expansion associated with the transformation which resulted in the final diameter to be higher than predicted by true strain analysis. But these results were very similar for low carbon steel and hence we can conclude that this was simply due to experimental error and even if there was some volume expansion due to actual transformation, it was insignificant and within experimental error.

The elastic modulus also decreased about 5% for all the alloys with increase in strain. But the change in the elastic modulus of high manganese alloys for 5% strain was almost equal if not higher than the change observed for other alloys with 15% deformation. This could be correlated to austenite transforming to martensite in high manganese alloys at a lower strain compared to other alloys. Again, a low carbon steel was tested in similar load-unload cycle and it too showed about 5% decrease in elastic modulus when strained to 15%.

While analyzing the d-spacing values, it was observed that, the intensity of the austenite peaks decreased and that of the ferrite peaks increased during transformation. This directly points to the fact that austenite was transforming to martensite as the stress increased. The martensite produced during transformation had a structure very similar to ferrite. This was further verified by the merging of the FCC 111 peak with the BCC 110 peak in case of alloys with high manganese content.

The main target of this research was to determine the stress and strain at which the transformation of austenite to martensite took place for each of the alloys. It was observed that high manganese alloys transformed at stress and strain which was much lower than the others. The transformation stress for the

nickel-manganese alloys was lower than that for the low nickel alloy. The high nickel alloy showed transformation at the highest stress.

The elastic diffraction constants and Poisson's ratio was calculated for all the important FCC and BCC planes for each of the alloys. This information will be very useful for future modeling of these alloy systems and developing a stress tensor. It was also observed that FCC planes bear most of the load while straining. When the austenite transforms to martensite, it undergoes expansion[58, 59], which may cause a compressive strain to develop on the neighboring ferrite planes.

Optical microcopy revealed that the microstructure was uniform is 3-dimensions, which was expected of a cast specimen. There were no visible change in the morphology of the phases before and after transformation. Also, the straining caused the graphite nodules to elongate in the direction of loading. SEM imaging using backscattered electrons for imaging showed different morphology of austenite formed due to different alloying elements. Alloying with manganese led to the formation of chunky austenite particles, while alloying with nickel formed plate-like austenite very similar in structure to conventional austempered ductile iron. Also, the austenite particles were distributed more evenly in the samples alloyed with nickel compared to the high manganese alloy where the austenite was segregated away from the graphite nodules. The alloy containing manganese and nickel shows a combination of plate like and blocky austenite.

Under the SEM, there were some very prominent microcracks observed perpendicular to the direction of loading, often originating from graphite nodules.

An EDS analysis suggests that manganese preferentially segregates in the austenite and silicon to the ferrite. The distribution of nickel was very uniform throughout the whole sample.

TEM studies performed on samples tested previously at HFIR showed some very prominent twinning in the high Ni alloy but no twinning was observed in the high manganese alloy.

Future research plans that could be pursued following this thesis are:

- Analysis of the volume expansion expected due to transformation of austenite to martensite.
- Calculation of intergranular and intragranular stresses and partioning of stress between the phases.
- Examination of the development of residual stresses during tensile loading.

- Auger electron spectroscopy or TEM elemental analysis to determine the composition of each of the phases present.
- TEM work to thoroughly characterize the active deformation mechanisms and to calculate the SFE using stacking faults
- EBSD using the documented lattice parameters
- Stress tensor modeling using the elastic diffraction constants as gathered from the experimental data.

References

1. Erdogan, M., V. Kilicli, and B. Demir, *Transformation characteristics of ductile iron austempered from intercritical austenitizing temperature ranges.* Journal of Materials Science, 2009. **44**(5): p. 1394-1403.

2. Kilicli, V. and M. Erdogan, *Tensile properties of partially austenitised and austempered ductile irons with dual matrix structures.* Materials Science and Technology, 2006. **22**(8): p. 919-928.

3. Druschitz, A.P. and D.C. Fitzgerald, *Machinable austempered cast iron article having improved machinability, fatigue performance, and resistance to environmental cracking*, US Patent No. 7,497,915 (2009), Intermet Corporation, Troy, MI: United States.

4. Timokhina, I., P. Hodgson, and E. Pereloma, *Effect of microstructure on the stability of retained austenite in transformation-induced-plasticity steels.* Metallurgical and Materials Transactions A, 2004. **35**(8): p. 2331-2341.

5. Reisner, G., et al., *The modeling of retained austenite in low-alloyed TRIP steels.* JOM Journal of the Minerals, Metals and Materials Society, 1997. **49**(9): p. 62-65.

6. Daber, S., K. Ravishankar, and P. Prasad Rao, *Influence of austenitising temperature on the formation of strain induced martensite in austempered ductile iron.* Journal of Materials Science, 2008. **43**(14): p. 4929-4937.

7. Rousiere, D. and J. Aranzabal, *Development of mixed (ferrito-ausferritic) structures for spheroidal graphite irons.* Metallurgical Science and Technology, 2000. **18**(1): p. 24-29.

8. Aranzabal, J., et al., *Development of a new mixed (ferritic-ausferritic) ductile iron for automotive suspension parts.* INTERNATIONAL JOURNAL OF CAST METALS RESEARCH, 2003. **16**(1/3): p. 185-190.

9. Basso, A.D., R.A. Martínez, and J.A. Sikora, *Influence of austenitising and austempering temperatures on microstructure and properties of dual phase ADI.* Materials Science and Technology, 2007. **23**(11): p. 1321-1326.

10. Aristizabal, R.E., et al., *Intercritically Austempered Ductile Iron.* Transactions of the American Foundry Society, 2011. **119**: p. 407-412.

11. Druschitz, A.P. and D. Fitzgerald, *MADI^{TM}: introducing a new, machinable austempered ductile iron.* SAE Technical Paper #2003-01-1287, 2003.

12. Druschitz, A.P., D. Fitzgerald, and I. Hoegfeldt. *Lightweight crankshafts*. in *SAE Technical Paper #2006-01-0016,* 2006.

13. Druschitz, A.P., et al. *Machinability of MADI^{TM}*. in *SAE technical Paper #2005-01-1684,* 2005.

14. Druschitz, A.P., T. Prucha, and I. Hoegfeldt. *MADI^{TM} for powertrain applications*. in *Global Powertrain Conference*. 2005. Ann Arbor, MI.

15. Keough, J. and K. Hayrynen, *Automotive Applications of Austempered Ductile Iron (ADI): A Critical Review.* SAE Technical Paper, 2000. **01-0764**.

16. Committee, A.S.M.I.H., *ASM Handbook, Volume 01 - Properties and Selection: Irons, Steels, and High-Performance Alloys*, ASM International. p. 33-55.

17. Sorelmetal, *The Sorelmetal Book of Ductile Iron*2004: Rio Tinto iron & titanium.

18. Cho, G.S., et al., *Effects of Alloying Elements on the Microstructures and Mechanical Properties of Heavy Section Ductile Cast Iron.* Journal of Materials Science and Technology, 2007. **23**(1): p. 97-101.

19. Davies, R., *Influence of martensite composition and content on the properties of dual phase steels.* Metallurgical and Materials Transactions A, 1978. **9**(5): p. 671-679.

20. Lacaze, J., *An assessment of the Fe-C-Si system.* Metallurgical transactions. A, Physical metallurgy and materials science, 1991. **22**(10): p. 2211-2223.

21. Herring, D.H. *Heat Treatments of Cast Irons*. 2004 December 2004; Available from: http://www.heat-treat-doctor.com/documents/CastIrons.pdf.

22. Speich, G., V. Demarest, and R. Miller, *Formation of Austenite During Intercritical Annealing of Dual-Phase Steels.* Metallurgical and Materials Transactions A, 1981. **12**(8): p. 1419-1428.

23. Yi, J., I. Kim, and H. Choi, *Austenitization during intercritical annealing of an Fe-C-Si-Mn dual-phase steel.* Metallurgical and Materials Transactions A, 1985. **16**(7): p. 1237-1245.

24. Erdogan, M., *Effect of austenite dispersion on phase transformation in dual phase steel.* Scripta Materialia, 2003. **48**(5): p. 501-506.

25. Kocatepe, K., *Effect of martensite volume fraction and its morphology on the tensile properties of ferritic ductile iron with dual matrix structures.* Journal of materials processing technology, 2006. **178**(1-3): p. 44-51.

26. Kilicli, V., *Effect of ausferrite volume fraction and morphology on tensile properties of partially austenitised and austempered ductile irons with dual matrix structures.* International Journal of Cast Metals Research, 2007. **20**(4): p. 202-214.

27. Aristizabal, R.E., R.D. Foley, and A.P. Druschitz. *Intercritically austenitized quenched and tempered ductile iron*. AFS Technical Paper, 2012.

28. Wade, N., *Mechanical properties of ductile cast iron with duplex matrix.* Transactions of the Iron and Steel Institute of Japan, 1981. **21**(2): p. 117.

29. *The Sorelmetal Book of Ductile Iron*2004: Rio Tinto iron & titanium. 23-37, 123-129.

30. Aranzabal, J., *ADI-Development of a new mixed (ferritic-ausferritic) ductile iron for automotive suspension parts*. INTERNATIONAL JOURNAL OF CAST METALS RESEARCH, 2003. **16**(1-3): p. 185.

31. Druschitz, A.P, Fitzgerald, D.C, (Concord, VA, US), *Machinable austempered cast iron article having improved machinability, fatigue performance, and resistance to environmental cracking and a method of making the same*,US Patent No. 7,070,666 (2006): United States.

32. Aristizabal, R.E., *Intercritical Heat Treatments in Ductile Iron and Steels*, in *Material Science and Engineering, PhD Dissertation* 2012, University of Alabama, Birmingham.

33. *The Effects of Alloying Elements on Iron-Carbon Alloys.* Key to Metal database.

34. Bain, E.C. and M. American Society for. *Functions of the alloying elements in steel*. Cleveland: American Society for Metals.

35. Callister, W.D., *Materials Science And Engineering: An Introduction*. Fifth ed2000: John Wiley & Sons.

36. Reardon, A.C., *Metallurgy for the Non-Metallurgist*2012: A S M International.

37. Dieter, G.E., *Mechanical Metallurgy*. SI-Metric edition ed. McGraw-Hill Series in Material Science and Engineering, ed. M.B. Bever, et al.: McGraw-Hill Book Company.

38. Herrera, C., D. Ponge, and D. Raabe, *Design of a novel Mn-based 1 GPa duplex stainless TRIP steel with 60% ductility by a reduction of austenite stability.* Acta Materialia, 2011. **59**(11): p. 4653-4664.

39. Schramm, R.E. and R.P. Reed, *Stacking-Fault Energies of 7 Commercial Austenitic Stainless-Steels.* Metallurgical Transactions a-Physical Metallurgy and Materials Science, 1975. **6**(7): p. 1345-1351.

40. Haidemenopoulos, G.N., et al., *Thermodynamics-Based Alloy Design Criteria for Austenite Stabilization and Transformation Toughening in the Fe-Ni-Co System.* Journal of Alloys and Compounds, 1995. **220**(1-2): p. 142-147.

41. Bleck, W., K. Hulka, and K. Papamentellos, *Effect of niobium on the mechanical properties of TRIP steels.* Materials science forum, 1998. **284**: p. 327.

42. Druschitz, A., et al., *Neutron Diffraction Studies of Intercritically Austempered Ductile Irons.* SAE International Journal of Materials & Manufacturing, 2011. **4**(1): p. 111-118.

43. Kaufmann, E.N., *Characterization of materials*2003: Wiley-Interscience.

44. Zrník, J., et al., *Retained austenite stability investigation in TRIP steel using neutron diffraction.* Materials science & engineering. A, Structural materials : properties, microstructure and processing, 2006. **437**(1): p. 114-119.

45. Zrník, J., et al., *In Situ Neutron Diffraction Analysis of Phase Transformation Kinetics in TRIP Steel.* Materials science forum, 2005. **502**: p. 339.

46. Jenkus, P., et al., *Neutron Diffraction Studies of Si-Mn Trip Steel In Situ upon Thermomechanical Processing.* Journal of neutron research, 2004. **12**(1-3): p. 243-248.

47. Oliver, E.C., et al., *Neutron-diffraction study of stress-induced martensitic transformation in TRIP steel.* Applied physics. A, Materials science & processing, 2002. **74**(0): p. s1143-s1145.

48. Druschitz, A.P., *In Situ Studies of Intercritically Austempered Ductile Iron Using Neutron Diffraction.* Metallurgical and materials transactions. A, Physical metallurgy and materials science, 2012. **43**(5): p. 1468-1476.

49. SNS-ORNL. *VULCAN Sample Dimensions*. 2011 07/26/2011; Available from: http://neutrons.ornl.gov/vulcan/_media/vulcan-sample-geometry.pdf.

50. ORNL. *How SNS works*. Available from: http://neutrons.ornl.gov/facilities/SNS/works.shtml#ion.

51. SNS-ORNL. *The Engineering Materials Diffractometer at SNS*. VULCAN-fact sheet]. Available from: http://neutrons.ornl.gov/vulcan/.

52. Wang, X.L., et al., *VULCAN—The engineering diffractometer at the SNS.* Physica B: Condensed Matter, 2006. **385–386, Part 1**(0): p. 673-675.

53. An, K. *VDRIVE Manual*. [web manual] 2012 02/29/2012; Available from: http://www.ornl.gov/~k6e/VDRIVE.

54. White, P.S., J.R. Rodgers, and Y. Le Page, *CRYSTMET: a database of the structures and powder patterns of metals and intermetallics.* Acta Crystallographica Section B, 2002. **58**(3-1): p. 343-348.

55. Standard, A., *Standard Practice for X-Ray Determination of Retained Austenite in Steel with Near Random Crystallographic Orientation*, 2008, ASTM International: West Conshohocken, PA. p. 716-721.

56. Schiffbauer, J.D., *Introduction to SEM: Signals, contrast, and X-rays*, 2012, NCFL-ICTAS, Virginia Tech: Virginia Tech.

57. Chopra, O.K. and A.S. Rao, *A review of irradiation effects on LWR core internal materials – IASCC susceptibility and crack growth rates of austenitic stainless steels.* Journal of Nuclear Materials, 2011. **409**(3): p. 235-256.

58. Ahlers, M., *The martensitic transformation.* Revista Materia, 2004. **9**: p. 169-183.

59. Kelly, P.M. and J. Nutting, *The Martensite Transformation in Carbon Steels.* Proceedings of the Royal Society of London. Series A. Mathematical and Physical Sciences, 1960. **259**(1296): p. 45-58.

60. Chung, D.H. and W.R. Buessem, *The Elastic Anisotropy of Crystals.* Journal of Applied Physics, 1967. **38**(5): p. 2010-2012.

Appendix A

A.i True stress-true strain curves and engineering stress-engineering strain curves for the tested alloys

The charts provided below are a continuation of data from section 4.1. The discussions are included in the mentioned section.

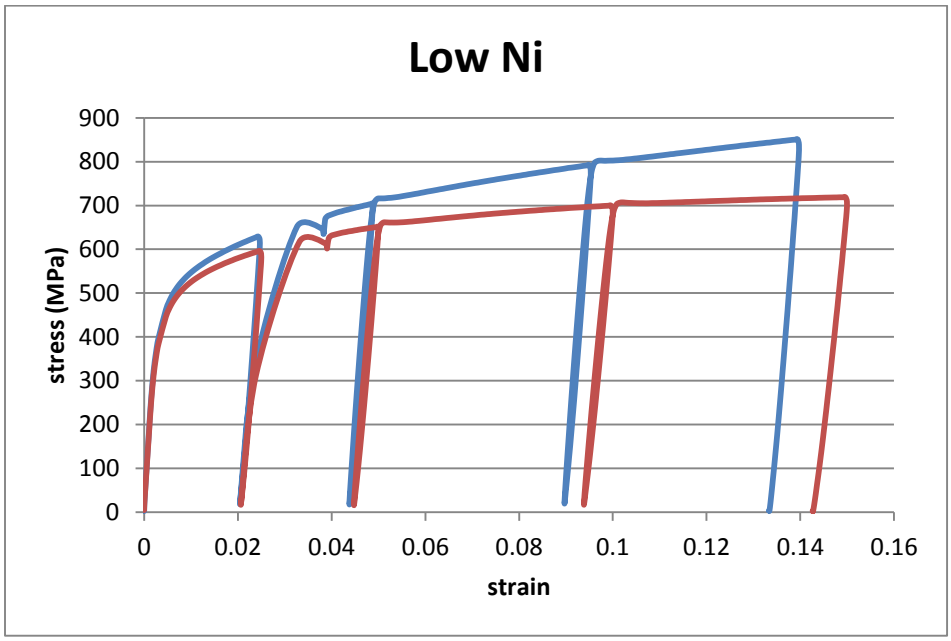

Figure A-1: True stress-true strain curve (blue) and engineering stress-engineering strain curve (red) for Low Ni alloy

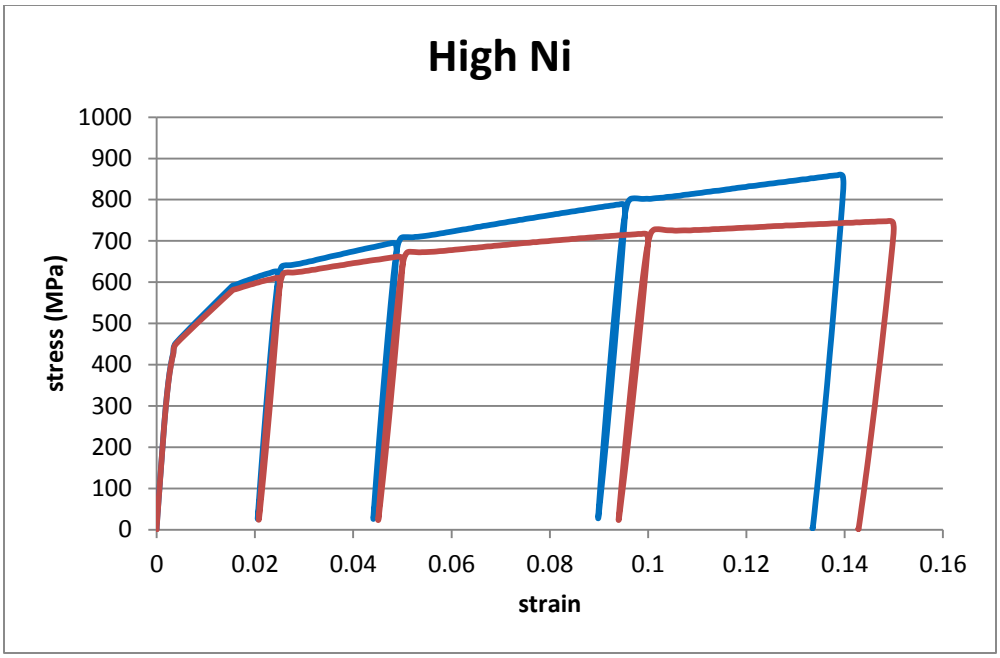

Figure A-2: True stress-true strain curve (blue) and engineering stress-engineering strain curve (red) for High Ni alloy

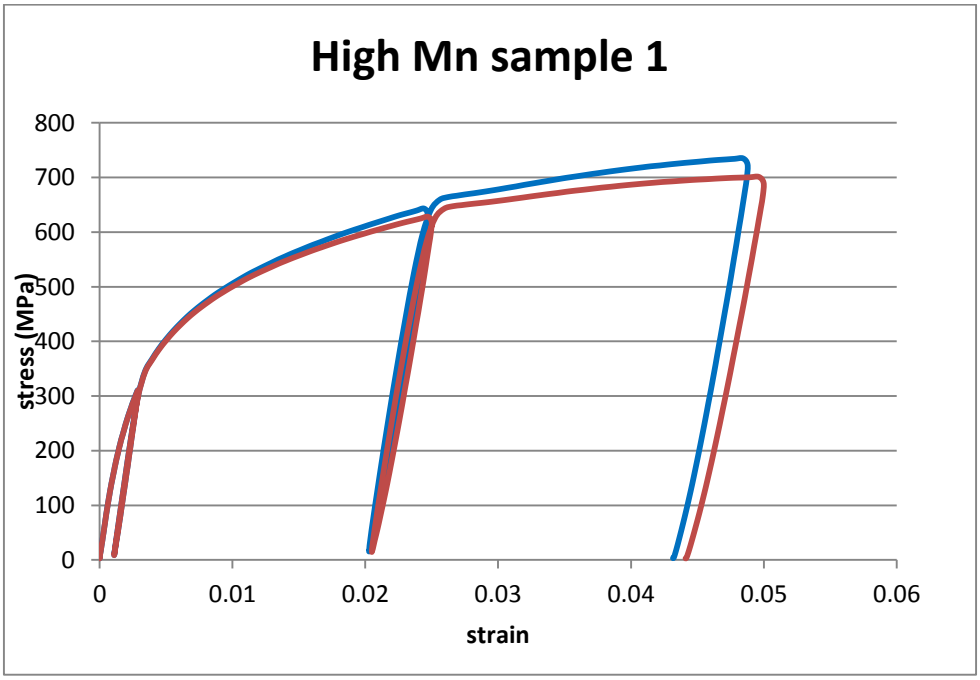

Figure A-3: True stress-true strain curve (blue) and engineering stress-engineering strain curve (red) for High Mn alloy (sample 1)

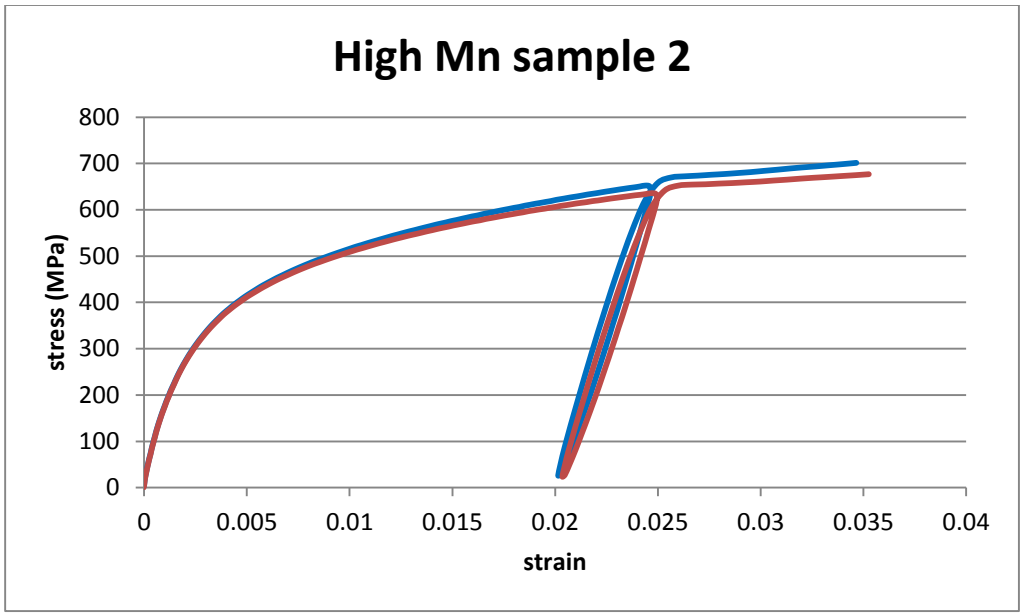

Figure A-4: True stress-true strain curve (blue) and engineering stress-engineering strain curve (red) for High Mn alloy (sample 2)

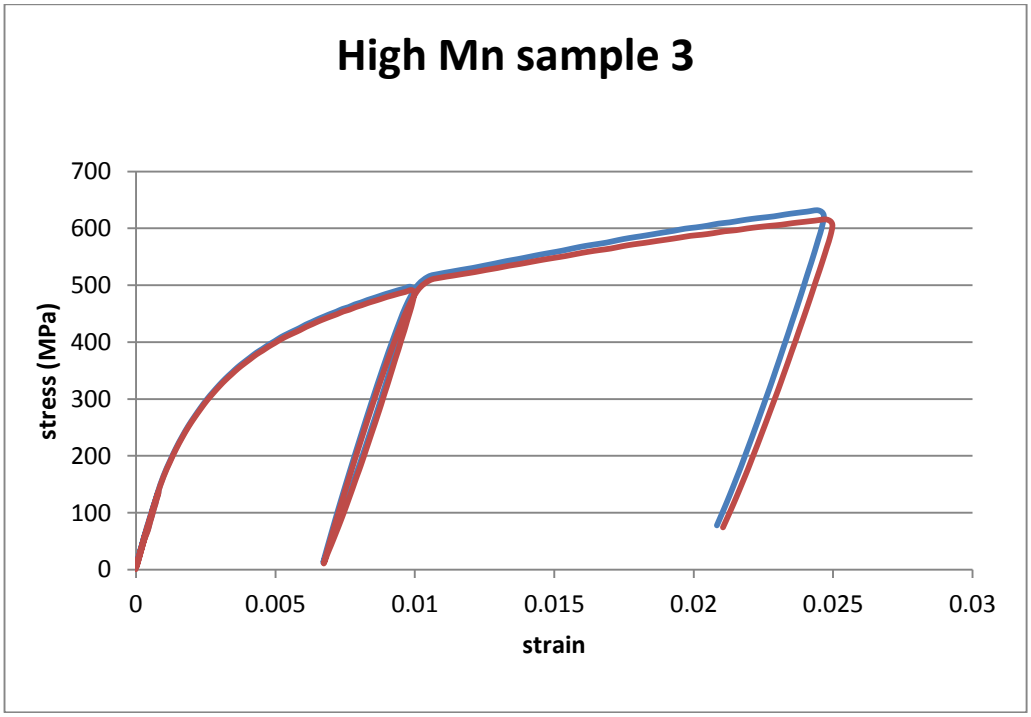

Figure A-5: True stress true-strain curve(blue) and engineering stress-engineering strain curve (red) for High Mn alloy (sample 3)

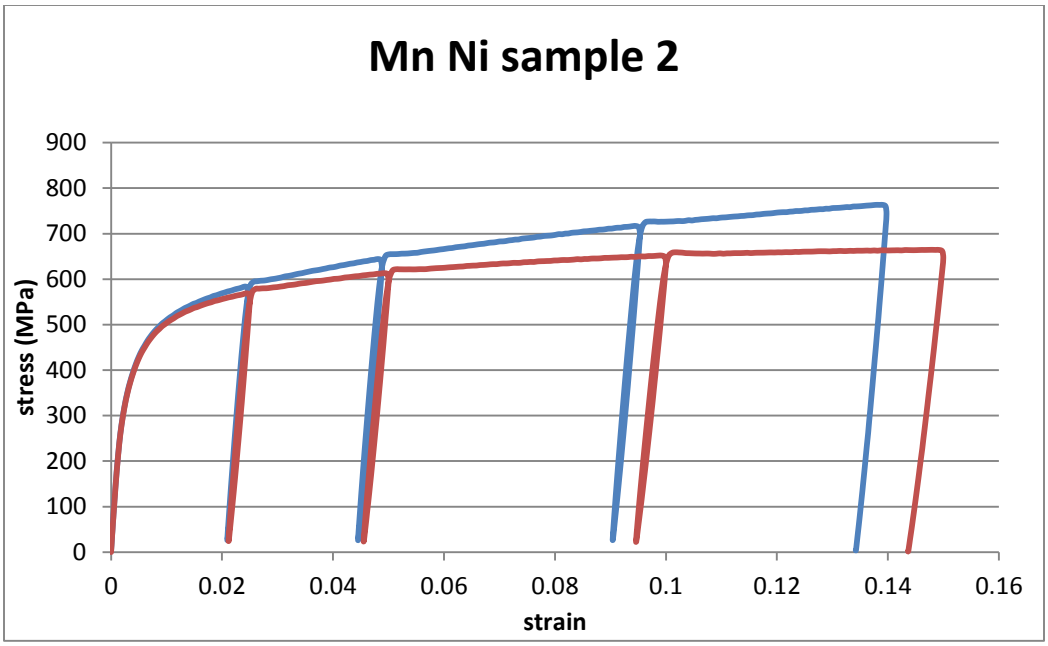

Figure A-6: True stress-true strain curve (blue) and engineering stress-engineering strain curve (red) for Ni Mn alloy (sample 2)

A.ii Tensile test on IADI, MADI and Low Carbon Steel

The interrupted tensile test was done in Virginia Tech without any exposure to neutron beam on IADI, MADI and low carbon steel to measure the diameter at various strain levels. The crosshead speeds for various levels are provided in table A-1.

Table A-1: Crosshead speeds at various strain levels

strain	crosshead speed (mm/min)
0%	
0.02%	0.1
0.10%	0.2
0.50%	0.3
1%	0.4
2.50%	0.5
5%	1
UNLOAD (to 10N)	1
7.50%	1
10%	1
UNLOAD (to 10N)	1
12.50%	1
15%	1

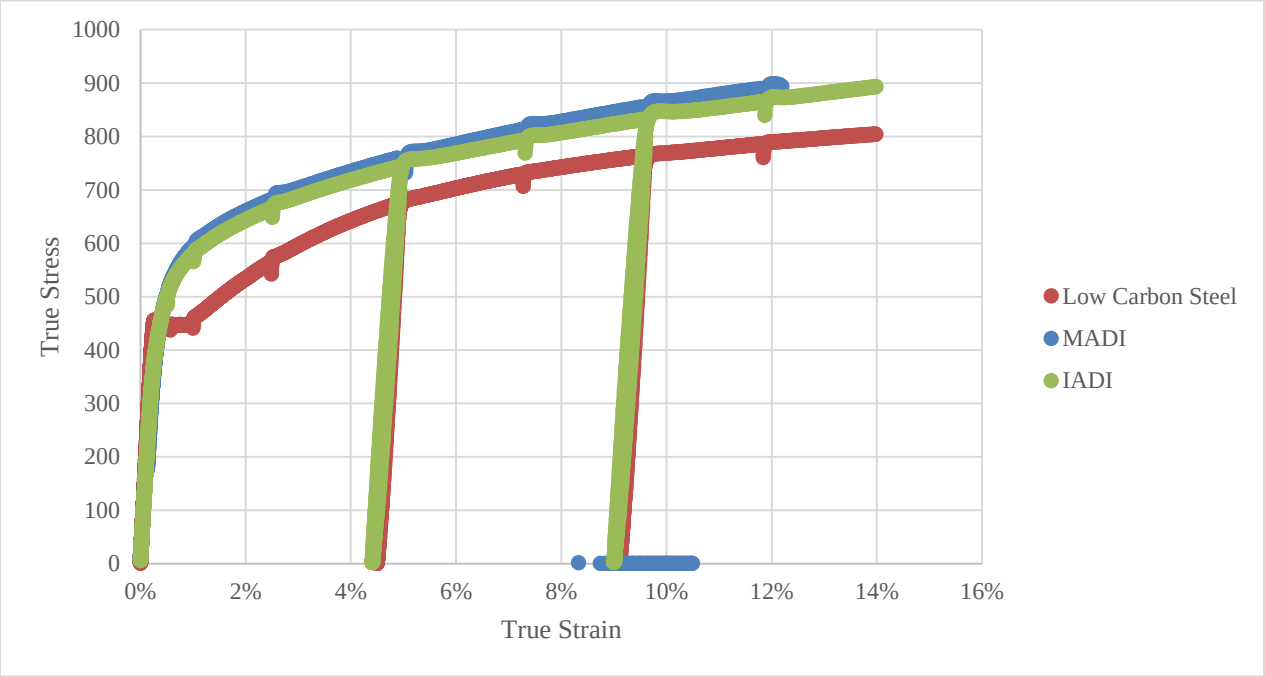

Figure A-7: True stress true strain data for IADI, MADI and Low Carbon Steel

The true stress true strain curve for the tested material are given in figure A-7.

The change in volume and diameter for MADI and low carbon steel is given in table A-2 and A-3. The same information about IADI is in section 4.1. The discussions are also included in that section.

Table A-2: Change in Volume and Diameter in MADI

MADI						
Engineering Strain	True Strain	Diameter Calculated (in mm)	Diameter Measured (in mm)	Difference (in mm)	Difference (% of initial diameter)	Apparent Volume change (%)
-0.00001	0.0000	6.27	6.27	0.00	5E-04	0.0000
0.00020	0.0002	6.27	6.27	0.00	0.010	0.0200
0.00100	0.0009	6.27	6.27	0.00	0.050	0.1000
0.00500	0.0049	6.25	6.20	0.05	0.867	1.7314
0.01000	0.0099	6.24	6.19	0.05	0.780	1.5609
0.02501	0.0247	6.19	6.16	0.03	0.527	1.0639
0.05001	0.0487	6.12	6.11	0.01	0.141	0.2895
0.07501	0.0723	6.05	6.08	0.03	0.522	1.0845
0.10003	0.0953	5.98	6.03	0.05	0.827	1.7428

0.12505	0.1178	5.91	5.98	0.07	1.096	2.3385

Table A-3: Change in Volume and Diameter in Low Carbon Steel

Low Carbon Steel (Re-bar)						
Engineering Strain	True Strain	Diameter Calculated (in mm)	Diameter Measured (in mm)	Difference (in mm)	Difference (% of initial diameter)	Apparent Volume change (%)
0	0	8.23	8.23	0.00	0.0000	0.0000
0.0002	0.0002	8.23	8.23	0.00	0.0099	0.0200
0.0010	0.0010	8.23	8.22	0.01	0.0715	0.1431
0.0050	0.0049	8.21	8.20	0.01	0.1154	0.2313
0.0100	0.0099	8.19	8.20	0.01	0.1317	0.2650
0.0250	0.0247	8.13	8.16	0.03	0.3769	0.7648
0.0500	0.0488	8.03	8.05	0.02	0.2233	0.4582
0.0459	0.0449	8.05	8.05	0.00	0.0345	0.0707
0.0750	0.0723	7.94	7.98	0.04	0.5142	1.0691
0.1000	0.0953	7.85	7.90	0.05	0.6453	1.3582
0.0953	0.0910	7.86	7.89	0.03	0.3181	0.6671
0.1250	0.1178	7.76	7.83	0.07	0.8588	1.8301
0.1500	0.1398	7.67	7.73	0.06	0.6745	1.4521

Appendix B: Calculation of Elastic Modulus

The graphs here are continuation of section 4.2. The discussion about these figures is in the mentioned section.

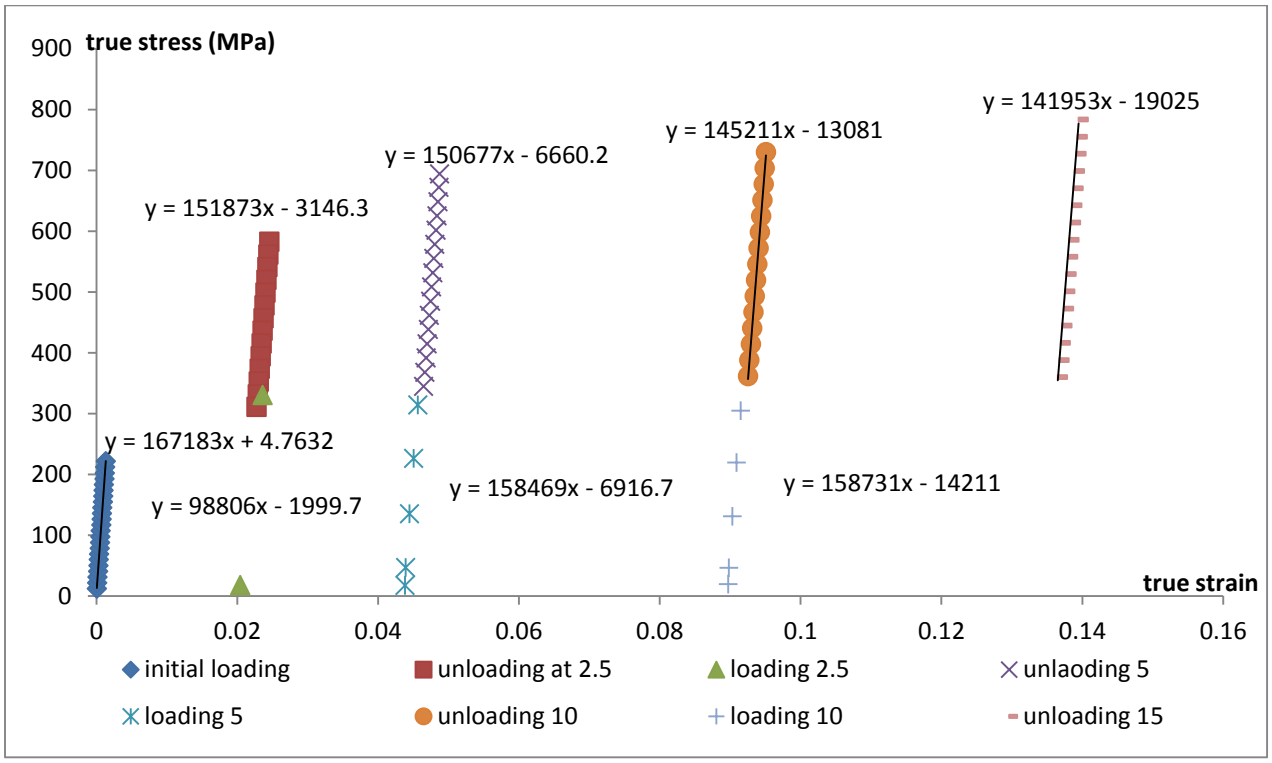

Figure B-1: Modulus data for Low Ni alloy showing linear region of loading/unloading cycles

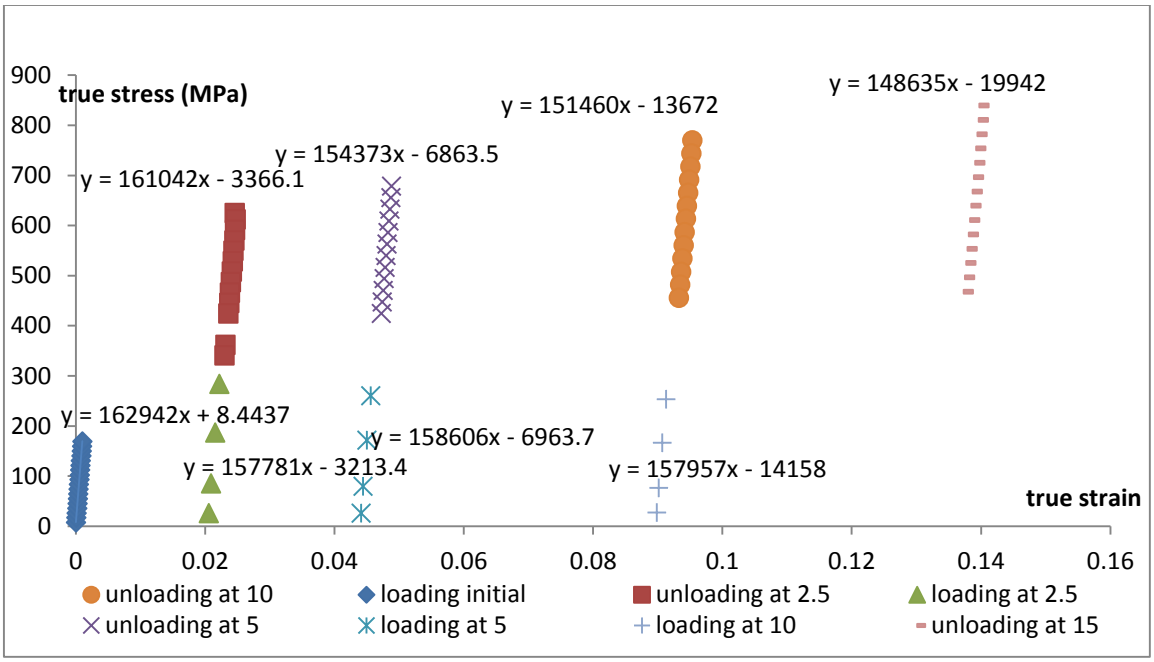

Figure B-2: Modulus data for High Ni alloy showing linear region of loading/unloading cycles

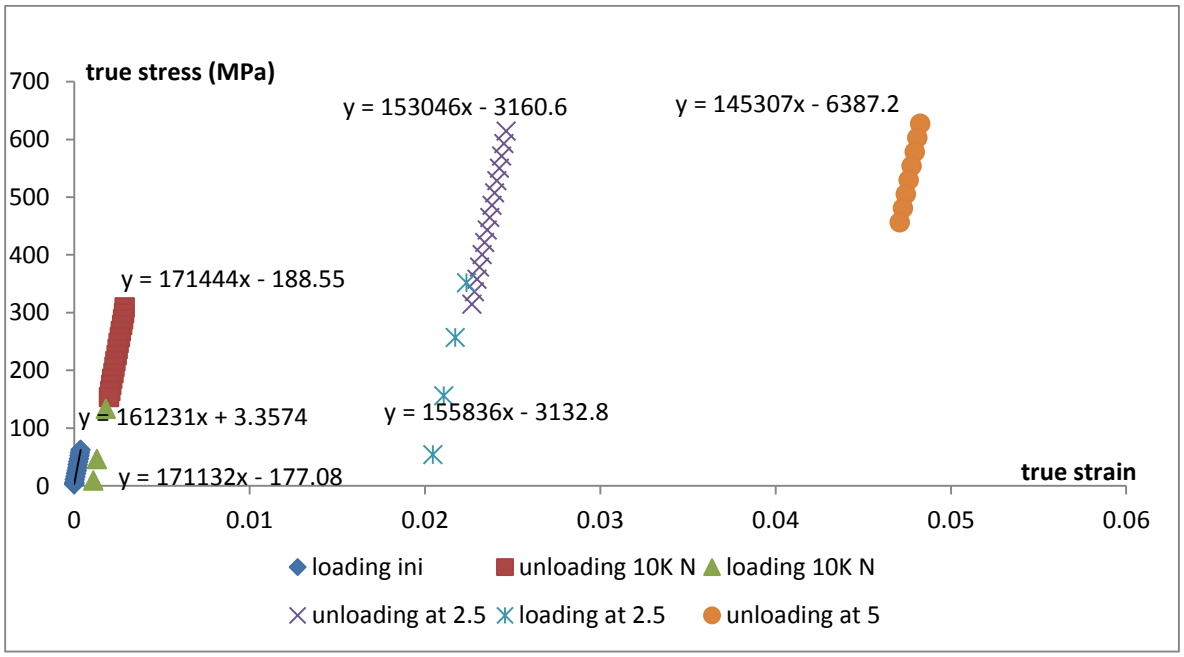

Figure B-3: Modulus data for High Mn alloy (sample 1) showing linear region of loading/unloading cycles

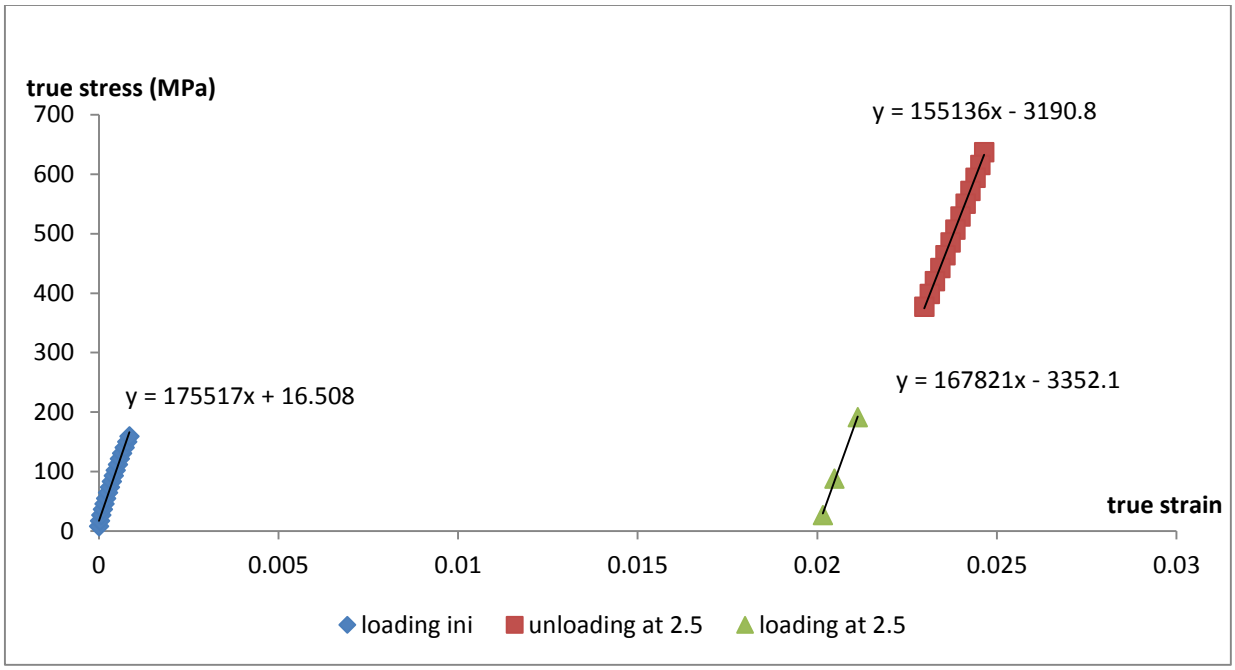

Figure B-4: Modulus data for High Mn alloy (sample 2) showing linear region of loading/unloading cycles

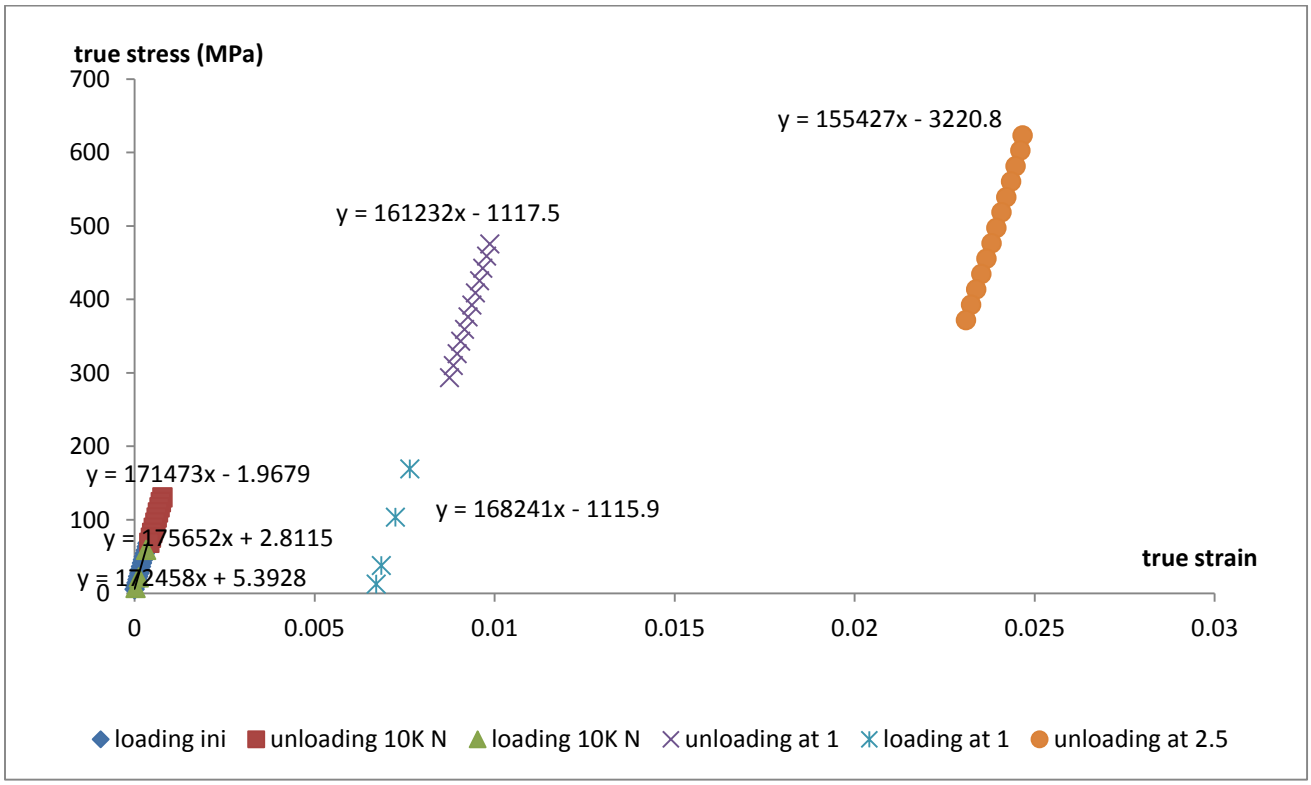

Figure B-5: Modulus data for High Mn alloy (sample 3) showing linear region of loading/unloading cycles

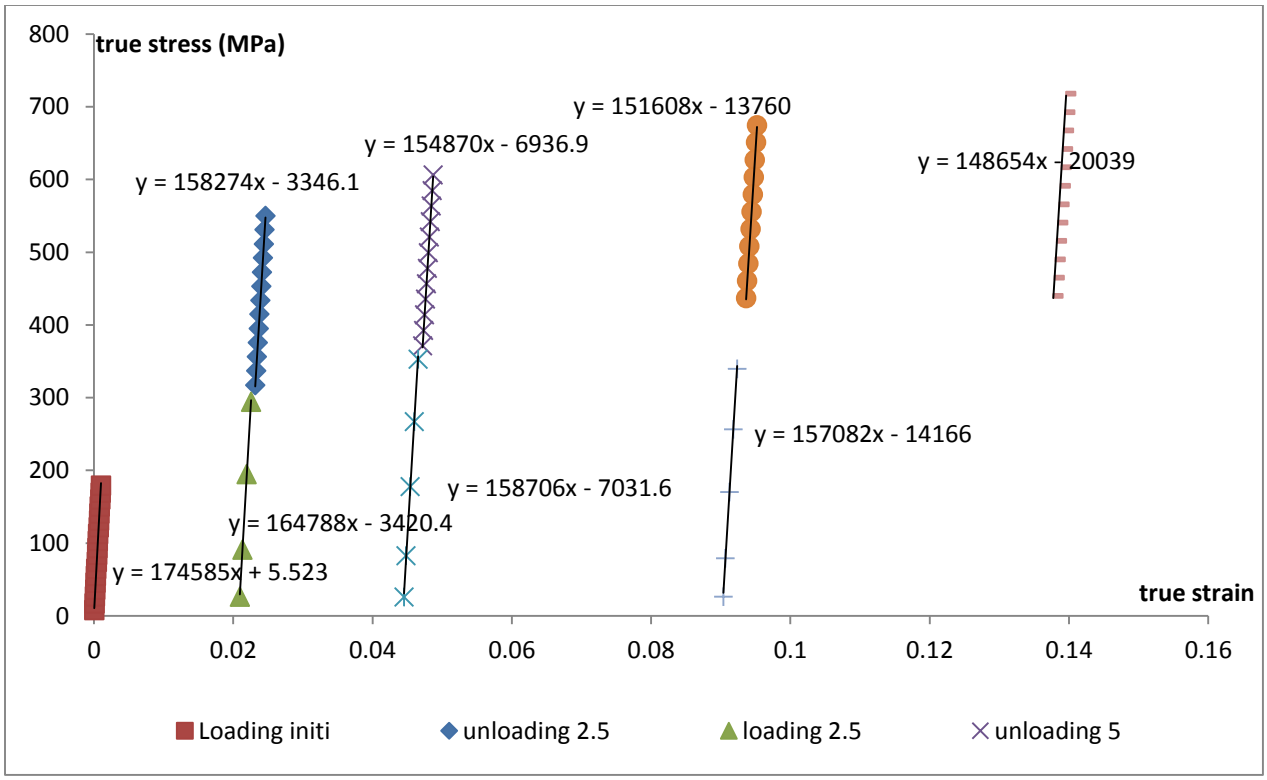

Figure B-6: Modulus data for Ni Mn alloy (sample 2) showing linear region of loading/unloading cycles

Appendix C: Spectral Analysis

C.i Intensity histograms for different alloys

The figures in this section are continued from section 4.3. The discussions about these figures are included in the mentioned section

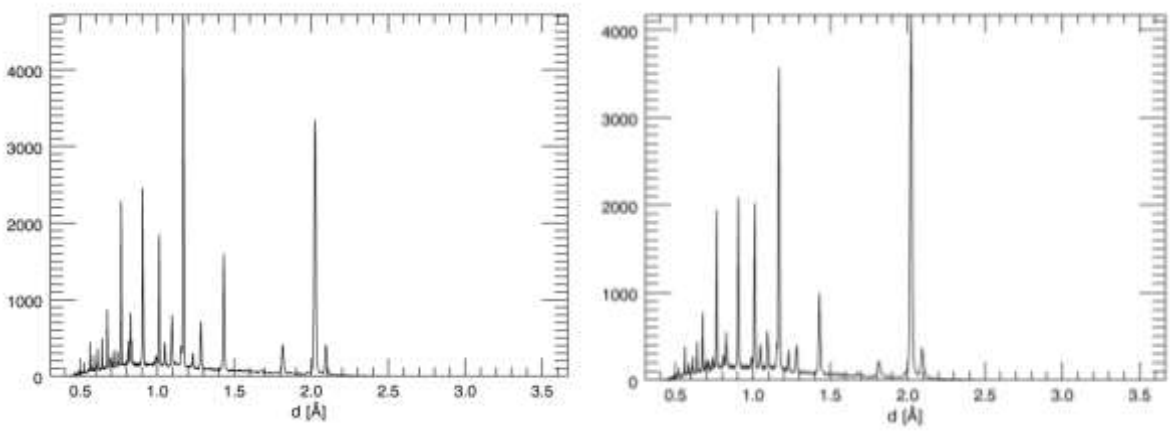

(a) (b)

Figure C-1: Intensity histograms for (a) run 1 and (b) run 500 for low nickel alloy

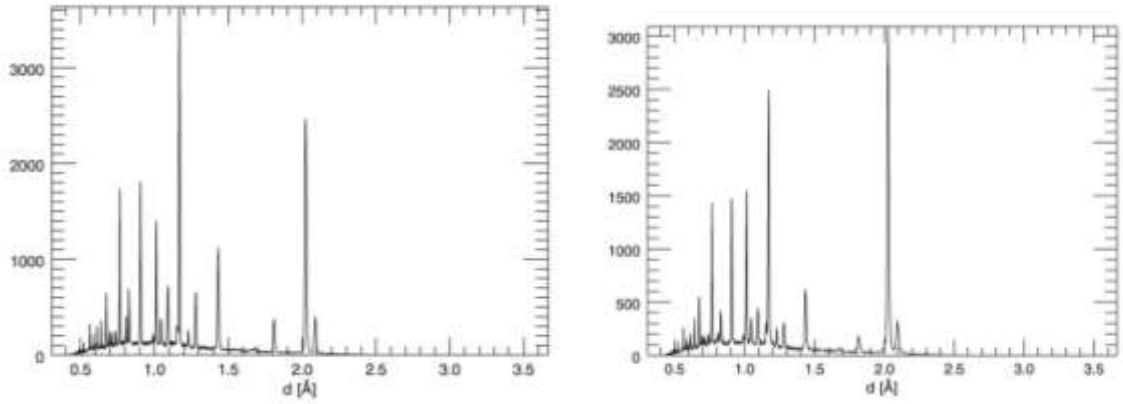

(a) (b)

Figure C-2: Intensity histograms for (a) run 2 and (b) run 400 for high nickel alloy

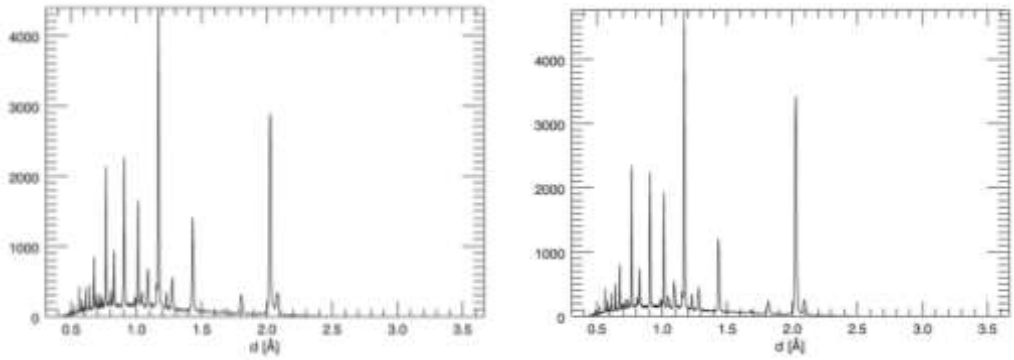

(a) (b)

Figure C-3: Intensity histograms for (a) run 2 and (b) run 160 for high manganese alloy (sample 1)

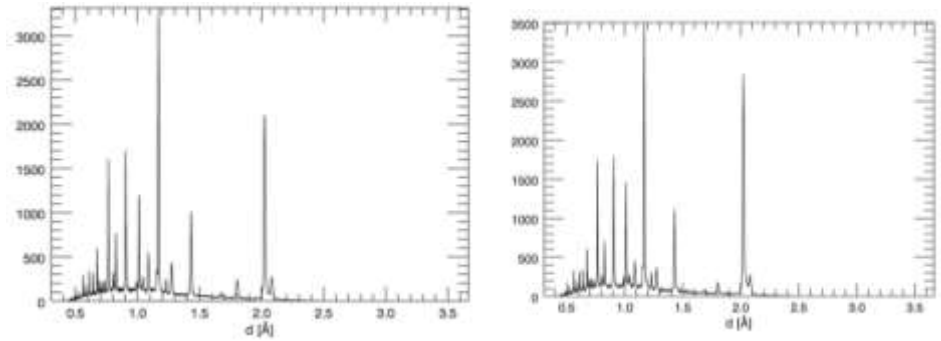

(a) (b)

Figure C-4: Intensity histograms for (a) run 1 and (b) run 200 for high manganese alloy (sample 2)

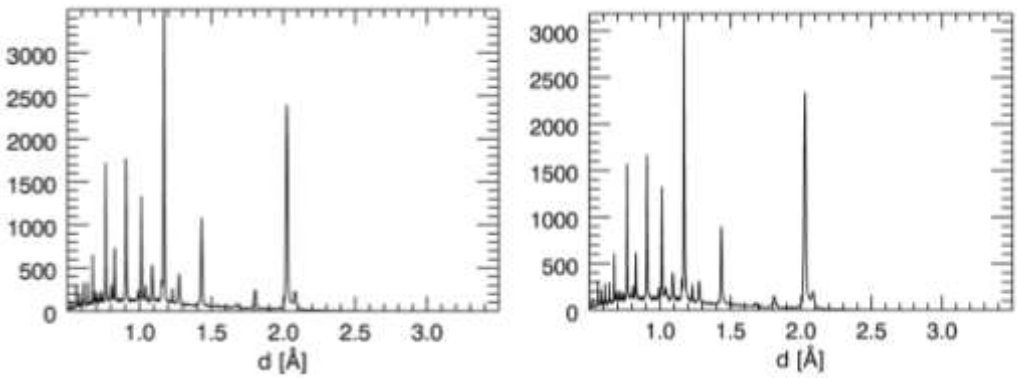

(a) (b)

Figure C-5: Intensity histograms for (a) run 2 and (b) run 200 for high manganese alloy (sample 3)

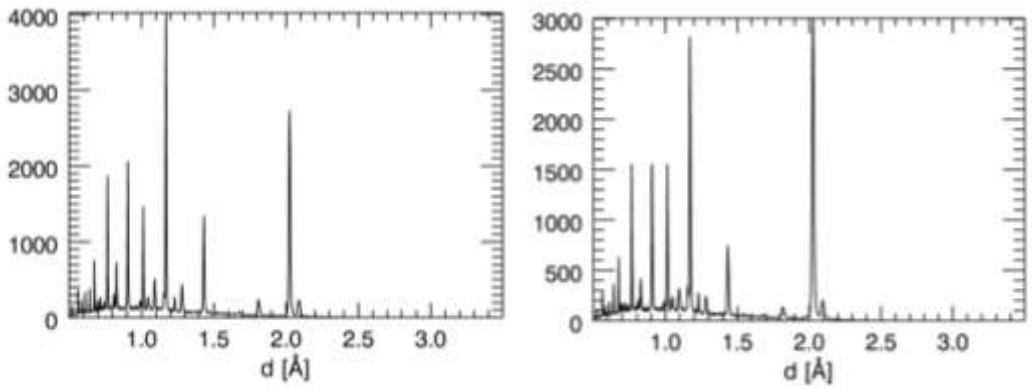

(a) (b)

Figure C-6: Intensity histograms for (a) run 2 and (b) run 400 for nickel manganese alloy (sample 2)

C.ii Peak positions and base width

The peak positions correspond to the d-spacing of the FCC, BCC and HCP carbon planes. This data can be used to predict the carbon content in the phases.

C.ii.i Low Ni alloy

data tag	d spacing (Angstrom)	width
FCC 111	2.104	0.05
BCC 110	2.03	0.05
FCC 200	1.825	0.03
BCC 200	1.436	0.025
FCC 220	1.287	0.02
BCC 211	1.172	0.03
C HCP 112	1.155	0.03
FCC 311	1.099	0.02
FCC 222	1.052	0.01
BCC 220	1.015	0.04
C HCP 114	0.9932	0.04
BCC 310, FCC 400	0.0909	0.02
FCC 331	0.8353	0.04
BCC 222	0.8285	0.04
FCC 420	0.8149	0.04
BCC 321	0.7677	0.03
FCC 422	0.7434	0.03
BCC 400	0.7194	0.05
FCC 511	0.7011	0.05
BCC 411	0.677	0.05
BCC 420, FCC 440	0.6423	0.02
BCC 332	0.6116	0.2
FCC 600	0.6069	0.2

C.ii.ii High Ni Alloy

data tag	d spacing (Angstrom)	width
FCC 111	2.083	0.05
BCC 110	2.024	0.05
FCC 200	1.804	0.03
C HCP 004	1.673	0.04
BCC 200	1.431	0.03
FCC 220	1.275	0.05
C HCP 110	1.23	0.05
BCC 211	1.169	0.03
C HCP 112	1.155	0.03
FCC 311	1.088	0.02
FCC 222	1.041	0.05
BCC 220	1.012	0.05
C HCP 106	0.9912	0.05
BCC 310	0.9061	0.02
BCC 222	0.8275	0.03
FCC 420	0.8065	0.03
BCC 321	0.7652	0.02
FCC 422	0.7358	0.02
BCC 400	0.7156	0.015
FCC 333	0.6948	0.03
BCC 330,411	0.6746	0.03
BCC 420	0.6402	0.01
BCC 332	0.61	0.02
BCC 422	0.5844	0.01

C.ii.iii High Mn alloy

data tag	d spacing (Angstrom)	width
FCC 111	2.088	0.1
BCC 110	2.024	0.1
FCC 200	1.808	0.03
C HCP 004	1.669	0.03
BCC 200	1.431	0.03
FCC 220	1.28	0.02
C HCP 110	1.231	0.01
BCC 211	1.169	0.03
C HCP 103	1.154	0.03
FCC 311	1.093	0.02
FCC 222, C HCP201	1.045	0.02
BCC 220	1.012	0.1
C HCP 114	0.9915	0.1
BCC 310	0.9051	0.02

BCC 222	0.8262	0.03
FCC 420	0.8097	0.03
BCC 321	0.7652	0.06
FCC 422	0.738	0.06
BCC 400	0.7154	0.03
FCC 333	0.6957	0.03
BCC 411	0.6745	0.02
BCC 420, FCC 440	0.6404	0.01
FCC 600, 442, BCC 332	0.6099	0.06
FCC 600, 442*	0.6033	0.06
BCC 422	0.5842	0.02

C.ii.iv Ni-Mn alloys

data tag	d spacing (Angstrom)	width
FCC 111	2.09	0.1
BCC 110	2.024	0.1
FCC 200	1.81	0.03
C HCP 004	1.674	0.03
BCC 200	1.432	0.03
FCC 220	1.281	0.02
C HCP 110	1.231	0.02
BCC 211	1.169	0.04
C HCP 112	1.155	0.04
FCC 311	1.093	0.02
FCC 222	1.045	0.02
BCC 220	1.012	0.04
C HCP 114, 106	0.9921	0.04
BCC 310	0.906	0.02
BCC 222	0.8264	0.04
FCC 420	0.8083	0.04
BCC 321	0.7649	0.03
FCC 422	0.7379	0.01
BCC 400	0.7158	0.05
FCC 333, 511	0.6961	0.05
BCC 330	0.6748	0.02
BCC 420, FCC 440	0.6404	0.01
BCC 332	0.6101	0.02
FCC 600,442	0.6043	0.02
BCC 422	0.5838	0.02

C.iii Surface Plots of Intensity histograms

The figures are an extension of section 4.3. The discussion about these figures is included in the mentioned section.

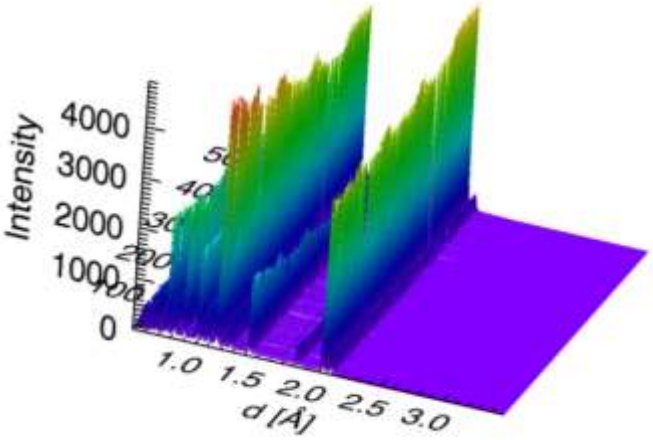

Figure C-7: Surface plot for low nickel alloy

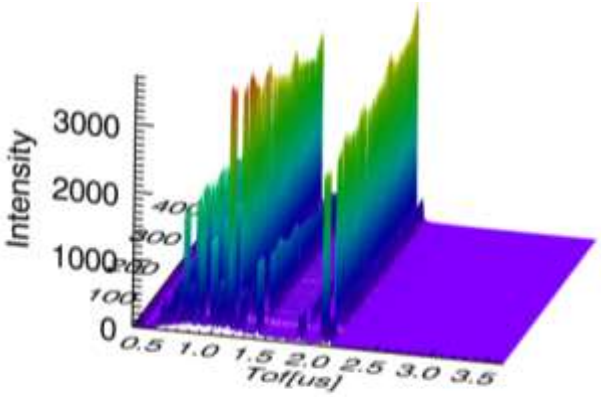

Figure C-8: Surface plot for high nickel alloy

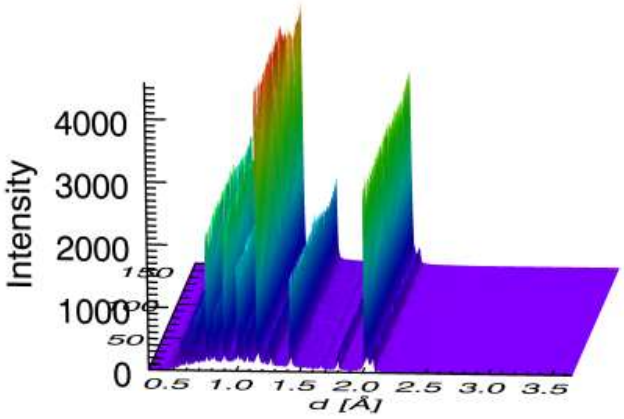

Figure C-9: Surface plot high manganese alloy (sample 1)

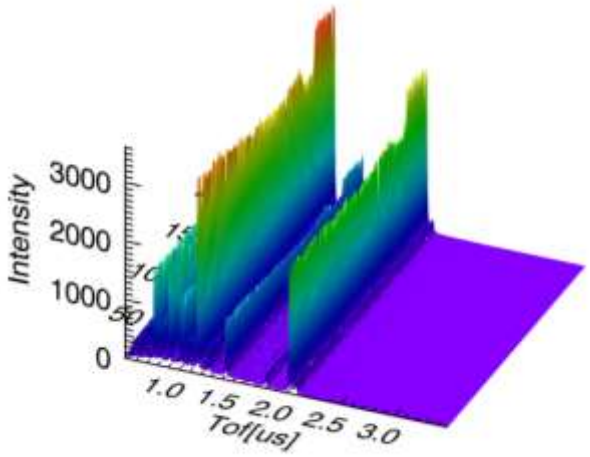

Figure C-10: Surface plot high manganese alloy (sample 2)

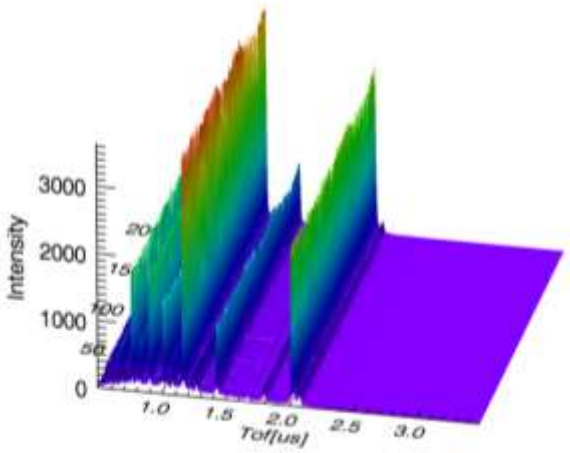

Figure C-11: Surface plot for high manganese alloy (sample 3)

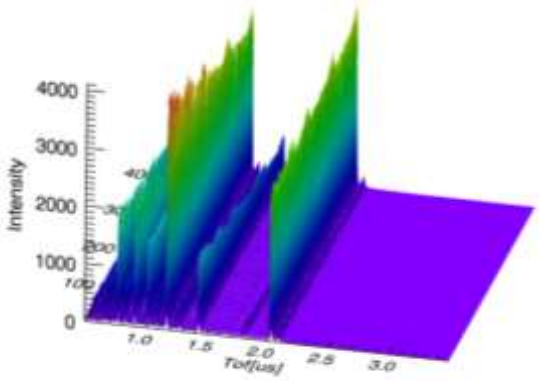

Figure C-12: Surface plot for nickel manganese alloy (sample 2)

Appendix D: True stress and strain at transformation

D.i True stress vs. rationalized fraction of austenite for different alloys

These figures are a continuation of section 4.4.1. Discussions and analysis using these figures are included in the mentioned section.

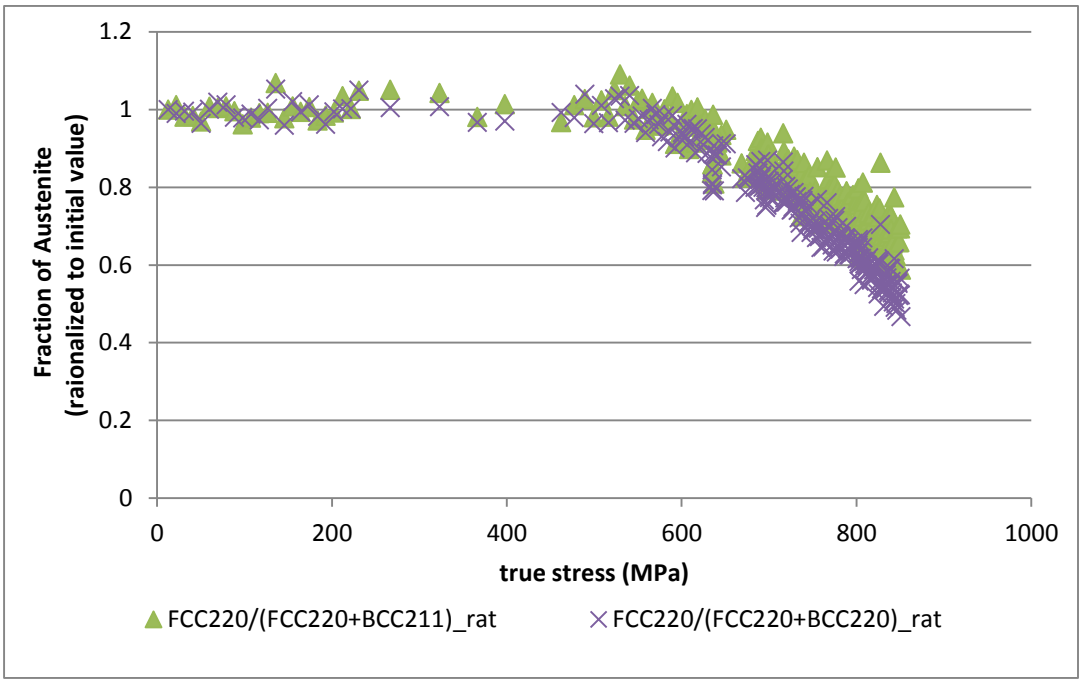

Figure D-1: Rationalized fraction of austenite vs true stress for low Ni (selected peaks)

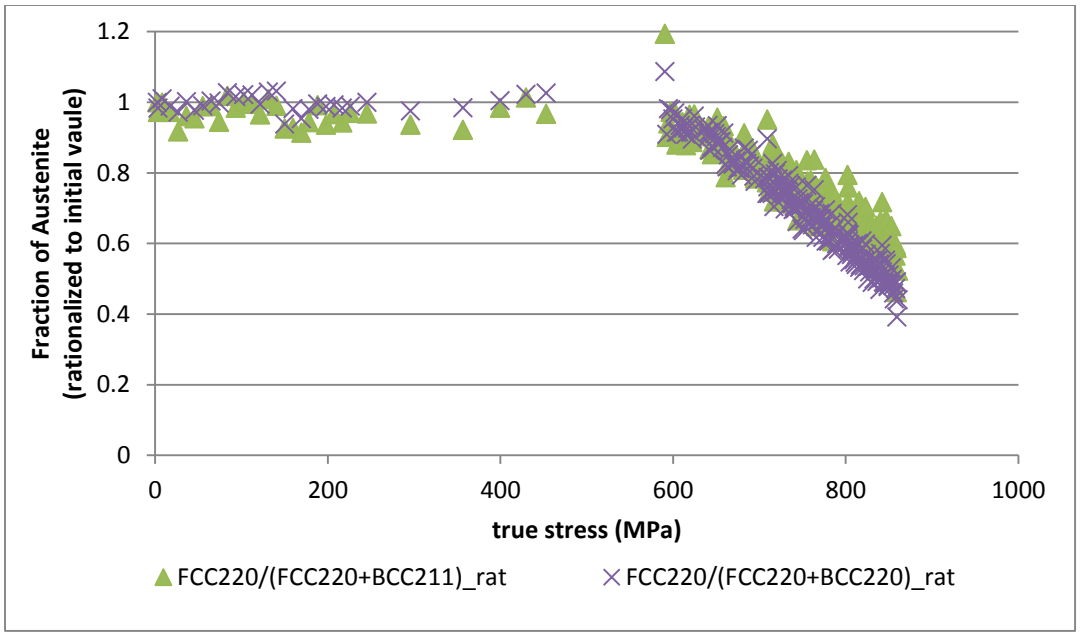

Figure D-2: Rationalized fraction of austenite vs true stress for high Ni alloy

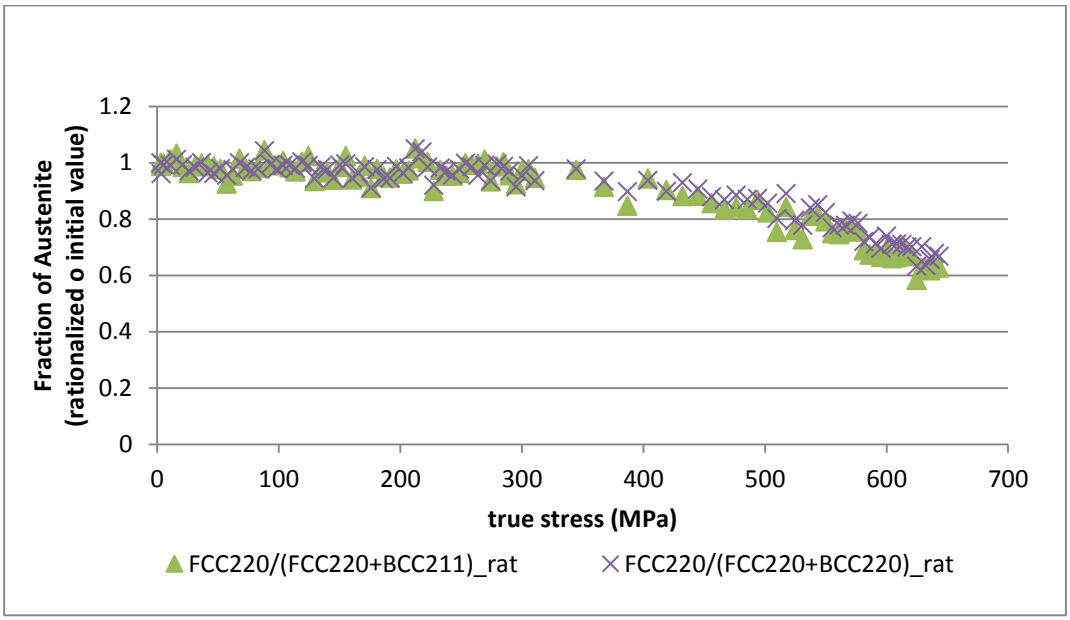

Figure D-3: Rationalized fraction of austenite vs true stress for high Mn alloy (sample 1)

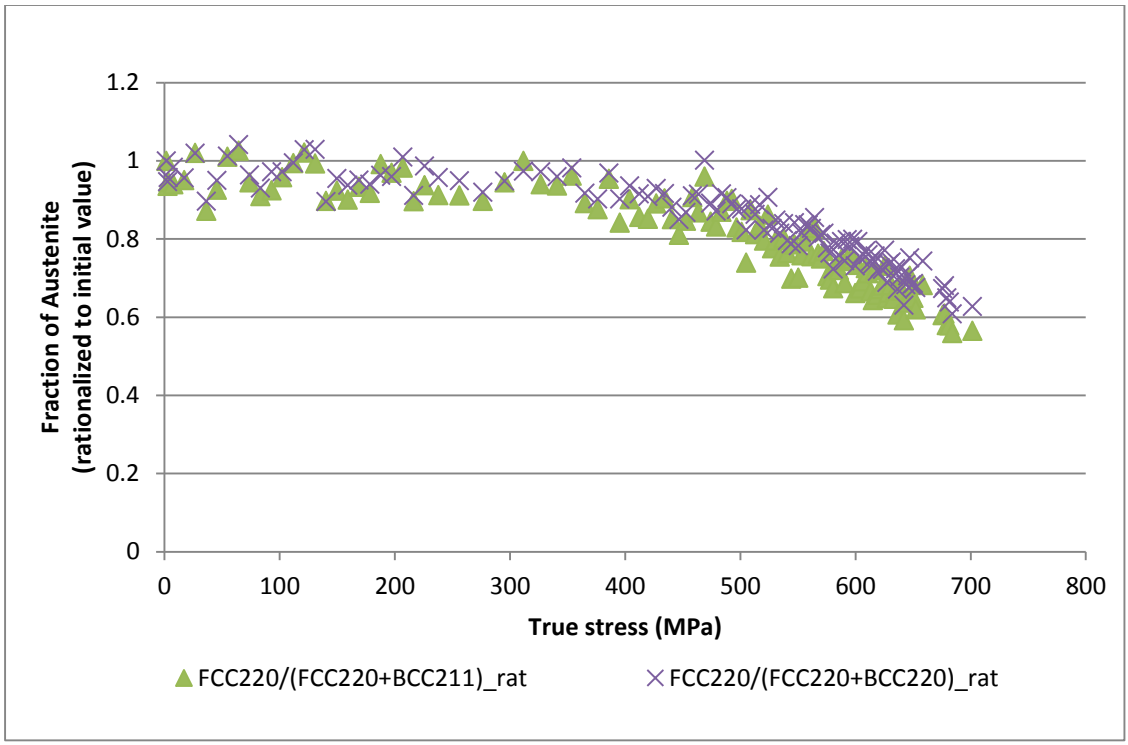

Figure D-4: Rationalized fraction of austenite vs true stress for high Mn alloy (sample 2)

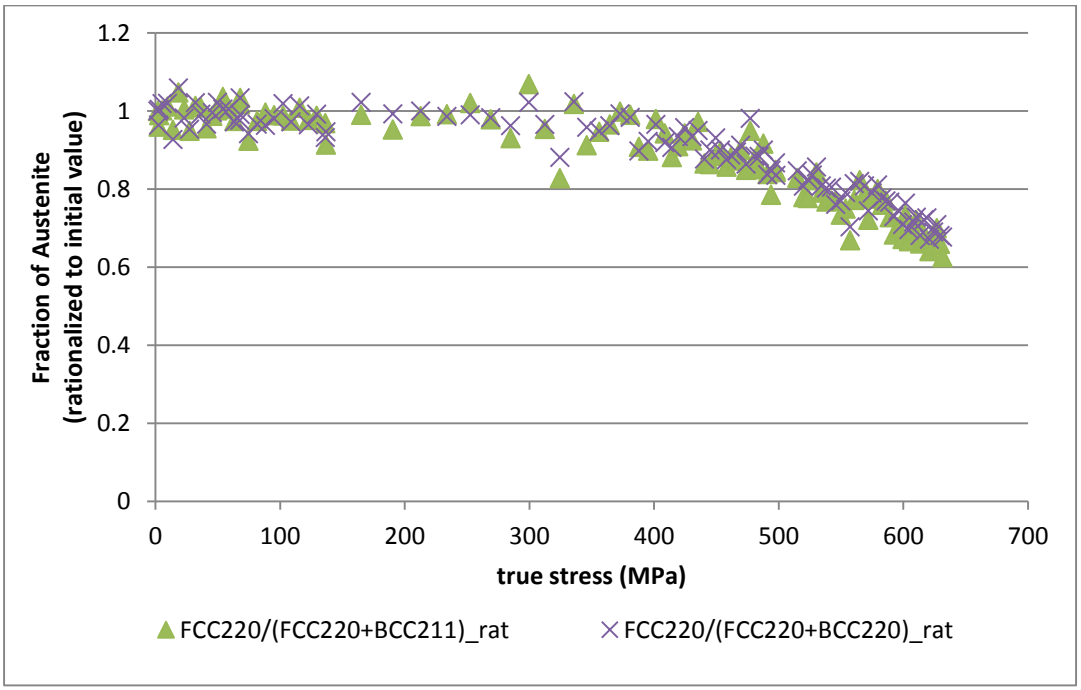

Figure D-5: Rationalized fraction of austenite vs true stress for high Mn alloy (sample 3)

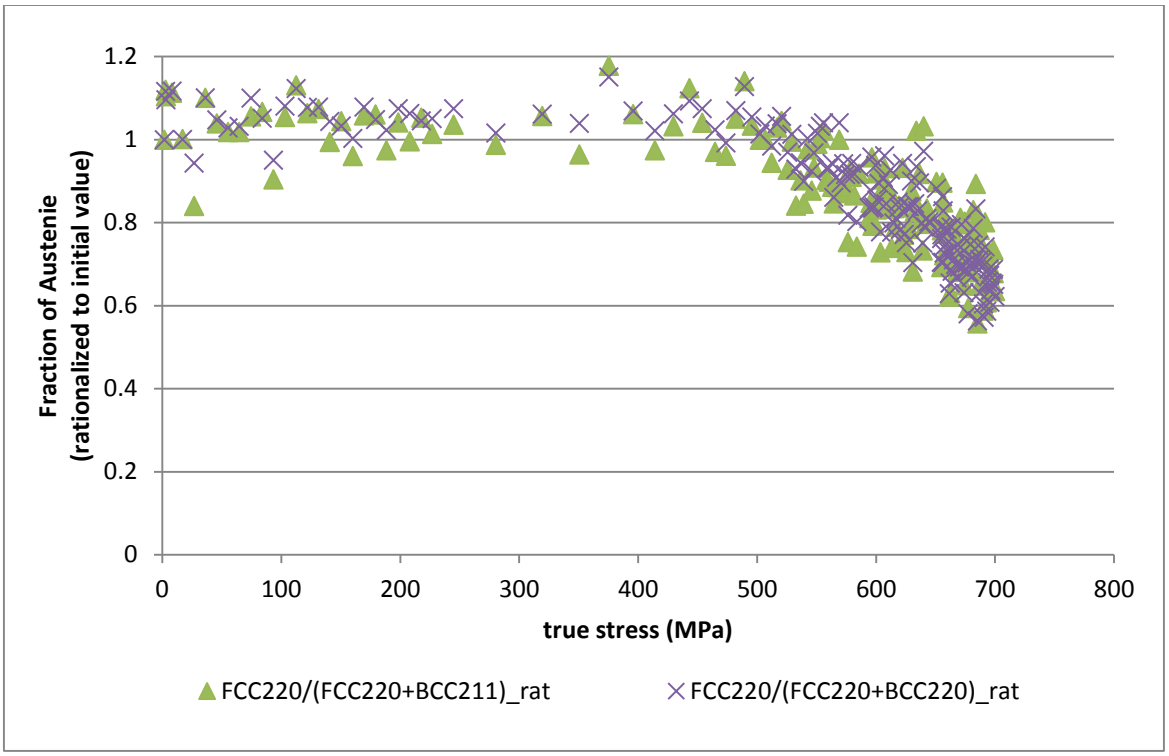

Figure D-6: Rationalized fraction of austenite vs true stress for Ni-Mn alloy (sample 2)

D.ii True strain vs. rationalized fraction of austenite for different alloys

These figures are continuation of section 4.4.1. Discussions and analysis using these figures are included in the mentioned section.

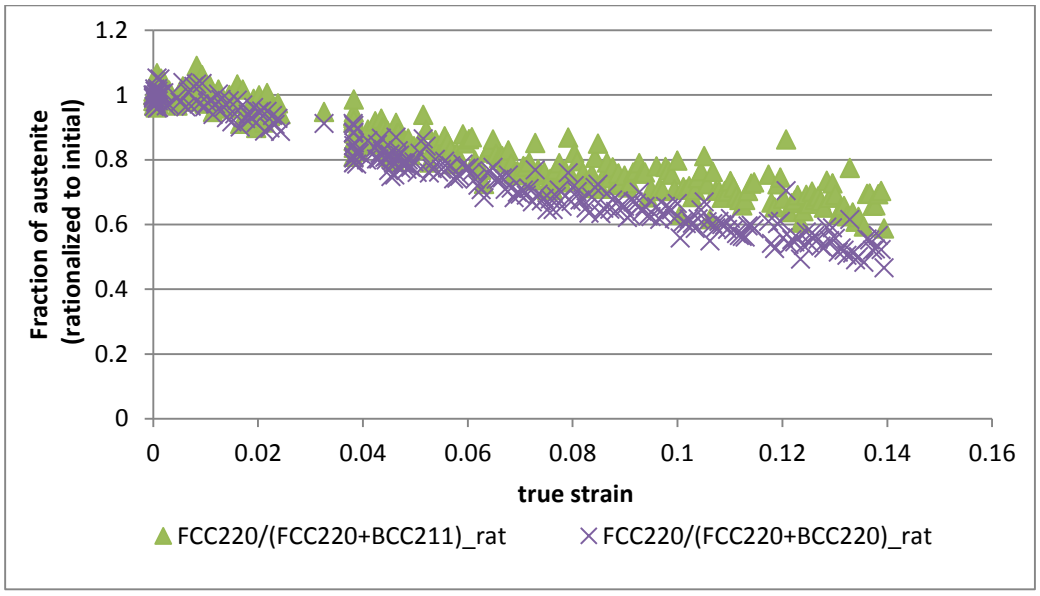

Figure D-7: True strain vs. fraction of austenite (rationalized to initial) for low Ni alloy

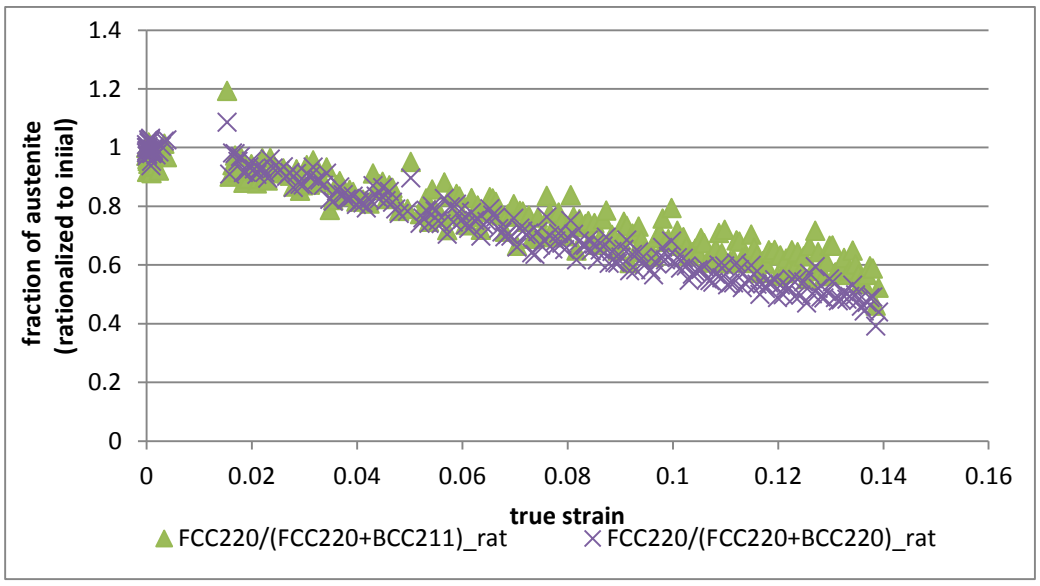

Figure D-8: True strain vs. fraction of austenite (rationalized to initial) for high Ni alloy

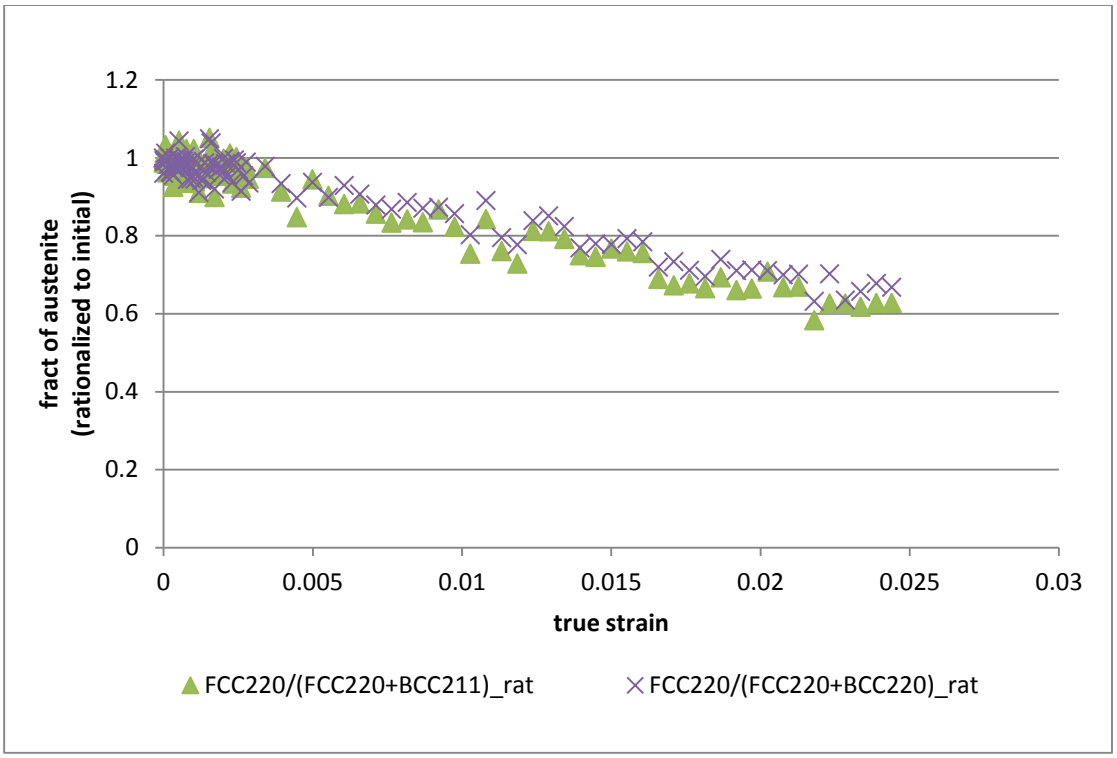

Figure D-9: True strain vs. fraction of austenite (rationalized to initial) for high Mn alloy (sample 1)

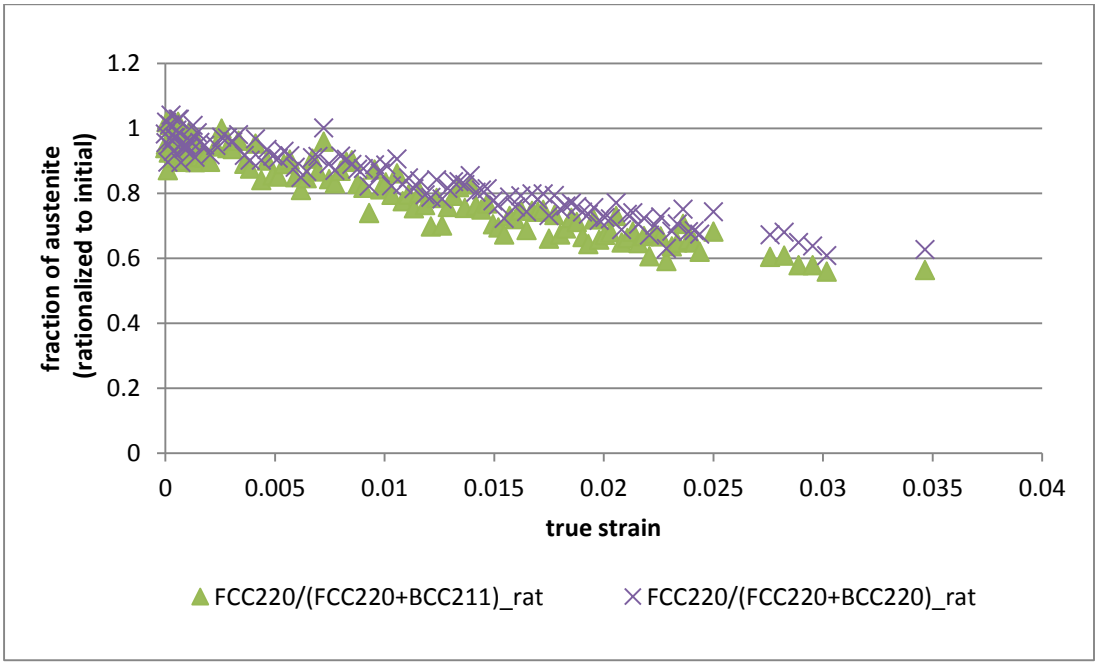

Figure D-10: True strain vs. fraction of austenite (rationalized to initial) for high Mn alloy (sample 2)

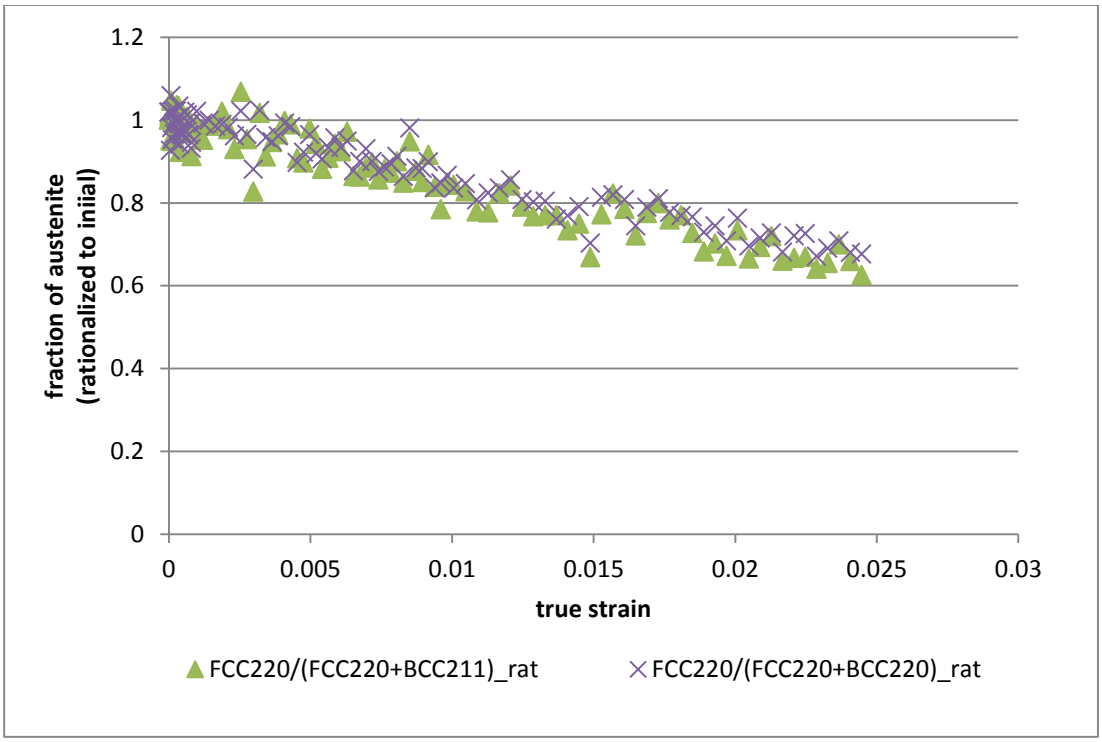

Figure D-11: True strain vs. fraction of austenite (rationalized to initial) for high Mn alloy (sample 3)

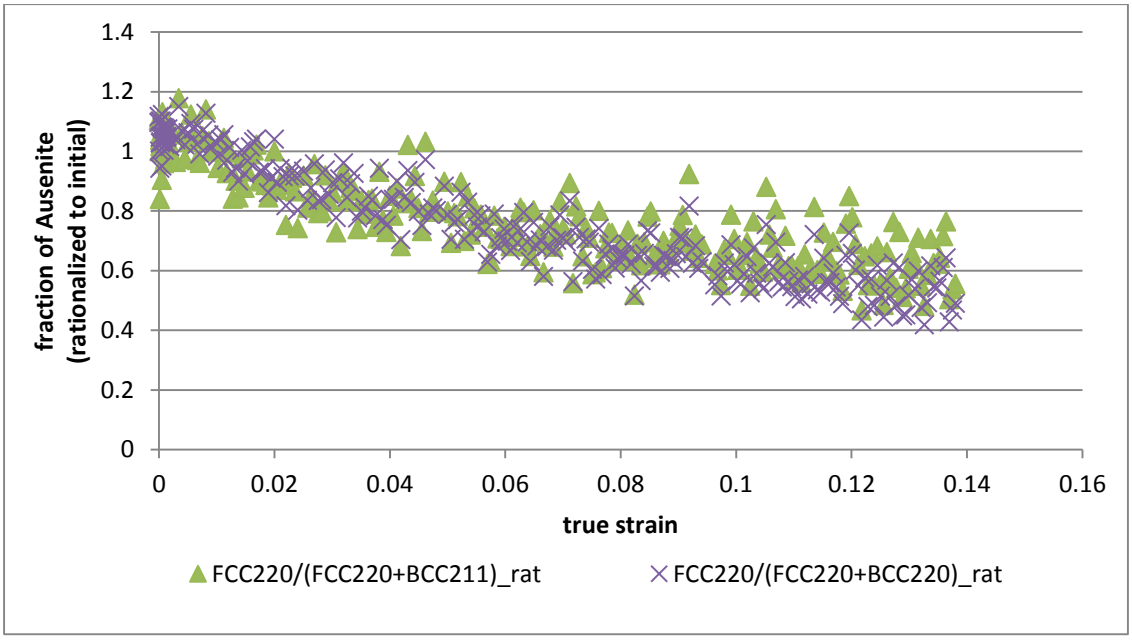

Figure D-12: True strain vs. fraction of austenite (rationalized to initial) for Ni-Mn alloy (sample 2)

Appendix E: Elastic Diffraction Constant

E.i True Stress vs. Lattice Strain

These figures are a continuation of section 4.5. Discussions and analysis using these figures are included in the mentioned section.

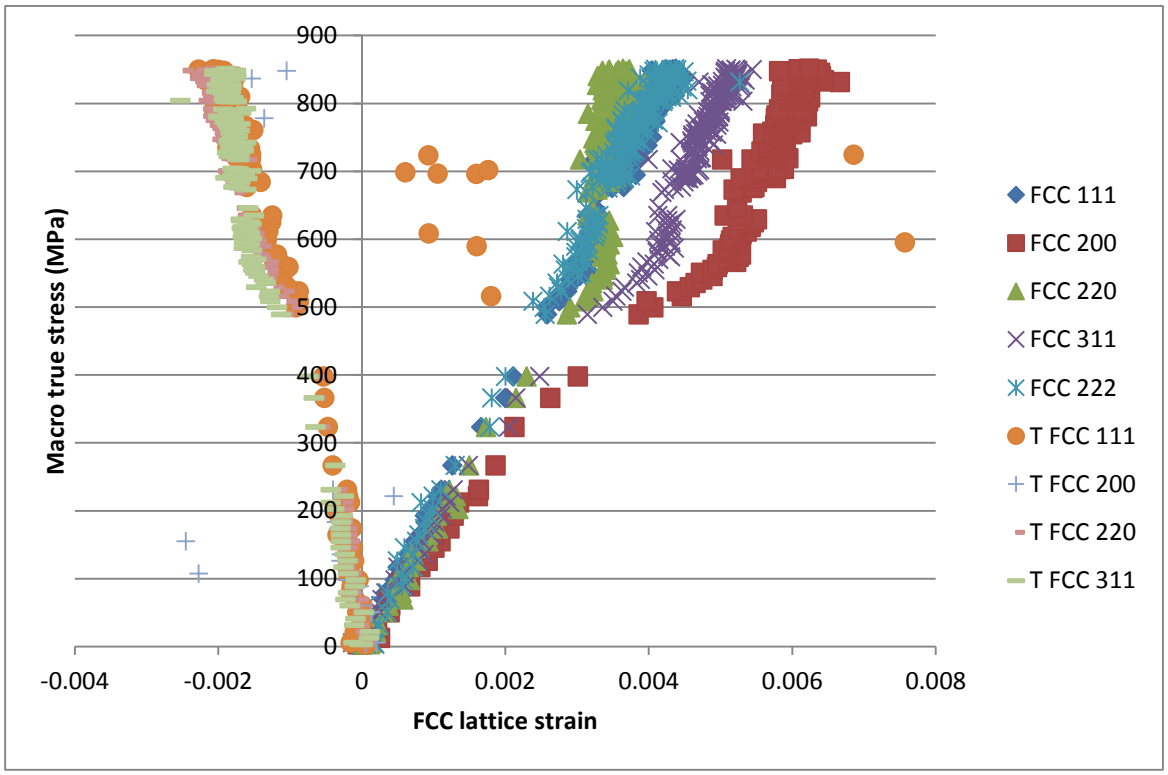

Figure E-1: True stress vs. lattice strains for FCC planes in low Ni alloy

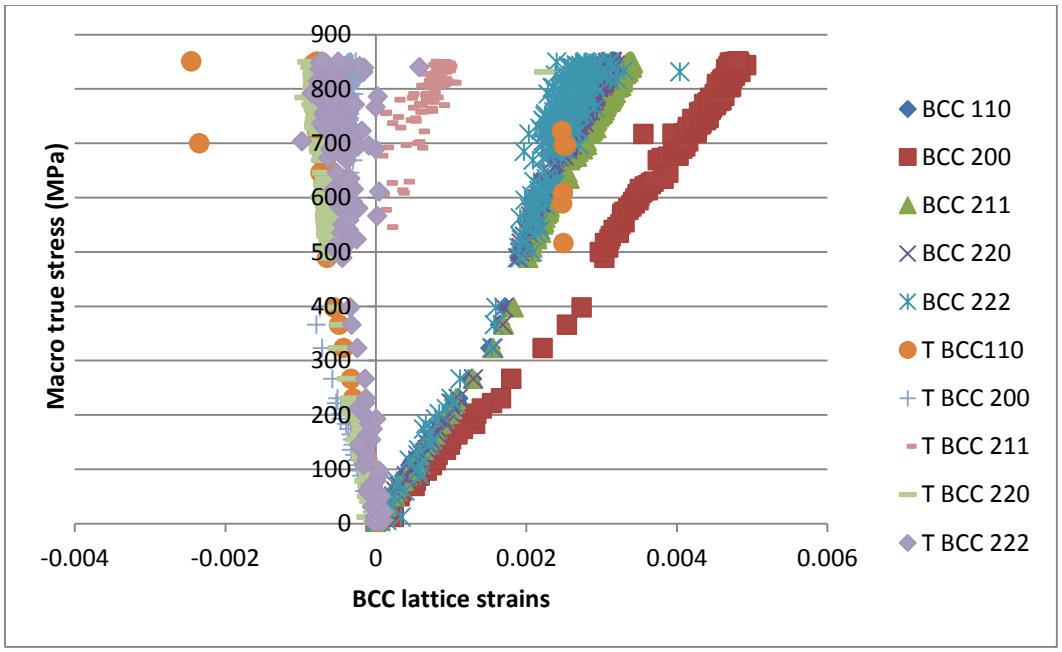

Figure E-2: True stress vs. lattice strains for BCC planes in low Ni alloy

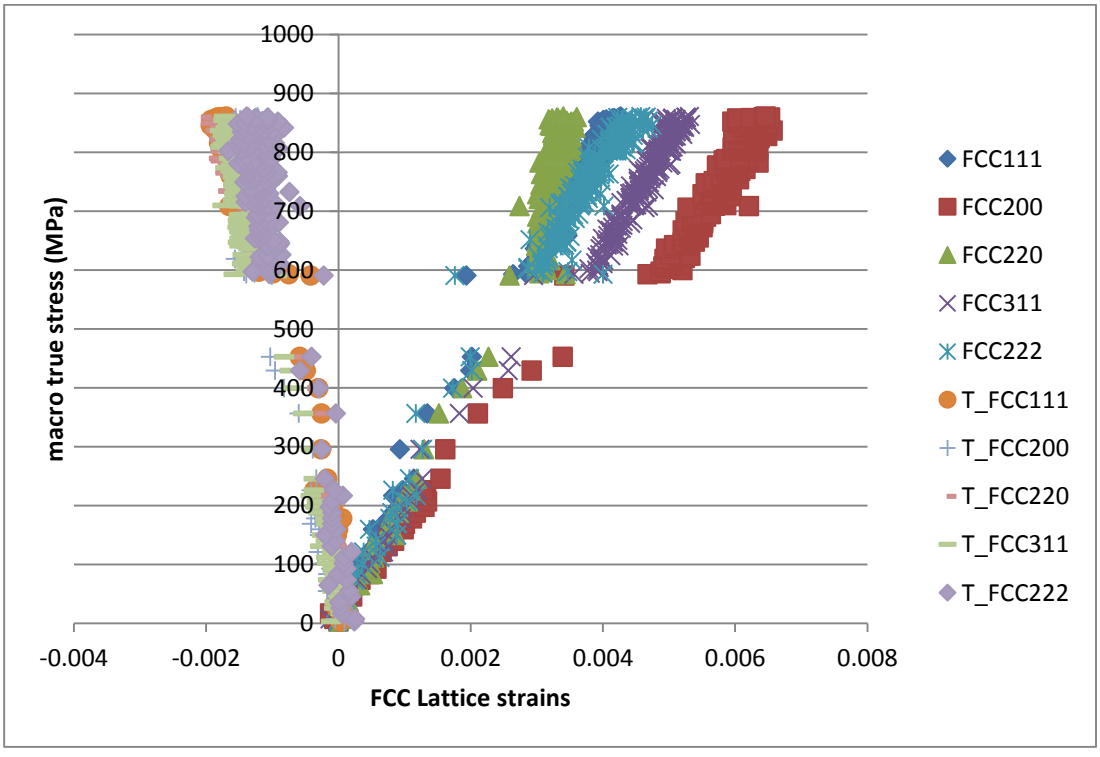

Figure E-3: True stress vs. lattice strains for FCC planes in high Ni alloy

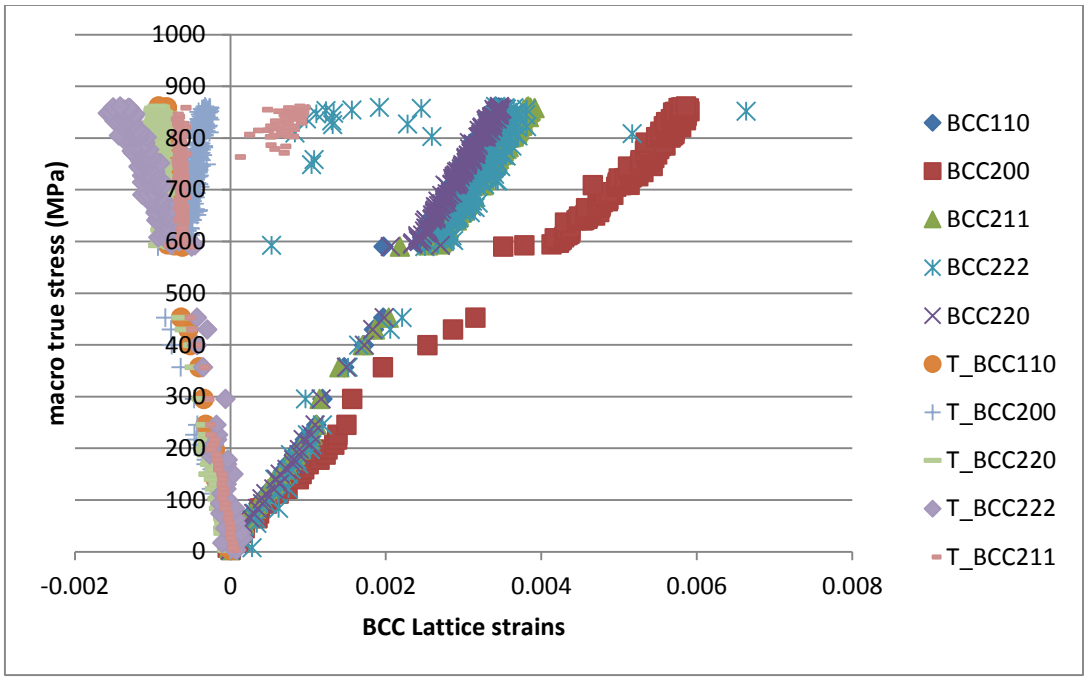

Figure E-4: True stress vs. lattice strains for BCC planes in high Ni alloy

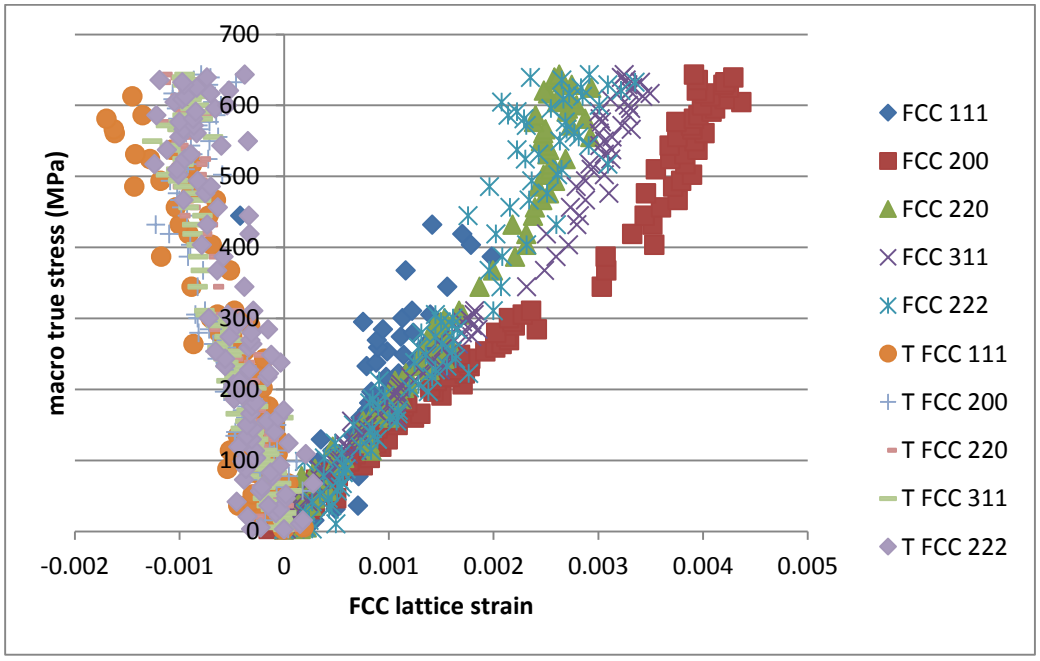

Figure E-5: True stress vs. lattice strains for FCC planes in high Mn alloy (sample 1)

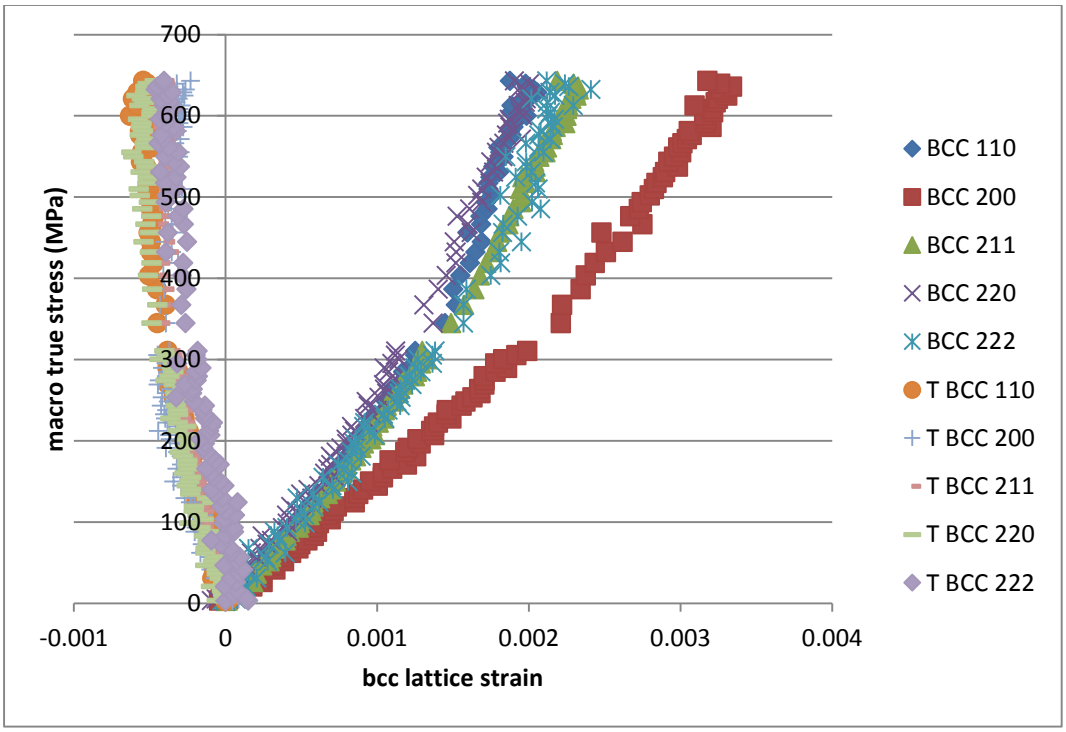

Figure E-6: True stress vs. lattice strains for BCC planes in high Mn alloy (sample 1)

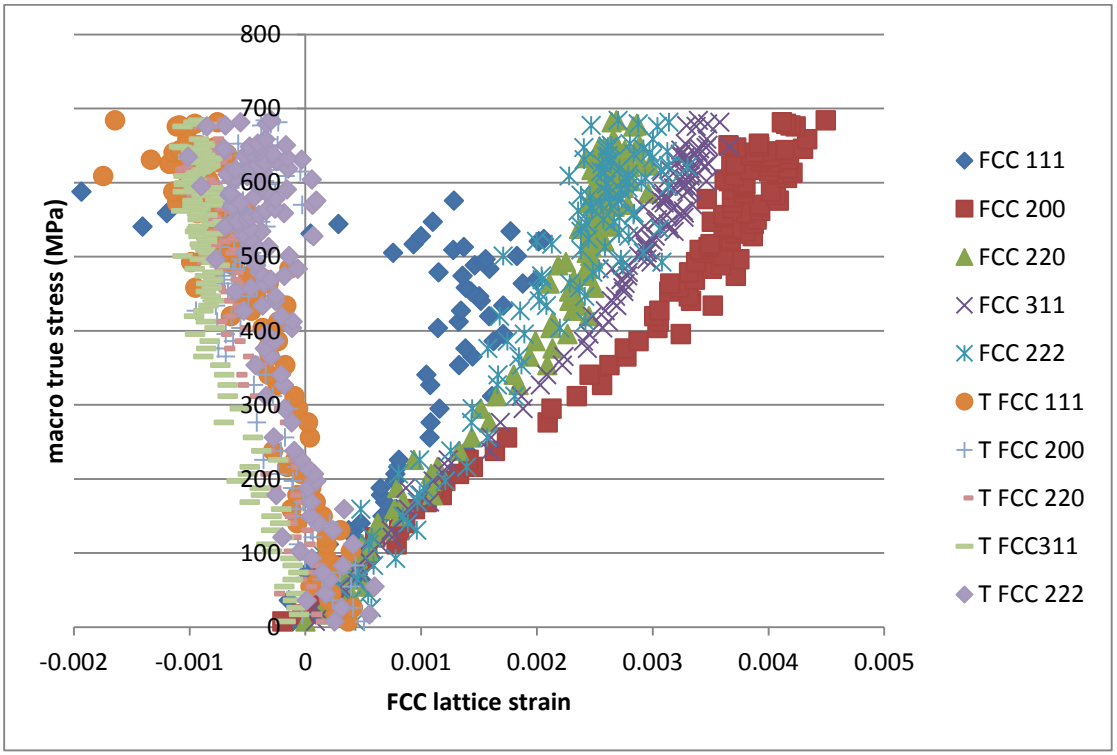

Figure E-7: True stress vs. lattice strains for FCC planes in high Mn alloy (sample 2)

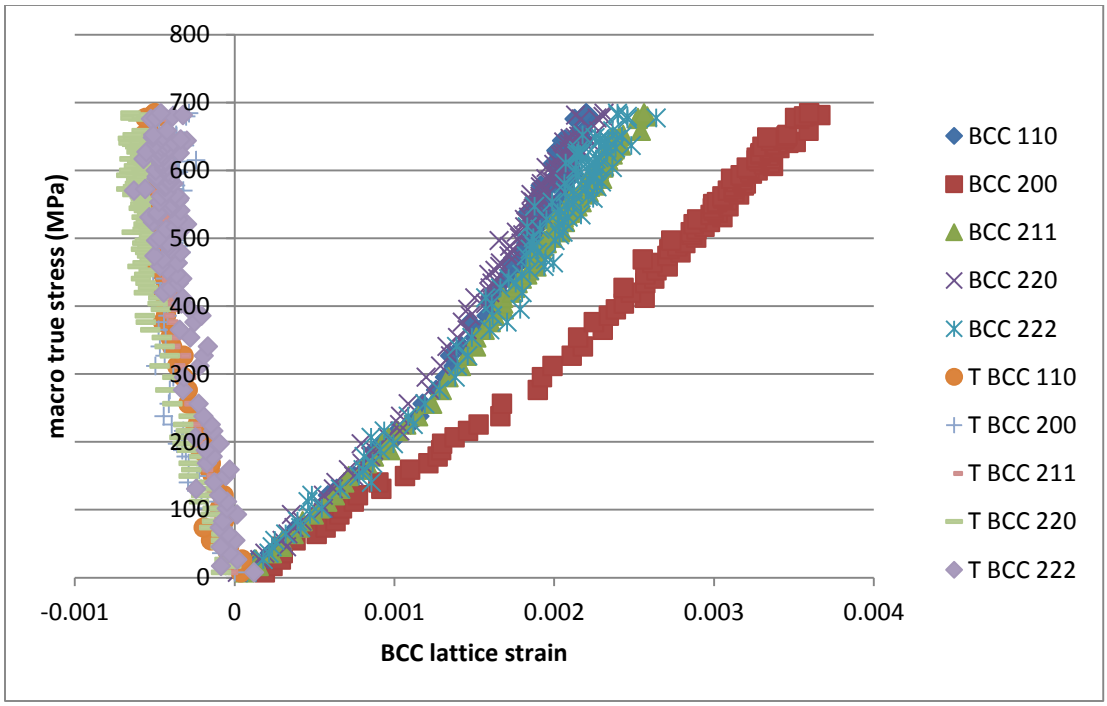

Figure E-8: True stress vs. lattice strains for BCC planes in high Mn alloy (sample 2)

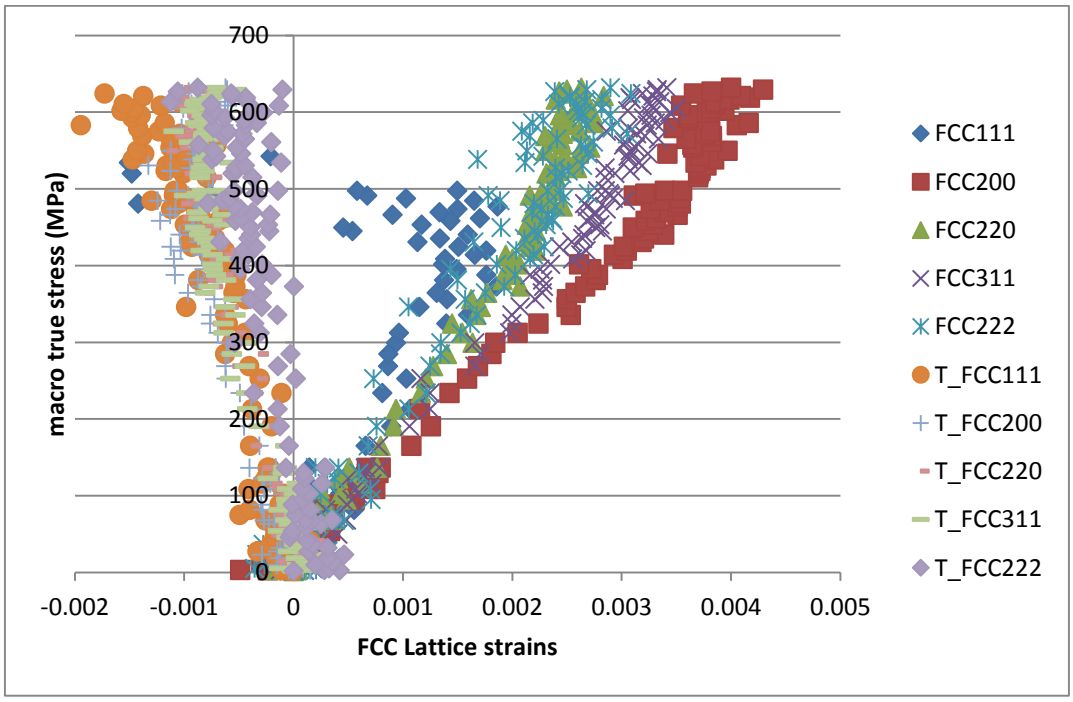

Figure E-9: True stress vs. lattice strains for FCC planes in high Mn alloy (sample 3)

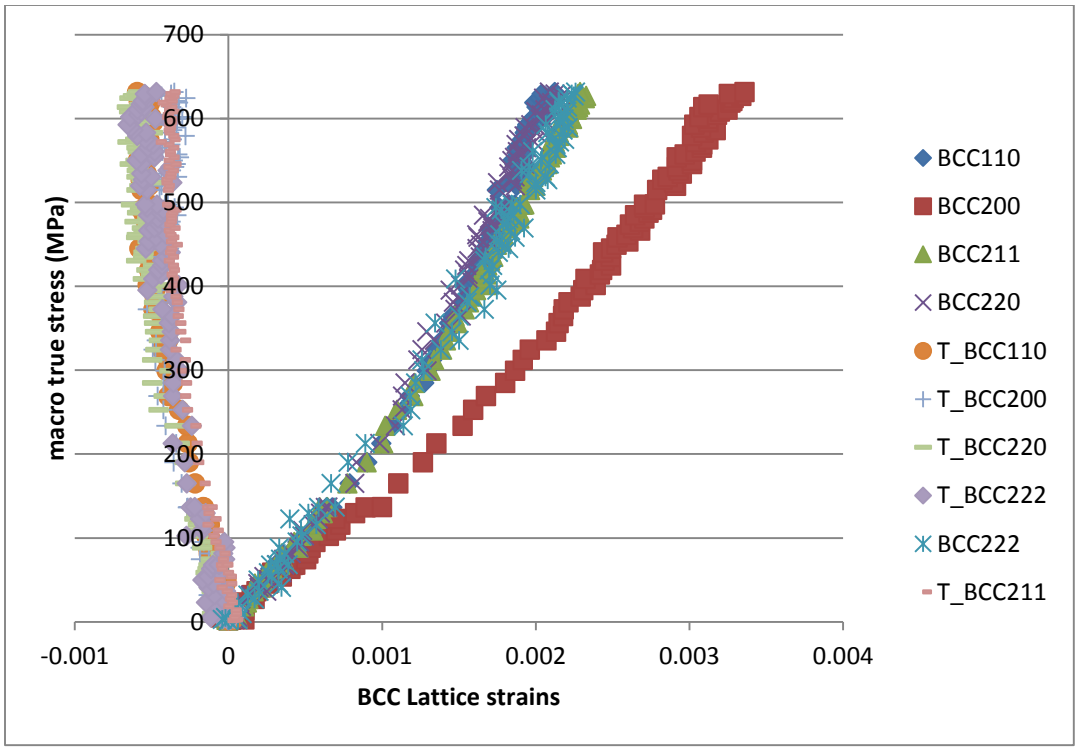

Figure E-10: True stress vs. lattice strains for BCC planes in high Mn alloy (sample 3)

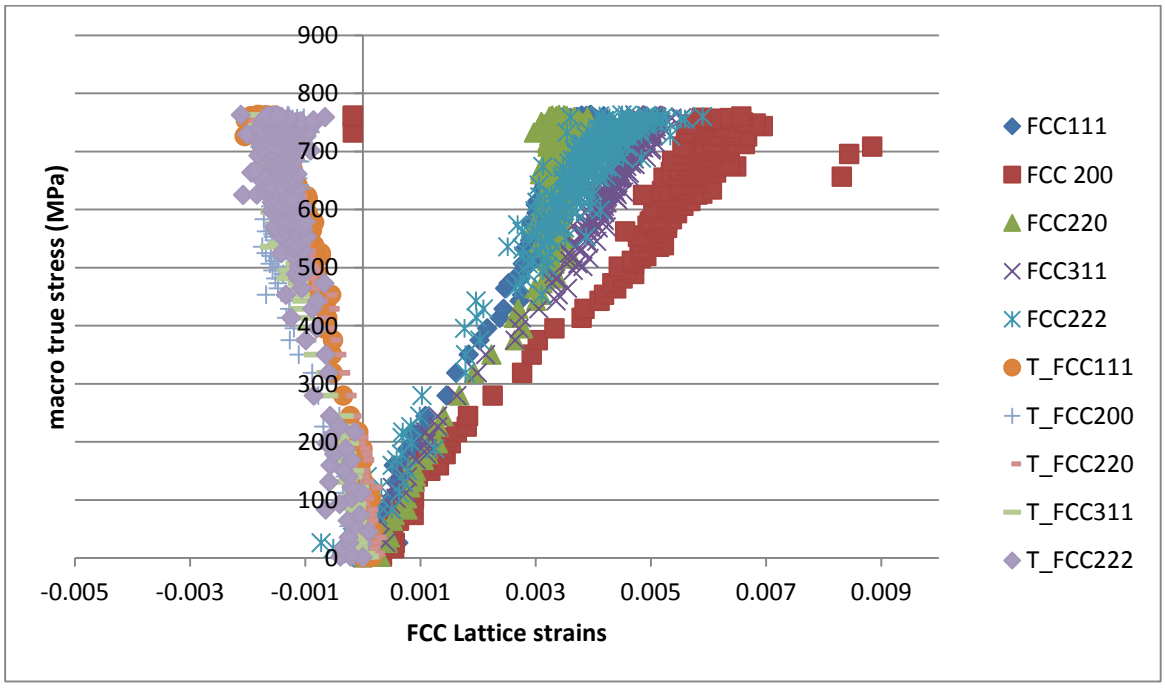

Figure E-11: True stress vs. lattice strains for FCC planes in Ni-Mn alloy (sample 2)

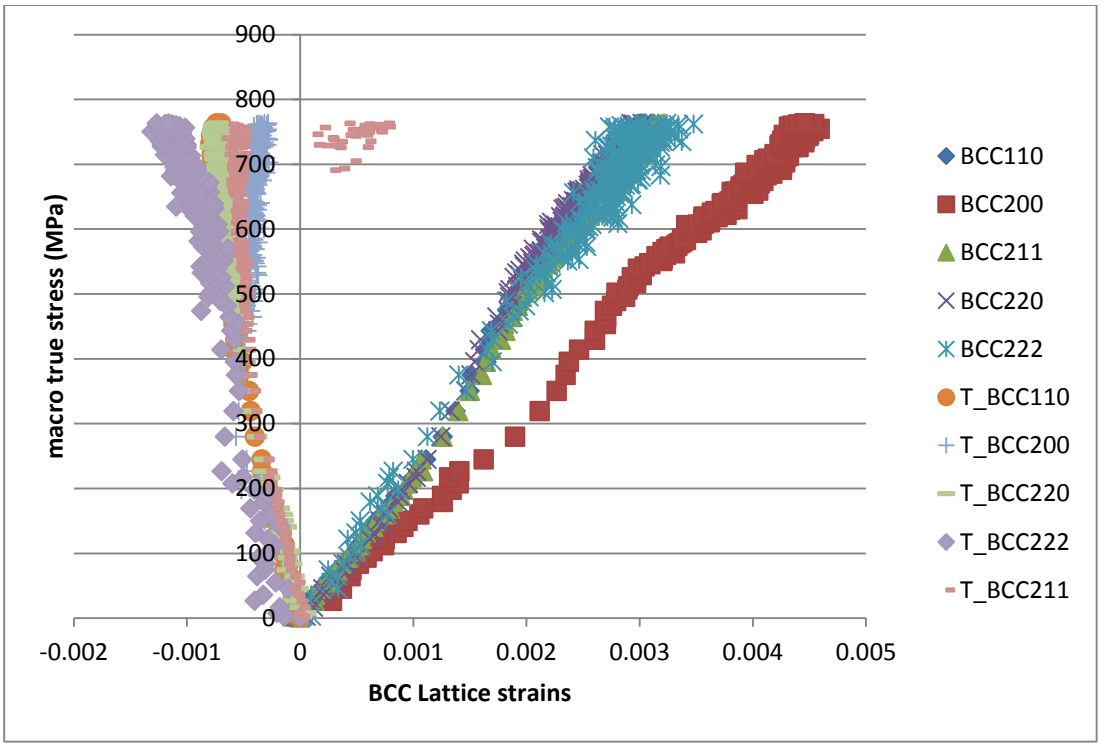

Figure E-12: True stress vs. lattice strains for BCC planes in Ni-Mn alloy (sample 2)

E.ii Lattice Diffraction data for all planes for the tested alloy chemistries

This Table is an extended version of the Table 4.14.

Table E-1: DEC and Poisson's ratio for the FCC and BCC planes

Alloy	FCC/BCC	(hkl)	DEC (long)	DEC (tran)	Poisson's Ratio
Low Ni	FCC	111	182	-552	0.2422
		200	138	-334	0.247
		220	173	-529	0.2921
		311	156	-460	0.2871
		222	197	N/A	N/A
		331	159	-340	N/A
		420	163	-383	0.2673
		422	165	-552	0.2395
		511	147	N/A	N/A
		600	N/A	N/A	N/A
	BCC	110	204	-670	0.3004
		200	140	-416	0.3337
		211	201	-712	0.2784
		220	202	-667	0.2832
		222	226	-974	0.2125
		321	213	-674	0.2919
		400	141	N/A	N/A
		411	176	N/A	N/A
		332	194	N/A	N/A
High Ni	FCC	111	196	-481	N/A
		200	144	-309	0.3347
		220	187	-450	0.2704
		311	164	-391	0.2453
		222	172	-209	0.2837
		420	141	-252	0.3355
		422	158	N/A	N/A
		333,511	1925	N/A	N/A
		442,600	N/A	N/A	N/A
	BCC	110	206	-694	0.2763
		200	154	-447	0.3123
		211	216	-807	0.2545
		220	203	-632	0.2907
		310	168	-470	0.3315
		222	187	-323	N/A
		321	206	-622	0.2936
		400	106	N/A	N/A

Alloy	FCC/BCC	(hkl)	DEC (long)	DEC (tran)	Poisson's Ratio
		330	168	-466	0.2722
		420	168	-359	0.3611
		332	197	N/A	N/A
		442	215	-273	0.278
High Mn	FCC	111	196	-449	0.2992
		200	123	-319	0.3047
		220	175	-416	0.3219
		311	152	-403	0.347
		222	172	-442	0.263
		420	130	N/A	N/A
		422	130	N/A	N/A
		333	158	N/A	N/A
	BCC	110	238	-749	0.3088
		200	159	-592	0.2471
		211	231	-853	0.2625
		220	240	-757	0.2901
		310	172	-621	0.2621
		222	220	-729	0.2445
		321	224	-777	0.2726
		400	N/A	N/A	N/A
		330,411	190	-583	0.2792
		420	187	-477	0.2477
		332	218	-408	0.2142
		422	188	N/A	N/A
Ni-Mn	FCC	111	172	-555	0.2378
		200	158	-490	0.2981
		220	169	-447	0.2771
		311	162	-697	0.2147
		222	216	-321	0.27771
		331	152	-465	0.2348
		420	128	-217	0.3177
		422	N/A	N/A	N/A
		511,333	N/A	N/A	N/A
		600,442	170	N/A	N/A
	BCC	110	209	-726	0.2754
		200	149	-449	0.3262
		211	213	-754	0.2751
		220	212	-763	0.2685
		310	167	-507	0.3189
		222	N/A	N/A	N/A
		321	208	-735	0.2672
		400	130	N/A	N/A

Alloy	FCC/BCC	(hkl)	DEC (long)	DEC (tran)	Poisson's Ratio
		411	180	-506	0.3275
		332	211	N/A	N/A
		420	170	-448	0.2867
		422	190	-364	0.3022

NOTE: The EDC and Poisson's ratio values with poor linear data fit have been removed.

Appendix F : Residual Strain analysis

These figures are continuation of section 4.6. Discussions and analysis using these figures are included in the mentioned section.

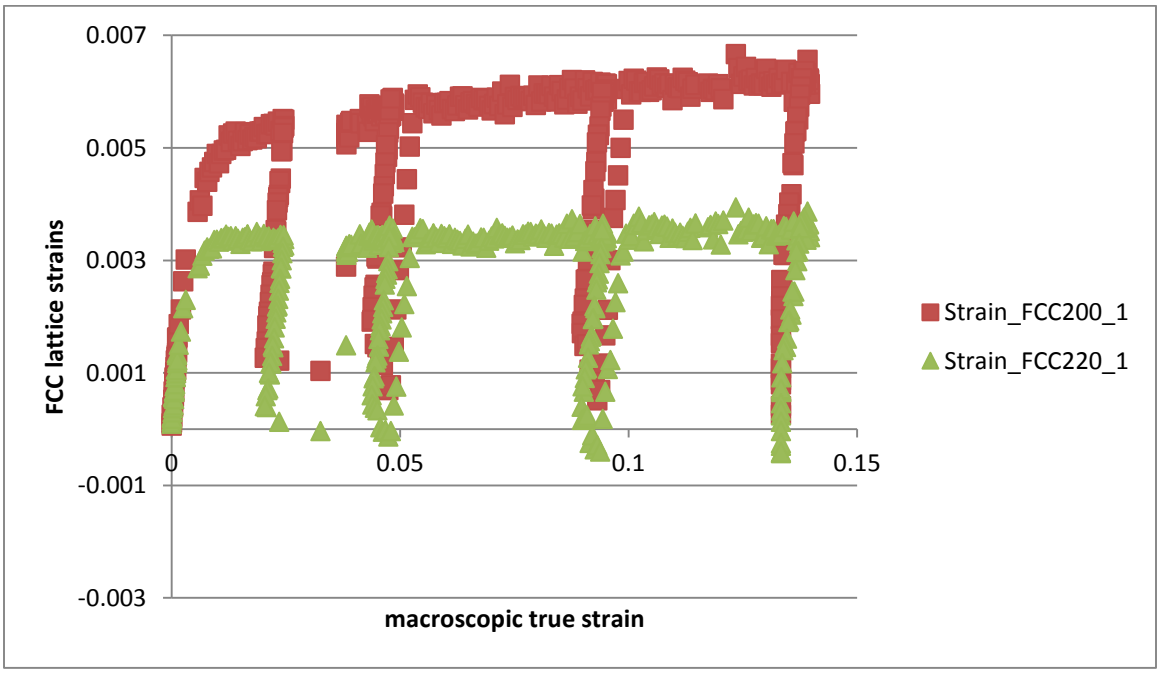

Figure F-1: True strain vs. longitudinal lattice strains for FCC planes in low Ni alloy

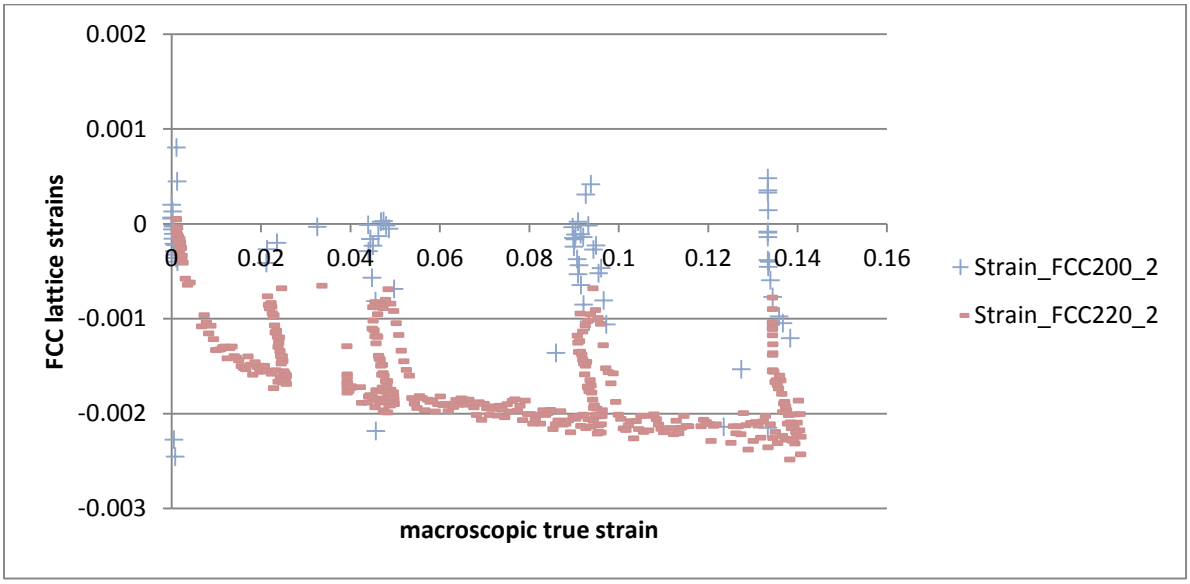

Figure F-2: True strain vs. transverse lattice strains for FCC planes in low Ni alloy

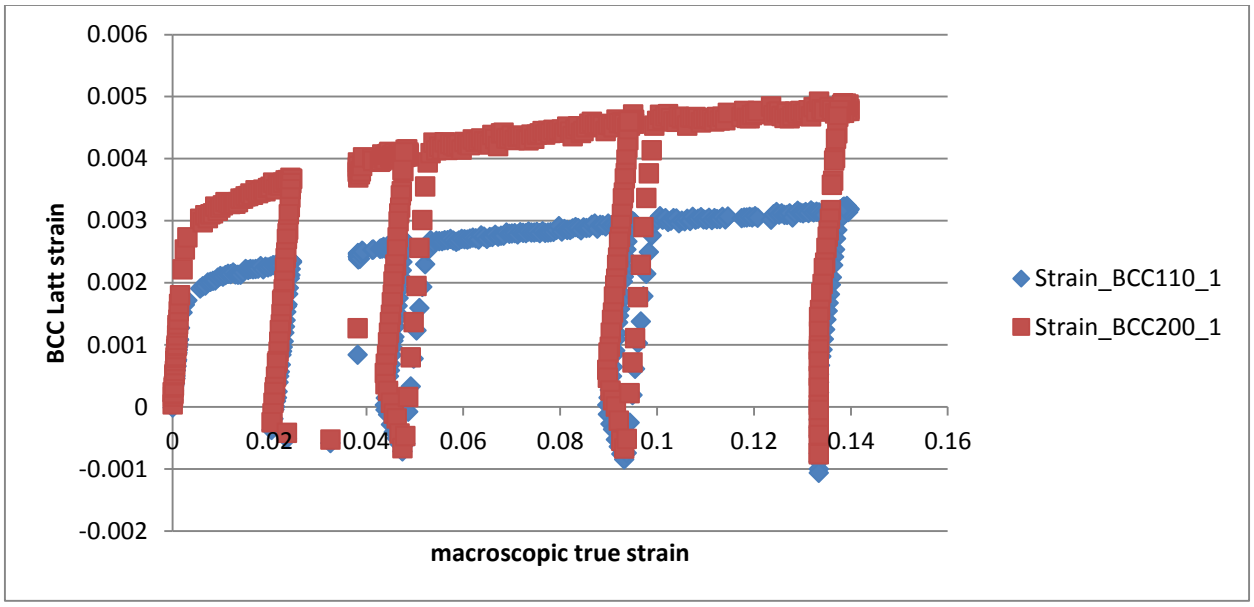

Figure F-3: True strain vs. longitudinal lattice strains for BCC planes in low Ni alloy

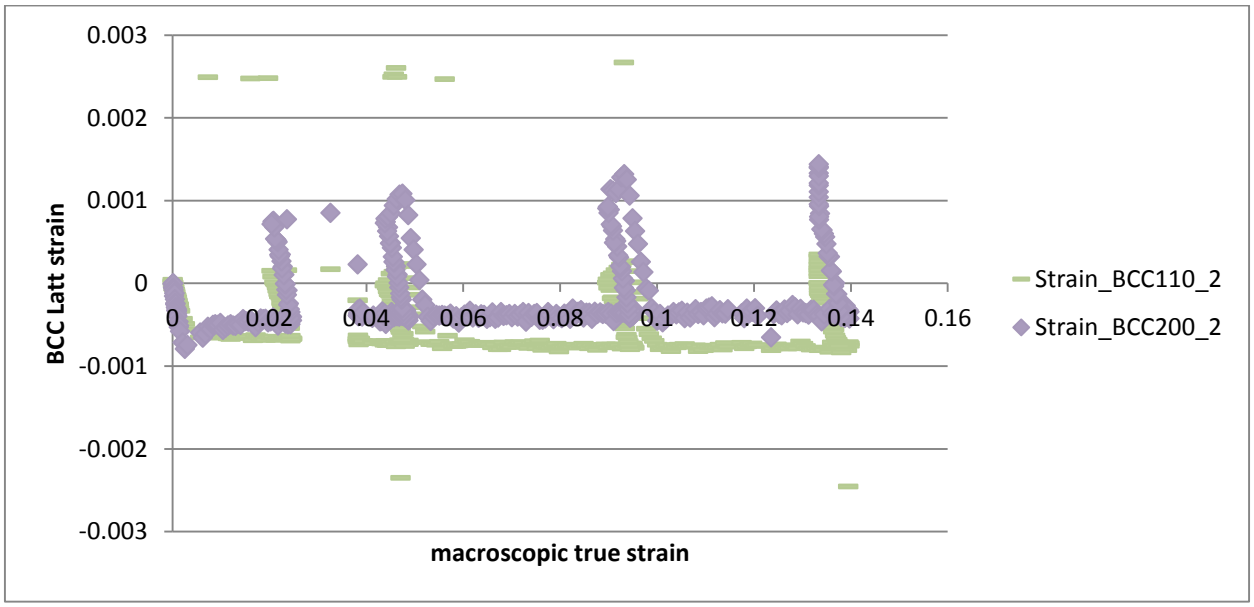

Figure F-4: True strain vs. transverse lattice strains for BCC planes in low Ni alloy

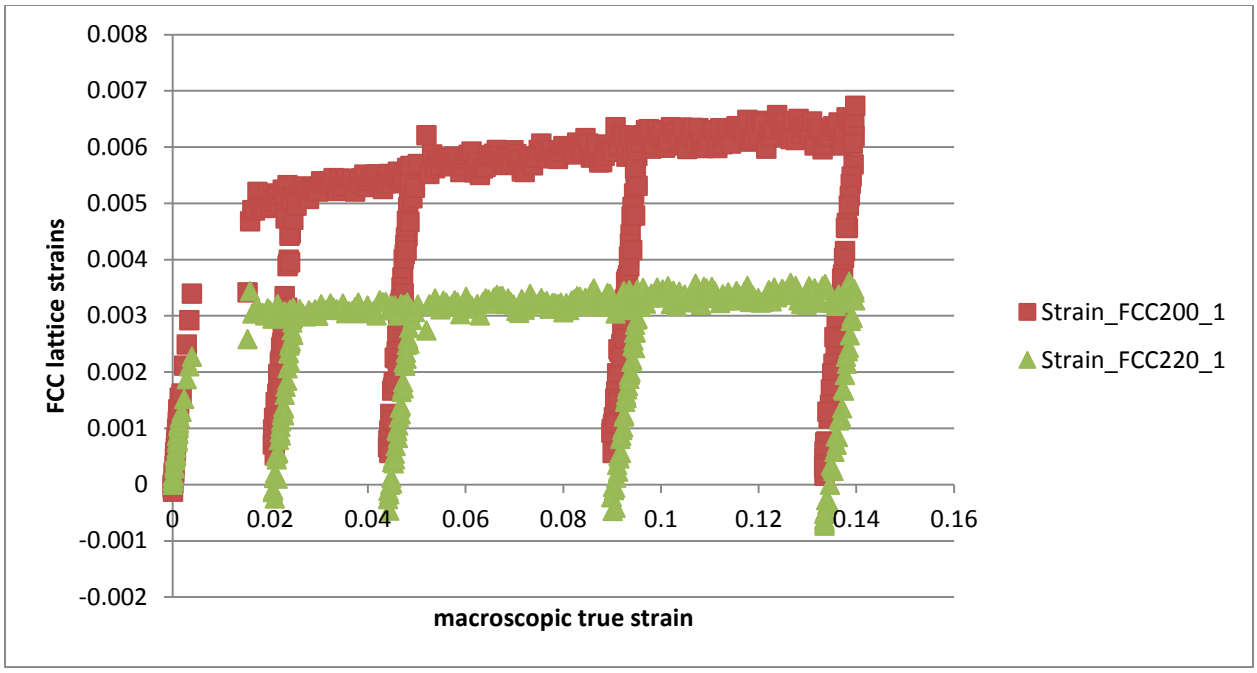

Figure F-5: True strain vs. longitudinal lattice strains for FCC planes in high Ni alloy

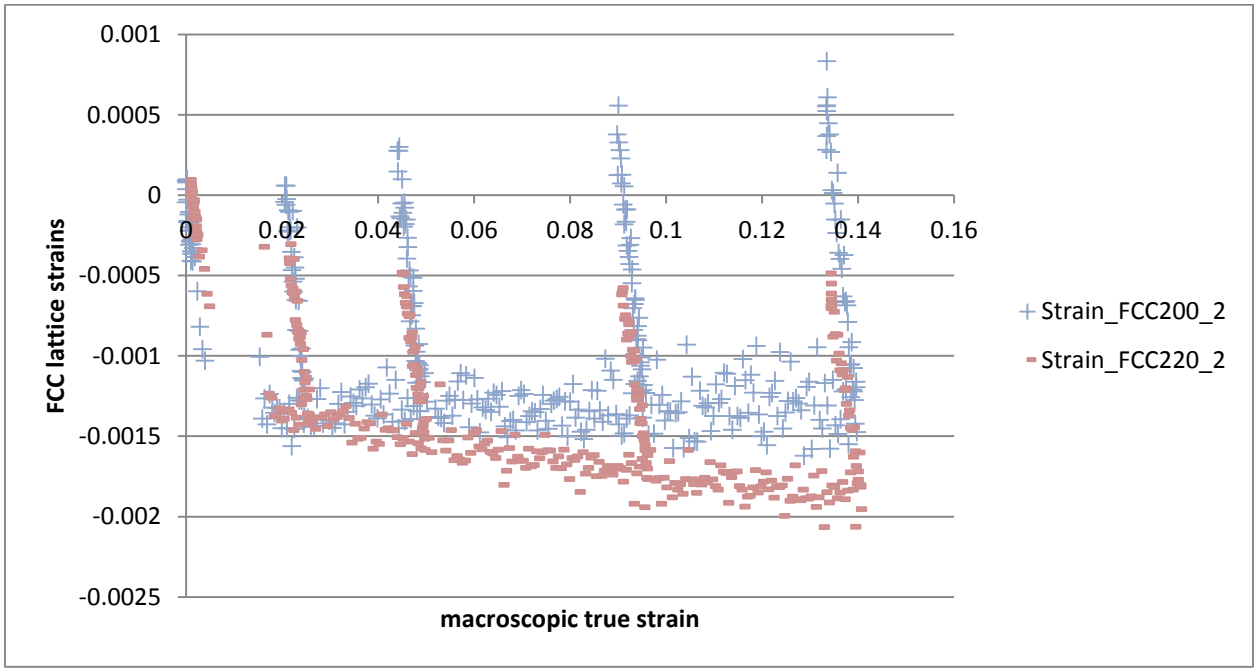

Figure F-6: True strain vs. transverse lattice strains for FCC planes in high Ni alloy

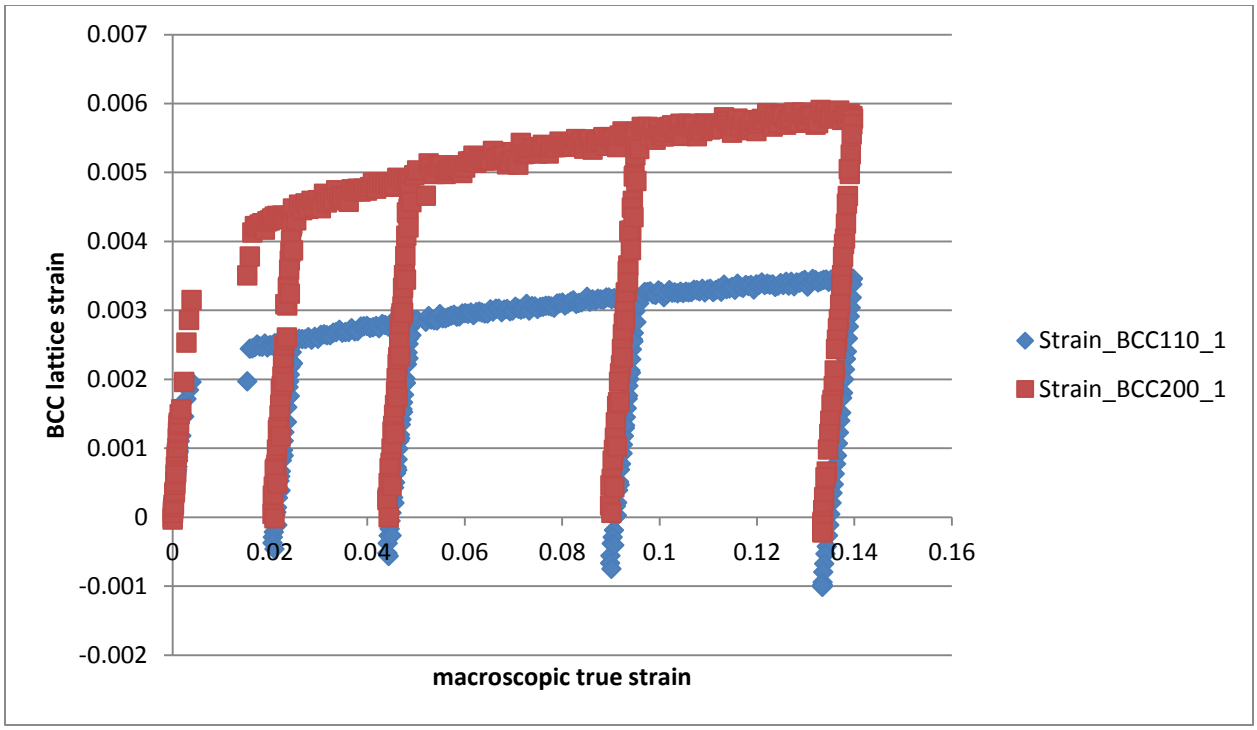

Figure F-7: True strain vs. longitudinal lattice strains for BCC planes in high Ni alloy

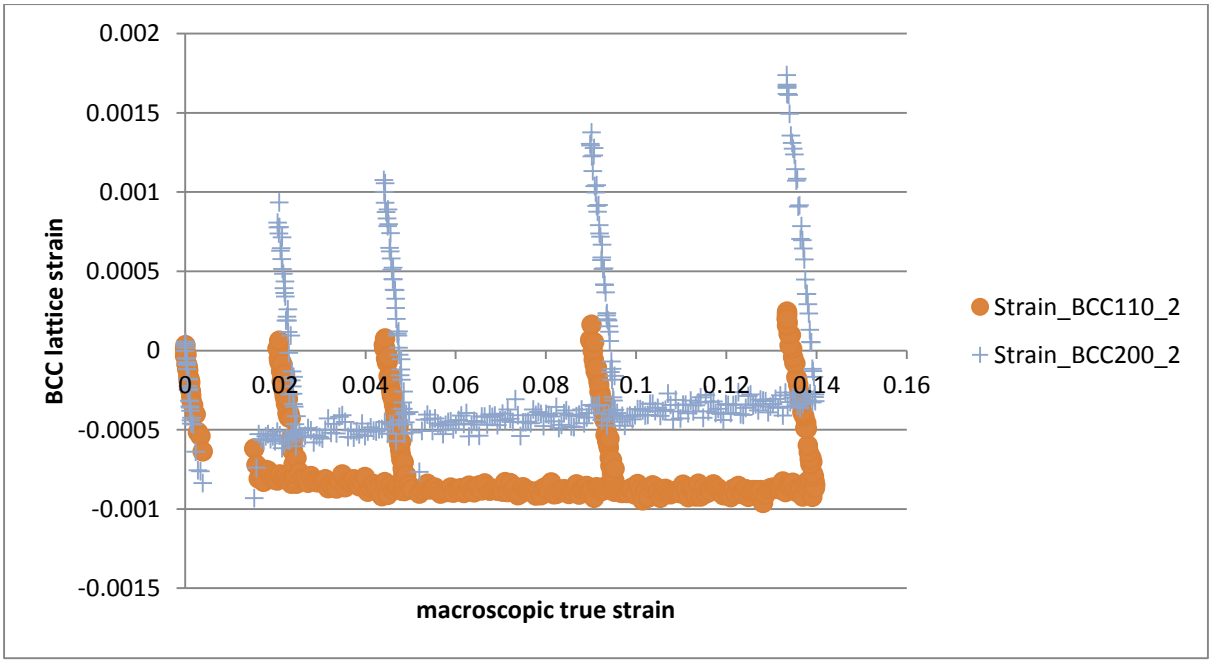

Figure F-8: True strain vs. longitudinal lattice strains for BCC planes in high Ni alloy

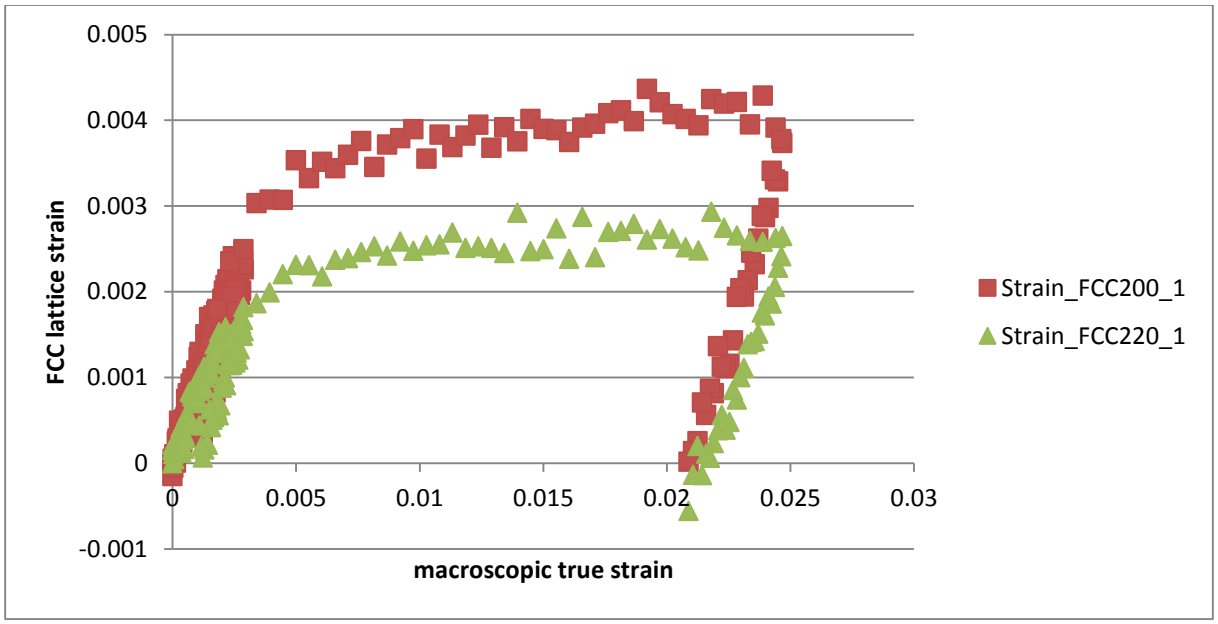

Figure F-9: True strain vs. longitudinal lattice strains for FCC planes in high Mn alloy (sample 1)

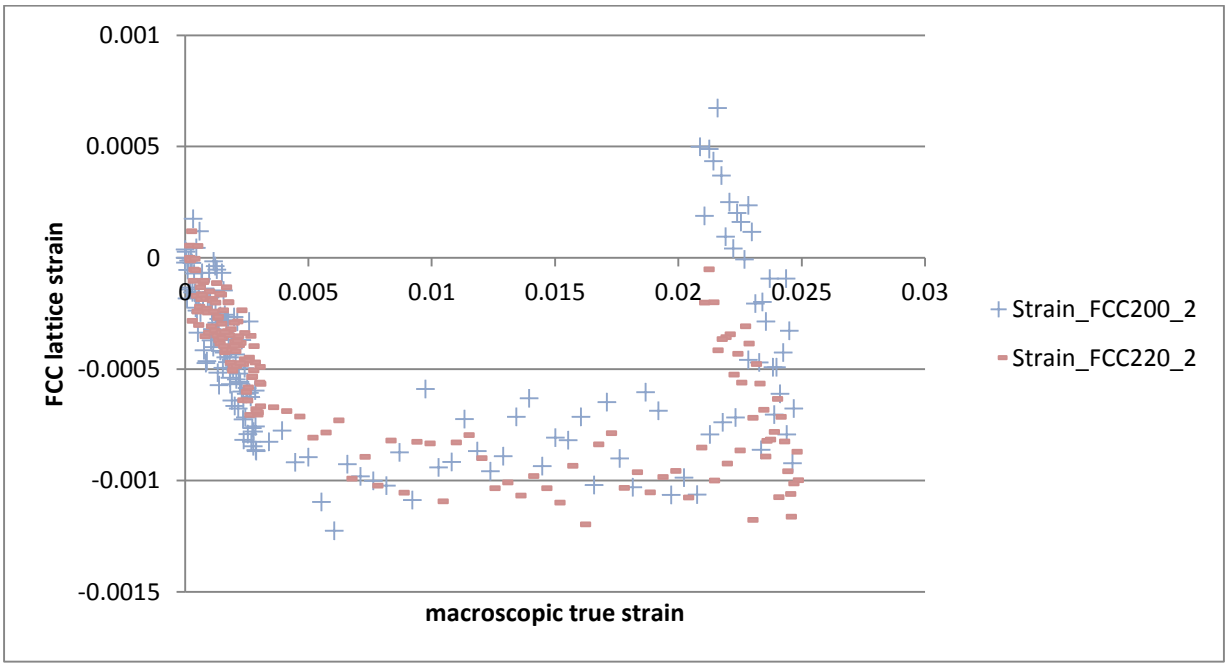

Figure F-10: True strain vs. transverse lattice strains for FCC planes in high Mn alloy (sample 1)

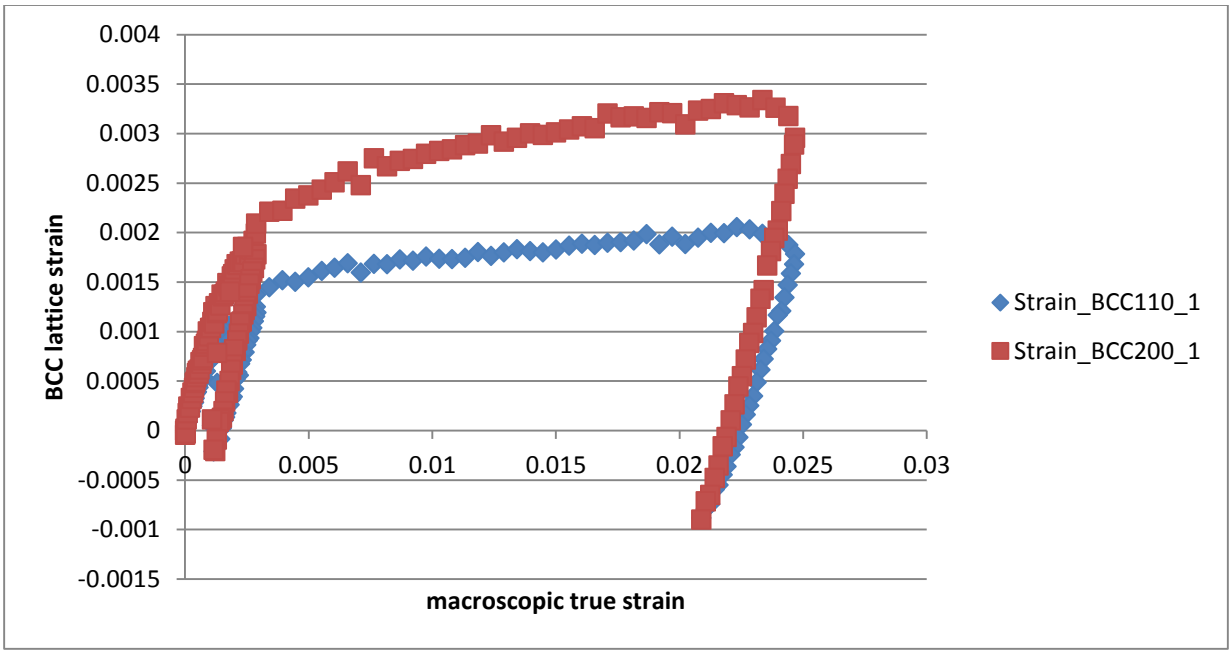

Figure F-11: True strain vs. longitudinal lattice strains for BCC planes in high Mn alloy (sample 1)

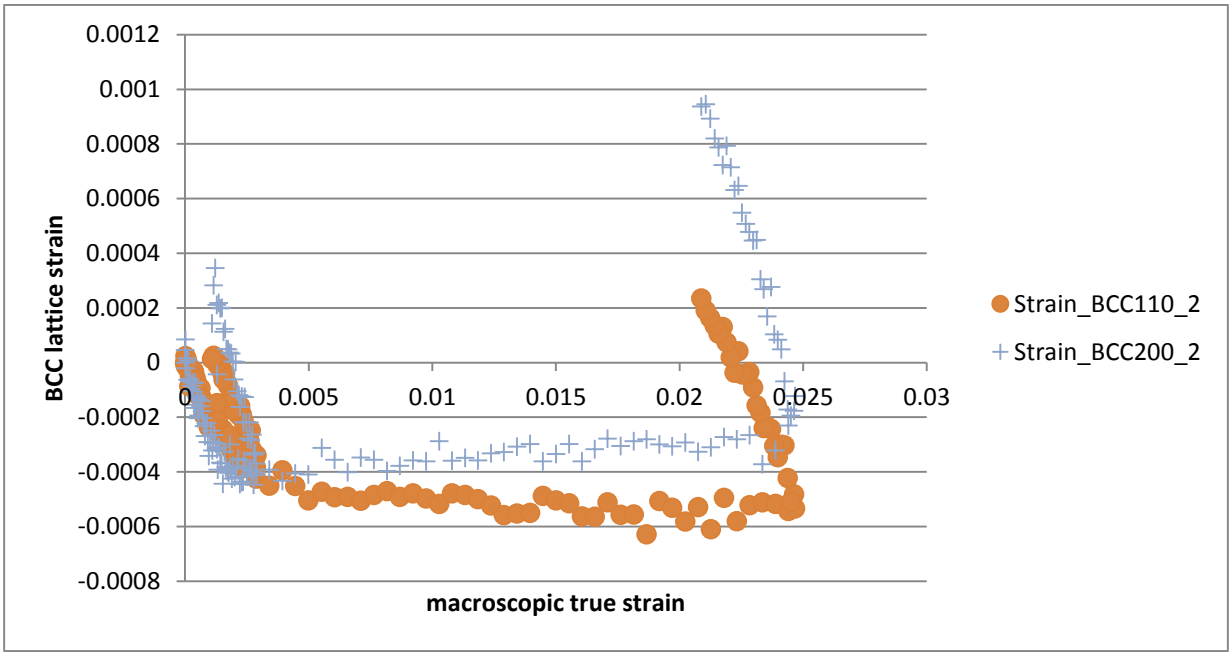

Figure F-12: True strain vs. transverse lattice strains for BCC planes in high Mn alloy (sample 1)

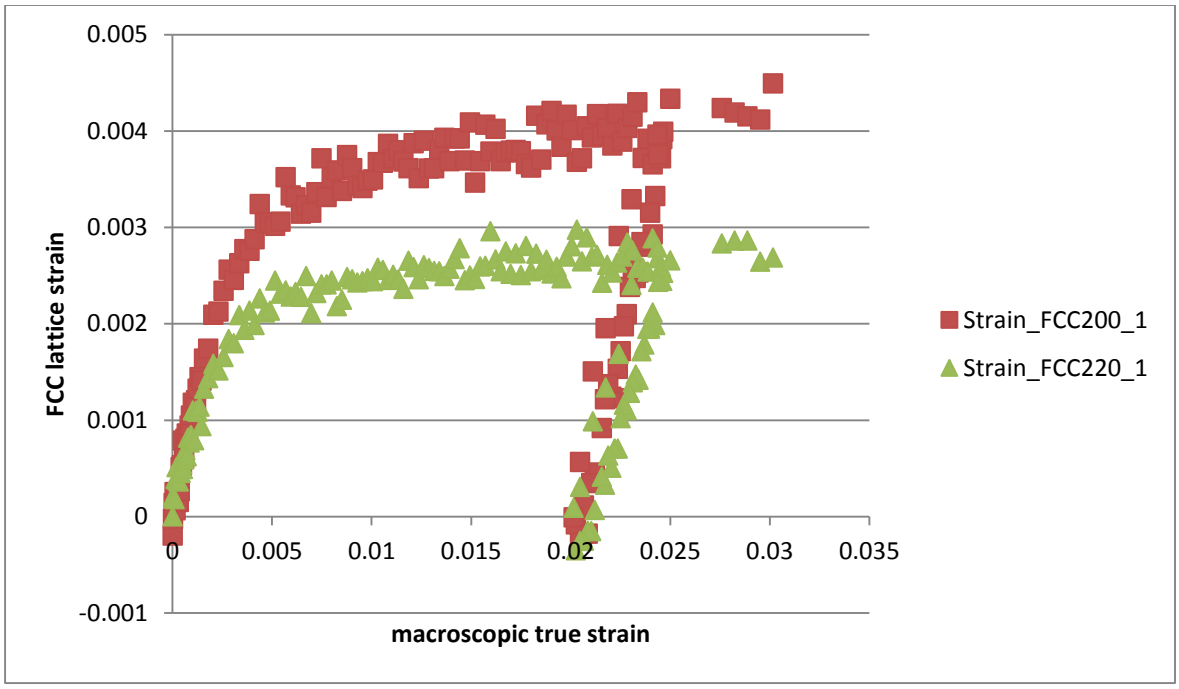

Figure F-13: True strain vs. longitudinal lattice strains for FCC planes in high Mn alloy (sample 2)

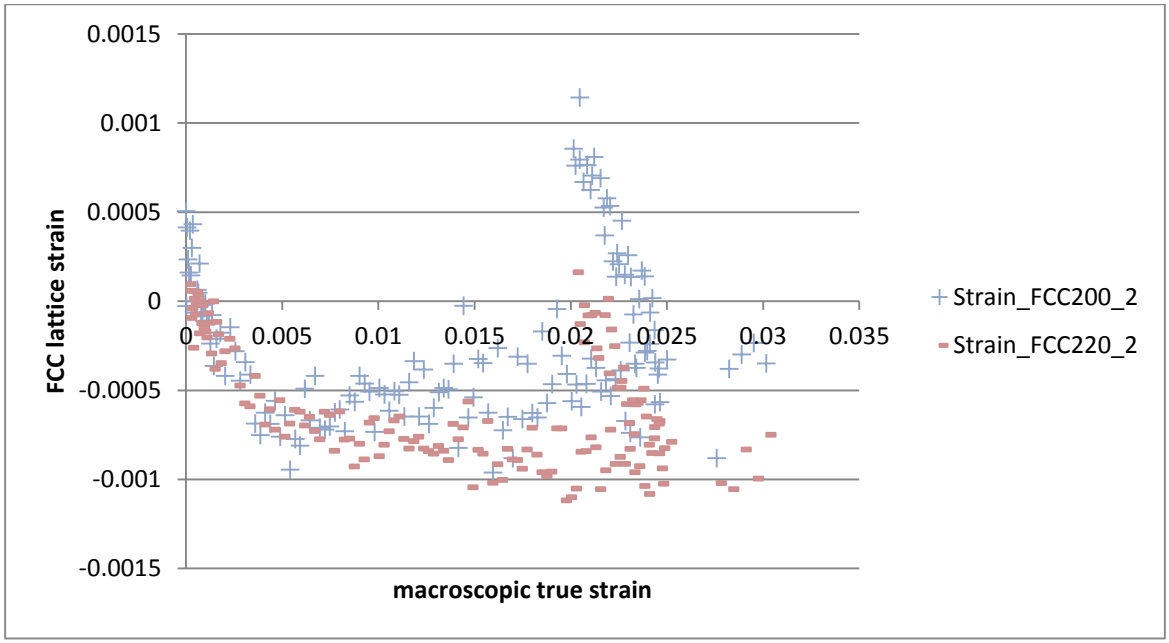

Figure F-14: True strain vs. transverse lattice strains for FCC planes in high Mn alloy (sample 2)

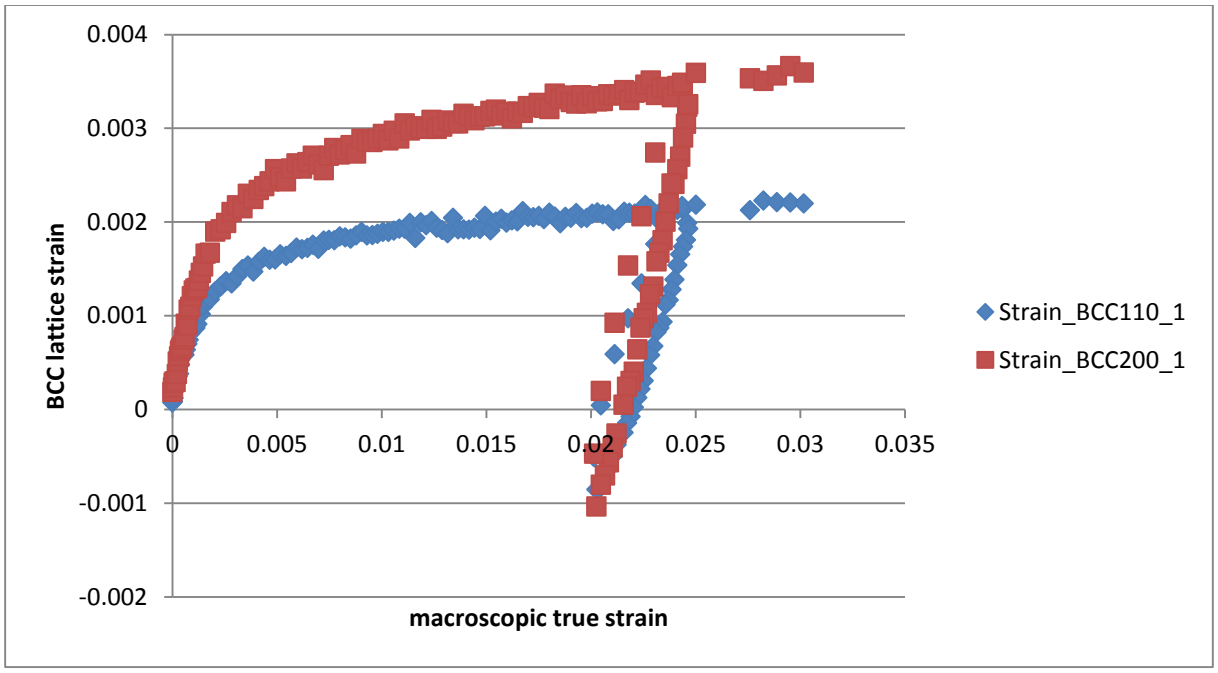

Figure F-15: True strain vs. longitudinal lattice strains for BCC planes in high Mn alloy (sample 2)

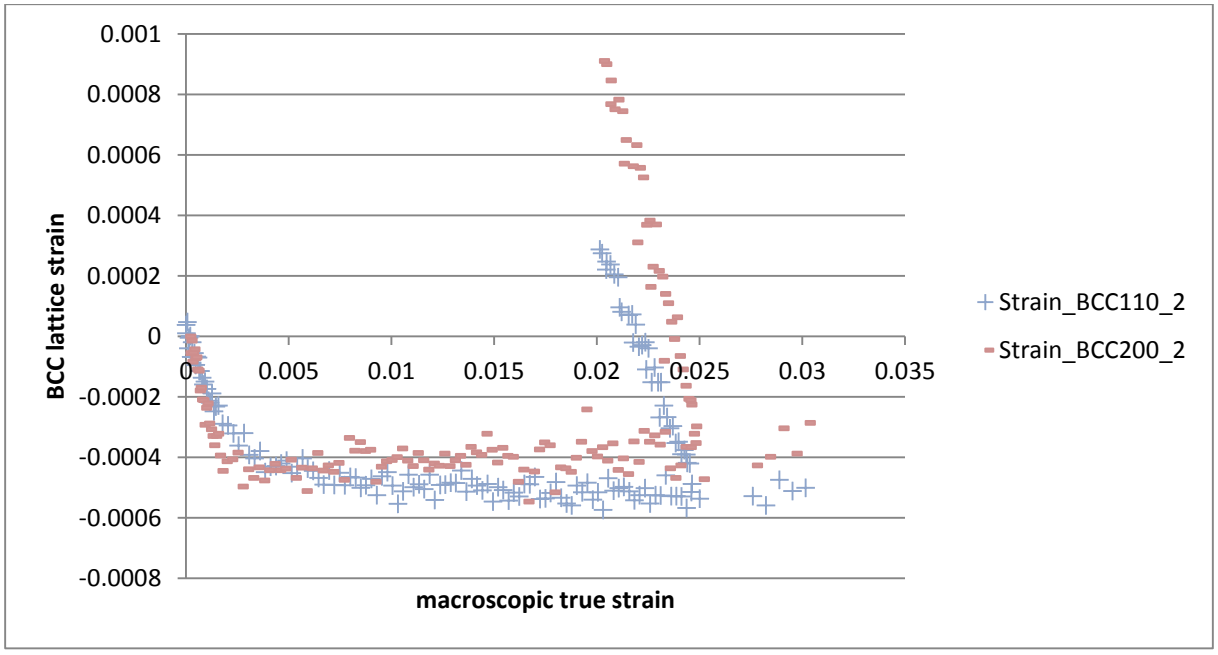

Figure F-16: True strain vs. transverse lattice strains for BCC planes in high Mn alloy (sample 2)

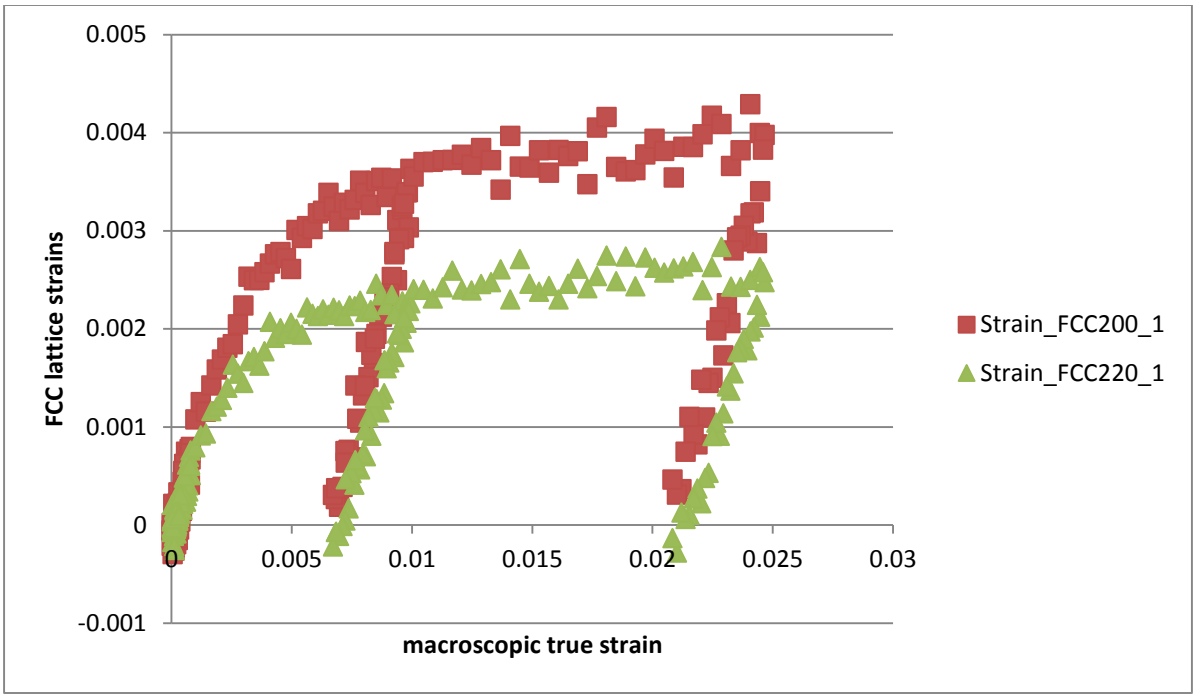

Figure F-17: True strain vs. longitudinal lattice strains for FCC planes in high Mn alloy (sample 3)

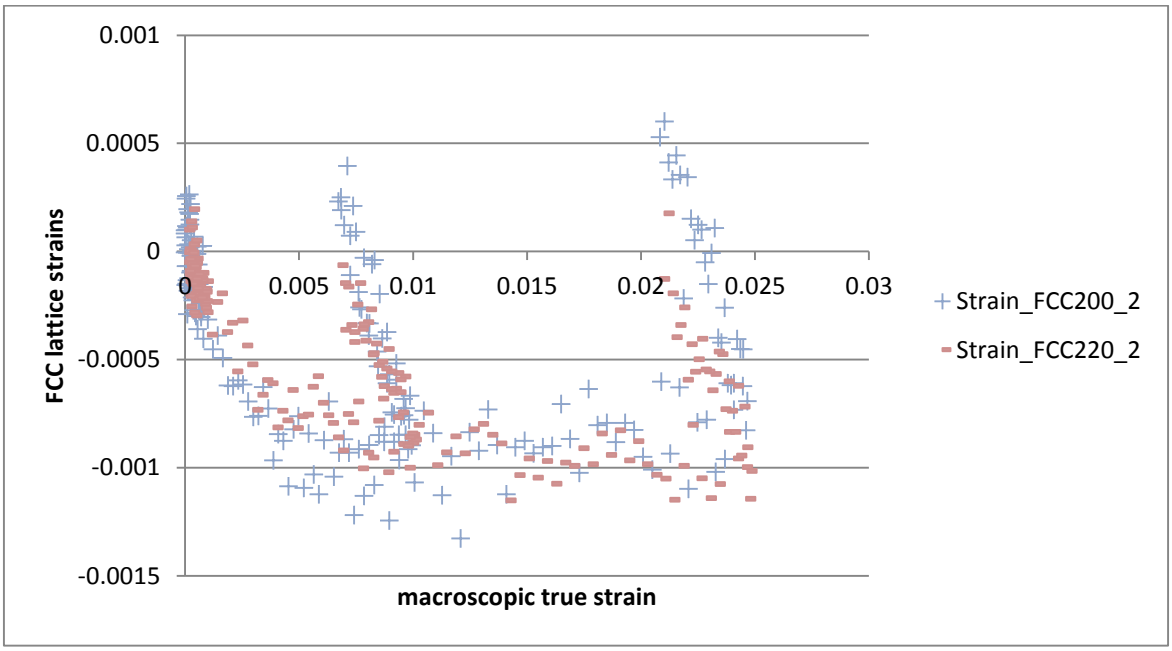

Figure F-18: True strain vs. transverse lattice strains for FCC planes in high Mn alloy (sample 3)

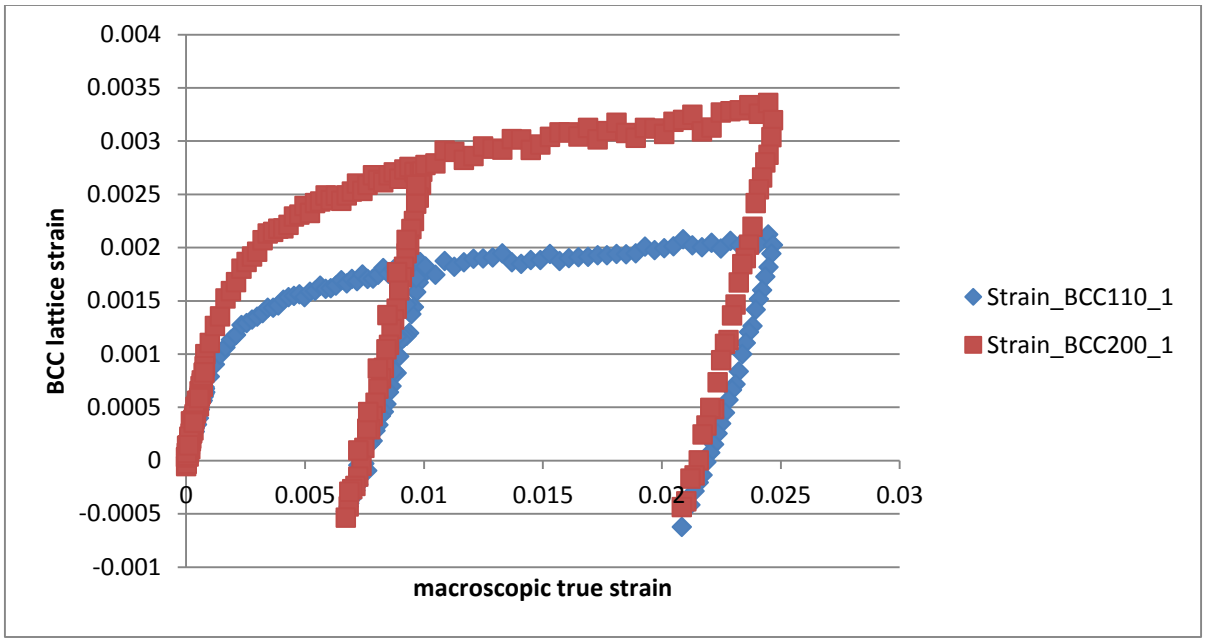

Figure F-19: True strain vs. longitudinal lattice strains for BCC planes in high Mn alloy (sample 3)

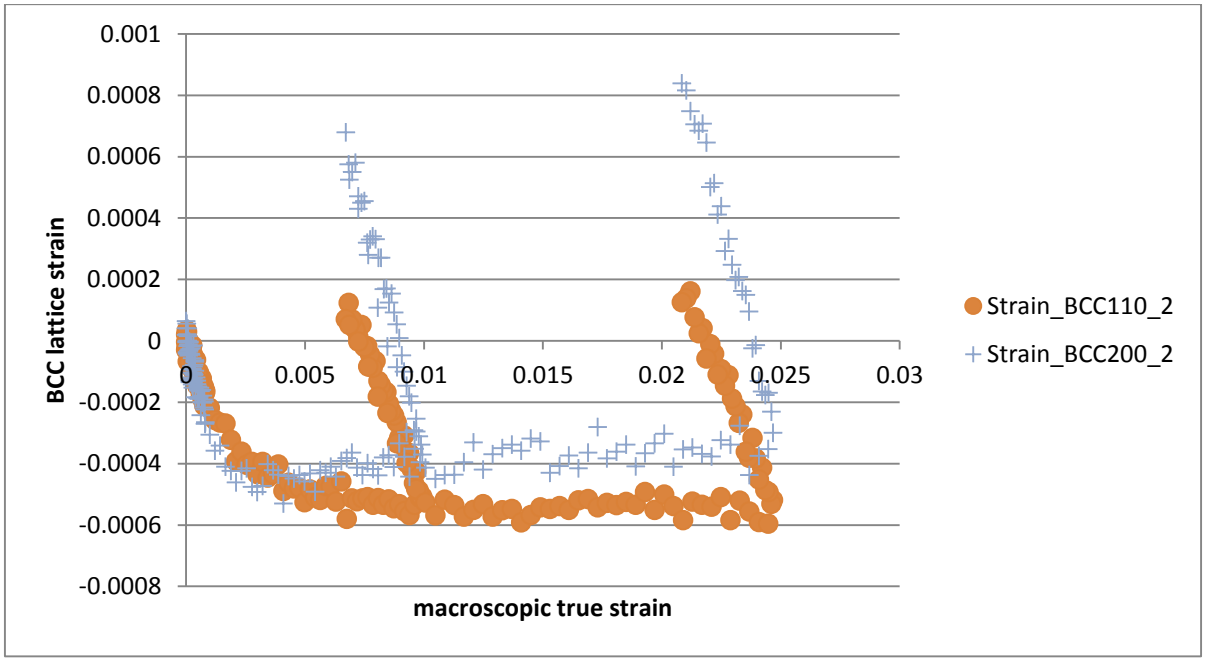

Figure F-20: True strain vs. transverse lattice strains for BCC planes in high Mn alloy (sample 3)

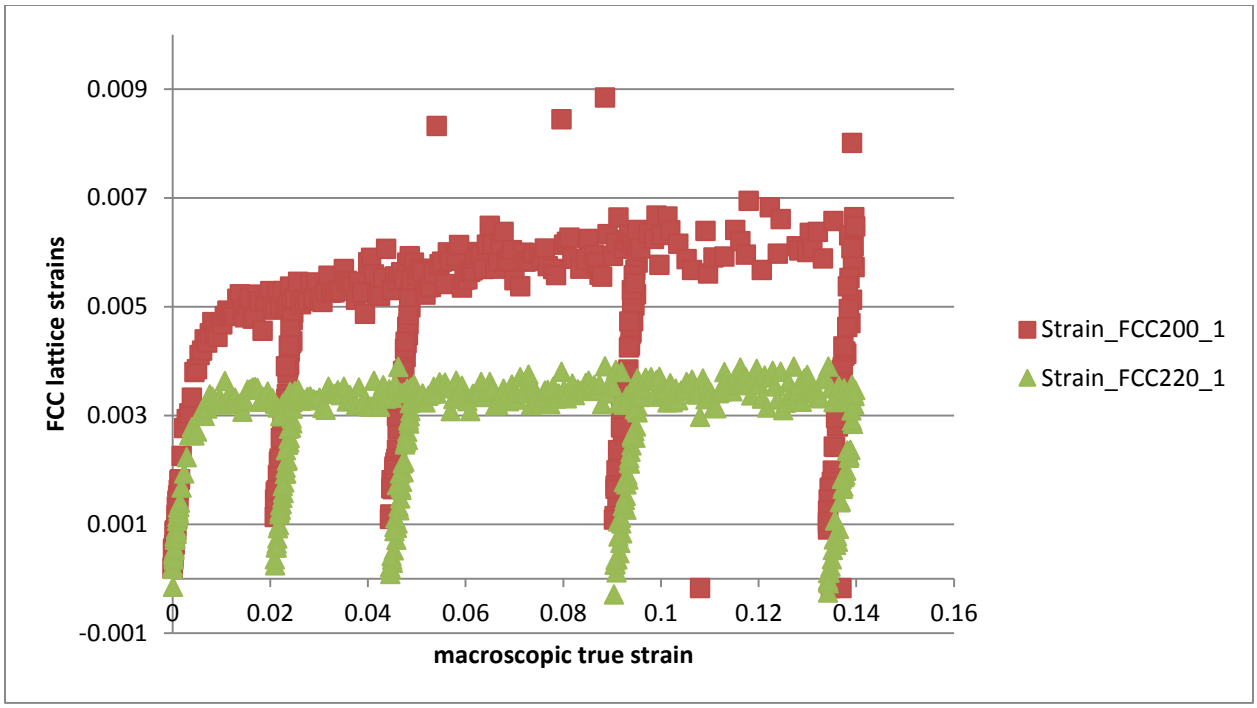

Figure F-21: True strain vs. longitudinal lattice strains for FCC planes in Ni-Mn alloy (sample 2)

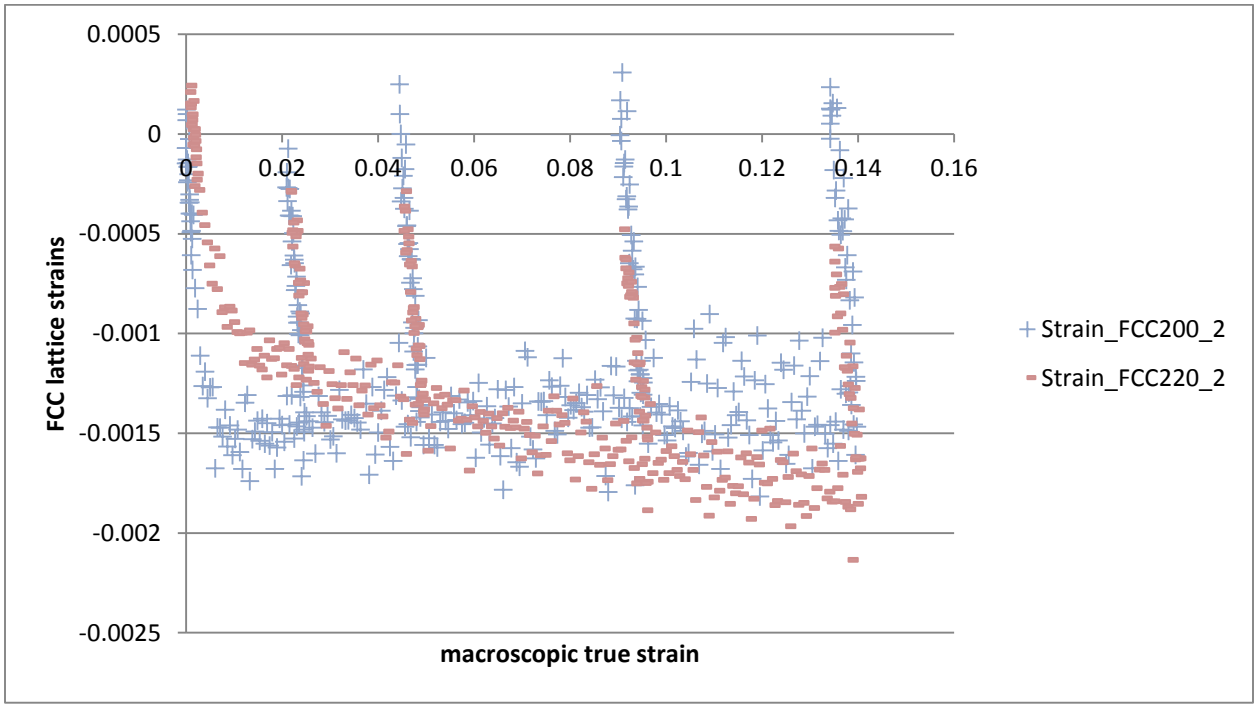

Figure F-22: True strain vs. transverse lattice strains for FCC planes in Ni-Mn alloy (sample 2)

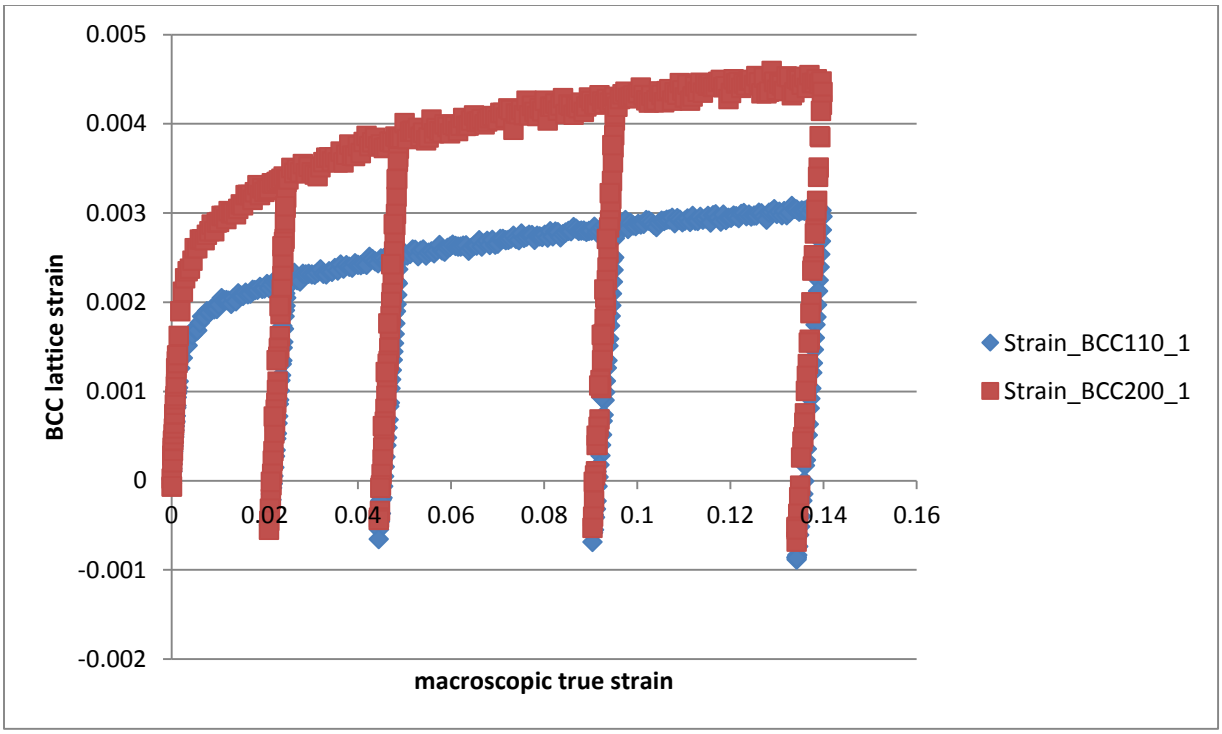

Figure F-23: True strain vs. longitudinal lattice strains for BCC planes in Ni-Mn alloy (sample 2)

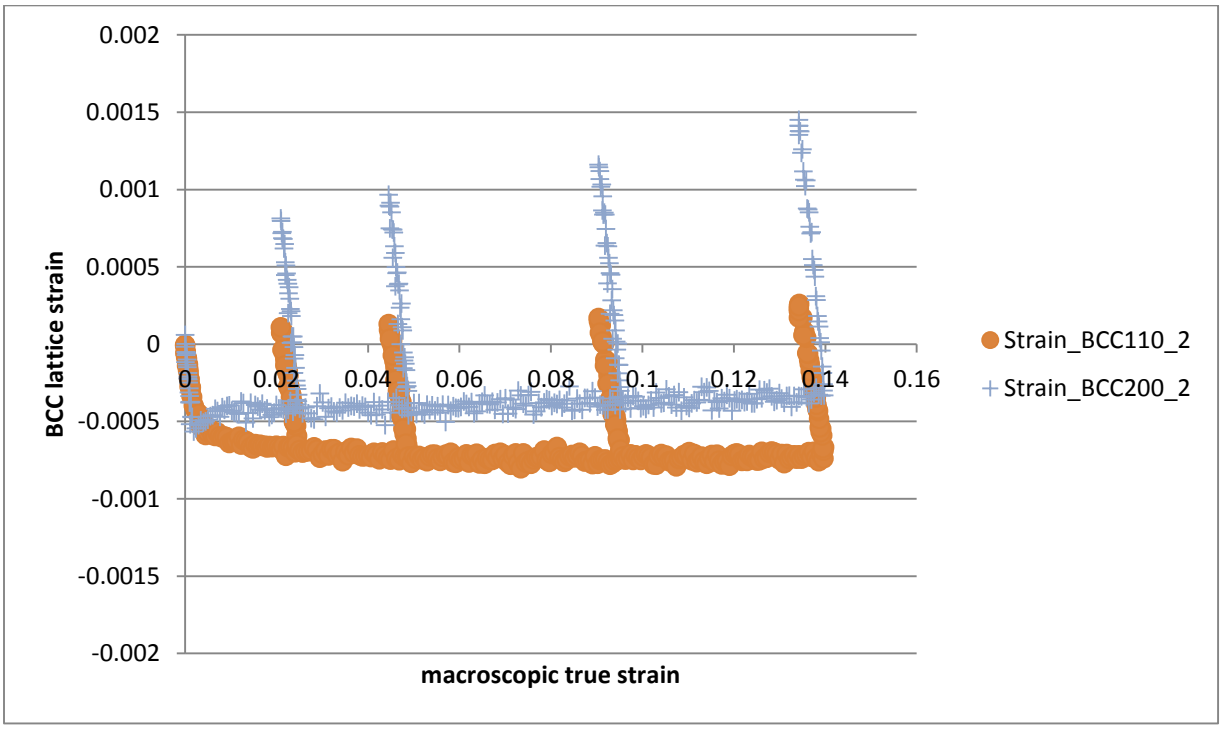

Figure F-24: True strain vs. transverse lattice strains for BCC planes in Ni-Mn alloy (sample 2)